

**High throughput methods for synthesis and impedance
characterisation of ABO_3 gas sensing materials**

Von der Fakultät für Mathematik, Informatik und Naturwissenschaften der Rheinisch-
Westfälischen Technischen Hochschule Aachen zur Erlangung des akademischen
Grades einer Doktorin der Naturwissenschaften genehmigte Dissertation

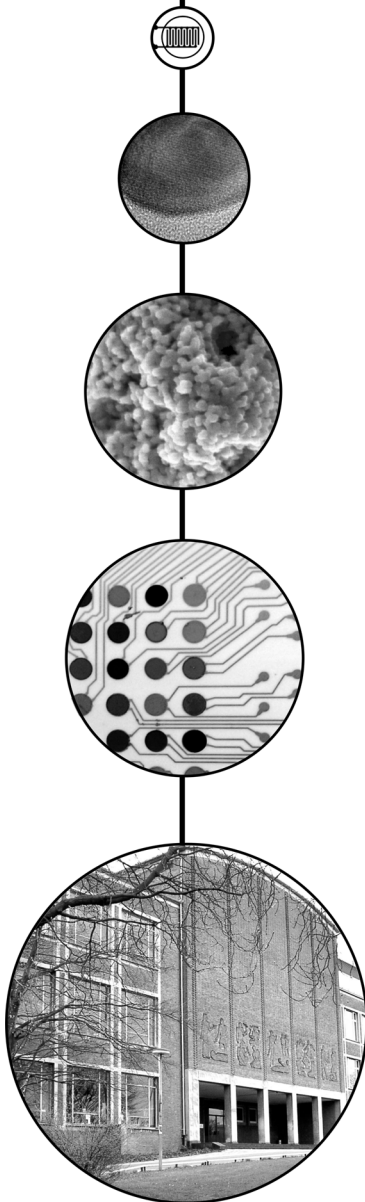
vorgelegt von

Diplom-Chemikerin Maïke Siemons
aus Stolberg im Rheinland

Berichter: Universitätsprofessor Dr. U. Simon
Universitätsprofessor Dr. W. F. Maier

Tag der mündlichen Prüfung: 21.12.2006

Diese Dissertation ist auf den Internetseiten der Hochschulbibliothek online
verfügbar.



**High throughput methods for
synthesis
and
impedance characterisation
of ABO_3 gas sensing materials**

The work presented in this thesis was carried out at the Institute of Inorganic Chemistry of the RWTH Aachen University under supervision of Prof. Dr. Ulrich Simon between September 2003 and September 2006.

I would like to thank Prof. Dr. U. Simon for giving me the opportunity to work on an exciting research topic with freedom, excellent conditions, and support.

I would like to thank Prof. Dr. W. F. Maier for his co-mentorship.

für meine Lieben



[kri'etiv' w3:k iz' plet]

Quotation by Stephen Nachmanovitch

Parts of this thesis have been published or submitted:

- M. Siemons, Th. Weirich, J. Mayer, U. Simon, Preparation of nanosized perovskite-type oxides via polyol method, *Z. Anorg. Allg. Chem.* 630 (2004) 2083-2089.
- D. Sanders, M. Siemons, T. Koplin, U. Simon, Development of a High-Throughput Impedance Spectroscopy Screening System (HT-IS) for Characterization of Novel Nanoscaled Gas Sensing Materials, *Mater. Res. Soc. Symp. Proc.* (2005) Vol. 876E.
- M. Siemons, U. Simon, Preparation and Gas Sensing Properties of Nanocrystalline La-doped CoTiO_3 , *Sens. Actuators B* 120(1) (2006) 110-118.
- M. Siemons, A. Leifert U. Simon, Preparation and gas sensing characteristics of nanoparticulate p-type semiconducting rare-earth orthoferrites LnFeO_3 and orthochromites LnCrO_3 ($\text{Ln}=\text{La, Pr, Nd, Sm, Eu, Gd, Tb, Dy, Ho, Er, Tm, Yb, Lu}$), *Adv. Funct. Mater.* (2006) in press.
- M. Siemons, U. Simon, Preparation and gas sensing characteristics of nanoparticulate p-type semiconducting rare-earth orthoferrites and orthochromites, *Sens. Actuators B* (2006) submitted.
- M. Siemons, U. Simon, Polyol-mediated Synthesis of LnCrO_3 ($\text{Ln}=\text{La, Pr, Sm-Lu}$), *Z. Anorg. Allg. Chem.* 632(12-13) (2006) 2159.
- M. Siemons, U. Simon, Impedometric Screening of Gas-sensitive Inorganic Materials in Combinatorial methodologies of development of chemical and biological sensors, edited by Drs. R. A. Potyrailo and V. M. Mirsky, Springer (2006) submitted.
- M. Siemons, U. Simon, High throughput screening of the sensing properties of doped SmFeO_3 , *Sol. State Phenom.* (2006) accepted.
- T. J. Koplin, M. Siemons, C. Océn-Valéntin, D. Sanders, U. Simon, Workflow for High-Throughput Screening of Gas Sensing Materials, *Sensors*, 6 (2006) 298-307.
- S. Roggan, C. Limberg, B. Ziemer, M. Siemons, U. Simon, The reactivity and properties of $[-\text{O-Bi}^{\text{III}}\cdots\text{O=Mo-}]_n$ chains, *Inorganic Chemistry* 45(22) (2006) 9020-9031.

Other publications:

- M. Siemons, T. J. Koplin, D. Sanders, U. Simon, Hochdurchsatz-Impedanzspektroskopie (HT-IS) zur Entwicklung von Gassensoren, *Technische Mitteilungen* 1/2 (2006) 198-202.
 - T. J. Koplin, M. Siemons, D. Sanders, U. Simon, Kombinatorische Materialforschung: Mit Hochdurchsatz zu neuen Sensormaterialien, *GIT Labor-Fachzeitschrift*, 50(4) (2006) 292-296.
-

Contents

1.	Introduction	1
2.	Basic Knowledge	3
2.1	Bulk conductivity and surface states	4
2.2	Physical and chemical adsorption	5
2.3	Sensing mechanism	8
2.4	Key performances of a sensor	10
2.4.1	Sensitivity	10
2.4.2	Selectivity	11
2.4.3	Stability	11
2.4.4	Speed	12
2.5	Influences on key performances	12
2.5.1	Temperature	12
2.5.2	Crystallite size	13
2.5.3	Surface dopants	14
2.5.4	Volume dopants	16
2.5.5	Film thickness	16
2.6	ABO ₃ materials	17
2.7	The polyol mediated synthesis	20
2.8	High throughput and combinatorial approach in sensor material synthesis	22
2.9	Multielectrode array substrate and thick film deposition	24
2.10	High throughput impedance spectroscopy (HT-IS) setup	28
2.11	Impedance spectroscopy	29
3.	Results and discussion	35
3.1	Material Preparation	35
3.2	CoTiO ₃	42
3.2.1	Electrical characterisation	45
3.2.2	Automated data fitting of impedance spectra	46
3.2.3	Electrical characterisation of CoTiO ₃	49
3.2.4	Volume doped CoTiO ₃	51

3.2.5	Further investigations on $\text{CoTiO}_3\text{:La}$	60
3.2.5.1	Characterisation	60
3.2.5.2	Electrical and gas sensing properties	64
3.2.5.3	Cross-sensitivity towards humidity	67
3.2.5.4	Gas concentration dependence	68
3.2.5.5	Long-term behaviour of $\text{CoTiO}_3\text{:La}$	69
3.2.5.6	Surface doped $\text{CoTiO}_3\text{:La}$	72
3.2.5.6.1	Response and recovery behaviour of Au and Pd doped $\text{CoTiO}_3\text{:La}$	78
3.2.5.6.2	Characterisation of Au and Pd surface dopants on $\text{CoTiO}_3\text{:La}$	80
3.2.5.6.3	Surface doping of a Au/Pd mixture on $\text{CoTiO}_3\text{:La}$	85
3.2.5.7	Solid surface doping of $\text{CoTiO}_3\text{:La}$	87
3.2.6	Summary of CoTiO_3 -related investigations	91
3.2.7	Capacitance analysis of doped CoTiO_3	92
3.3	LnMO_3 compounds	96
3.3.1	Preparation and characterisation of LnMO_3 compounds	96
3.3.2	Electrical and gas sensing properties of LnFeO_3	104
3.3.2.1	Response times and concentration dependence	109
3.3.2.2	Influence of humidity on the sensitivity of TmFeO_3	114
3.3.3	Electrical and gas sensing properties of LnCrO_3	117
3.3.4	Summary of LnMO_3 -related investigations	119
3.3.5	Further investigation on SmFeO_3	120
3.3.5.1	Preparation of volume doped SmFeO_3	120
3.3.5.2	Electrical and gas sensing properties of volume doped SmFeO_3	127
3.3.5.3	Electrical and gas sensing properties of surface doped SmFeO_3	134
3.3.5.4	Electrical and gas sensing properties of solid surface doped SmFeO_3	140
3.3.5.5	Summary of investigations on doped SmFeO_3	146
3.3.6	Binding energy model	147
4.	Conclusion	152
5.	References	154

6.	Experimental Details	167
6.1	General synthesis procedure	169
6.1.1	Synthesis of different ABO_3	169
6.1.2	Synthesis of LnCrO_3 materials	173
6.1.3	Synthesis of LnFeO_3 materials	174
6.1.4	Synthesis of volume doped SmFeO_3	175
6.1.5	Synthesis of volume doped CoTiO_3	177
7.	Appendix	179
7.1	Characteristics of ABO_3 materials	179
7.2	Response and recovery ability of volume doped CoTiO_3	193
7.3	Response and recovery ability of surface doped SmFeO_3	196

List of Abbreviation

AC	alternating current
at%	atomic percent
BF	bright field
C	capacity
CPE	constant phase element
DC	direct current
DEG	diethylene glycol
DS	Debye-Scherrer crystallite size
ϵ_r	dielectric constant
ϵ_0	permittivity of free charge
e	electron charge
E_A	activation energy
E_F	Fermi level
EDX	energy dispersiv X-ray analysis
EfTEM	energy-filtered TEM
EPMA	electron probe micro analysis
eV_{surf}	height of band bending
f	frequency
HAADF	high-angle annular dark field
HRTEM	high resolution transmission electron microscopy
HTE	high throughput experimentation
HT-IS	high throughput impedance spectroscopy
IDC	interdigital capacitor
IR	infrared
IS	impedance spectroscopy
k	Boltzmann constant
L_D	Debye-length
Λ_{air}	space charge layer
μ	charge carrier mobility
μ_{O^-}	electrochemical potential for O^-
R	resistance
rh	relative humidity
σ	conductivity
S	absolute sensitivity
S_Δ	relative sensitivity
SEM	scanning electron microscopy
Θ	diffraction angle
τ	relaxation time
τ_{50}	response time

t	Goldschmidt tolerance factor
T	temperature
TEM	transmission electron microscopy
TPD	temperature programmed desorption
V _{rms}	input alternating voltage
XRD	X-ray diffraction
ω	angular frequency
Y*	admittance
Z*	complex impedance
Z'	real part of impedance
Z''	imaginary part of impedance

Units

Å	Angstrøm
°C	degree Celcius
K	Kelvin
min	minute
mL	milli liter
µm	micro meter
nm	nano meter
pm	pico meter
ppm	parts per million
s	second
Ω	Ohm

1. Introduction

Gas monitoring has become a growing demand stemming from strategies for intelligent process management, environmental protection, and medical diagnostics as well as from the domestic and automotive sectors. The four key parameters identifying a good sensor are sensitivity, selectivity, stability, and speed [Ko01]. However, the majority of research on the development of fast responding, sensitive, and especially highly selective gas sensor materials is restricted to improvement of known systems and is not directed towards the search for alternative sensor materials. Therefore current commercial gas sensors are based on a few n-type conducting semiconductor materials, like SnO_2 , ZnO , WO_3 , Fe_2O_3 or TiO_2 , or, for more demanding applications, on sensor arrays of these materials, enhancing selectivity with appropriate complex signal analysis. The sensing properties are based on a number of different processes like material synthesis, sample preparation, sample treatment, and measuring method. Despite various research efforts, sensitivity and selectivity of the materials are not predictable.

The use of high throughput experimentation (HTE) techniques accelerates material synthesis and characterisation and thus enables an investigation of a multitude of different materials [Am04, Se01]. HTE also allows the application of combinatorial strategies, which expedite the time-consuming process of evolutionary optimisation of selected material properties. Our group has already developed a high throughput impedance spectroscopy (HT-IS) setup for analysis of gas sensing properties of metal oxides together with a broad variety of surface doping elements [Fr04, Br05, Si05, Ko06]. With selected examples, it was demonstrated that materials with desired properties can be found in a variety of different combinations of metal oxides and surface dopants [Sa04, Ko06b].

This work reports on the investigation of gas sensing properties of different p-type ABO_3 compounds by use of high throughput impedance spectroscopy. The methods applied should answer the following questions:

- Is it possible to synthesise a wide range of different p-type ABO_3 materials via the polyol mediated synthesis which is known for metal and metal oxide nanoparticle synthesis [Fi82, Fe04]?

- Can substrate plates of diverse metal-doped oxides be rapidly synthesised and screened for gas sensing properties?
- What are the effects of composition changes in the materials on the gas sensitivity?
- Is it possible to improve the gas sensing properties of p-type ABO_3 materials by doping?
- Are there trends in gas sensing performance as a function of composition that might improve the understanding of structure-property relationships?

The thesis is organised as follows:

Chapter 1 gives an introduction to the topic of chemical gas sensor research and the motivation/aims of this work.

Chapter 2 discusses the measurement principles of metal oxide semiconductor gas sensors and introduces the family of ABO_3 compounds investigated in this work.

Chapter 3 details the workflow from synthesis to gas sensing measurements and discusses the screening results.

Chapter 4 summarises the presented work, highlighting the main achievements.

2. Basic knowledge

The use of semiconductors as gas sensing layers goes back to 1953 when Brattain and Bardeen first reported gas sensing effects on Germanium [Br53]. This observation was followed by the discovery of gas sensing effects on metal oxides by Seiyama in 1962 [Se62, Se66]. Finally, Taguchi [Ta62, Fi02] brought metal oxides as gas sensors to the commercial market. Nowadays, millions of gas sensors are sold every year. The mass market for gas sensors is growing because of increasing demand in multiple areas. Chemical sensors are not only used for industrial facilities (H_2 , CH_4 , etc.) but also in domestic appliances (hydrocarbons [Ja06b]) and air quality monitoring (NO_x [Tr99], NH_3 [Ro05]). Common applications include early fire detectors (CO [Ba03]), car cabin air quality monitoring (VOC, hydrocarbons [Ya05]), detection of hazardous chemical agents to provide safety in public places, just to mention a few examples. The main differences between classical analytical instruments and sensors are cost, size, and accuracy. In contrast to classical analytical instruments sensors are low-cost small devices with lower lifetime and accuracy.

A gas sensor is a device which provides an electrical output in response to a change in the ambient gas atmosphere [Fr06]. In general, the field of gas sensors is divided into a number of different measuring principles. Gas detection can be performed by IR-detectors, electrochemical cells, quartz microbalances, pellistors, and resistive semiconductive metal oxide sensors [Mo97]. This work will focus on the latter ones. The gas sensor can be divided into a receptor function and a transducer function. Figure 2.1 shows the receptor and transducer function of a semiconductor gas sensor. The receptor, in this case the metal oxide surface, interacts specifically with the target gas, while the transducer function, accomplished here by the sensor layer with its microstructure, transforms the chemical/physical signal into an easily measurable electrical one. In addition, an element which enables the detection of a change in output resistance of the sensing layer is shown [Fr06, Ya05].

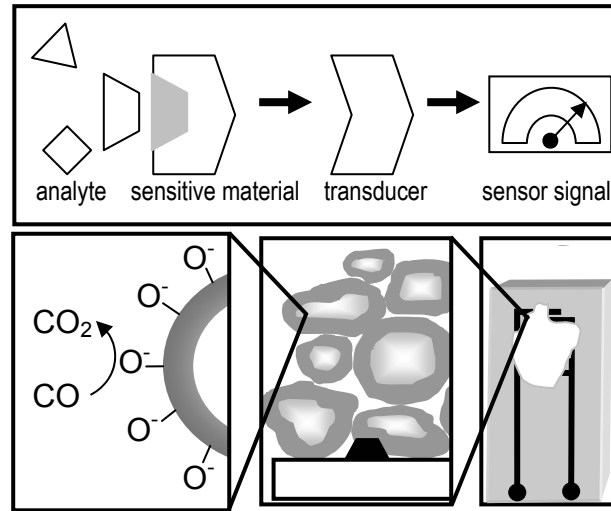


Figure 2.1: Sensor device model.

Resistive semiconductive metal oxide sensors show a change in the concentration of conduction species as a result of chemical reactions at the surface with different adsorbed gas species. These reactions modify the defect structure of the oxide surface layer to a depth of a few μm or less. The operating temperature must be low enough to allow sufficient surface adsorption but high enough for surface reaction and charge transfer between the surface layer and the bulk interior. The working temperature of these sensors is usually lower than that of the bulk conduction based gas sensors. Typically values between 200° and 500°C are used, depending on the base material and the target application. A high performance gas sensor has a high sensitivity to the few selected pollutants and provides a stable and reproducible signal over long time periods.

Many investigations in the field of sensor research have been performed on SnO_2 making this material a model system for oxide-based sensors [Ba96]. The following paragraphs give an introduction to the working principles of resistive gas sensing materials.

2.1 Bulk conductivity and surface states

The resistance of a homogeneous bulk material with conductivity σ , length l and cross section A can be calculated according to:

$$R = \frac{l}{\sigma \cdot A} \quad (2.1)$$

Semiconductors show conductivities which are located between those of conductors and insulators, having an electronic band gap smaller than 5 eV. The conductivity of a semiconductor crystal can be described as the sum of electronic ($\sigma_{e,p}$) and ionic conductivity ($\sigma_{ion,j}$), if the conduction processes are considered to be independent. In the temperature range investigated in this work (200-500°C) the ionic contribution can be neglected for the materials. Thus,

$$\sigma = \sigma_e + \sigma_p + \sum \sigma_{ion,i} \approx \sigma_e + \sigma_p = e(p\mu_p + n\mu_e) \quad (2.2)$$

where $\mu_{e,p}$ are the mobilities of electrons and holes, e is the elementary charge and n and p , the charge carrier concentrations for an intrinsic semiconductor [Me00b].

In an extrinsic semiconductor additional donor and acceptor levels appear due to doping of the material. The extrinsic doping shifts the Fermi level towards the conduction band for n-doped semiconductors or towards the valence band for p-doped semiconductors.

At the surface of a metal oxide material a change of the electronic band structure can be observed. Sites of varying reactivity can be found. These so-called surface states are localised electronic energy levels at the surface. Surface states can be differentiated as intrinsic or extrinsic states. Intrinsic surface states result from non-ideal stoichiometry, bulk defects like surface atoms with unoccupied or unsaturated orbitals (“dangling bonds”) or interstitial defects; extrinsic surface states originate from the adsorption of gases or impurities (dopants) on the surface. Surface cations provide acceptor-like surface states (electron traps) near the conduction band, while surface anions provide donor-like surface states (hole-traps) near the valence band. Surface states are able to exchange electrons with the bulk, which makes them important for the change in electrical conductivity due to reaction in ambient gas atmospheres.

2.2 Physical and chemical adsorption

If gases interact with a metal oxide surface layer, the adsorption can be classified as physisorption or chemisorption. Physisorption is the first step in the interaction between an analyte and the solid surface. A gaseous molecule approaching the surface is slightly polarised and induces an equivalent dipole in the adsorbent. In case of chemical adsorption, a strong interaction involving electron transfer occurs. The binding

energies are of similar strength as those of chemical bonds (>0.5 eV). The adsorption process is not only dependent on the nature of the adsorbate and adsorbent but also on the availability of adsorbate (partial pressure) and the temperature. In gaseous environments, there is a state of constant adsorption and desorption in a thermodynamic equilibrium situation.

Atoms or molecules adsorbed on a surface can capture electrons from or inject electrons into the bulk to form a localized electron energy state at the surface (extrinsic surface state).

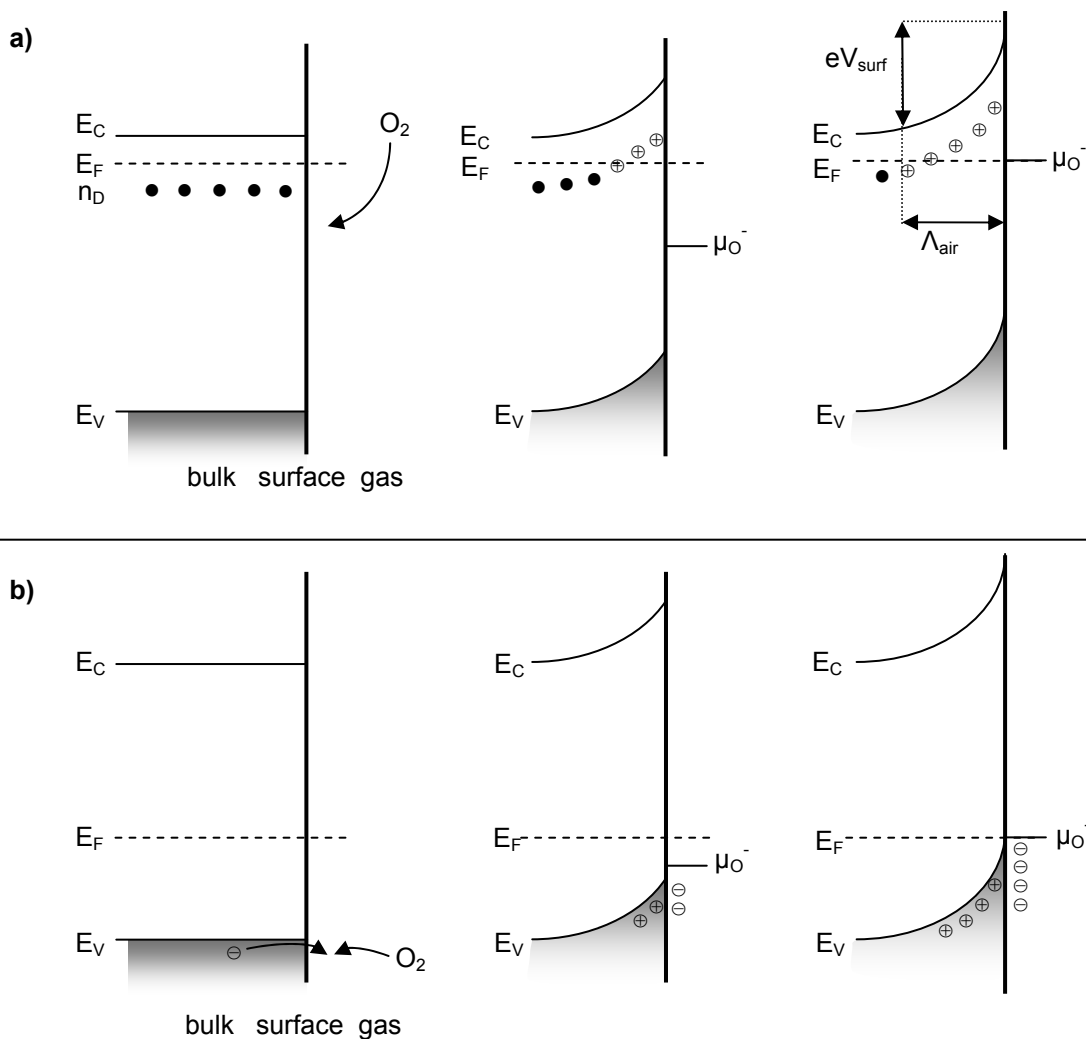


Figure 2.2: Band bending model for **a)** n-type semiconductor and **b)** p-type semiconductor.

The adsorption of oxygen on an ionic crystal can occur in molecular or atomic form. The electrochemical potential of the oxygen adsorbate becomes lower than that of the Fermi level causing a transfer of electrons from the bulk to the adsorbed oxygen by the process shown below:



where [S] is an unoccupied chemisorption site S;

$\text{O}_{2(\text{gas})}$ is an oxygen molecule in the ambient atmosphere;

e^- is an electron, and $\text{O}_{\beta(\text{ads})}^{-\alpha}$ is a chemisorbed oxygen species with

$\alpha=1$ for singly ionised forms

$\alpha=2$ for doubly ionised forms

$\beta=1$ for atomic forms

and $\beta=2$ for molecular forms [Ba01].

These charged species are bound via chemisorption to the surface. The presence of these species on SnO_2 have been analysed by TPD, FTIR and EPR [Ba99, Pa03].

The O_2^- molecule is predominant at temperatures below 150°C. From 150° to 500°C, which is the predominant temperature range in this work, the O^- species dominates.

The electrochemical potential of the surface state (μ_{O^-}) whose level is lower than the Fermi level in bulk will capture electrons from the conduction band. This induces a hole accumulation layer (Λ_{air}) beneath the surface for n-semiconductors and from the valence band for p-type semiconductors (as shown in Figure 2.2). The holes in the accumulation layer and the associated space charge induce a potential (surface band bending) that increase μ_{O^-} . The negative countercharge (oxygen species) balances the excess holes accumulated in the metal oxide. Unlike a metal, a semiconductor does not have a large amount of mobile free charge carriers available at the surface. The positive charge will therefore be formed in the bulk, resulting in the mentioned space charge region. The height (eV_{surf}) and depth (Λ_{air}) of the band bending depends on the surface charge. At the same time Λ_{air} depends on the Debye length L_D , which is characteristic of the semiconductor material for a particular donor concentration:

$$L_D = \sqrt{\frac{\epsilon_0 \cdot \epsilon_r \cdot k \cdot T}{e^2 \cdot n_d}} \quad (2.4)$$

with the dielectric constant ϵ_r , the permittivity of free charge ϵ_0 , the Boltzmann constant k , the operating temperature T , the electron charge e , and the carrier concentration n_d , which corresponds to the donor concentration assuming full ionisation [Fr06]. The Debye length is high for a low density of free charge carriers in

the volume. The decrease of charge carriers near the surface decreases the rate and energy for further adsorptions [Gö96].

As long as μ_{O^-} is below E_F , electrons are transferred from the metal oxide to the surface adsorbates. In equilibrium, the surface Fermi level position is pinned at μ_{O^-} . The effect of oxygen adsorption on n-type semiconductors is a decrease of surface conductivity, while in the case of a p-type semiconductor, the band bending results in an accumulation of charge carriers (holes) near the surface, which leads to increased surface conductivity (as shown in Figure 2.2b).

2.3 Sensing mechanism

Upon exposure of an n-type metal oxide to a reducing gas such as CO, the gas reacts with the adsorbed oxygen species, releasing the trapped electron to the conduction band and increasing the conductance (see Figure 2.3).



A lower steady-state surface coverage of the adsorbates is established. The conductance is determined by the variation in the barrier height at the intergranular contact. An increase in CO concentration decreases the barrier height and subsequently increases the conductance [Gö85].

The mechanism for oxidising gases such as NO_2 is not the same as for reducing gases. These molecules will be directly chemisorbed on the metal oxide surface. NO_2 occupies additional surface states, and further electrons are extracted from the semiconductor:



In addition an intercation with adsorbed oxygen may occur:



These reactions result in an increase of the barrier height and in lower conductivity of n-type semiconductors.

On p-type metal oxides the adsorbed oxygen acts as surface acceptor state, abstracting electrons from the valence band and hence increasing the charge carrier (hole) concentration at the grain surface. The consumption of oxygen adsorbates by reaction with reducing gases leads to an increase of resistance, which is the opposite

of the effect for n-type metal oxides. Conversely, the adsorption of oxidising gases results in a decrease in resistance.

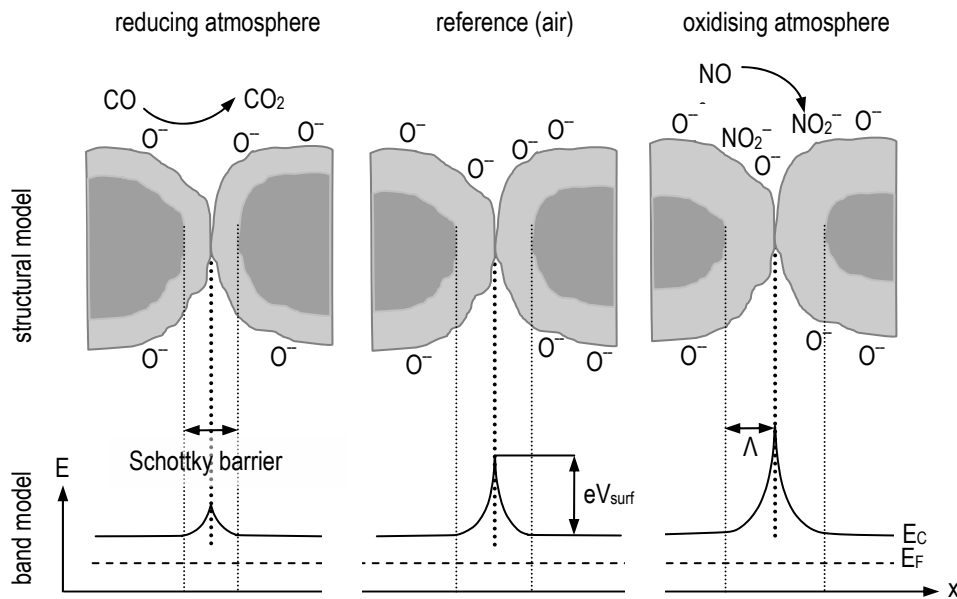


Figure 2.3: Band and structural model for n-type semiconductors under reducing, oxidising and reference atmosphere.

However, a sintered SnO_2 ceramic is likely to incorporate more than one type of intergranular contact. Each crystallite is connected to several neighbours by either neck-type or barrier-type contacts. Since barrier-type contacts usually show much larger resistance than neck-type contacts, it is more favourable for electrons to pass through the barrier contacts [Pa03]. Therefore the response characteristics of a real sensor are critically dependent on the fabrication method and thermal treatment of the ceramic.

Thick film sensors consist of numerous different sintered particles. The conductivity of a film of particles is assembled from a bulk part and a surface part. Depending on the degree of sintering, the charge carriers have to overcome different heights of energy barriers (Figure 2.4). In the case of two particles touching, the charge carriers have to overcome eV_{surf} at the grain boundary. In the case of sinter necks, the potential barrier is lower than the energy barrier in the aforementioned case.

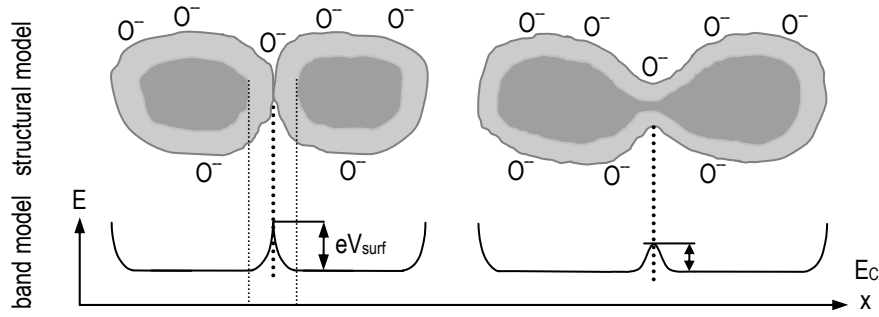


Figure 2.4: Band bending for different sintered grains.

2.4 Key performances of a Sensor

Sensors were evaluated for four key performance aspects: sensitivity, selectivity, stability and speed.

2.4.1 Sensitivity

Sensitivity is defined as the ratio of the resistance of a sensing material in the presence of an analyte to the baseline resistance measured in air (reference gas).

Hence, the absolute sensitivity S of a material to a test gas is defined by:

$$S = \frac{R_g}{R_r} \quad R_g > R_r$$

$$S = \frac{R_r}{R_g} \quad R_g < R_r,$$
(2.8)

where R_g is the resistance obtained from the measurement under test gas conditions, while R_r is the reference resistance value for a measurement under synthetic air.

Our group describes the response of a material to a test gas by the relative sensitivity S_Δ , which is defined as

$$S_\Delta = -\frac{R_g - R_r}{R_g} \quad R_g > R_r$$

$$S_\Delta = +\frac{R_r - R_g}{R_r} \quad R_g < R_r$$
(2.9)

where values for S_Δ range from 1 to -1. Decrease of resistance while applying a test gas gives values between 0 and 1, rise of resistance results correspondingly in values for S_Δ between -1 and 0. Using S_Δ instead of the commonly used sensitivity S

including algebraic signs turned out to be beneficial for the data mining process in our high throughput workflow. Furthermore it allows an immediate differentiation between n- and p-type semiconducting materials and/or the differentiation between oxidising and reducing test gases, respectively.

2.4.2 Selectivity

Selectivity of a sensor is defined as the ability to differentiate between analytes. A high selectivity is desired for different applications of a sensor material. Cross-sensitivities are drawbacks of the commonly used and well-known materials such as SnO_2 and ZnO . The selectivity can be calculated by the ratio:

$$\text{Selectivity} = \frac{S_{(\text{target})}}{S_{(\text{cross})}} \quad (2.10)$$

where $S_{(\text{target})}$ is the sensitivity of the target gas, and $S_{(\text{cross})}$ is the sensitivity of a cross-sensitive gas at a regarded temperature.

To improve the selectivity, different strategies can be used; however, at present, sensor selectivity remains, for the most part, empirical. Selectivity can be influenced by use of filtration membranes. In this case the sensing material can be protected from gases which should not react on the surface. This has been realised by covering layers with defined pore size as zeolithes for example [Mo82, Sa05, Tr04]. Teflon layers are useful in preventing humidity influences, and barium carbonate can be used as a sulphur oxide adsorbant to prevent poisoning of $\text{La}_{1-x}\text{Sr}_x\text{Ti}_{1-y}\text{Fe}_y\text{O}_3$ (LSTF) sensing materials [Re03]. Another possibility is the use of multi-layer sensors to enhance selectivity. In recent years, interest has grown in the development of “electronic noses” to detect mixed gases. To gain the desired selectivity, such a device generally consists of an array of chemical sensors, each one sensitive to a specific gas. The signal of such devices is then processed by a multivariate data analysis [Co00, Go04, Pa04].

2.4.3 Stability

Stability of a sensor is determined by evaluating both the baseline conductance and the signal response (sensitivity) to various concentrations of analytes over time. Complete recovery can be restricted by desorption processes that are very slow or by irreversible changes at the surface (poisoning). A gradual change in the baseline

signal from the sensor is called baseline drift, while a change in the specific response to the analyte is termed as sensitivity drift (span drift). In contrast to the selectivity and sensitivity issues, the problem of stability is rarely addressed in the literature. The problem of stability can be overcome by use of high-temperature stable materials like the perovskite materials investigated in this work.

2.4.4 Speed

The speed of a sensor is described by its response and recovery times. The response time is the time to reach steady-state conditions in test gas ambience, while the recovery time is the time to return to the baseline value. These values depend on the adsorption and desorption kinetics of the surface-gas reaction. Since most sensors approach the final signal asymptotically, response time is usually defined as the time needed to reach 50% (τ_{50} -value) or 90% (τ_{90} -value) of the final signal (for a given concentration of gas). The recovery time is usually expressed as the time for the signal to fall below 50% or 10% of the maximum response.

2.5 Influences on key performances

The sensitivity and selectivity of a certain material can be influenced by different parameters. Some of these effects are addressed in the following sections.

2.5.1 Temperature

The sensitivity of a semiconductor gas sensor is a function of the steady state surface coverage of oxygen adsorbates relative to that in air.

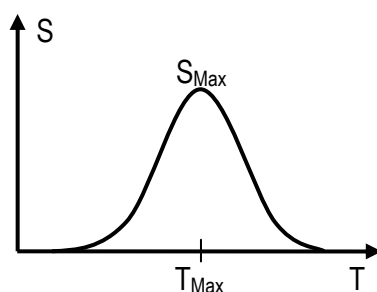


Figure 2.5. Temperature dependence of the sensitivity, often referred to as a volcano shape [Ya05].

A sensor shows maximum sensitivity (S_{Max}) at a certain temperature (T_{Max}) depending on the gas species to be detected as shown in Figure 2.5. This results

from the temperature-dependent equilibrium coverage of oxygen adsorbate in air, in addition to the temperature-dependent equilibrium and time constant of the reaction between the oxygen adsorbate and the target gas, and at least from the diffusivity of the gases through the porous medium.

This means that at low temperatures, where the equilibrium coverage of the oxygen adsorbate in air is high, the reaction rate between gas and oxygen species is low; the sensitivity is low. On the other hand, at high temperatures, where the rate of removal of oxygen adsorbate becomes high due to the vigorous reaction between analyte and oxygen species, the equilibrium oxygen coverage is low and the sensitivity remains low [Pa03].

2.5.2 Crystallite size

Films based on metal oxide nanoparticles have attracted great interest in different applications such as battery materials, photochromic windows, and solar cells. Several nanostructured materials have been used to prepare nanoparticle-based sensor films (e. g. SnO_2 , TiO_2). Porous films composed of nanoparticles have a high internal surface area, the extent of which is dependent on the size of the nanoparticle building blocks. For porous nanoparticle films in the order of $1\ \mu\text{m}$ thickness, the internal surface can attain an overall surface area more than 100 times greater than the projected area [Be06], as shown in Figure 2.6. A porous nanoparticle film can offer much higher sensitivity than a similar compact film with only the top surface area available for interaction, which is also of interest when considering surface conductivity.

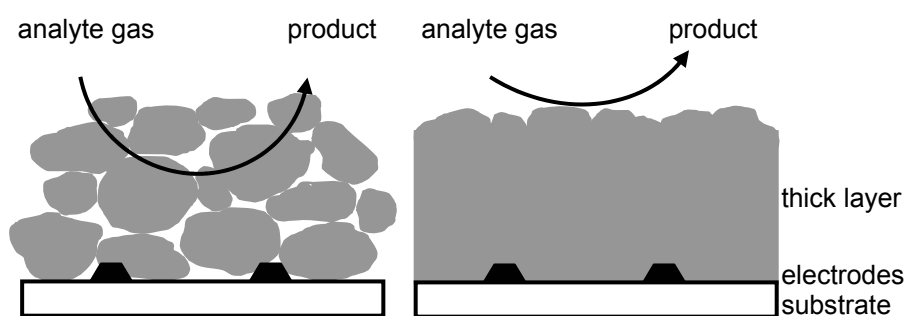


Figure 2.6: Comparison between compact and porous layer. On compact layers the reaction takes place on the geometrical surface whereas on porous layers all particle surfaces are included.

If n-type semiconductor grains have a grain radius $r < \Lambda_{\text{air}}$, the band bending will extend throughout the complete grain. With further decrease of the radius the depleted areas start to overlap, and the electrical properties are predominantly determined by surface states. If the surface potential barrier falls below the thermal energy $eV_{\text{surface}} < kT$, the so called “flat-band condition” will be achieved and no difference between surface and bulk will be observed.[Gö95] The effect of reducing gases for example can be approximated by a shift in bands relative to the Fermi energy (see Figure 2.7). This results in an increase of sensitivity correlated to larger particle sizes.

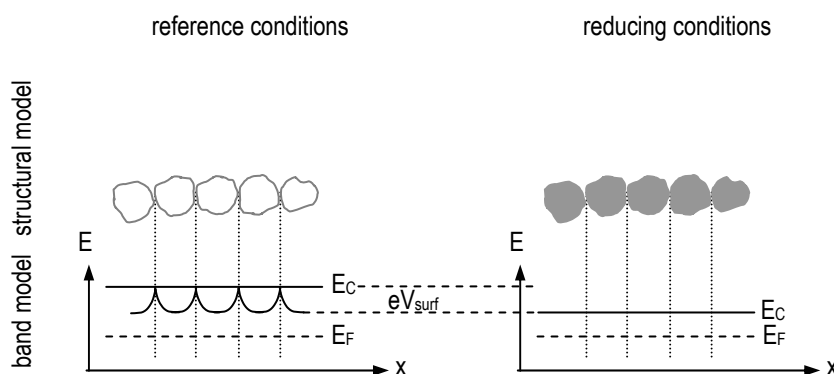


Figure 2.7: Flat-band condition for grain radius $r < \Lambda_{\text{air}}$ in air (left) and reducing test gas (right).

Pure SnO_2 sensors exhibit drastic changes in resistance as a function of grain size combined with change in sensitivity [Sh99]. Also, Yamazoe et al. observed a sensitivity increase as the grain size decreased, with an especially drastic increase when the diameter of the crystallite was $\sim \Lambda_{\text{air}}$ (~ 6 nm), where total depletion of grains occurs. Thus, small particles in porous layers are a crucial factor for high sensitivity [Ya03b].

2.5.3 Surface dopants

To promote the sensitivity, shorter response times, and possibly the selectivity towards certain gases, a small amount of noble metal and oxidic catalysts are added to the sensor material in the form of fine dispersions with diameters of a few nanometers. The dopants are usually added via impregnation and therefore are located mainly at the surface of the grains. Surface impregnation adds new reactive sites to the surface of the semiconductor. However, the complex behaviour of

dopants and their influence on the gas sensing properties of metal oxides is still not completely understood.

Three models for the influence of surface dopants are discussed in the literature and are shown in Figure 2.8. The first case is the Fermi level control (electronic sensitisation). Oxygen is adsorbed on the dopant clusters and traps electrons from the metal. The dopant, in turn, removes electrons from the supporting semiconductor, which leads to a shift in the Fermi level and an electron-depleted charge layer near the interface. Upon exposure to reducing analytes the doping additive is reduced, releasing electrons back to the semiconductor (e. g. $\text{Ag}_2\text{O}@\text{SnO}_2$ [Ya91]).

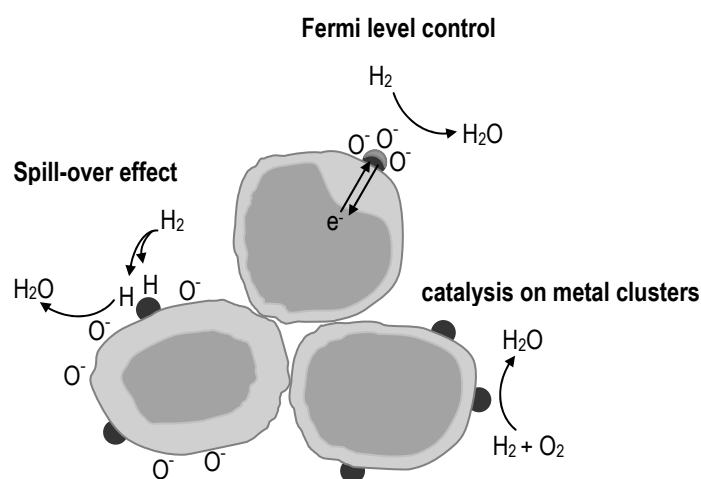


Figure 2.8: Influences of dopants on the sensing properties of metal oxides.

The second model represents the Spill-over mechanism (chemical sensitisation). Deposited clusters of noble metals (e. g. $\text{Pt}@\text{SnO}_2$ [Ko90], $\text{Pt}@\text{ZnO}$ [Sa85]) provide preferred adsorption sites for the target analyte. Activated fragments are transferred (spilled over) onto the semiconductor surface to react with the chemisorbed oxygen species. In this case, oxygen spill-over is often an issue [Mo87]. A higher coverage of the surface with interacting species is achieved.

The third model describes the catalysis by metal clusters. This reaction takes place exclusively on the cluster. The catalytic oxidation of the analyte can be connected to a local temperature rise. The temperature increase influences the conductivity in this region and may therefore increase the sensitivity. A change of T_{Max} to smaller values has been observed [Ca02], and can be ascribed to such catalytic phenomena.

However, the real situation is far more complex and the doping influences are widely debated [Ar02].

2.5.3 Volume dopants

Another possibility of doping is the incorporation of metal ions in the synthesis of the metal oxides. Volume doping is known to influence the electrical properties of metal oxides. Also, changes in gas sensing behaviour due to volume doping have been reported. Song et al. reported that Pb-doping can improve sensitivity, selectivity and response time of LaFeO_3 [So05]. Huang et al. showed an influence on sensitivity when doping LaCrO_3 with TiO_2 [Hu96]. They assert that positively charged ionic-type defects created by dopants act as trapping sites to adsorb oxygen. However, the mechanism of how these volume dopants enhance gas sensitivity is not fully understood.

2.5.5 Film Thickness

Thicker films have a higher baseline conductance than thinner films because of a higher number of conduction pathways as compared to thinner films. The improved sensitivity of thicker films is a result of the higher internal area [Be06]. The optimal film thickness depends on the degree of interaction between the analyte and the sensor material. For a strongly interactive analyte-sensor combination, the optimal film thickness is relatively thin since the analyte will never penetrate deeply into the porous film before interacting with the sensor surface. For a much less interactive system, the optimal film thickness will be larger because the analyte can penetrate more deeply into the film before interacting with the surface and producing a sensing signal.

2.6 ABO₃ materials [Ga69, Gi94, Oh74, Zh04b]

The preparation of specific tailor-made mixed oxides with desired properties is one of the main topics of research in catalysis and sensor materials. Among the mixed metal oxides, perovskite-type oxides (general formula ABO₃) remain prominent because of the broad diversity of properties that can be obtained due to the fact that around 90% of the metallic elements are known to form perovskite-type oxide structures. In addition, the possibility of synthesising multicomponent perovskites by partial substitution of cations in the A- and B-site is a great advantage. ABO₃ materials may become the sensing materials of the future [Kh01]. They are already developed e. g. for carbon monoxide [La95, Ma05, Ar88], oxygen [Ge91] and NO [Tr95] sensing. Perovskite oxides show a high thermal and chemical stability in catalytic reactions [Cr02]. Structures of the type A⁺B⁵⁺O₃, A²⁺B⁴⁺O₃ and A³⁺B³⁺O₃ exist depending on the valency of the metals used. Generally, for ABO₃ structures, two extreme cases exist:

- A and B cations are approximately of equal size and of a size suitable for coordination within the octahedral interstitial site of a close-packed oxide framework.
- A cations are of comparable size to O²⁻ which together with oxygen can form AO₃ close-packed layers with high coordination numbers in the A-site.

Oxides of the first type tend to adopt sesquioxide structures, such as corundum or ilmenite, while oxides of the second group form linked BO₆ octahedra and AO₃ close-packed layers, such as perovskite structures.

The ilmenite structure consists of a hexagonal close-packed oxygen framework in which the cations are distributed in two thirds of the available octahedral interstices. According to geometric arguments, the octahedral interstices will accommodate ions with radii approximately equal to $(2^{0.5}-1)r$, where r is the radius of O²⁻ (i. e. 1.38 Å). This relationship, however, is an approximation, and a certain degree of deviation from the ideal close-packed state may occur. Figure 2.9 shows the unit cell of CoTiO₃ as an example of an ilmenite structure.

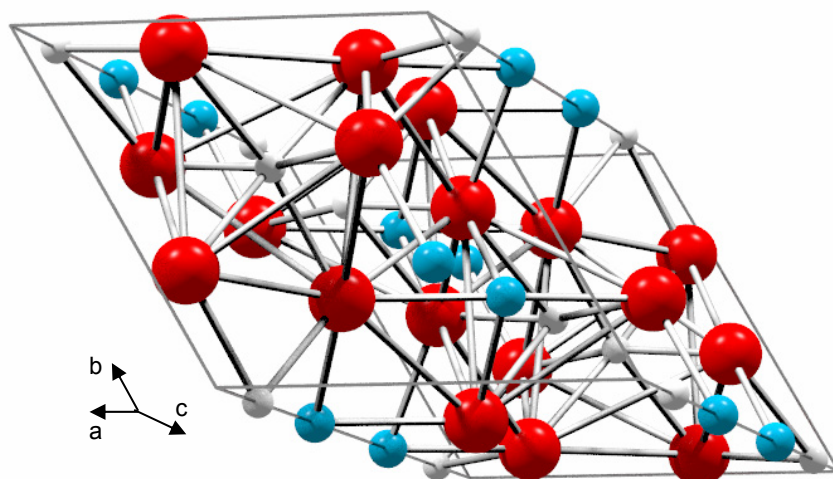


Figure 2.9: Unit cell of $\text{Co}(\text{●})\text{Ti}(\text{○})\text{O}_3(\text{●})$, ilmenite structure.

The ideal perovskite structure is cubic with the A cations in 12-fold coordination and the B cations in 6-fold coordination. The A-site is situated at the body center of the cubic unit cell, the B site at each of the eight corners, and the oxygen atoms at each of the centers of the 12 edges as shown in Figure 2.10 for SrTiO_3 . In the orthorhombic distortion the A cations and the oxygen ions are displaced from their cubic positions. Consequently the 12 oxygen polyhedra around the A cations are quite distorted, so that the 12 A-O distances vary over a large range. Also, the oxygen octahedra around the B cations are distorted, but their distortion is far less than that of the polyhedra around the A cations.

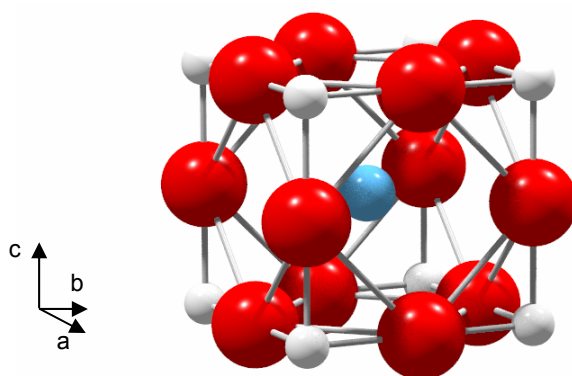


Figure 2.10: Ideal perovskite structure of $\text{Sr}(\text{●})\text{Ti}(\text{○})\text{O}_3(\text{●})$.

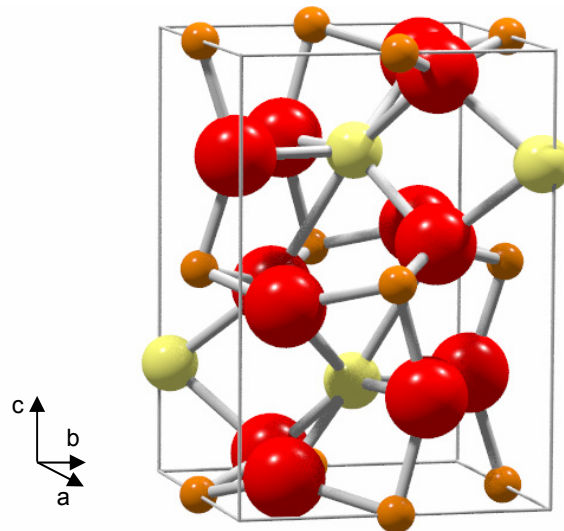


Figure 2.11: Orthorhombic $\text{Gd}(\text{yellow})\text{Fe}(\text{orange})\text{O}_3(\text{red})$.

Combinations of many trivalent first-row transition-metal oxides and rare-earth oxides form orthorhombic perovskites as thermodynamically stable phases.[Ge56] GdFeO_3 is considered the prototype of this series (shown in Figure 2.11); the rare-earth orthochromites, orthovanadites, orthorhodites and orthoaluminates are isostructural. Perovskites and distorted perovskite-type structures are formed for A and B cations having a wide range of radii, provided the A cation is large enough to form close-packed layers with O^{2-} , and the B cation is small enough to adopt an octahedral oxygen coordination environment. As the radius of the A cation decreases, the A and B cations will ultimately adopt a different structure, often the ilmenite structure, which can accommodate cations that are both smaller and closer in size to one another better.

To predict which of the above mentioned structures will be favoured for a given pair of cations, the so-called Goldschmidt tolerance factor t [Go26, Ga69] can be used:

$$t = \frac{(r_A + r_O)}{\sqrt{2}(r_B + r_O)} \quad (2.11)$$

with r_A , the ionic radius of the larger cation, r_B , the radius of the smaller cation and r_O the ionic radius of the oxygen anion. For $0.99 > t > 0.77$ the perovskite structure is often formed, while for $t < 0.77$ the sesquioxide structures appear. The ideal cubic perovskite structure appears in a few cases for t -values close to 1 and at high temperatures.

Classical methods for perovskite oxide preparation include the equimolar oxide mixing synthesis and the decomposition synthesis. A newer method is the so called polyol mediated synthesis, which will be described in the following paragraph.

2.7 The polyol mediated synthesis

The increasing demand for oxide nanoparticles in the wide field of nanotechnology has motivated considerable research on their preparation. For many purposes, synthesis of nanoscale materials exhibiting well-defined properties such as particle diameter, particles shape, or pore structure is an important challenge to preparative chemistry [Fi00]. In this context a number of novel synthetic routes have been described (e. g. ball milling, microwave plasma, co-precipitation in reverse micelles, sol-gel synthesis, hydrothermal synthesis, molten salt synthesis, gas phase-based methods). Reproducibly controlling simultaneously over particle structure, surface chemistry, crystal structure, and assembly remains an elusive goal. The conventional reaction technique for the perovskite-type oxides used in this work is the solid-state reaction, which has some unavoidable drawbacks like high calcination temperature ($\sim 1100\text{-}1500^\circ\text{C}$) and a weak control over the particle size distribution. In contrast, chemical solution techniques, especially *chimie douce* solutions, have several advantages: the ease of chemical composition control, the low processing temperature, and the applicability to substrates of any size and shape.

The polyol mediated synthesis is a suitable reaction method for the preparation of metal oxide nanoparticles. Approximately 24 years ago, Figlarz et al. introduced this method as a new synthesis strategy that allowed preparation of finely dispersed metals with well-defined morphology by reduction of metal cations in a polyol medium [Fi82]. In the last years, the method was modified and used for the preparation of metal oxides [Me00, Fe01a, Fe01b, Fe04], hydroxy salts [Po00], phosphates [Fe03], and sulfides [Fe01c]. The polyol mediated synthesis allows the mixing of the reactants at the molecular level. In this procedure, “polyol” stands as a general term for polyalcohols with high boiling temperatures and sufficient ability to solve inorganic salts at elevated temperature. Liquid polyols are interesting among nonaqueous solvents. They are hydrogen-bonded liquids, like water, with a high relative permittivity value, and are able to dissolve and complex many ionic inorganic compounds. In addition, polyol reactions can be carried out under atmospheric

pressure up to 250°C, much higher than reactions in water or monoalcohols. Based on this type of synthesis, a metal precursor is heated in a high boiling alcohol. In the case of noble metals, the metal cations are easily reduced by the alcohol to form particles of the elemental metals [Ch04]. In contrast, while adding a defined amount of hydrolysing agent (p. e. water, acid, base), metal cations precipitate to yield nanoscaled oxide particles. An agglomeration of the particles is prevented due to the chelating effect of the solvent, and the particle growth is limited. To prepare phosphates or sulfides, a concentrated solution of $(\text{NH}_4)\text{H}_2\text{PO}_4$ or $(\text{NH}_2)_2\text{CS}$ in water is added as a hydrolysing agent ([Fe01c, Fe03]).

The precise reaction mechanism for oxide formation is complex and not fully understood or predictable. Poul et al. worked on the reaction of acetate, chloride and sulfate precursors [Po03]. The precipitation of the solid depends on the metal salt anion, the hydrolysis ratio, and on the reaction temperature. As in the sol-gel method, acetate precursors lead to the formation of intermediate alkoxyacetate complexes which are stable towards reduction. The complexing agent can act as an unidentate or bridging group towards the cation. Oxides or hydroxides are obtained in a polyol via hydrolysis and inorganic polymerisation of such intermediate precursors (alkoxyacetates). At higher temperatures, forced hydrolysis and inorganic polymerisation remove the acetate anion, and oxides are obtained. Using chlorides or sulfates, the anion remains in the first shell of the cation, making it difficult to control the morphology of the particles. If water (also crystal water) is absent, the formation of metal particles is still preferred. Thermal analysis and determination of B.E.T.-surfaces has been done by Feldmann [Fe04]. The monodisperse morphology as well as the colloidal stability of the particles in diethylene glycol (DEG) prove the surface-active role of DEG. Feldmann reported that during synthesis the metal oxide nanoparticles are covered with diethylene glycol layers. He also showed that admixing of water can collapse the stable suspension because of exchange of DEG molecules on the surface with water molecules, which results in agglomeration of the particles. Temperature treatment up to 550°C is necessary to remove and degenerate the chelating DEG layer completely.

Materials obtained from this method may occur as crystalline or amorphous. A treatment at moderate temperatures results in crystalline nanoparticles with homogenous phase composition [Si04].

This method for the synthesis of inorganic materials has a number of advantages over more conventional synthetic procedures: ability to obtain high-purity materials, low processing temperatures, and homogenous multicomponent systems. An advantage of using the polyol mediated synthesis for high throughput and combinatorial work is the wide applicability for preparation of various oxides under mild reaction conditions. Especially attractive is the possibility of a smart halide-free preparation method that avoids contamination of the sensing material with remaining halide ions as in other syntheses. The obtained nanostructures offer very high surface areas due to the high porosity of the particle layers, which makes them suitable for sensing thick films. All in all, the polyol method has received considerable attention because of its simplicity and the advantage over most other methods in preparing highly pure mixed oxides.

2.8 High throughput and combinatorial approach in sensor material synthesis

Until recently, the scope of materials research has been mostly limited to systems with only one or two individual components. With rapidly growing demands for better functional materials, complex materials are receiving more and more attention in the materials research community [Sc04]. In sensor research, materials are typically discovered and optimised by an empirical trial and error process that is both time-consuming and costly. Obviously, the discovery process gets even more difficult and time-consuming when the materials include more elements. This time-consuming process inhibits the search for sensing materials with optimal behaviour [Ma99]. Success is often restricted to flukes. Compared to the possible combinations of ternary or quaternary systems that one might reasonably synthesise and which could exhibit several phases, it becomes clear that large numbers of compositions have yet to be examined for their gas sensing properties. It seems obvious that this challenge will not be met if one relies on traditional materials science techniques alone [Li99].

In addition, conventional studies are usually performed on individual samples of discrete compositions, often missing important correlations between different compositions. Thus, it is not surprising that correlations are missed in light of the complexity of modern materials and the importance of defects, dopants etc. in controlling properties.

A possible way to overcome these problems is the use of high throughput and combinatorial approaches. The use of high throughput experimentation (HTE) techniques accelerates material synthesis and characterisation and thus enables an investigation of a multitude of different materials compared to a 'one at a time' strategy. In addition, HTE allows the application of combinatorial strategies, in which algorithms define new material combinations based on previous characterisations. These processes are successfully used in the pharmaceutical and biotechnology industries. In these fields, automation of the fabrication of multivariate specimen arrays, screening, and analysis techniques enabled the development of important new drugs and drug variants [Am02, Am04].

The first experiments using high throughput experimentation in materials science were published in the 1960s [Ke65, Mi67, Ha70]. Experimentation in these years was limited by the analysis and data reduction equipment, which did not have the speed, automation and/or resolution required. More recently, Xiang et al. improved the combinatorial approach in material sciences [Xi95, Xi97]. They applied a combinatorial method to study superconducting oxide compounds. Since then, HTE and combinatorial strategies were established in material sciences, e. g. in the development of improved heterogeneous catalysts [Mo96, Ja99, Ha04], phosphors [Da98], magnetoresistive materials [Br95], photochemical materials [Ba02], and microwave dielectrics [Ch98]. Van Dover et al. analysed dielectric behaviour of materials in response to capacitance measurements [va98]. Reichenbach et al. described the combinatorial synthesis of perovskite-type oxide powders and their catalytic activity in CO oxidation reactions [Re01]. These high throughput research efforts are also extensively discussed in previous reviewing papers [Ja99, Se01, Yo02]. Aronova et al. tested combinatorial libraries of semiconductor sensors for the application as inorganic electronic noses [Ar03]. However, up to now examples on resistive gas sensing materials research are still rare.

The materials in HTE approaches are typically combined to create a library with common features, like one base material, gaining diversity by addition of dopants or additives. High throughput characterisation (screening) can be achieved by using sample plates containing several materials under test resulting in parallel processing of time consuming steps in the characterisation workflow. HTE methods should allow to rapidly screen a large number of solid-state materials and therefore should have a dramatic impact on the search for new classes of gas sensing materials with enhanced properties. In addition, these methods may help to map structure-property relationships, a central goal in materials science [Am02].

The approach presented here is a search for novel and improved gas sensor materials and is focussed on semiconducting ABO_3 oxides derived from the polyol method using an HTE impedance spectroscopy (HT-IS) system. The starting point of this work was a collaborative research project between industrial and academic research groups, focussing the development of electrical and optical sensors by use of high throughput processes [Br04, KOMB]. In this approach large collections of different materials are rapidly processed with the help of laboratory robotic systems and screened for specific properties of interest.

The next section briefly describes the high throughput workflow and its corresponding steps within.

2.9 Multielectrode array substrate and thick film deposition

For the high throughput screening in this investigation a multielectrode array substrate has been developed, on which 64 different materials can be characterised electrically. This multielectrode array consists of screen-printed platinum leads on an Al_2O_3 ceramic substrate (side length 106 mm) forming 64 interdigital capacitors (IDCs) as shown in Figure 2.12. One IDC consists of 12 electrode fingers with width of 125 μm . The distance between the electrode fingers is 150 μm . The platinum IDC has a structure width of 2.5 mm and each well has a diameter of 5 mm [Si02]. The array is applicable for resistive as well as for capacitive measurements. In addition, the design allows efficient and automated pipetting, and robot assisted sample preparation and coating. Positions on the substrate plates are labeled with numbers: each vertical column is labeled from top to bottom, while each horizontal row is

labeled from left to right with numbers 1 to 8. In position descriptions the row number is followed by the column number. For example, the position on the top left corner is termed 11 and the position in the bottom right corner is termed 88. All sample plates have a unique inscription composed of two capital letters and a number, for example: AC2017. These inscriptions allow identification and efficient searching for different wells on every sample plate stored in a data base.

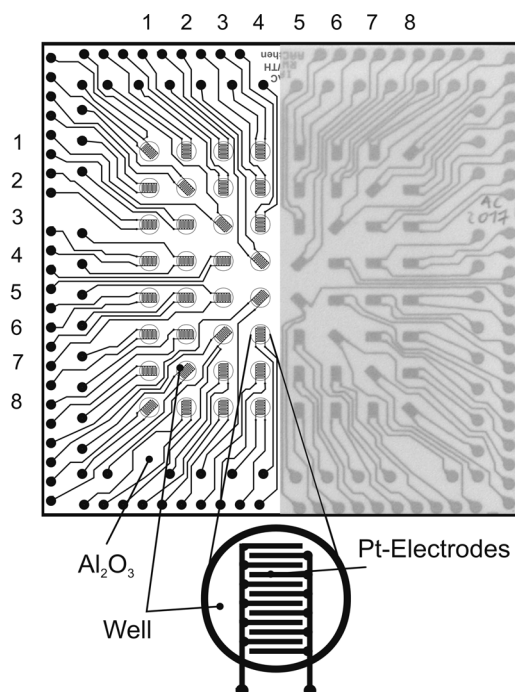


Figure 2.12. Scheme (left) and photograph (right) of substrate plate with 8x8 interdigitated electrode array.

Sample thick films can be applied directly to the electrode structure. The films were deposited in an assembly of individual cells that formed an 8x8 array (Figure 2.13). The design is similar to the sol-gel reactor set-up described in [Fr04]. In brief, the assembly consisted of a teflon block (①) 17 mm in thickness with 4 mm diameter holes positioned according to the substrate plate design. Each well had a viton fitting (O-ring, ②) for sealing against the substrate. The block was affixed to the electrode substrate (③), forming 64 wells (volume per well 214 μL). The base (④) and top plate (⑤) were made of metal. A viton plate (⑥) was placed between the substrate plate and the metal base to evenly distribute the pressure from the screws (⑦).

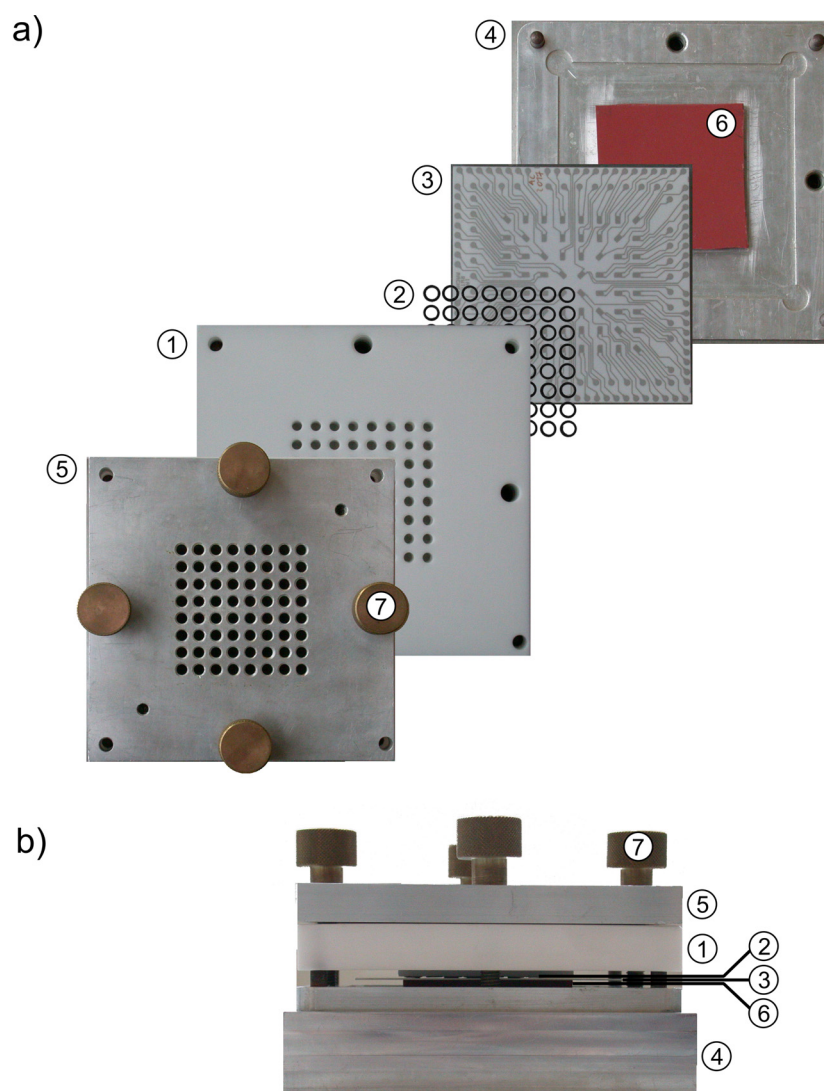


Figure 2.13: Reactor set-up for thick film deposition, a) top view, b) side view.

This design is well-suited for automated synthesis with pipetting robots. Figure 2.14 shows the commercial laboratory robotic system used here (Lissy, Zinsser Analytic GmbH).

Each module of the layout was designed for the desired application. The parallel reactor (④) allows space-saving syntheses of 21 different materials under reflux [Ko06b]. In addition the system enables thick film deposition (③) from suspensions (⑦) and surface doping of materials (⑧). All positions are addressed by computer software and the layout can be adapted to meet varying demands.

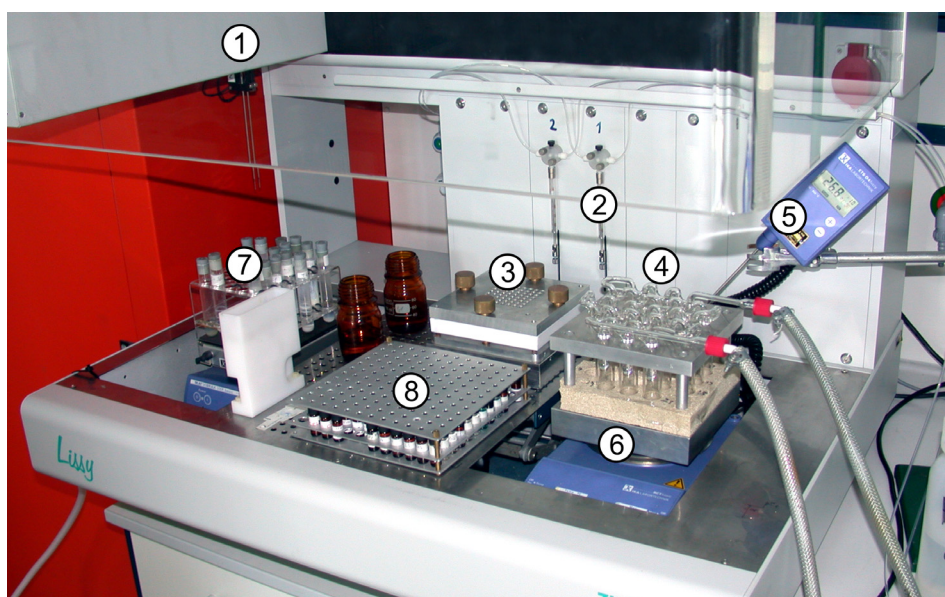


Figure 2.14: Laboratory robotic system (Lissy, Zinsser Analytic GmbH). ① Robot arm with needles, ② robot syringes, ③ coating station, ④ parallel reactor (21 syntheses under reflux), ⑤ temperature control, ⑥ heater and isolation, ⑦ shaker with test tubes (suspensions), ⑧ stack for surface dopant solutions (adapted from [Ko06b]).

2.10 High throughput impedance spectroscopy (HT-IS) setup

Electrical impedance measurements are crucial in many applications including measurements of superconductivity, magnetoresistivity, ferroelectric, and above all, in the here shown case, gas sensing properties. A contact probe consisting of a matrix of spring-loaded contact pins was used. This system is capable of measuring the 2-probe conductivity of 64 samples in one experiment. The multi-sample measurement is accomplished by a computer-controlled multichannel switching and data acquisition system. Temperature, gas control, and data acquisition are fully automated by computer software. Figure 2.15 shows the setup schematically.

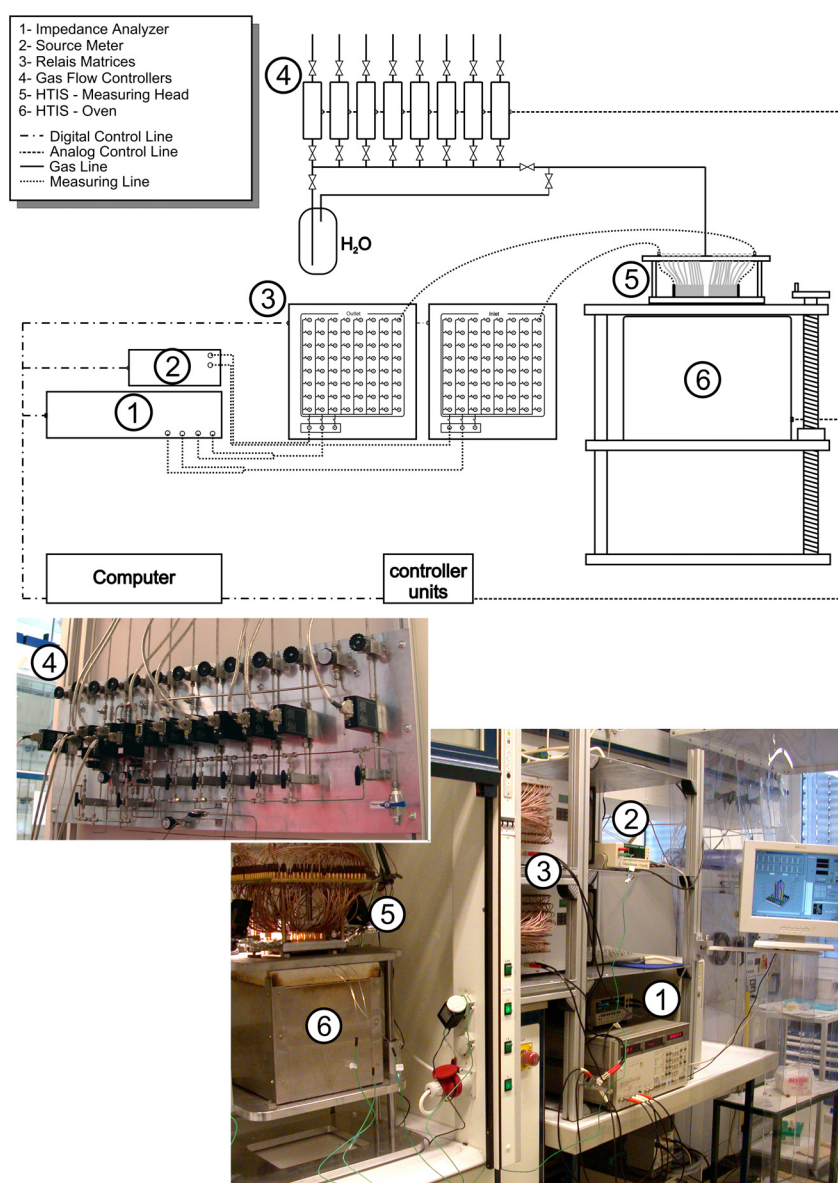


Figure 2.15: Scheme and photograph of the HT-IS Setup. Only two measuring lines are displayed in the scheme to preserve clarity. (adapted from [Si05, Sa04])

Time consuming steps like heating or sample conditioning can be proceeded in parallel. Sample plates (coated arrays) are inserted in the measuring head (⑤). The leads to each IDC are electrically connected via Al_2O_3 -covered platinum wires in the measuring head. Constant contact pressure is assured using spring loaded contact tips that connect the IDCs via high frequency capable relay matrices (multiplexers, ③) to the measuring instruments(①, ②). The measuring head is inserted into an oven which can heat samples up to 800°C (⑥). A set of gas flow controllers (④) is used to compose the different test gases. In addition, the test gases can be humidified by bubbling the carrier gas through a water reservoir at room temperature. The test gases are led to a quartz glass bell that covers all sample positions on a plate. Recently, further developments of the gas inlet have been realised. To prevent a test gas gradient on the sample plate, the quartz glass bell was replaced by a dispenser of 64 Al_2O_3 -tubes that ensures an individual gas supply for each sample position. For technical details see [Si05, Ko06b].

2.11 Impedance spectroscopy

This chapter presents the fundamentals of impedance spectroscopy which are of interest for the understanding and interpreting the performed measurements. A more detailed description can be found in [Ma87].

Impedance spectroscopy (IS) is a powerful method of characterising different electric properties of materials and their interfaces. The dynamics of bound or mobile charges in the bulk or interface regions of various different solid or liquid materials can be investigated. A great advantage is the non-destructive nature of the analysis. The general approach is to apply an electrical stimulus to electrodes and observe the response. IS measurements can be carried out in the time, or in the frequency domain. In our approach impedance is measured in the frequency domain by applying a single-frequency voltage to the electrodes-sample-system and measuring the phase shift and amplitude of the resulting current.

If an alternating voltage U^* is applied to an electrochemical cell (i. e. sensing layer on IDC structure) an electrical current I^* through the cell will be observed. The occurring current may be phase shifted around φ in comparison to the applied voltage.

With variation of the angular frequency ω , which describes the alternating voltage applied, the impedance is given by

$$Z^*(\omega) = \frac{U^*(\omega)}{I^*(\omega)} = Z'(\omega) + iZ''(\omega) \quad (2.12)$$

where i is the imaginary number. This impedance is a vector quantity which can be visualised in the Gaussian plane with either rectangular or polar coordinates, as shown in Figure 2.16:

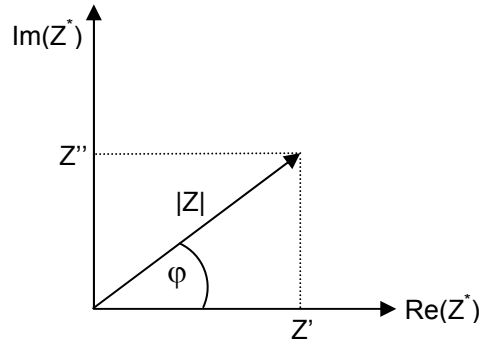


Figure 2.16: Impedance as vector plot (Argand plot).

The real part and the imaginary part of the complex impedance are given by

$$\text{Re}(Z^*) = Z' = |Z^*| \cos \varphi \quad (2.13)$$

$$\text{Im}(Z^*) = Z'' = |Z^*| \sin \varphi \quad (2.14)$$

with the phase angle

$$\varphi = \arctan\left(\frac{Z''}{Z'}\right) \quad (2.15)$$

and the absolute value

$$|Z^*| = \sqrt{Z'^2 + Z''^2} \quad (2.16)$$

In the regarded frequency range (typically 0,1Hz-10⁷Hz) an electrical field can interact with a solid material in two principle ways. These are the translational motion of charge carriers and the reorientation of defects having electric dipole moments. The first interaction leads to a (dc) conductivity σ which is in phase with the electric stimulus and is given by

$$\vec{I} = \sigma \cdot \vec{E} \quad (2.17)$$

where \vec{E} is the electric field. This translational motion of charge carriers can be described with an ideal ohmic resistance.

The second type of interaction leads to a displacement current

$$\bar{i} = \frac{d\bar{D}}{dt} \quad (2.18)$$

where \bar{D} is the electric displacement, which is defined as the total charge density on the electrodes:

$$\bar{D} = \varepsilon_0 \cdot \bar{E} + \bar{P} \quad (2.19)$$

where ε_0 is the permittivity of free space, and \bar{P} is the polarisation of the dielectric material. In real material systems both interactions are present and form a discrete relaxation process with the time constant $\tau=RC$. Different processes can be analysed from the impedance function derived from measurement if their relaxation times are in the observed frequency range.

IS measurements can be described with the help of circuit equivalents made up of ideal resistors, capacitors, inductances, and theoretically distributed circuit equivalents. With the help of these circuit equivalents and taking into account Kirchhoffs laws, different processes may be extracted from impedance data of complex systems, if their relaxation times differ from each other. By doing so, it is possible to investigate the individual processes.

In the following section the circuit equivalents for an ohmic resistance and a capacitance are introduced.

- Ohmic resistance R

Since the impedance is by definition a complex quantity, the impedance can only be real if $\varphi = 0$ and thus $Z^*(\omega)=Z'=R$. In this case Z' is frequency-independent. Figure 2.17a shows voltage and current versus time. Figure 2.17b shows the so-called Argand plot. In this case the imaginary part is plotted versus the real part of the complex impedance.

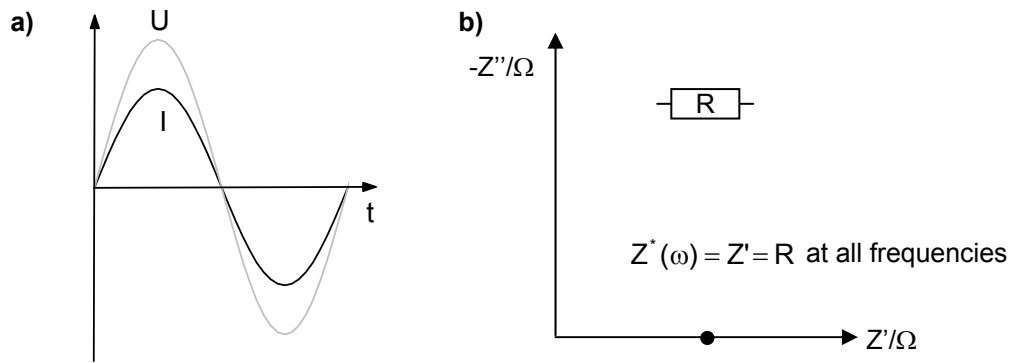


Figure 2.17: a) Voltage and current characteristics versus time and
b) Argand plot of a pure ohmic resistance.

▪ Capacitance C

In case of a pure capacitance the real part of the impedance remains zero. The impedance is frequency dependent and only imaginary. The current is ahead of the voltage ($\varphi = \pi/2$). Figure 2.18 a shows the voltage and current behaviour, and b the Argand plot.

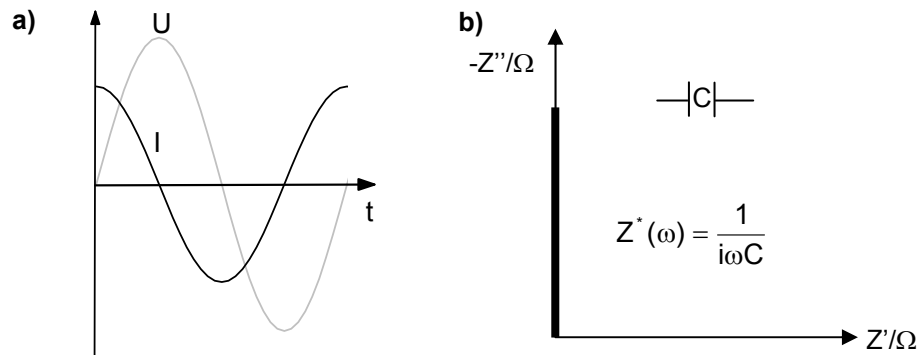


Figure 2.18: a) Voltage and current behaviour versus time and b) Argand plot of a pure capacitance.

Combining R and C to a parallel circuit, the impedance is given by the sum of the contributions from resistance and capacitance:

$$Z^*(\omega) = R + \frac{1}{i\omega C} = \frac{R}{1 + R \cdot i\omega C} \quad (2.20)$$

This shows a symmetric semicircle in the Argand plot (see Figure 2.19).

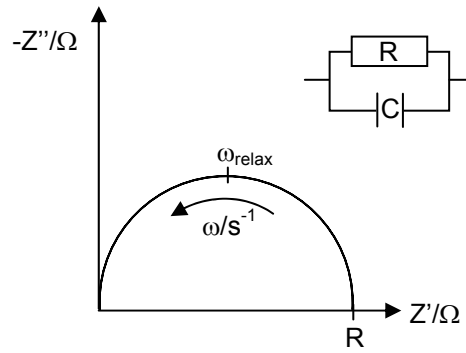


Figure 2.19: Argand plot and circuit equivalent for a parallel RC circuit.

At lower frequencies the capacitor is shut off and the current flows through the resistor. Z is the ohmic resistance; the imaginary part is zero. At high frequencies a displacement current passes through the capacitor, and the resistor is shorted out. In this case both the real and the imaginary part are zero. In between these frequencies the current is running through both the capacitor and the resistor. The maximum of the shown semicircle is at the relaxation frequency $\omega_{\text{relax}} = \tau^{-1} = (RC)^{-1}$

Another possible graphical depiction is the so-called Bode plot in which the frequency response is plotted. Figure 2.20 shows the real and imaginary part of the impedance plotted versus the log frequency for a parallel RC circuit.

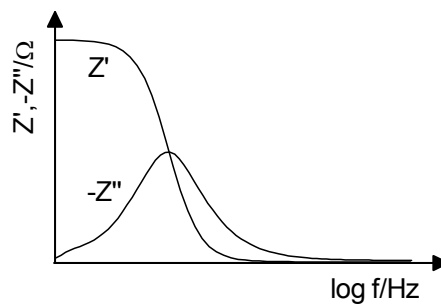


Figure 2.20: Real and imaginary part of the complex impedance versus frequency (Bode plot).

An advantage of this depiction is the frequency development of the observed values. Finally, there are several other quantities related to the impedance that are called immittances. The admittance is the corresponding ac electric conductivity, which is defined as:

$$Y^*(\omega) = \frac{1}{Z^*(\omega)} = Y'(\omega) + iY''(\omega) \quad (2.21)$$

The modulus function is given by:

$$M^*(\omega) = i\omega CZ^*(\omega) = M'(\omega) - iM''(\omega) \quad (2.22)$$

The complex dielectric permittivity is the inverse function of the modulus function and thus

$$\varepsilon^*(\omega) = \frac{1}{M^*(\omega)} = \frac{Y^*(\omega)}{i\omega C} = \varepsilon'(\omega) - i\varepsilon''(\omega) \quad (2.23)$$

Determination of resistance values and capacities due to data fitting are described in chapter 3.2.2.

3. Results and Discussion

3.1 Material preparation

The following chapters present the results of the work. First, material preparation and characterisation is shown, and sensor preparation and measurements follow. Figure 3.1 displays the complete workflow. The workflow can be sectioned into powder preparation and sensor fabrication.

▪ Powder preparation

Stoichiometric amounts of suitable metal precursors were dispersed in diethylene glycol (DEG, Merck, 99.99%). The mixture was heated up to T_1 (80 °C-170 °C) while stirring until a clear solution was obtained. If necessary, a sufficient surplus of hydrolysis agent was added in order to achieve full hydrolysis. The emerging suspension was heated for 5 h up to T_2 (160 °C-190 °C) and then cooled to room temperature. The preparation resulted in stable suspensions with a standard concentration in all experiments of typically 1 wt% (solid to DEG). For further characterisation the solid material was separated from the suspension via centrifugation and washing with acetone. These “as synthesised” samples were dried at 60 °C. To obtain crystalline materials the suspensions were dried at 400 °C (1h) and then annealed at T_3 (700-900 °C) for 2-12 h. For each individual synthesis, reaction parameters needed to be optimised with respect to particle size, yield and purity. The preparation varied depending on the hydrolysis agent, i. e. in some cases an extra amount of water, acidic solution (HNO_3 or acetic acid) or base (KOH , H_2O_2 or NH_3 solution) was added. In other cases, the crystal water present in the starting compounds was sufficient for hydrolysis. The initial characterisation of the products was carried out by transmission powder XRD measurements on thin films. Powder morphology of the calcined materials was examined by SEM and TEM analysis.

▪ Sensor fabrication

For thick film fabrication the metal oxide powders were dispersed by mixing in a mortar with a solution of polyethylene imine (0.5 wt%) in water. Then the suspension was deposited onto microelectrode substrates by the introduced laboratory robotic system. Additionally, surface dopants could be deposited by impregnation of the films with metal salt solutions via the laboratory robotic system. The substrate was first dried for 48 h at room temperature in air. After that it was held for 12 h at 700 °C in air to remove the organic residues. Homogeneous thick films were formed, having a thickness between 50 and 100 μm . The ready prepared sample plates were

characterised by high throughput impedance spectroscopy with respect to their gas sensing properties. All results were stored in a data base which allowed data mining and helped to design new experiments in comparison to literature [Fr05].

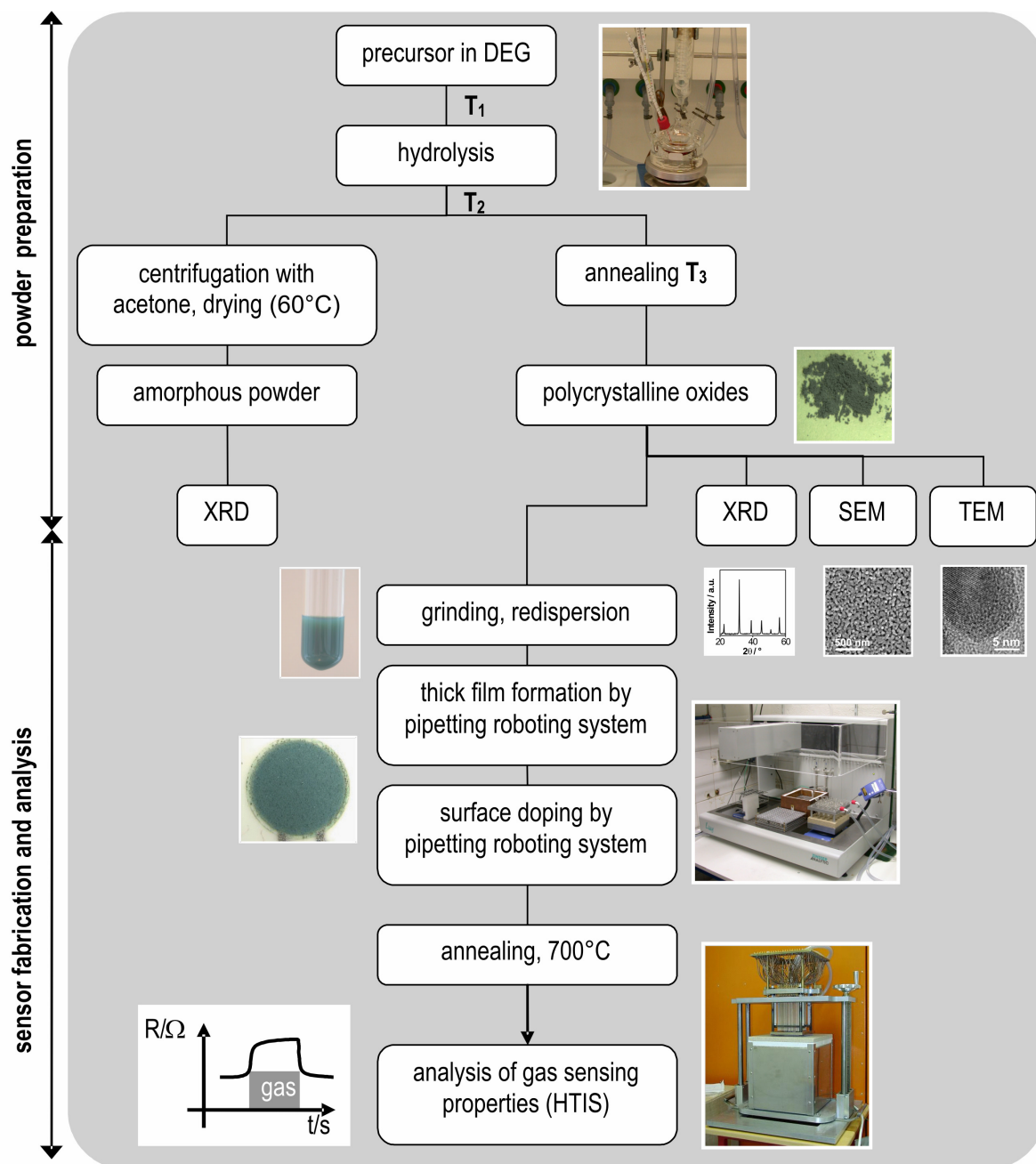


Figure 3.1: Flowchart summerising the preparation of ABO_3 thick film sensors based on polyol mediated synthesis.

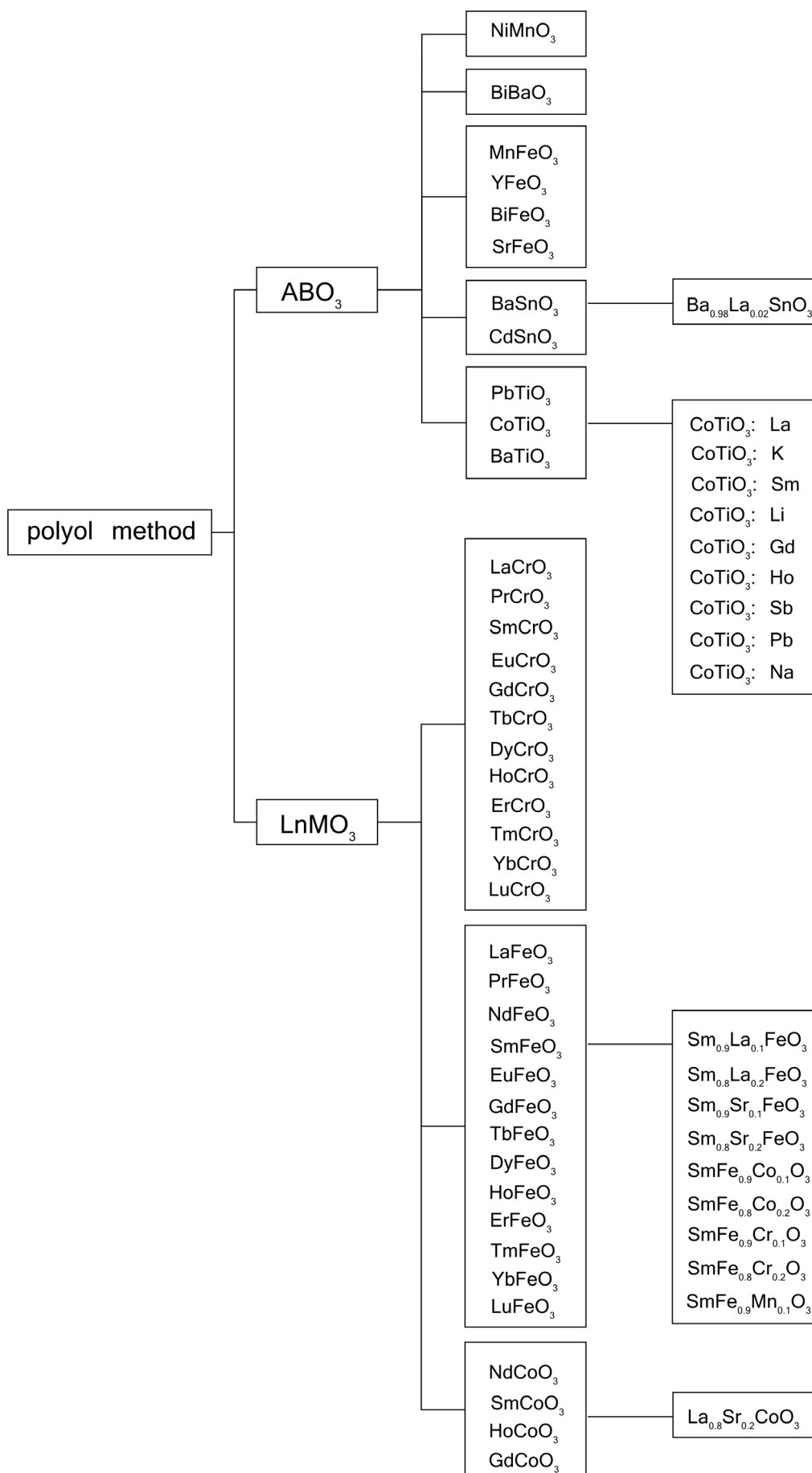


Figure 3.2. Prepared materials via the polyol mediated synthesis.

Figure 3.2 presents all ABO_3 materials prepared successfully in this work. They can be classified into two main groups: rare-earth containing $LnMO_3$ ($M=Co, Cr, Fe$) and ABO_3 materials containing only rare-earth elements as volume dopants. A detailed description of the preparation method for each perovskite oxide material is given in the experimental section (chapter 6).

In Figure 3.3 the ionic radii of the A and B cations of the prepared materials (without volume dopants) from Figure 3.2 are plotted. The solid lines form the perovskite region according to the Goldschmidt relation (see equation 2.11). All materials which have been revealed to have perovskite structure are indeed located in the defined region. Three materials, $NiMnO_3$, $FeMnO_3$ and $CoTiO_3$, form ilmenite compounds and can be localised at the left side of the plot, which indicates A and B cations of about the same size.

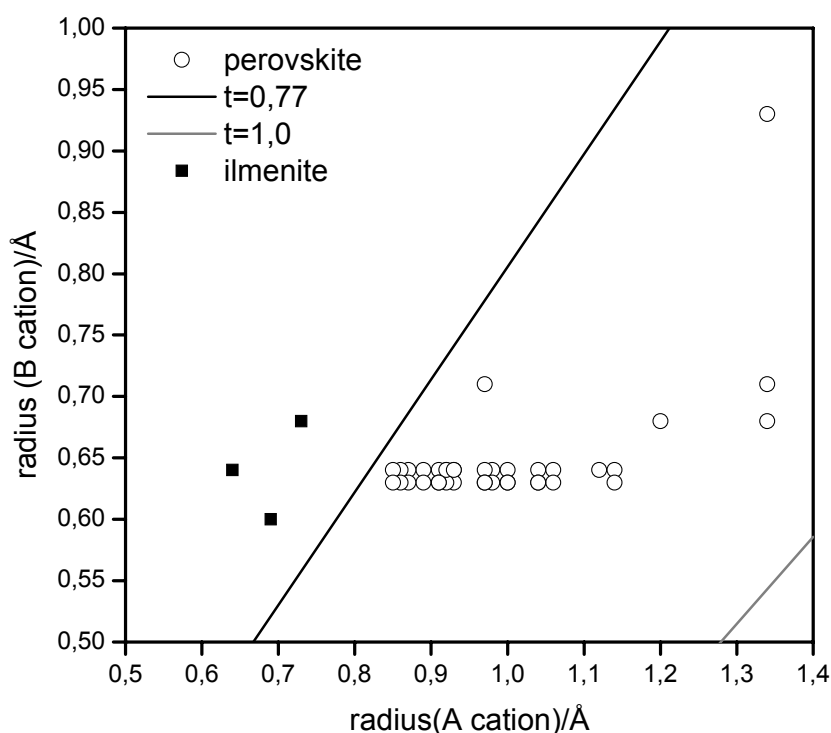


Figure 3.3: Ionic radius of A vs. ionic radius of B for the prepared undoped ABO_3 compounds. (Including 40 ABO_3 oxides with bivalent, trivalent and quadrivalent ions of different radii). The solid lines ($t=0.77$ and $t=1.0$) restrict the area of perovskite-type structure according to the Goldschmidt relation.

An example of the prepared materials is shown in Figure 3.4 and 3.5. The SEM picture shows the morphology of $MnFeO_3$ nanoparticles prepared by the polyol

method and annealed at 700°C for 12 h. The primary particle shape was almost spherical. The annealed particle agglomerates appeared as open porous structure which allowed good interpenetration of the admixed test gases. The XRD diffraction pattern revealed the crystallinity of the material after annealing without formation of any by-products. The as synthesised sample appeared as amorphous powder.

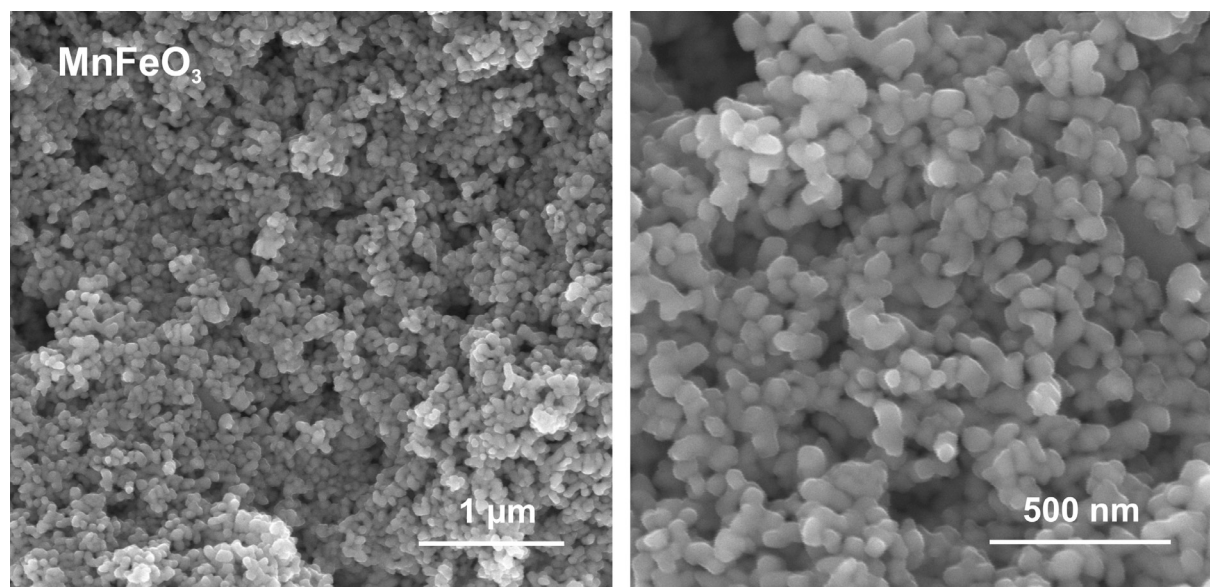


Figure 3.4: SEM picture of MnFeO₃ heated for 12 h at 700 °C.

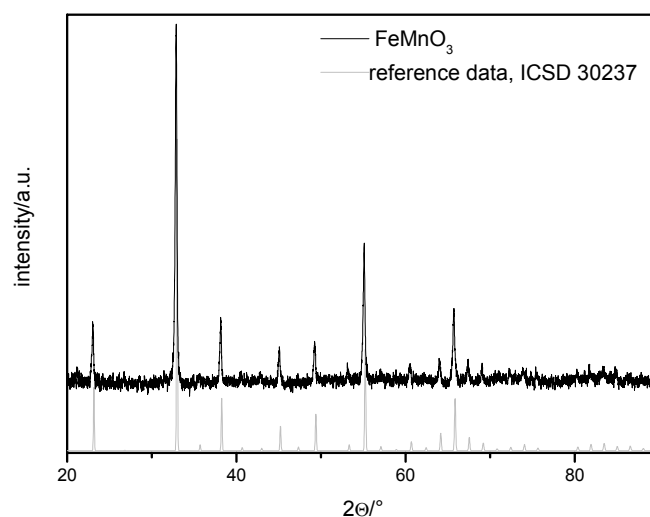


Figure 3.5: X-ray diffraction pattern of MnFeO₃ powder after annealing for 12 h at T = 700 °C.

SEM and XRD characteristics of the ABO₃ materials not discussed in the following text can be found in the Appendix.

All prepared materials have been used for layer preparation and have been characterised by impedance spectroscopy with regard to their gas sensing properties. The following chapter will concentrate on two p-type material classes. CoTiO_3 was chosen as the example ilmenite material. On the other hand, LnMO_3 ($\text{Ln}=\text{rare-earth}$, $\text{M}=\text{Fe}$, Cr) materials are also presented because of the possibility to compare 25 materials from the same period of the periodic table of elements.

NiMnO_3 , BiFeO_3 , MnFeO_3 and the LnCoO_3 compounds showed good conductivity but only poor sensing characteristics. This could be understood by taking into account the sensing mechanism. The percolation path in p-type sensing films goes through the surface of the materials. The bulk resistance is not expected to vary much after exposure to different gases. The conductance change should primarily come from the surface resistance variation. The bulk material is seen to be stoichiometric, which means the bulk resistance of the particles is higher than the surface resistance ($R_{\text{bulk}} \gg R_{\text{surf}}$). If the bulk resistance is close to the surface resistance, the sensitivity of the material will be diminished. If the bulk resistance is much lower than the surface resistance, low gas sensitivity will be expected. The bulk resistance needs to be higher than the surface resistance; otherwise the sample will have low or no gas sensitivity.

On the other hand, materials like BaTiO_3 , BaSnO_3 and BaBiO_3 showed very high resistances in the measured temperature range. They were not suitable for the use in the HT-IS setup due to instrumental limitations.

Beside the shown ABO_3 compounds different Mo-O-Bi complexes [Ro06] were used in the polyol mediated synthesis to produce bismuth molybdate ($\text{Bi}_2\text{O}_3 \cdot n\text{MoO}_3$, $n=1$, 2, or 3) nanoparticles. Bismuth molybdate phases might find application for example in catalysis or gas sensing. However, in the performed experiments the preparation of pure phases was not possible. In addition, the chelating effect of DEG seemed not to be strong enough for the exclusive preparation of nanoparticles. A detailed description of the compounds, syntheses and measurements can be found in [Ro06, Ro07].

Chapter 3.2 describes the investigations which have been made concerning CoTiO_3 , while chapter 3.3 concentrates on the work corresponding to the different rare-earth orthoferrites and orthochromites.

3.2. CoTiO₃

Ilmenite-type CoTiO₃ has earlier been studied for possible applications as catalysts [Ka84, Ya03, Br01] or as a high- κ dielectric [Pa01]. The possible application as a gas sensing material is restricted on a few examples in literature, namely the suitability for humidity detection in combination with Ta₂O₅ [To84], and ethanol [Ch99] detection as a nanocrystalline material.

The polyol method was applied for the synthesis of nanocrystalline CoTiO₃ and the gas sensing properties of the material have been screened. Figure 3.6 shows the X-ray diffraction pattern of the sample before and after calcination at 700 °C for 12 h.

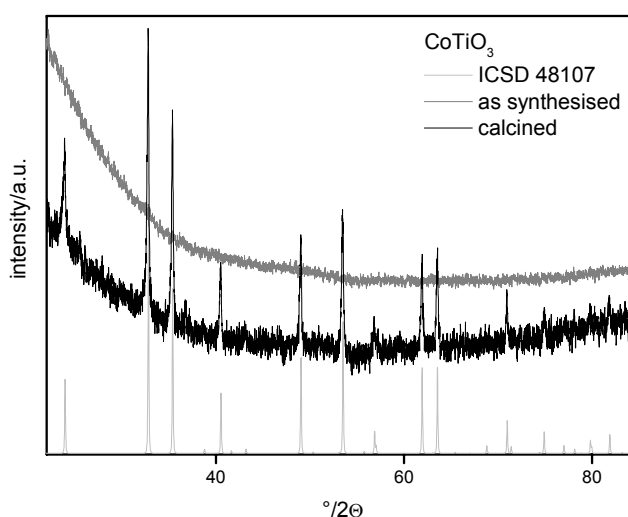


Figure 3.6: X-ray diffraction pattern of CoTiO₃

The material was found to be amorphous right after preparation (as synthesised) according to XRD analysis. After annealing at 700 °C for 12 h the material turned out to be highly crystalline. The powder X-ray diffraction pattern showed the formation of CoTiO₃. In some cases up to 10% of TiO₂ as by-product could be found. The lattice parameters of the trigonal phase were in good accordance with the reference data [Ki84]. The XRD lines were broad compared to the bulk material, indicating that nanometer sized particles have been formed.

Sharp X-ray interferences of powder samples are achieved if the size of coherent lattices is between 10^{-3} and $5 \cdot 10^{-5}$ cm [Kr94]. Powder samples consisting of crystallites smaller than $5 \cdot 10^{-5}$ cm show line broadening, and sharp interferences cannot be produced (as shown in Scheme 3.7). Even though nowadays detailed

techniques exist to evaluate XRD patterns with respect to the crystallite size and strain effects within the crystals, in this work only a basic XRD analysis is used for phase identification. Crystallite size is derived from measuring the broadening of a particular peak in a diffraction pattern associated with a particular planar reflection from within the crystal unit cell. It is inversely related to the full width at half maximum B of an individual peak, the more narrow the peak, the larger the crystallite size. In addition, the diffractometer used to measure the sample can also introduce a small amount of instrumental peak broadening. To achieve the real crystallite size, these broadenings have to be corrected. Determination of peak broadness due to the Scherrer equation [Sc18, Bi46] without further corrections gives a simple form for the range of the crystallite size. This size DS can then be calculated by:

$$DS = \frac{57.3 \cdot K \cdot \lambda}{B \cdot \cos \theta} \quad (3.1)$$

where λ is the wavelength (generally $\text{CuK}\alpha$ ray), 57.3 a correlation factor from degree to numerical values and θ the position of the peak. K is the shape factor of the average crystallite which varies depending on the crystallite shape from 0.89 to 1.39.

To obtain a more general idea of the overall crystallite allocation, an average crystallite size is determined using multiple peaks. The crystallite size is only equivalent to the grain size if the individual grains are perfect single crystals free of defects, grain boundaries or stacking faults. In addition, crystallite cores may be embedded into amorphous shells. Agglomerated primary particles may form secondary particles which may be bigger than the achieved crystallite size.

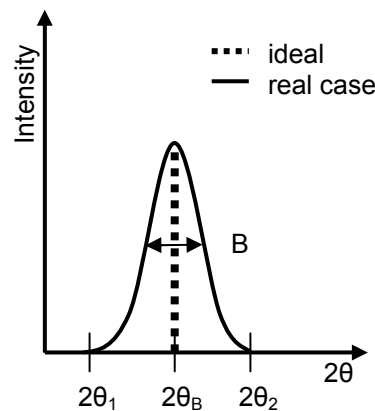


Figure 3.7: Line broadening due to small crystallite size.

The estimated mean crystallite size was around 96 nm. The particle size of the powder material as well as the size distribution was obtained from the SEM micrographs (local method). The SEM image of the annealed material is shown in Figure 3.8. Agglomerated almost spherical particles with a diameter of 50 to 120 nm can be seen; overall the material appeared as a highly porous network of interconnected particles.

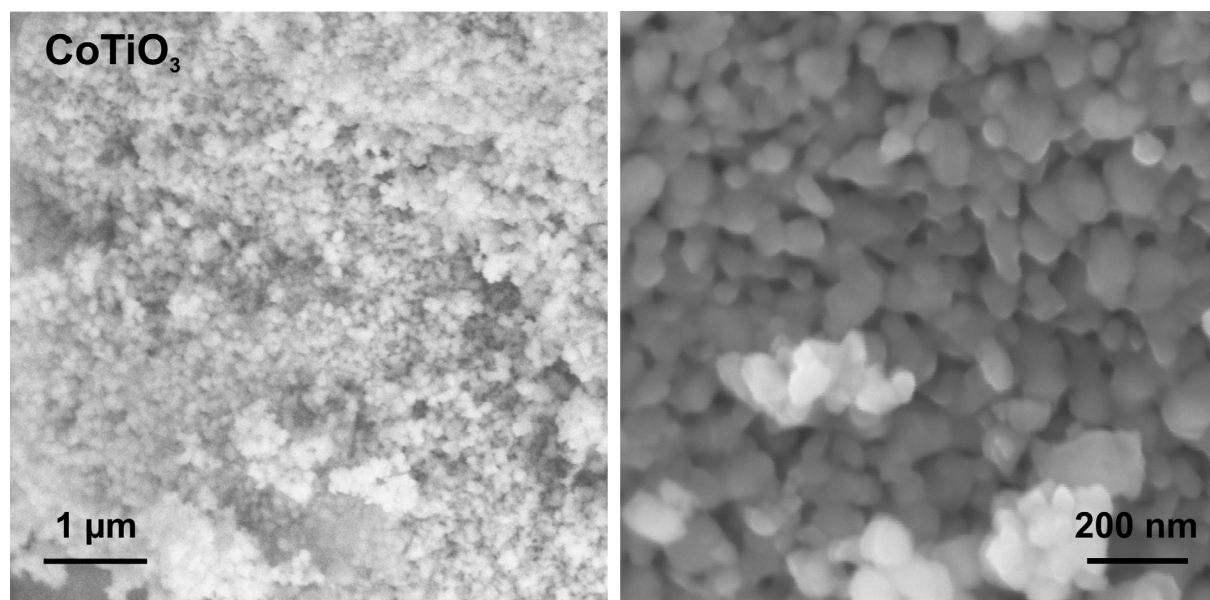


Figure 3.8: SEM images of CoTiO₃.

The synthesised powder was well suited for thick layer preparation on interdigital electrode structures (shown in chapter 2, Figure 2.12) of substrate plates. The material was dispersed by mixing in a mortar with a solution of polyethylene imine (0.5 wt%) in water. The resulting suspension had a concentration of 0.08 mol/L. The suspension was deposited into the Teflon wells (see chapter 2, Figure 2.13) by the laboratory robotic system (Lissy, Zinsser Analytic, as already shown in chapter 2, Figure 2.14). The substrate was first dried for 48 hours at room temperature in air. After that it was held for 12 h at 700 °C in air to remove the organic residues. Figure 3.9 shows that homogeneous thick films were formed.



Figure 3.9: Scheme of thick film deposition and photograph of thick film.

To compensate for possible gradients in gas concentration and temperature as well as single failures due to contact defects over the substrate three statistically selected positions were equipped with the same material composition.

3.2.1 Electrical characterisation

Electrical measurements were performed using an impedance analyzer (Agilent 4192 A) in a frequency range from 10 to 10^7 Hz (15 measuring points per frequency decade) and an amplitude of 100 mV (rms). The measurements were carried out in a temperature range between 500 to 200 °C in 25°-steps. Reference measurements were performed in synthetic air (air), which was also used as carrier gas for the test gases H₂, CO, NO₂, ethanol and propylene; for NO N₂ was chosen as the carrier gas in order to avoid formation of NO₂. For the gas sensing experiments, the test gases were mixed with synthetic air to reach a consistent volume flow of 100 sccm. Conditioning of the materials was carried out at 500 °C for 240 min under air and at the following temperatures for 90 min. The measuring gas sequence was H₂ (25 ppm), air, CO (50 ppm), air, NO (5 ppm), air, NO₂ (5 ppm), air, ethanol (40 ppm), air, propylene (25 ppm), air. The intermediate measurements in air allow the observation of the recovery ability of the sensor material before the next test gas is applied. Relative humidity of the gases was 45 % at room temperature in order to perform the measurements in a typical humidity range representative for ambient conditions. For sample conditioning, a preliminary gas flow was applied over 30 min to reach adsorption equilibrium.

The measurement of 64 samples in one gas atmosphere at a fixed temperature took about 30 min including impedance measurements with 91 single frequency measurements each.

In order to measure the response time of the individual samples, measurements at a single frequency (100 Hz) were performed. 100 Hz has been chosen to stay in the frequency independent part of the impedance spectra (quasi-dc plateau) but at the same time to allow fast measurements. Each measurement took 1.5 s, while the time interval between measurements was 4 s.

3.2.2 Automated data fitting of impedance spectra

Figure 3.10 shows the plot of the real part of the complex impedance versus the imaginary part for a parallel RC circuit equivalent (Argand plot). A semicircle with its centre on the real axis of the complex plane can be seen.

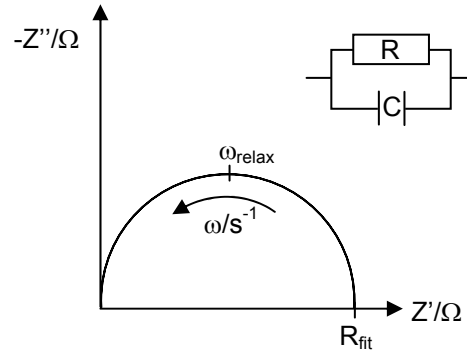


Figure 3.10: Argand plot and circuit equivalent for a parallel RC circuit.

Automated data fitting allows describing the impedance spectra as the impedance function of a circuit equivalent, e. g. consisting of a resistor and a capacitor in parallel. Also other elements like inductances or constant phase elements (CPE) could be implemented. The admittance of the parallel RC circuit is just the sum of the admittances of the two elements which give the impedance [Ma87]:

$$Z^* = \frac{R}{1 + R \cdot i\omega C} \quad (3.2)$$

From this $|Z|$ can be calculated as:

$$|Z| = \sqrt{\left(\frac{1}{R}\right)^2 + \omega^2 C^2}^{-1} \quad (3.3)$$

With the phase $\varphi = \arctan(R \cdot \omega C)$ the impedance function used for the real part Z' and the imaginary part Z'' given by:

$$Z' = \cos[\arctan(\omega \cdot R \cdot C)] \cdot \sqrt{\left(\frac{1}{R}\right)^2 + (\omega \cdot C)^2}^{-1} \quad (3.4)$$

$$Z'' = \sin[\arctan(\omega \cdot R \cdot C)] \cdot \sqrt{\left(\frac{1}{R}\right)^2 + (\omega \cdot C)^2}^{-1} \quad (3.5)$$

In this case R is the extrapolated DC-resistance of the material, C the capacitance and ω the angular frequency. The use of these fit functions reduces the complex impedance function describing the electrical properties of each material to one value

for the resistance and the capacitance, respectively. While the capacitance can be assigned to the geometric capacitance of the IDC, the resistance values under the respective measuring conditions are taken for the determination of the material sensitivity.

Samples with depressed semicircles have been adjusted with a CPE. The CPE is a non-intuitive circuit element. In case of a resistance R and a CPE in parallel we observe the arc of a circle with the centre some distance below the x-axis in the Argand plot (as shown in figure 3.11). The corresponding circuit equivalent is called a ZARC-element [Ma87].

$$Z^* = \frac{R}{1 + R \cdot Q(i \cdot \omega)^n} \quad (3.6)$$

where R_{fit} is the low frequency real-axis intercept, n is related to the depression angle, i is the imaginary number and Q has the numerical value of the admittance Y at ω [Or02].

$$Y^* = Q \cdot (i \cdot \omega)^n \quad \text{for } 0 < n < 1 \quad (3.7)$$

$$Y^* = i \cdot \omega \cdot C \quad \text{for } n = 1 \quad (3.8)$$

The behaviour of a resistor in parallel with an ideal capacitor (see above) is recovered when n is 1 ($Q=C$). When n is close to 1, the CPE resembles a capacitor, but the phase angle is not 90° . The real capacitance can be calculated from Q and n . When n is zero, only a resistive influence is found.

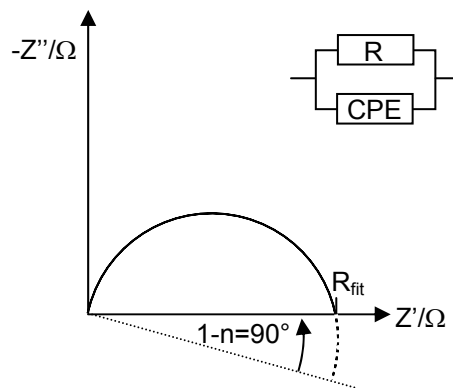


Figure 3.11: Argand plot and circuit equivalent for a ZARC-element.

The admittance of the parallel RCPE circuit is the sum of the admittances of the two elements which are used in the fit data.

If the capacitor is replaced by a constant phase element in the analysis of the performed measurements, a slight refinement of the fitting results is obtained, whereas n is typically larger than 0.9. Thus, for further evaluation we regarded the adaptation of a parallel RC-element to be sufficient.

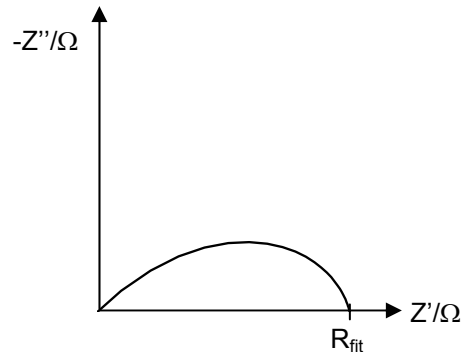


Figure 3.12: Argand plot for a sample where measurement connection compensation is needed.

If materials have small resistances, which causes high currents, a damping of the impedance occurs (see figure 3.12). This damping ΔZ_f is due to the measurement connection and for the used impedance analyser given as:

$$\Delta Z_f = -0.38 \cdot \Delta L \cdot f^2 \quad (3.9)$$

(according to:[Ag91])

where f is the measuring frequency, ΔL is the difference between the used measurement connection and the already intern compensated measurement connection by the impedance analyser. For compensation of damping, the simulated impedances are charged with the calculated damping as follows:

$$Z'_{\text{total}} = Z' + Z' \cdot \Delta Z_f \quad (3.10)$$

$$Z''_{\text{total}} = Z'' + Z'' \cdot \Delta Z_f \quad (3.11)$$

For small frequencies ($f \rightarrow 0$) ΔZ_f becomes zero. For high frequency ΔZ_f comes into account, and the semicircle is depressed into a linear function. ΔL was implemented as a fit variable whose value lies typically around $3.9 \text{ m} \pm 0.3 \text{ m}$. Finally, analysis of the difference between simulated and measured impedance diagrams gives the failure value of the fitting. Validation of the fit quality (in %) is included in the fit file. For further information see [Sa04].

The extracted R values are then used to calculate the relative or absolute sensitivity of the materials.

3.2.3 Electrical characterisation of CoTiO₃

Figure 3.13 shows a plot of the real part of the complex impedance versus the imaginary part (Argand plot) for CoTiO₃ in synthetic air at 500 °C. The plot, which is representative for all other CoTiO₃-samples measured, shows a slightly depressed semicircle.

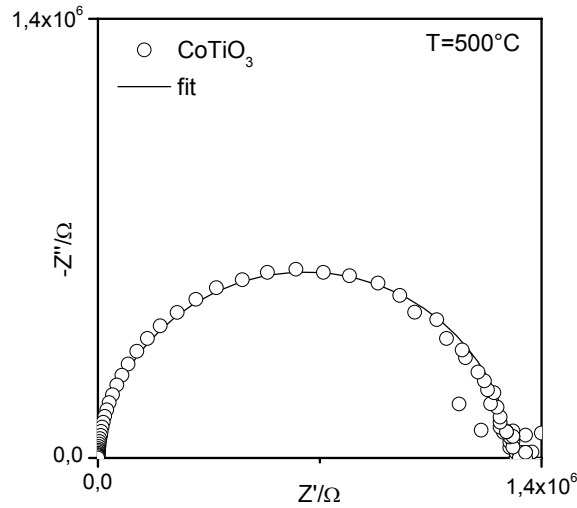


Figure 3.13: Argand plot of a CoTiO₃ sample at 500°C.

The resistance values under the respective measuring conditions were taken for the determination of the materials' sensitivity using equation 2.8 and 2.9. The material showed p-type behaviour, i. e. an increase of resistance due to admixing of reducing gases. Figure 3.14 shows the fingerprint (bar chart) of CoTiO₃, where S_{Δ} for each gas at 475 °C is shown. It illustrates that the undoped material showed high sensitivity towards propylene and ethanol with a weak cross sensitivity towards other gases. However, for undoped CoTiO₃, no reliable impedance spectroscopic results could be obtained at temperatures below 450°C due to high resistances of the material. For lower temperatures, DC measurements using a Keithley 2400 source meter at a measuring voltage of 1V have been taken into account; gas sequence and preconditioning times remained the same.

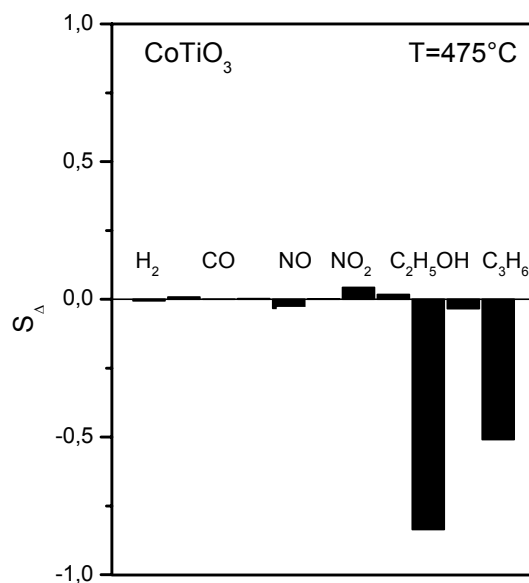


Figure 3.14: Fingerprint of CoTiO₃ towards different test gases.

In accordance with the literature published by Chu et al., the measured sensitivity to 40 ppm ethanol was located in between the values found by Chu for 50 and 100 ppm ethanol. However, the temperature of maximum sensitivity was shifted by 25°C with respect to Chu's value, as shown in Figure 3.15.

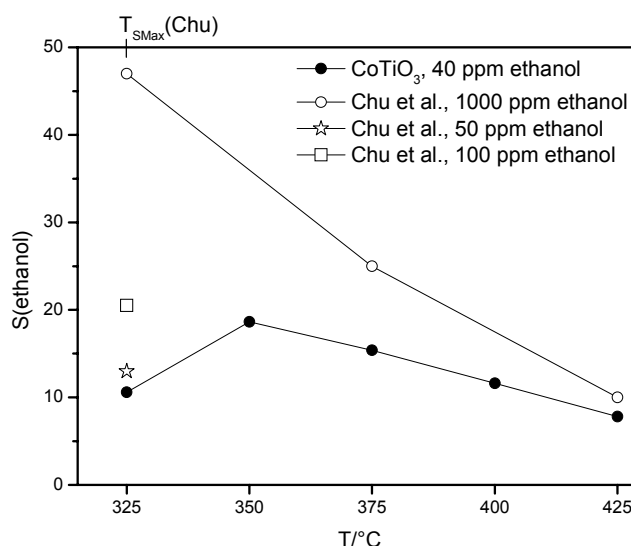


Figure 3.15: Temperature dependence of ethanol sensitivity of CoTiO₃ in comparison to Chu et al.

The overall low conductivity together with the thermal stability of these materials suggested possible sensor applications only at higher temperatures.

In the following discussion, it will be illustrated that CoTiO_3 was doped with different metal ions in order to study the effects of volume doping on the electrical and sensing properties.

3.2.4 Volume doped CoTiO_3

CoTiO_3 is a potential candidate for use as ethanol sensor. However, the high resistance of CoTiO_3 is a disadvantage in application. Partial substitution may lower the resistance values.

Different metal salts ($\text{La}(\text{NO}_3)_3 \cdot 6\text{H}_2\text{O}$, $\text{K}(\text{CH}_3\text{COO})$, $\text{Sm}(\text{NO}_3)_3 \cdot 6\text{H}_2\text{O}$, LiNO_3 , $\text{Gd}(\text{CH}_3\text{COO})_3 \cdot n\text{H}_2\text{O}$, $\text{Ho}(\text{NO}_3)_3 \cdot 5\text{H}_2\text{O}$, $\text{Sb}(\text{CH}_3\text{COO})_3$, $\text{Pb}(\text{CH}_3\text{COO})_2 \cdot 3\text{H}_2\text{O}$, $\text{Na}(\text{CH}_3\text{COO}) \cdot 3\text{H}_2\text{O}$) have been introduced as volume dopants (2 at%). The doping was inserted in the polyol method described previously. K, Li, Na, Sm, La and Ho were inserted in the reaction with a smaller amount of Co, while Gd, Sb, Pb, La, Sm and Ho were inserted with less Ti. Indices A and B are used for dopants (La, Sm, Ho) which have been inserted with less Co and less Ti. A detailed description of the synthesis can be found in the experimental data. Figure 3.15 shows exemplary the X-ray diffraction pattern of La-doped CoTiO_3 .

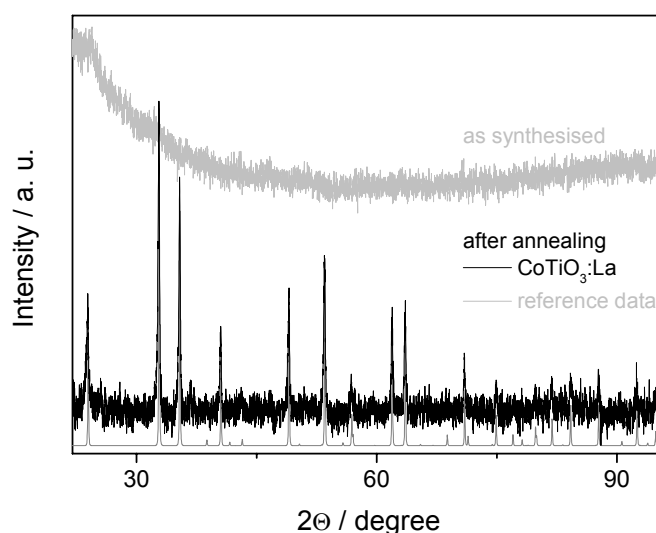


Figure 3.15: X-ray diffraction pattern of $\text{CoTiO}_3\text{:La}$ powder before and after annealing for 12 h at $T = 700\text{ }^\circ\text{C}$.

All “as synthesised” samples were amorphous right after preparation. The XRD values of the calcined samples were in good agreement with those reported in ICSD

file number 48107 for CoTiO_3 . There were no indications of how and where the volume dopants were inserted into the CoTiO_3 lattice. The amount of dopant was too small to see in the by-product of formed oxides or a remarkable shift of lattice parameters in the X-ray diffraction. All patterns showed the same structure as CoTiO_3 .

EDX and XRF measurements were able to proof the presence of the volume dopants. However, the amount of dopant was in the range of the detection limit that means no quantitative information was achieved.

Figure 3.16 gives the scanning electron micrographs (SEM) showing the top view of the different volume doped CoTiO_3 -samples. Table 3.1 shows the calculated crystallite sizes and the primary particle size from SEM images respectively. $\text{CoTiO}_3\text{:La}_A$ and $\text{CoTiO}_3\text{:Sm}_A$ showed the smallest crystallite and particle sizes. However, in all shown samples the surface morphologies were similar to each other. The primary particle sizes resided in the same range and similarities to the thick film morphology can be found. All particles were agglomerated due to thermal treatment.

Table 3.1: Crystallite and particle sizes of volume doped CoTiO_3 materials.

<i>compound</i>	<i>DS(nm)</i>	<i>SEM(nm)*</i>
CoTiO_3	85	50-120
$\text{CoTiO}_3\text{:La}_A$	61	30-70
$\text{CoTiO}_3\text{:La}_B$	83	70-120
$\text{CoTiO}_3\text{:K}$	96	80-140
$\text{CoTiO}_3\text{:Li}$	106	70-130
$\text{CoTiO}_3\text{:Na}$	90	70-100
$\text{CoTiO}_3\text{:Sb}$	83	70-100
$\text{CoTiO}_3\text{:Pb}$	94	70-100
$\text{CoTiO}_3\text{:Sm}_A$	58	50-90
$\text{CoTiO}_3\text{:Sm}_B$	85	60-100
$\text{CoTiO}_3\text{:Ho}_A$	76	60-90
$\text{CoTiO}_3\text{:Ho}_B$	76	60-90
$\text{CoTiO}_3\text{:Gd}$	86	50-90

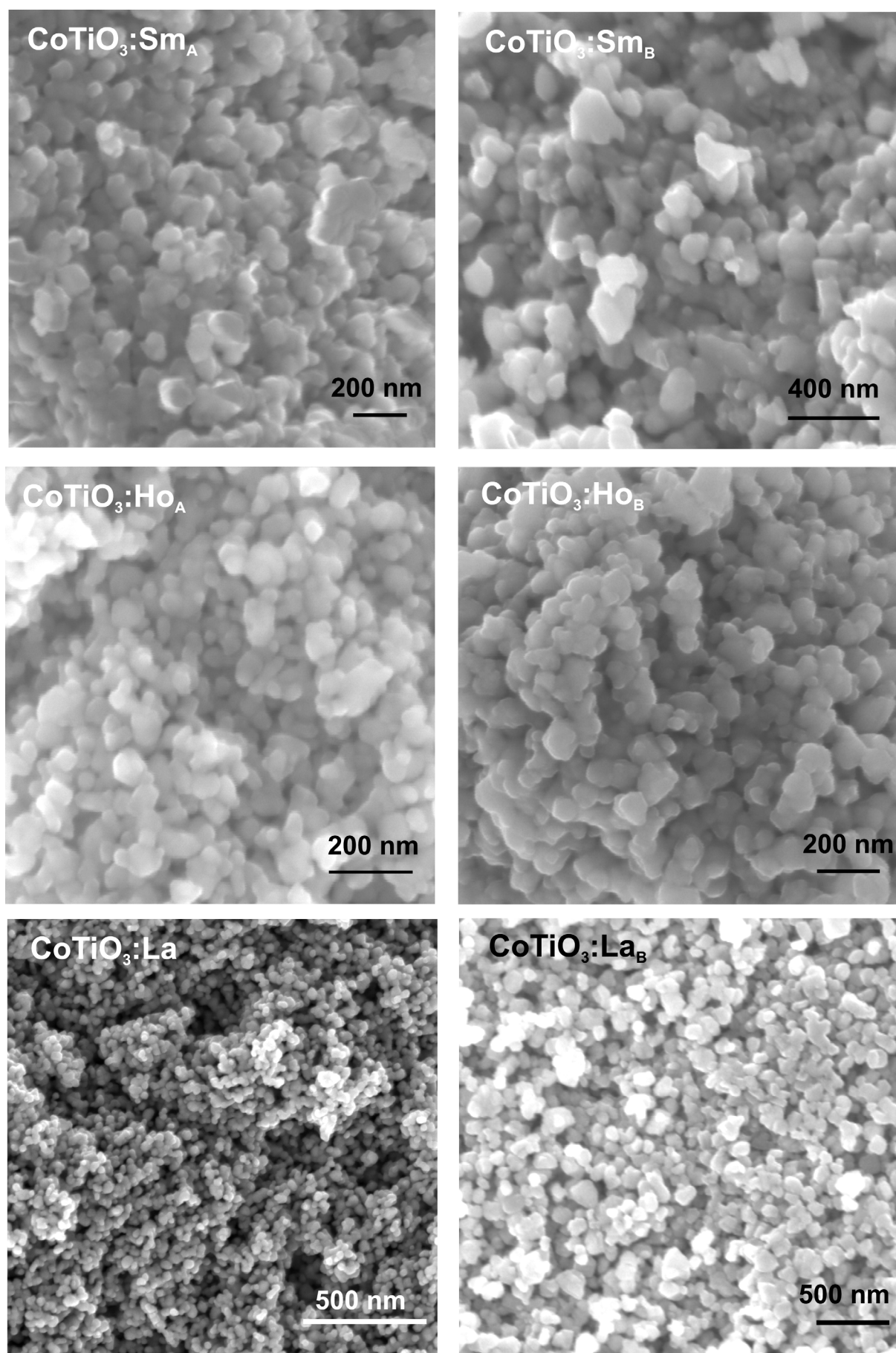


Figure 3.16: SEM pictures of the volume doped CoTiO_3 samples.

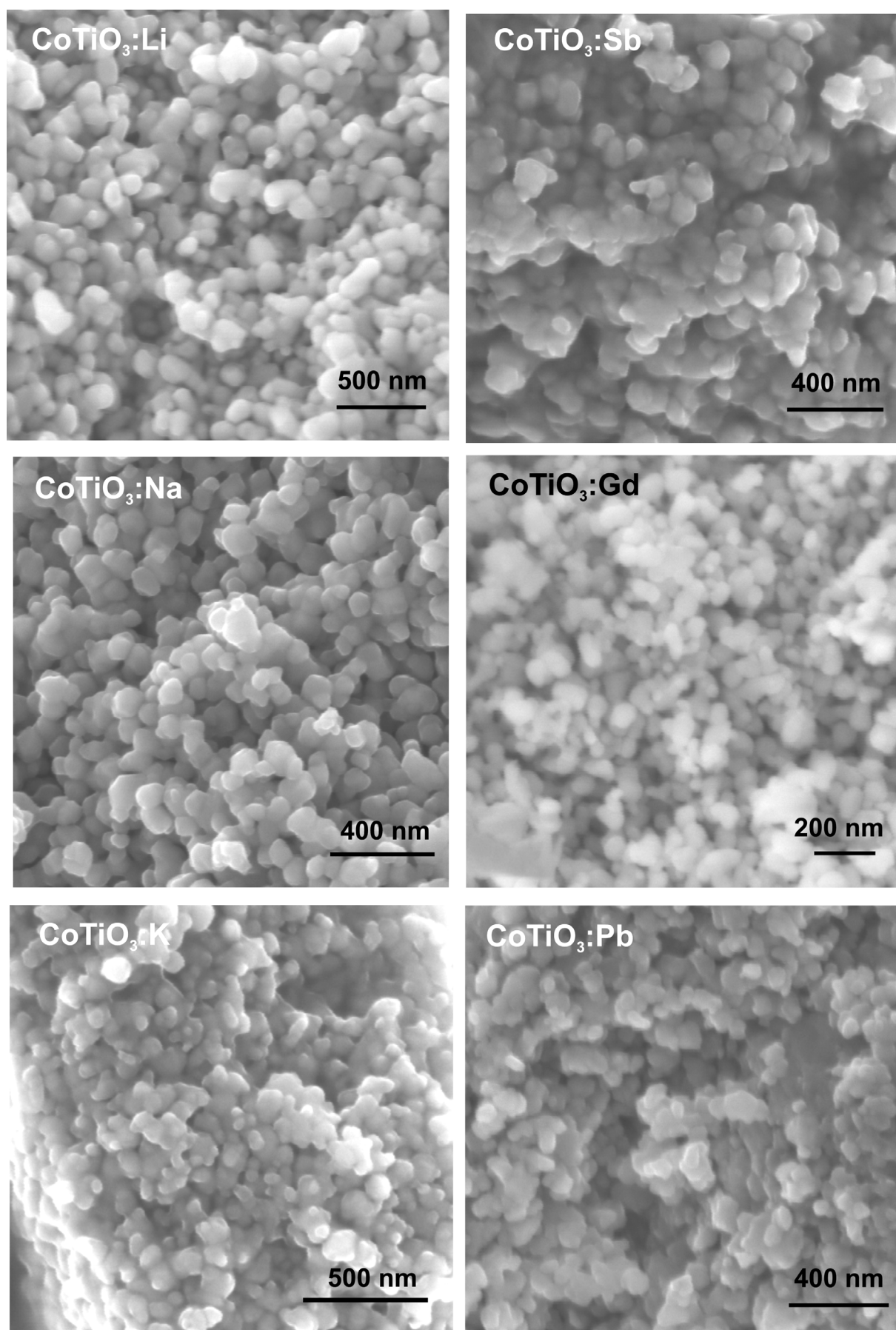


Figure 3.16: SEM pictures of the volume doped CoTiO_3 samples.

Figure 3.17 shows the Arrhenius plot of the undoped and volume doped samples. Almost all materials show an influence on the resistance of the CoTiO_3 . The undoped and the Gd-doped samples show highest resistances in a temperature range from 500 to 350°C. Below 375°C the antimony doped samples show the lowest conductance. All other materials have lower resistances. Lanthanum_A, potassium and lithium doped CoTiO_3 have lowest resistances over the whole temperature range. The lithium doped sample showed highest current of all, around 65-fold higher at 500°C and more than 20-fold higher at 375°C than that of the undoped CoTiO_3 . The lanthanum_A doped sample gave a 25-fold higher current at 500°C while the Pb-doped sample gave a rise in conductivity by about a factor of 5.

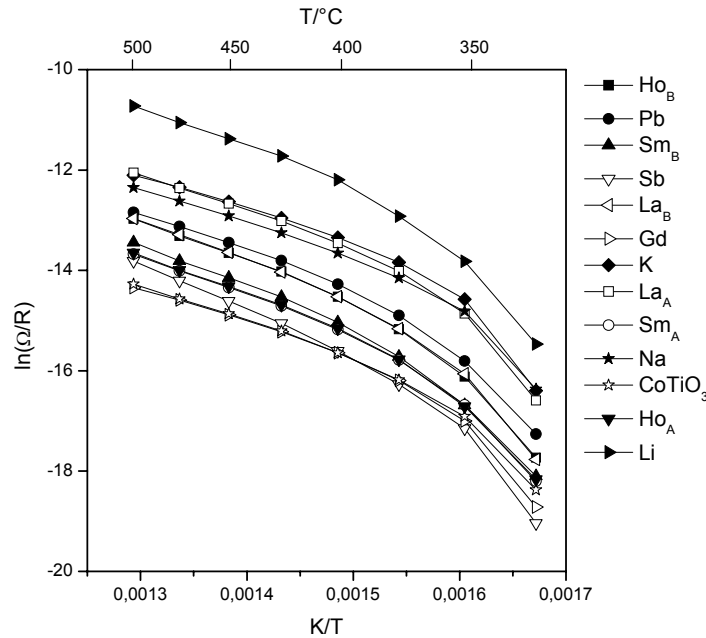


Figure 3.17: Arrhenius plot of volume doped CoTiO_3 samples (AC1015).

Figure 3.18 depicts the sensitivity of the volume doped materials towards ethanol over the whole temperature range. The sensitivity is enhanced significantly by the dopants. Outstanding is the high sensitivity of $\text{CoTiO}_3\text{:La}_A$ towards the test gas in the regarded temperature window. In addition, the temperature of maximum sensitivity (T_{max}) is influenced by the different volume dopants. For example, the undoped and lanthanum doped sample had a T_{max} of 350°C while the lithium doped sample showed maximum sensitivity towards ethanol at 400°C. In the temperature range from 500 to 375°C the undoped sample showed lowest sensitivity.

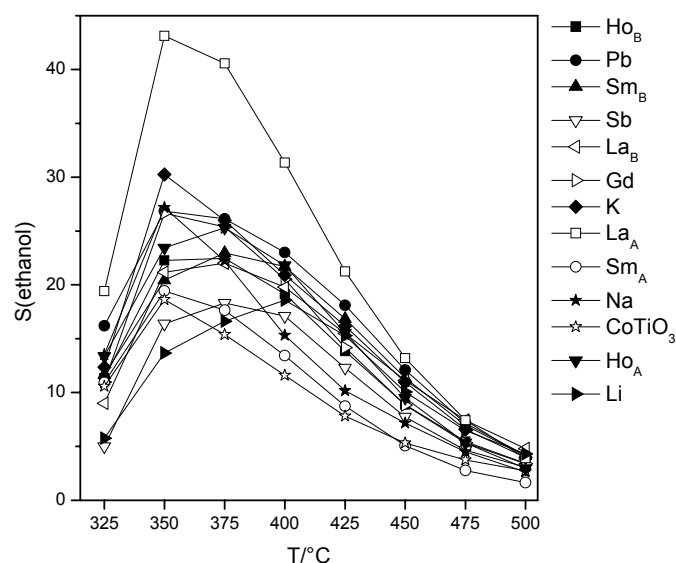


Figure 3.18: Sensitivity towards ethanol of all volume doped samples.

Along with sensitivity changes, the volume dopants also influence selectivity towards ethanol, which is depicted in Figure 3.19. Highest selectivity at 425°C was found for lead (12) and potassium (10) doped CoTiO_3 . The undoped material showed no pronounced selectivity which was also found for the holmium doped sample. The lanthanum_A doped sample, which showed highest ethanol sensitivity, is located in the middle range, meaning a selectivity of around 6. In addition, a temperature shift of maximum selectivity depending on the volume dopant was observed.

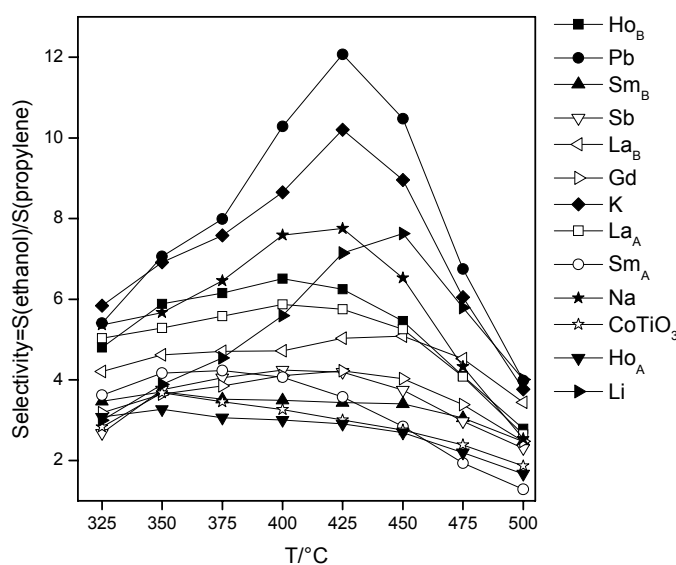


Figure 3.19: Selectivity towards ethanol.

Furthermore, response and recovery ability of the volume doped materials were measured at 500°C with different test gases. The undoped material showed a slow response and recovery behaviour. In the regarded time scale no saturation was achieved (see Figure 3.20). At this temperature no sensitivity towards CO was observed. NO acts as a reducing species, i.e. induces a rise in resistance, however the reaction is small.

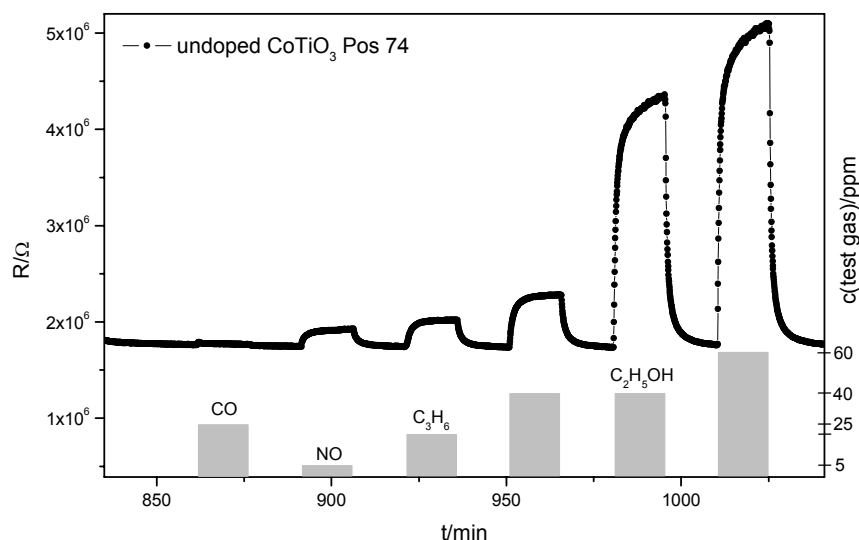


Figure 3.20: Response and recovery times of undoped CoTiO_3 at 500°C towards CO (25 ppm), NO (5 ppm), propylene (20, 40 ppm) and ethanol (40, 60 ppm).

A similar behaviour was observed for the sodium doped sample. In contrast, the addition of lead and lanthanum sped up response and recovery, and saturation/equilibrium was reached. Figure 3.21 shows a comparison between slow and fast responding samples.

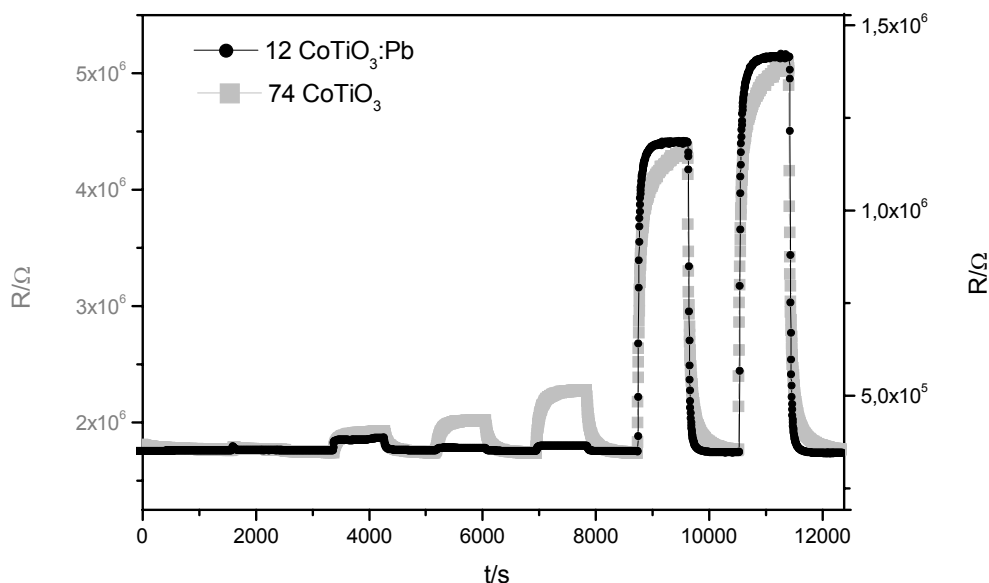


Figure 3.21a): CoTiO_3 and $\text{CoTiO}_3\text{:Pb}$. Response and recovery times at 500°C towards CO (25 ppm), NO (5 ppm), propylene (20, 40 ppm), and ethanol (40, 60 ppm).

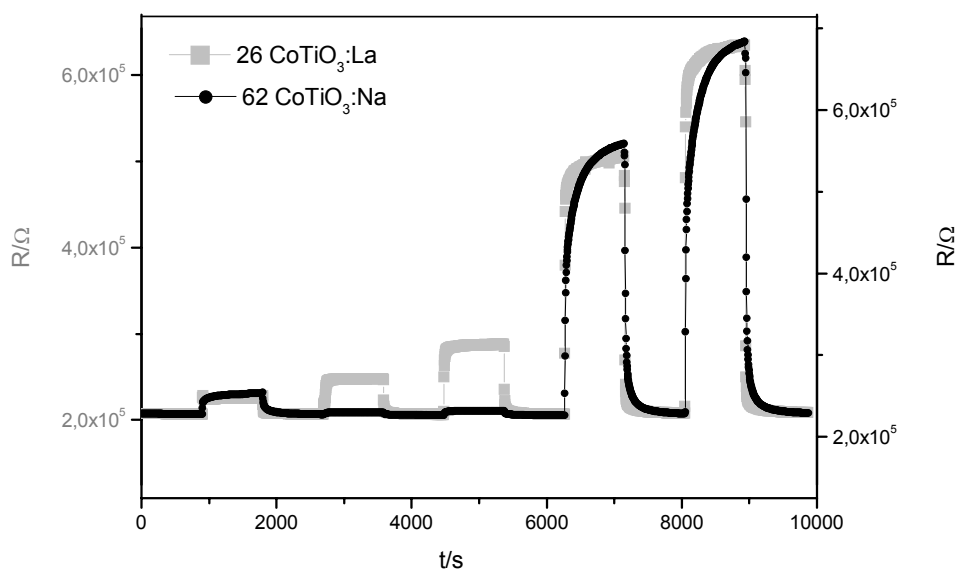


Figure 3.21b): $\text{CoTiO}_3\text{:La}_A$ and $\text{CoTiO}_3\text{:Na}$. Response and recovery times at 500°C towards NO (5 ppm), propylene (20, 40 ppm), and ethanol (40, 60 ppm).

Figure 3.22 depicts the response and recovery behaviour of $\text{CoTiO}_3\text{:Sm}_B$. In this case the response and recovery times were slow. However, the material was able to reach saturation in the given time.

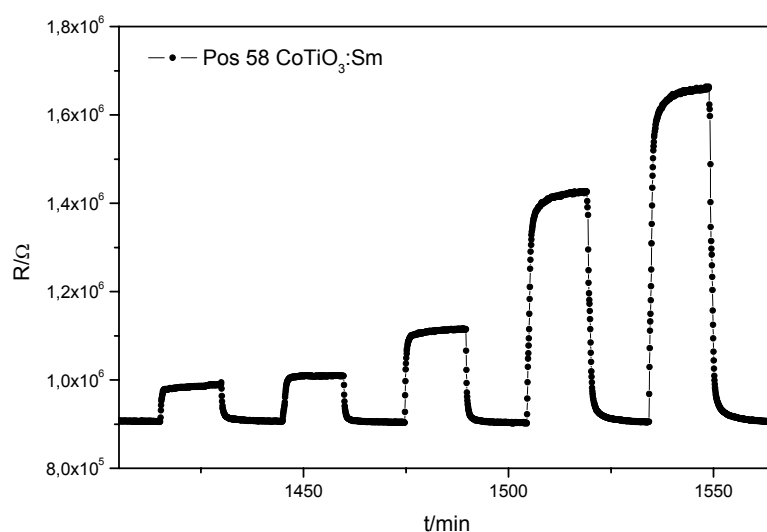


Figure 3.22: CoTiO₃:Sm. Response and recovery times at 500°C towards NO(5 ppm), propylene (20, 40 ppm) and, ethanol (40, 60 ppm).

The materials that showed faster response and recovery abilities also showed higher sensitivities. In addition, one also observed that after volume doping, all CoTiO₃ materials showed p-type behaviour with increasing resistance in reducing conditions. Further response and recovery plots of volume doped CoTiO₃ samples can be found in Appendix 7.2.

In summary, the electrical and sensitivity measurements showed that the dopants are included and influence the behaviour of the sensing base material. Only speculations can be made on the state of ionisation and position of the volume dopants. Different results were seen, for example, depending on whether lanthanum is added with an understoichiometric amount of cobalt or titanium. Even though one would expect a higher conductivity if titanium was displaced, the experiments showed the reverse behaviour. In addition the sensing activity of these two samples was not the same. These structural particularities were in fact not the question this work was concerned about and have to be solved in the future.

Along with the change in resistance, the volume dopants were able, also in only small amounts, to enhance the sensitivity and selectivity of the base material. The temperature of maximum sensitivity/selectivity may also be shifted by adding of volume dopants. In addition, changes in the response and recovery time were observed. Materials with higher sensitivities showed faster response and recovery

ability. However, the used volume dopants did not create new sensitivities towards the admixed test gases.

For further investigations, $\text{CoTiO}_3\text{:La}_A$ (from now on termed $\text{CoTiO}_3\text{:La}$) was used as the base material. This material was chosen from the regarded materials because of its

- highest ethanol sensitivity
- sufficient conductivity
- good response and recovery times
- better sensitivity in comparison to the undoped material.

3.2.5 Further investigations on $\text{CoTiO}_3\text{:La}$

3.2.5.1 Characterisation

The following section will concentrate on $\text{CoTiO}_3\text{:La}$. The material prepared via polyol mediated synthesis was found to be amorphous right after preparation as shown in the HRTEM image in Figure 3.23. The material was dried for one hour at 400°C . The fast Fourier transformation of the image confirms the absence of crystals.

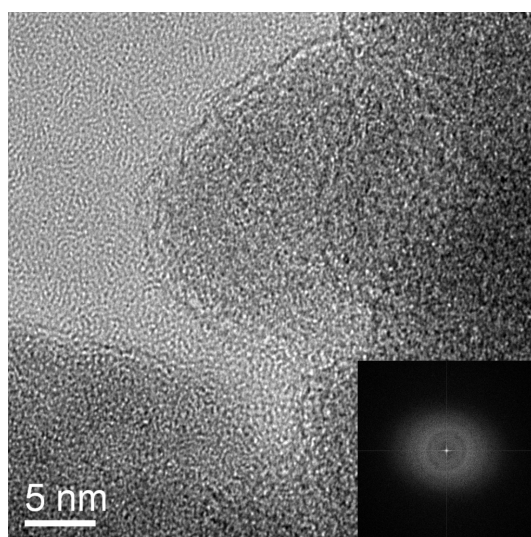


Figure 3.23: HRTEM picture and FFT of $\text{CoTiO}_3\text{:La}$ after drying at 400°C for 1 h.

After annealing at 700°C for 12 h the material turned out to be highly crystalline as shown in Figure 3.24. The electron diffraction pattern in the centre shows the presence of a polycrystalline sample. The concentric diffraction circles (with radius $1/d_{hkl}$) originate from the high number of statistically arranged crystallites in the sample. The powder X-ray diffraction pattern shown in 3.15 showed the formation of

a single phase compound with CoTiO_3 structure. The lattice parameters ($a=b=5.068(5)$ Å, $c=13.934(1)$ Å) of the trigonal phase found from Rietveld refinement [Ri69] are in good accordance with the reference data (ICSD 48107). The average crystallite size of the sample was determined using Scherrer's equation. The estimated crystallite size (61 nm) is in good agreement with the particle size obtained from the SEM picture. The SEM image is shown in Figure 3.25. Almost spherical particles with a diameter of 30 to 70 nm can be seen. The annealed material appeared as a highly porous network of almost uniform particles.

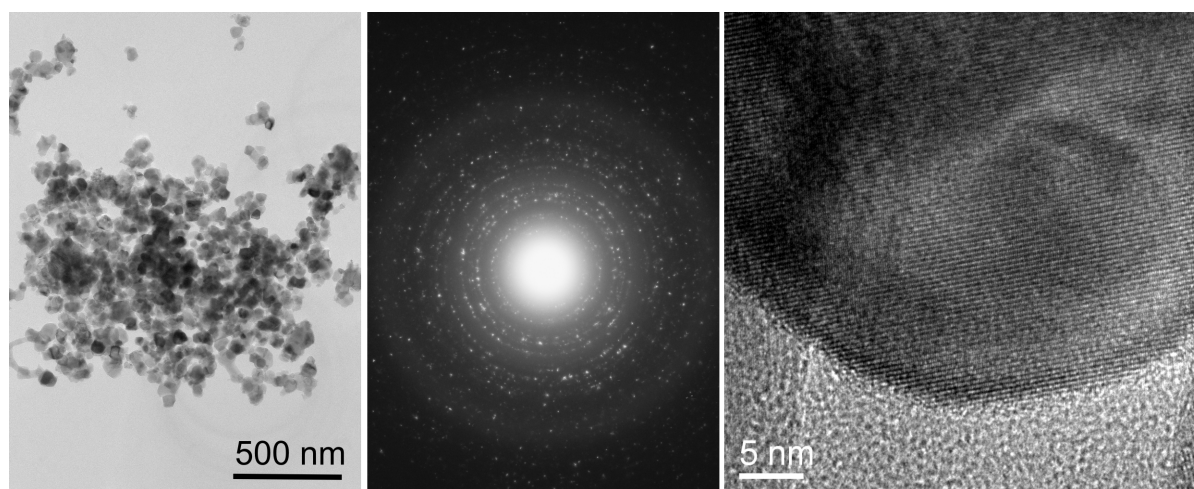


Figure 3.24: HRTEM pictures of $\text{CoTiO}_3\text{:La}$ annealed at 700 °C. The Fourier transformation gives evidence of the crystallinity of the particles.

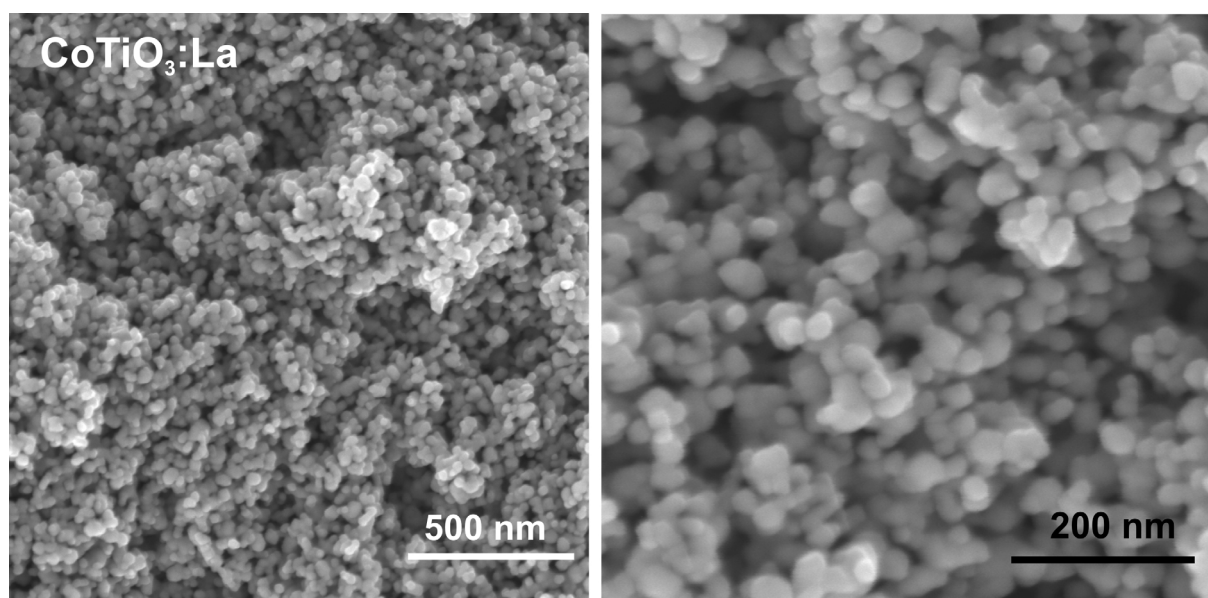


Figure 3.25: SEM pictures of $\text{CoTiO}_3\text{:La}$ heated for 12 h at 700 °C. Primary particles show diameters between 30 and 70 nm.

Figure 3.26 shows a cut edge of a sensor. The deposited metal oxide material remains as an open porous structure, which offers good interaction with the gas phase due to the high surface area.

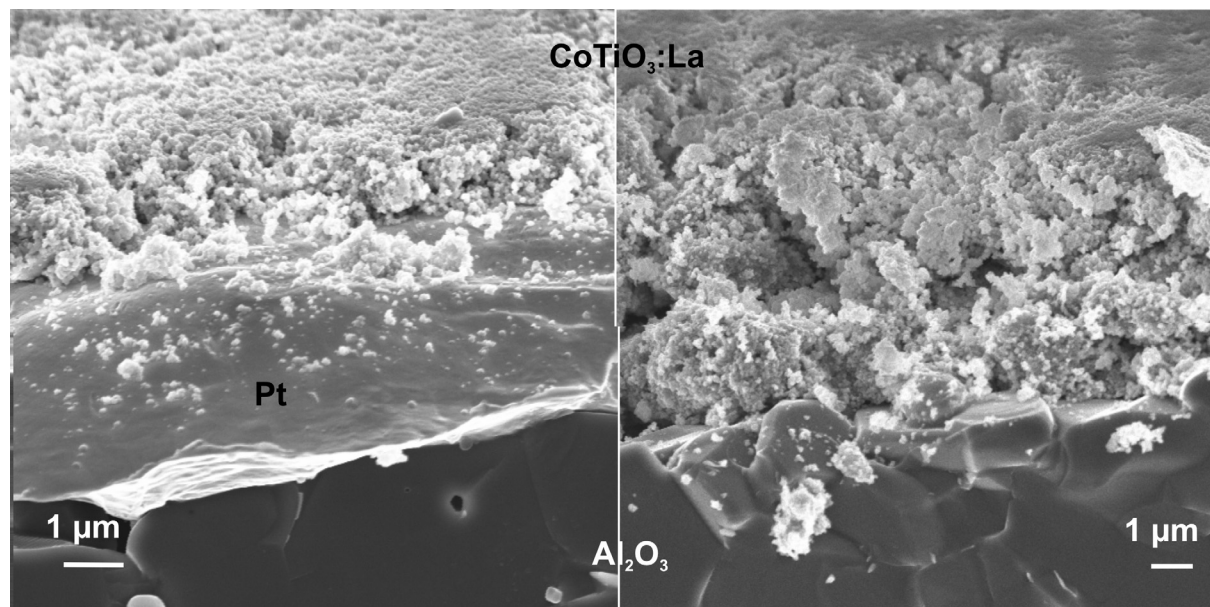


Figure 3.26: SEM picture of a CoTiO₃:La sensing layer on IDC structure.

Because the X-ray diffraction patterns did not show the volume dopants, different characterisation methods were used to visualise the volume dopant. From energy-filtered transmission electron microscopy (EFTM) measurements, it was seen that lanthanum is homogeneously dispersed in the material as shown in Figure 3.27.

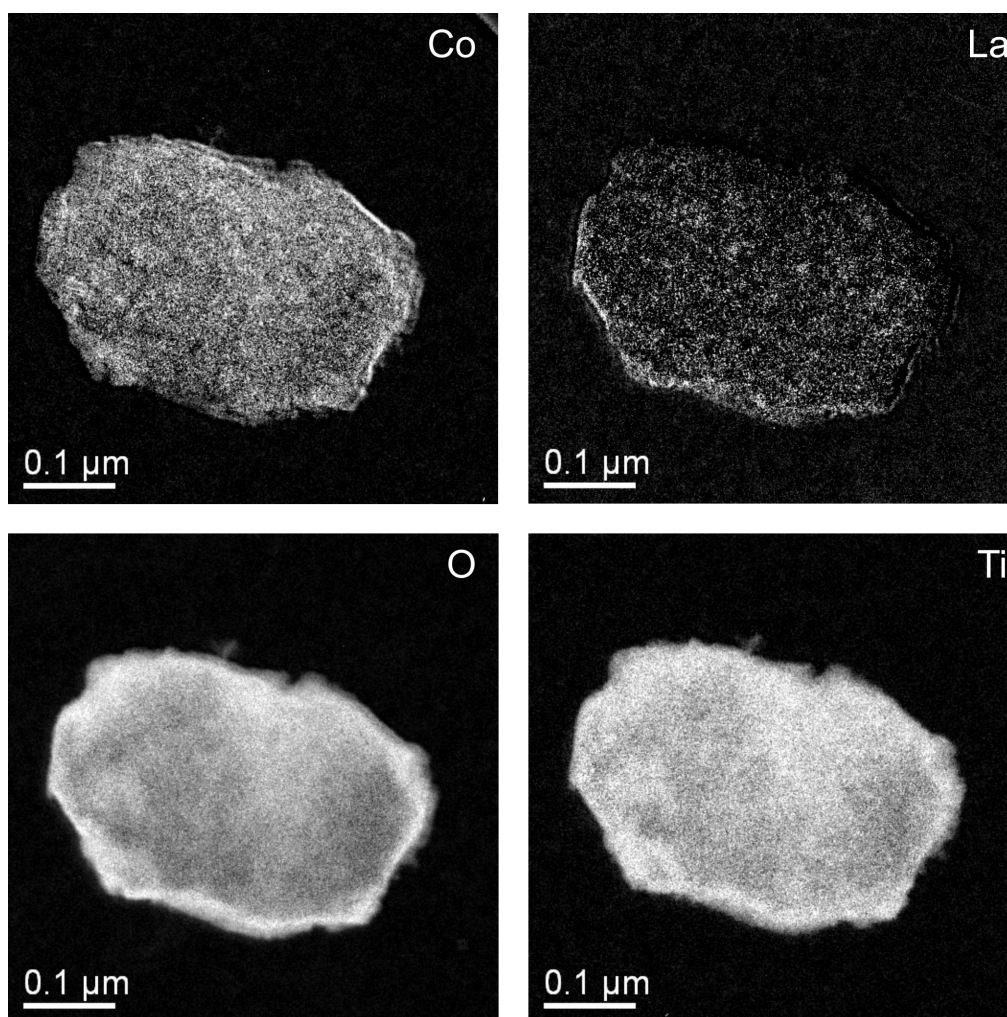


Figure 3.27: ETEM pictures of CoTiO₃:La.

However, the amount of lanthanum was too small to give a quantitative statement. Also, XRF measurements showed the presence of lanthanum, but the amount was in the range of the device error. Electron probe micro analysis (EPMA) was able to show the presence of 2.1 at% of lanthanum in the material. The question remains of how the lanthanum ions are inserted in the lattice, since the ion size is much bigger than that of cobalt or titanium.

3.2.5.2 Electrical and gas sensing properties

Figure 3.28 shows the plot of the real part of the complex impedance versus the imaginary part (Argand plot) for CoTiO_3 and $\text{CoTiO}_3:\text{La}$ in synthetic air at 475 °C.

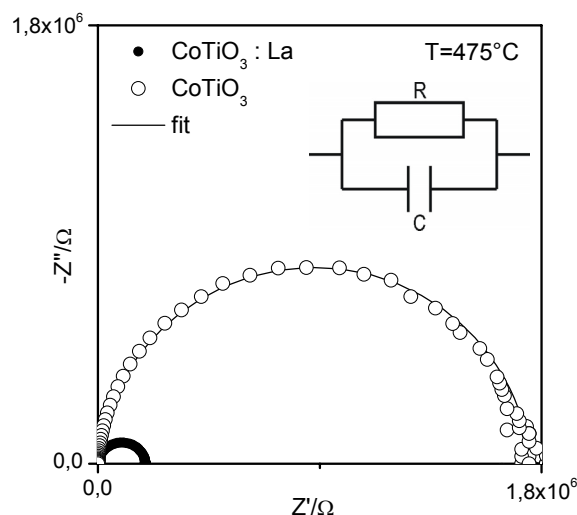


Figure 3.28: Argand plot and circuit equivalent. Volume doping with lanthanum enhances the conductivity of CoTiO_3 ($T=475^\circ\text{C}$).

Figure 3.29 shows the fingerprint (bar chart) of CoTiO_3 and $\text{CoTiO}_3:\text{La}$, where S_Δ for each material and each gas at 475 °C is shown. It illustrates that the undoped and volume doped material showed high sensitivity towards propylene and ethanol with a very weak cross sensitivity towards other gases as shown before. The volume doping showed an enhanced selectivity towards ethanol.

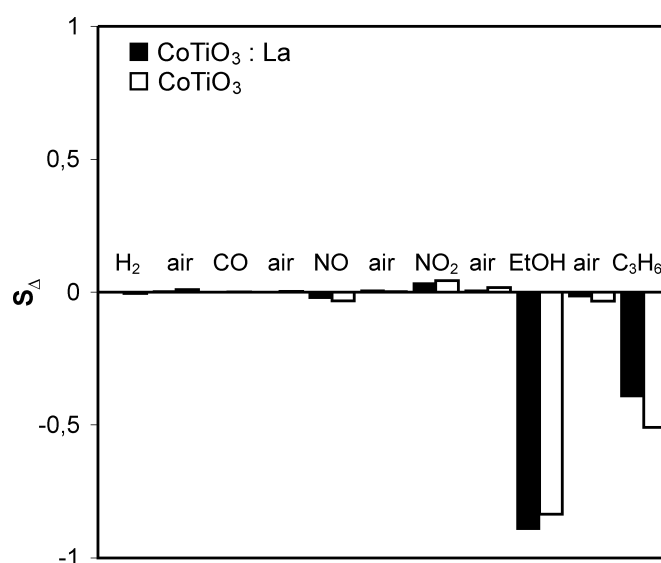


Figure 3.29: Fingerprint of $\text{CoTiO}_3:\text{La}$ and CoTiO_3 at 475 °C.

Figure 3.30 shows the Argand plot for synthetic air, propylene (25 ppm) and ethanol (40 ppm) at 400 °C. The p-semiconducting material showed an increase of resistivity compared to synthetic air when reducing gases like propylene and ethanol were applied.

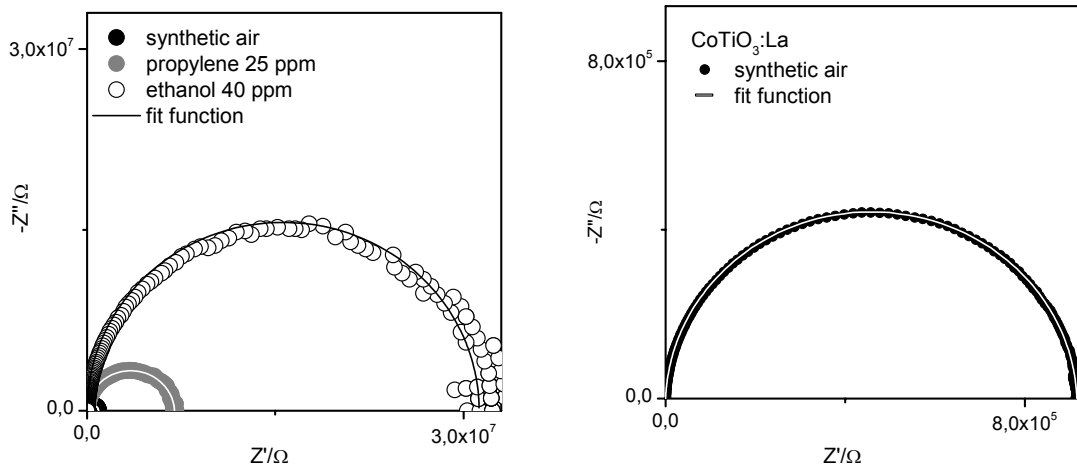


Figure 3.30: Argand plot of CoTiO₃:La in synthetic air, propylene and ethanol. The p-type semiconductor shows an increase of resistance compared to synthetic air when reducing gases are applied (T=400°C).

Figure 3.31 shows the relative sensitivity towards the tested gases versus the operating temperature. The material was highly sensitive and selective towards hydrocarbons at higher temperatures. At lower temperatures cross sensitivity towards other gases increased.

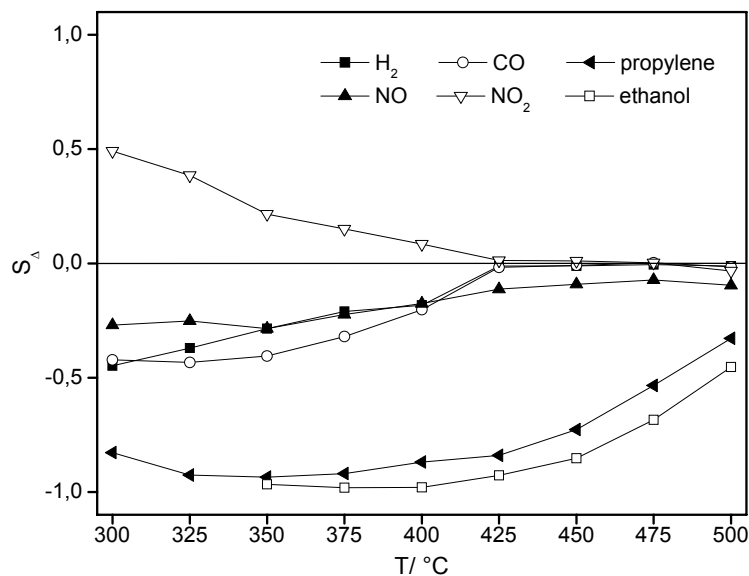


Figure 3.31: Relative sensitivity of CoTiO₃:La versus operating temperature (300-500°C) for various gases.

As compared to the results of Chu et al., who introduced the use of nanostructured CoTiO_3 for the detection of ethanol, this material showed a high sensitivity at 400°C only towards 40 ppm ethanol (compared to 1000 ppm ethanol). Figure 3.32 shows the temperature dependence of the literature sensitivities in comparison to the measured values for undoped and lanthanum doped CoTiO_3 . At 350°C the lanthanum doped sample showed sensitivities towards 40 ppm of ethanol that compete with Chu's values for 1000 ppm at temperature of maximum sensitivity. The selectivity $S_{40\text{ppm ethanol}}/S_{25\text{ppm propylene}}$ was 6.6 in comparison to Chu et al. where $S_{200\text{ppm ethanol}}/S_{100\text{ppm petrol}}$ was 4. Doping with only 2 at% of lanthanum created a highly sensitive hydrocarbon sensing material as compared to what is reported in the literature.

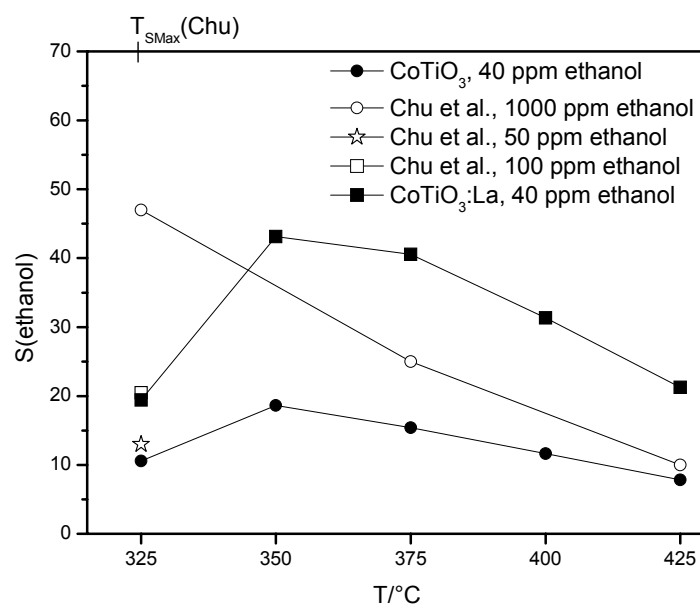


Figure 3.32: Temperature dependence of ethanol sensitivity of $\text{CoTiO}_3\text{:La}$ in comparison to Chu et al.

3.2.5.3 Cross-sensitivity towards humidity

The humidity response of the gas sensitive element was tested. Figure 3.33a) and b) show two examples of $\text{CoTiO}_3\text{:La}$ at 500 and 400°C. The resistance varied by $\pm 5\%$ when the relative air humidity was shifted from 0 to 90 %. The resistance variation in propylene over the same range was less than 1%. This practical insensitivity to water vapour can be contrasted with most commercially available tin oxide gas sensors, which show a change in conductance as a function of humidity [lh94].

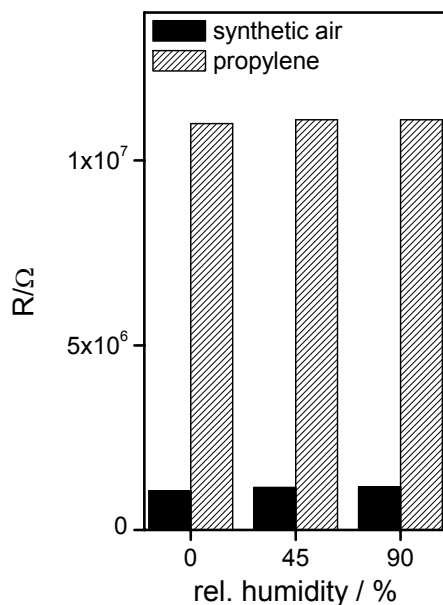


Figure 3.33a): Sensitivity of $\text{CoTiO}_3\text{:La}$ in humid and dry atmosphere at 400°C (AC1013, Position 57).

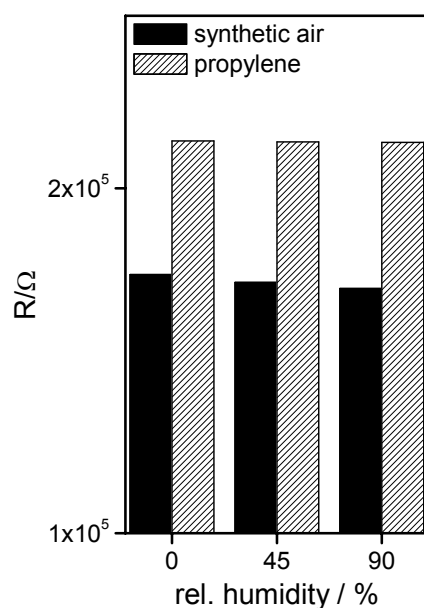


Figure 3.33b): Sensitivity of $\text{CoTiO}_3\text{:La}$ in humid and dry atmosphere at 500°C (AC1015, Position 52).

D.E. Williams' review described a p-type semiconducting titanium-substituted chromium oxide (CTO) that also showed a lack of response to water vapour. This has been the key to the successful commercial development of CTO as sensor material [Wi99]. Williams suggested that the metal cations associated with the oxygen defects determined the effect of water vapour. If these cations were Lewis bases like Sn^{2+} (at SnO_2 surface), the effect of water on electrical conductivity appears to be large, whereas with cations such as Cr^{3+} (CTO) at the surface, the effects of water vapour were much smaller [Wi99]. Also, the sensitivity of TiO_2 was much smaller than the sensitivity of SnO_2 [Du99]. Fukui et al. showed that incorporation of acidic metals like Co and Cr into tin oxide enhanced the stability towards humidity changes [Fu98]. The negligible cross sensitivity of $\text{CoTiO}_3\text{:La}$ to humidity changes may be caused by the chemical analogy to the systems described in the literature. The combination of Co and Ti seems to be promising to prevent large effects of water vapour.

3.2.5.4 Gas concentration dependence

Gas sensitivity as a function of propylene concentration is shown in Figure 3.34 for lanthanum doped CoTiO_3 . After a steep initial increase, the gas sensitivity tended towards an asymptote in the range of high concentrations of propylene. The data show that the response times decreased as the analyte concentration increased, which was attributed to the diffusion of analyte into a porous medium. The response times of less than 1 min were comparable to, and in many cases faster than times reported for other metal oxide conductometric sensors [Te05]. Sensor recovery times were slightly longer than onset times. The longer recovery times were attributed to the expected faster diffusion of analyte into as compared to out of the porous network [Be06]. Because the signal onset times were dependent on the analyte concentration, the response times could provide information that help to quantify the amount of analyte, beyond just the sensitivity response [Be06].

Figure 3.35 shows concentration steps of propylene at 500°C . Concentration was changed from 0 to 50 ppm. At the shown temperature a good response and recovery behaviour was observed. The cycle of two steps showed that response values were reproducible.

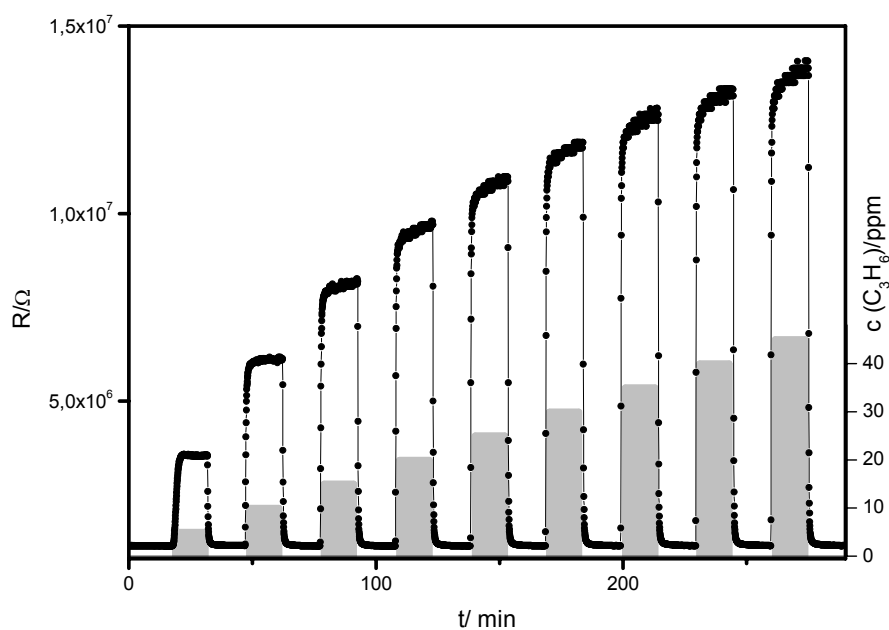


Figure 3.34: Response behaviour and concentration dependence of CoTiO₃:La towards propylene.
($T=400^\circ\text{C}$, $f=100\text{ Hz}$, $\Delta t=15\text{ min}$)

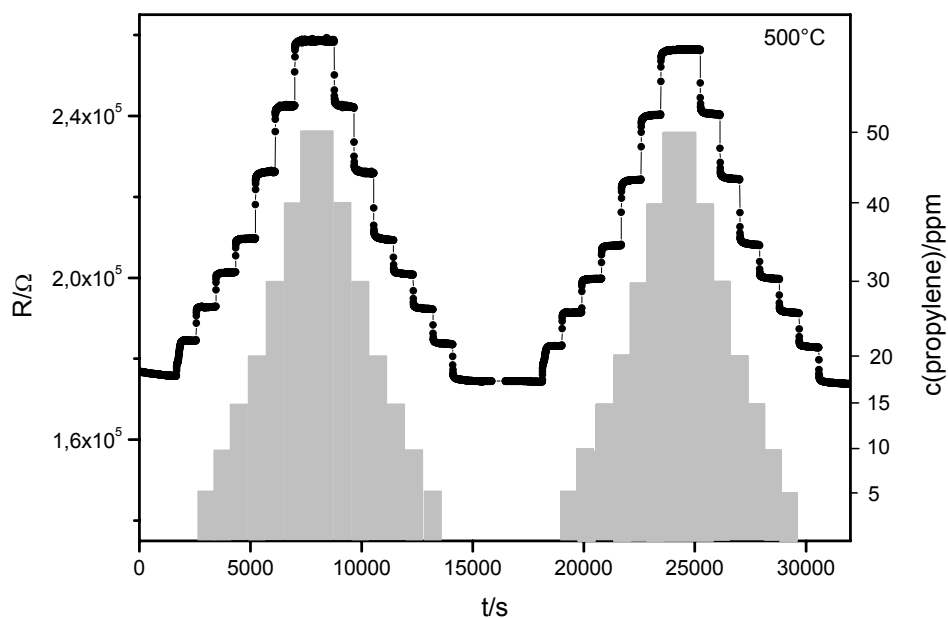


Figure 3.35: Concentration steps of propylene ($T=500^\circ\text{C}$, $f=100\text{ Hz}$, $\Delta t=15\text{ min}$).

3.2.5.5 Long-term stability of $\text{CoTiO}_3\text{:La}$

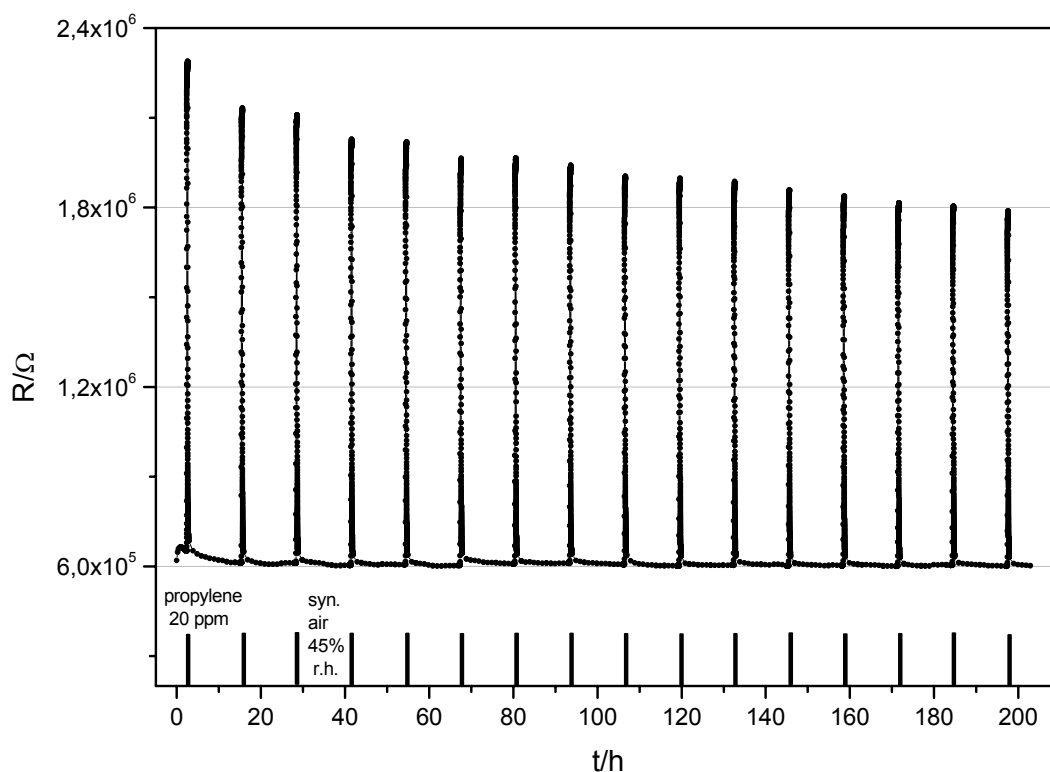


Figure 3.36: Long-term stability of $\text{CoTiO}_3\text{:La}$ at 400°C .

Another important parameter to consider when evaluating a sensor is its stability. It is useful to have both a stable baseline resistance and a reproducible signal change to a given analyte concentration. The stability of gas-sensitive elements' characteristics was tested over 9 days by periodic measurements of the sample resistance under air (45% r. h.) every hour and the response and recovery behaviour towards propylene (20 ppm) every 12 hours. This periodicity of stability testing corresponds to the real mode of operation of gas sensors working at a fixed temperature. Figure 3.36 shows the stability test for $\text{CoTiO}_3\text{:La}$. The sensitivity deviation (span drift) during 9 days was about 20 % of the absolute sensitivity. The main instability was observed during the first 3 days. The baseline resistance under synthetic air (45% r. h.) remained stable after the first day except a small variation. Therefore, in order to eliminate the initial instability, artificial aging of the sensitive element is advised before application. Next to these long-term tests, the sample plate was stored for 11 month under air and measured again in all applied gases and temperatures. The same sensitivities were achieved, showing once again the stability of the material (see Figure 3.37).

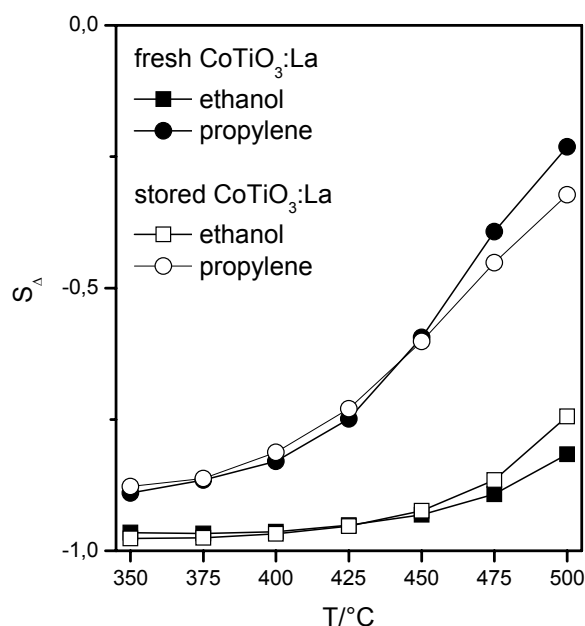


Figure 3.37: Comparison of sensitivities towards ethanol and propylene after storage (11 months) (sample plate AC1015, position 52).

The sample was characterised again after the storage and long-term test. Figure 3.38 shows the X-ray diffraction of the sample. No changes in the crystal structure occurred. In addition, no changes in the crystallite size were derived from the X-ray pattern. SEM pictures of the sample are shown in Figure 3.39. The open porous structure also remained after long term stability tests.

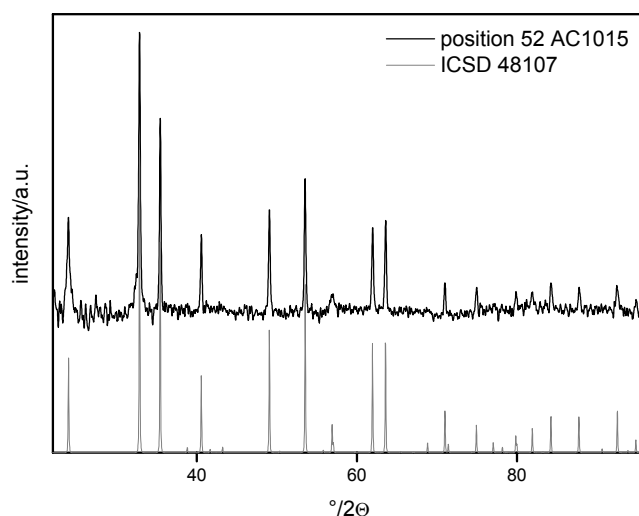


Figure 3.38: X-ray diffraction of position $\text{CoTiO}_3:\text{La}$ (scraped off position 52, AC1015) after long-term stability tests.

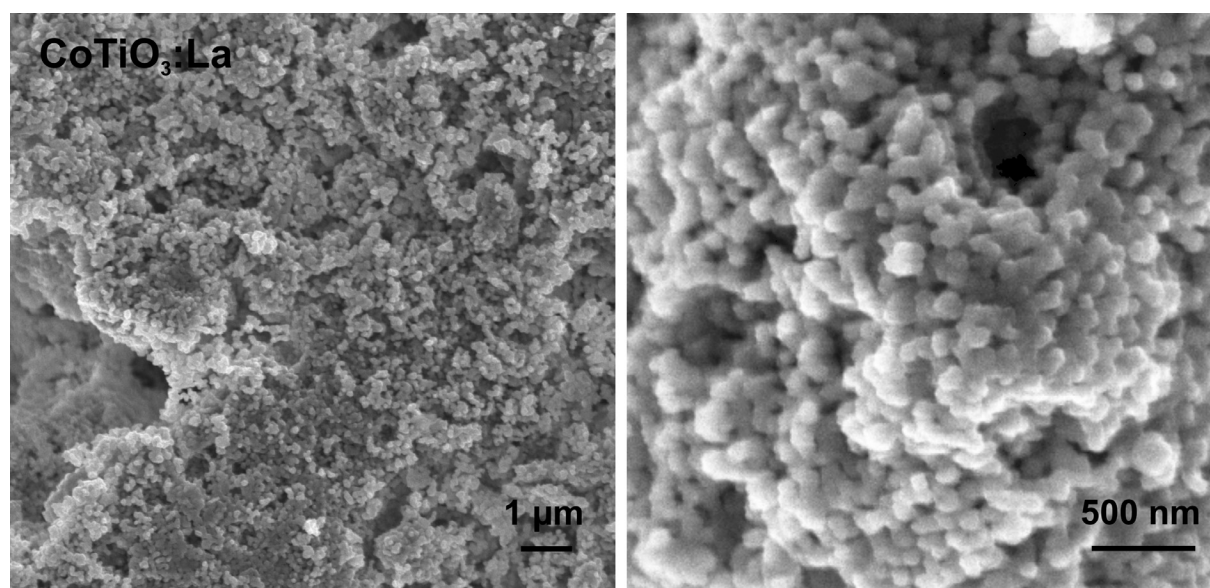


Figure 3.39: SEM image of CoTiO₃:La after long-term stability tests (position 52, AC1015).

3.2.5.6 Surface doped CoTiO₃:La [Si06]

The polyol method was applied for the synthesis of nanocrystalline CoTiO₃:La, and the use of HT-IS enabled the analysis of surface doping with different amounts of Au, Ce, Pd, Pt, Rh and Ru in order to find out the highest selectivity and sensitivity of the respective material compositions.

The applied doping elements were Au (as HAuCl₄·3H₂O), Ce (as (NH₄)₂Ce(NO₃)₆), Ir (as Ir(C₅H₇O₂)₃), Pd (as Pd(NO₃)₂·2H₂O), Pt (as Pt(NH₃)₄(NO₃)₂), Rh (as Rh(NO₃)₃·2H₂O) and Ru (as Ru(NO)(O₂C₂H₃)₃). The doping elements are known to increase the sensitivity and/or selectivity of different semiconductor gas sensing materials [El04][Sh99]. The distribution of the different material combinations are shown in Figure 3.40, which represents an 8x8 array with CoTiO₃:La as base material; diversity was achieved by variation of the surface doping species and its respective concentration. To compensate for possible gradients in gas concentration and temperature as well as single failures due to contact defects over the substrate, three statistically selected positions are equipped with the same material composition.

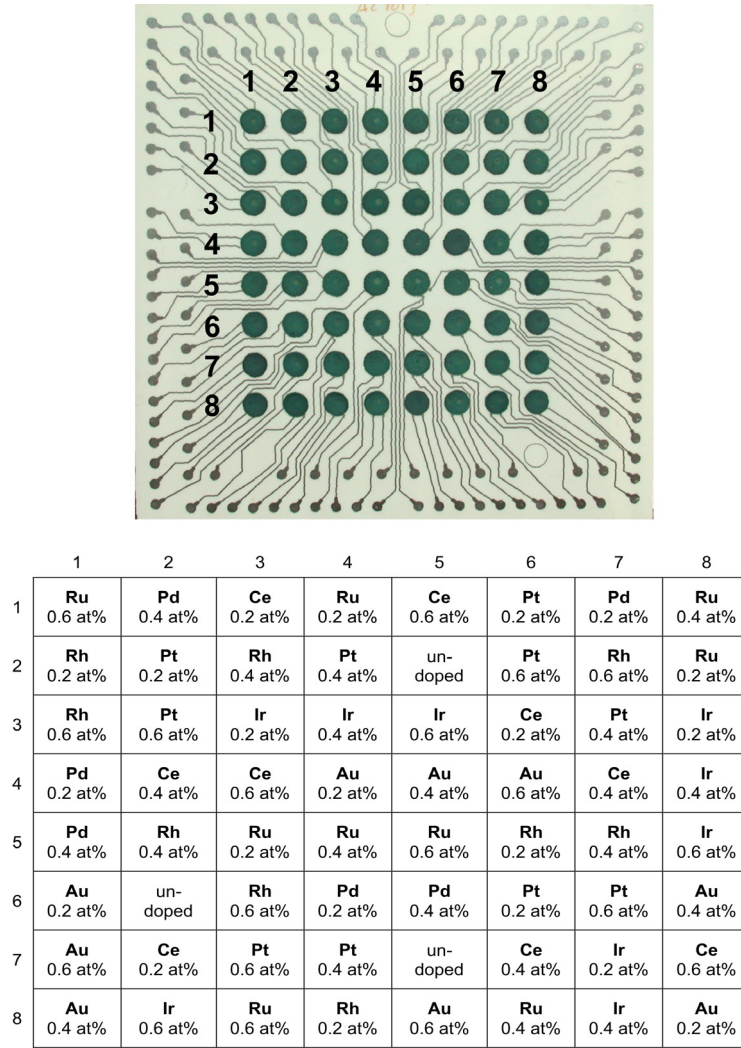


Figure 3.40: Picture of the prepared sample plate and distribution of the doping elements on the base material $\text{CoTiO}_3\text{:La}$ (AC1013).

The sample plate was measured with the same procedure described in chapter 3.2. Figure 3.41 exemplarily shows the Argand plots from the screening of AC1013. Measurements in synthetic air at three different temperatures (400, 375, 350°C) are shown.

As mentioned before the material showed approximately the behaviour of a parallel RC-circuit. The diameter of the semicircle, which is related to the ohmic resistance of the material dropped with increasing temperature as expected for semiconductors. Positions 16, 17, 24, 26, 35, 54, 66, 68, and 83 showed solely capacitive behaviour. This may occur due to insufficient contact between sample and IDC or defect conductor paths on the microelectrode array.

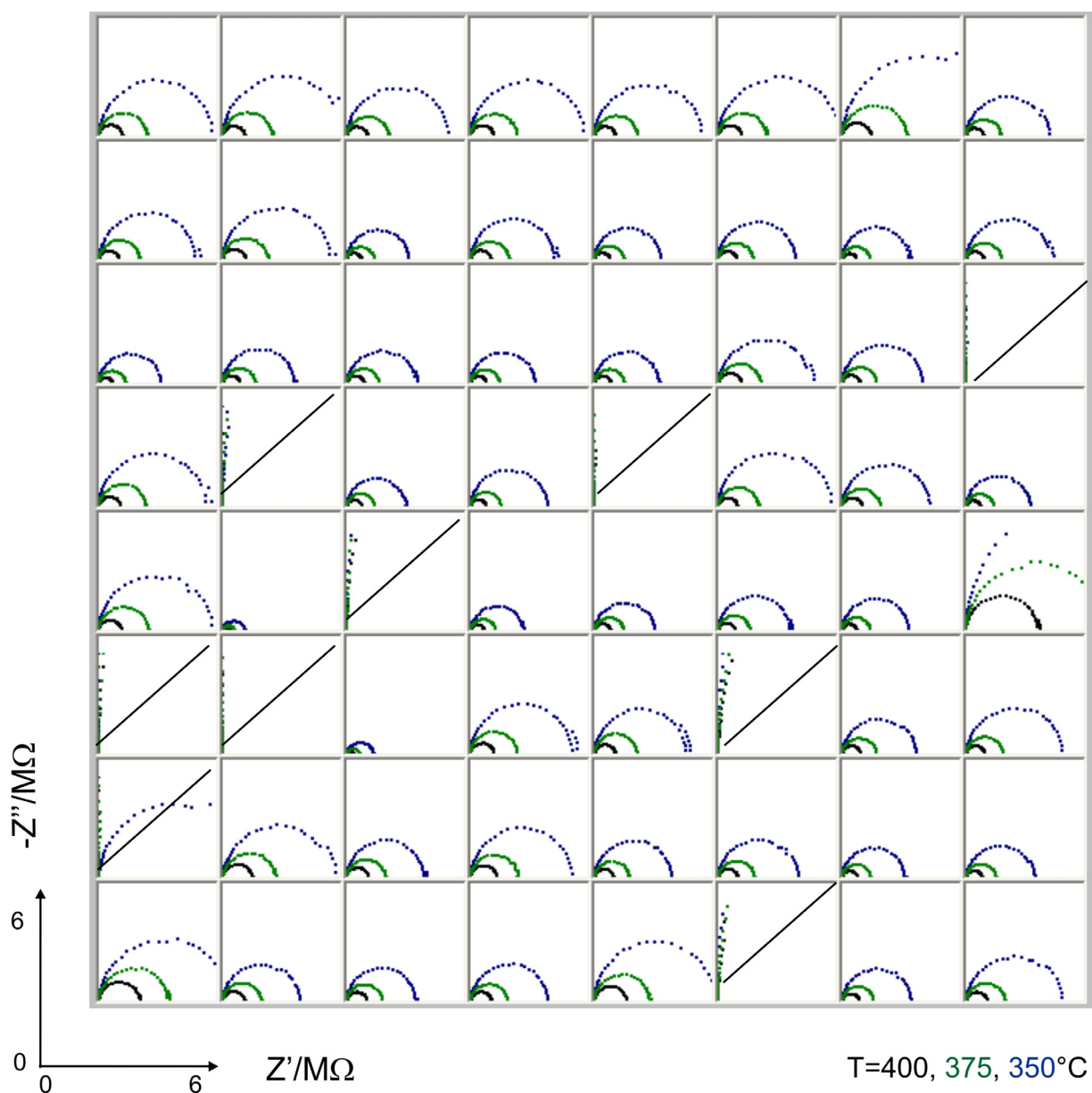


Figure 3.41: Argand plot of the sample plate AC1013 at 400, 375 and 350°C under synthetic air.

Figure 3.42 shows the fingerprint for the entire sample plate at 400°C. For defect positions no sensitivities were achieved. Equally occupied positions show good correspondence in the sensitivities. For the majority of the surface dopants no significant influence on the sensitivity was observed. The most pronounced effect on the sensitivity could be seen for Au and Pd doped materials, whereas almost no dependence on the concentration of the surface dopants was found.

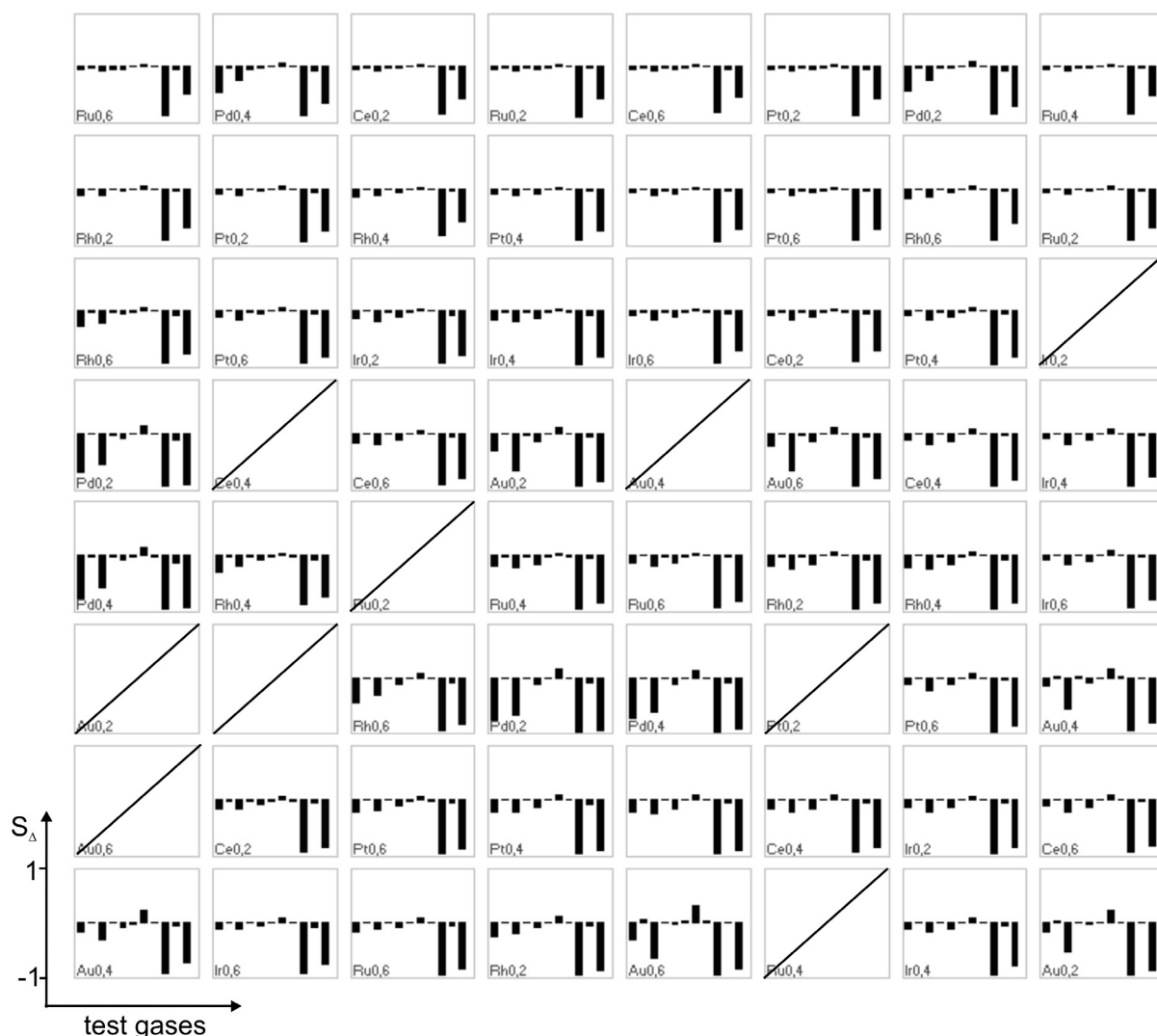


Figure 3.42: Fingerprint of the sample plate AC1013 at 400°C. Many surface dopants show the same sensitivities as the undoped material. Besides the nine fields, which reflect defects in the electrical contacts of the respective materials, the measurements show good reproducibility.

Figure 3.43 shows the temperature dependence of S_A for the samples doped with Au and Pd. For both metals high sensitivity towards ethanol and propylene remained like in the undoped base material. It is noticeable that platinum showed no significant sensitivity change, though it is known as a good supporting surfactant on n-type systems like SnO_2 [Ko05].

Au doping caused an increased sensitivity towards CO over the whole temperature range with a maximum at 325 °C. At the same time, the sensitivity towards hydrogen was increased, which was most pronounced at lower temperatures.

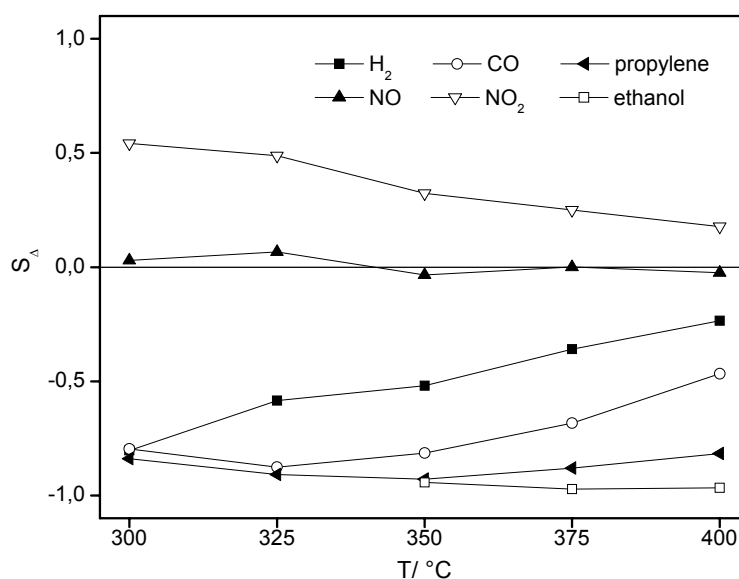


Figure 3.43a): Au@CoTiO₃: Relative sensitivity versus operating temperature (300-400°C) for various gases.

Remarkable changes also appeared in the sensitivity towards NO_x. While the undoped material showed an almost temperature independent S_{Δ} between -0.2 and -0.29 for NO, the sensitivity towards NO₂ decreased with increasing temperature from 0.5 to 0.1 between 300 and 400 °C. The Au-doped material showed a slightly increased sensitivity towards NO₂ whereas the sensitivity towards NO appeared to be suppressed.

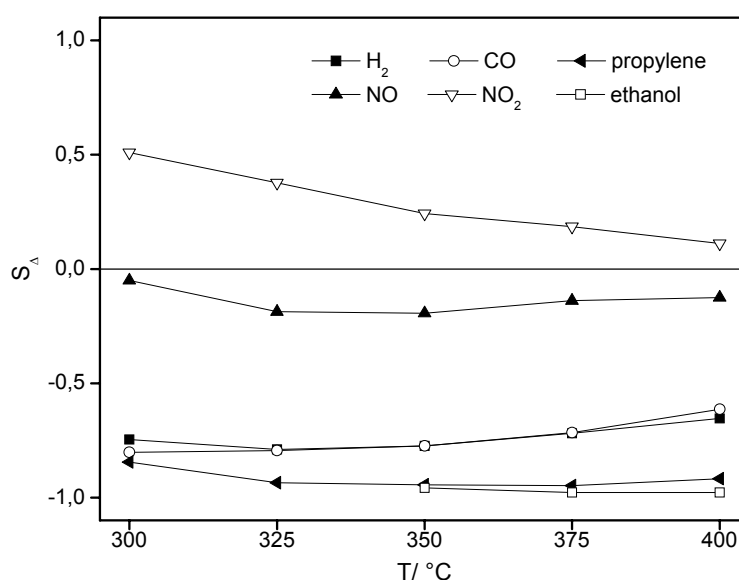


Figure 3.43b): Pd@CoTiO₃: Relative sensitivity versus operating temperature (300-400°C) for various gases.

Pd doping caused an increase of the sensitivity towards CO and H₂ over the whole temperature range (as is shown in Figure 3.34b)). In contrast, the sensitivities towards NO_x showed almost the same behaviour as was observed for the undoped material. The NO sensitivity showed a weak maximum at 350 °C while the highest sensitivity towards NO₂ was observed at 300 °C. S_Δ for CO and H₂ were significantly higher in comparison to the undoped base material. Also, a small maximum of the H₂-sensitivity was observed at 325 °C, while the sensitivity towards CO decreased with increasing temperature. At 300 °C the sensitivity towards CO differed only slightly from that towards propylene.

When a doping element is added to the surface, the equilibrium state and/or velocity of the surface reactions is modified. Au and Pd, well known as active catalysts for e.g. CO oxidation [Ja06, Ka06, Ha97, Sl05], hydrogen peroxide synthesis from H₂ and O₂ [So06] or hydrocarbon oxidation, have been confirmed to possess promoting effects on many semiconductor gas sensors. The doping element supports the catalytic conversion of the reducing gas into its respective oxidation product. This may be due to spill-over of activated fragments to the semiconductor surface to react with the adsorbed oxygen [Ko05]. On the other hand, the mentioned catalytic effect inducing a located temperature change and a change in resistance may cause the sensitivity change of the surface doped material. These models may describe the increased sensitivity of the Pd- and Au-doped materials towards H₂, NO₂ and CO observed here. The reaction towards the hydrocarbons originated from the metal oxide and therefore was not highly influenced by the surface dopant.

Most interesting for practical use is the almost fully suppressed sensitivity towards NO with a simultaneously pronounced sensitivity towards NO₂ observed for the Au-doped material. The NO-tolerance has also been seen in [Fi02b] and [Su95]. Sun et al. referred to lower NO sensitivity using Au electrodes compared to Pt electrodes and α-Fe₂O₃ thin films. The comparison of different electrode materials showed that they were able to promote sensitivities similarly to surface dopants. It was suggested that NO was oxidised to NO₂ prior to being detected and that Pt showed higher catalytic activity for spill over [Su95].

3.2.5.6.1 Response and recovery behaviour of Au and Pd doped $\text{CoTiO}_3\text{:La}$

These two interesting surface dopants were also screened for their response and recovery ability. Figure 3.44 shows the response to 5 ppm NO and NO_2 of gold doped $\text{CoTiO}_3\text{:La}$ at 350°C . As shown in the sensitivity-temperature plot, almost no cross-sensitivity towards NO was found at this temperature. The offsets at changing the gases can be understood by changing the carrier gas from synthetic air to nitrogen and adjusting the test gas flow. When the NO gas flow controller was opened the concentration of oxygen slightly decreases, which was shown by the rise in resistance. After adjustment of the test gas mixture, the equilibrium value was reached, and after changing from test gas to pure synthetic air, the resistance first dropped (higher oxygen concentration), and after a short adjustment time the base value at synthetic air was reached. This offset was only observed when measuring NO (the only test gas carried by nitrogen). The response towards NO_2 was fast (28 s) and equilibrium was reached in the regarded time scale; however, recovery was slower (~ 3.2 min).

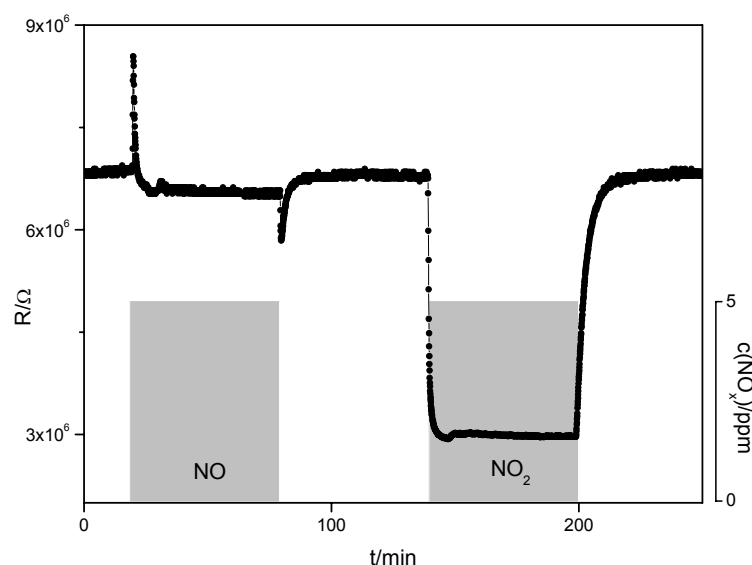


Figure 3.44: Response of Au@CoTiO₃:La to NO and NO_2 ($T=350^\circ\text{C}$).

Figure 3.45 shows the response of Au@CoTiO₃:La to carbon monoxide at two different temperatures. The response time at both temperatures was around 18 s. The recovery time was located in the same time scale. At lower temperatures the average deviation of the measurement values was higher because of the higher resistances. However, at lower temperatures the response change was higher, as expected; at 375°C the absolute sensitivity was 5.2 while at 350°C the sensitivity had

a value of 8. In comparison, Figure 3.46 depicts the response of Pd-doped $\text{CoTiO}_3\text{:La}$ towards 50 ppm of carbon monoxide at 375°C . The response time was 28 s, the sensitivity at this temperature around 3.2, and the recovery time corresponds to the response time. Both the Au- and Pd-doped materials seemed to be good CO sensing materials while the gold doped sample also showed excellent properties for an NO-tolerant NO_2 -sensing material at around 350°C . After finding these two interesting surface dopant-material combinations, the characterisation of these surface dopants was of interest. These characterisation studies are described in the following section.

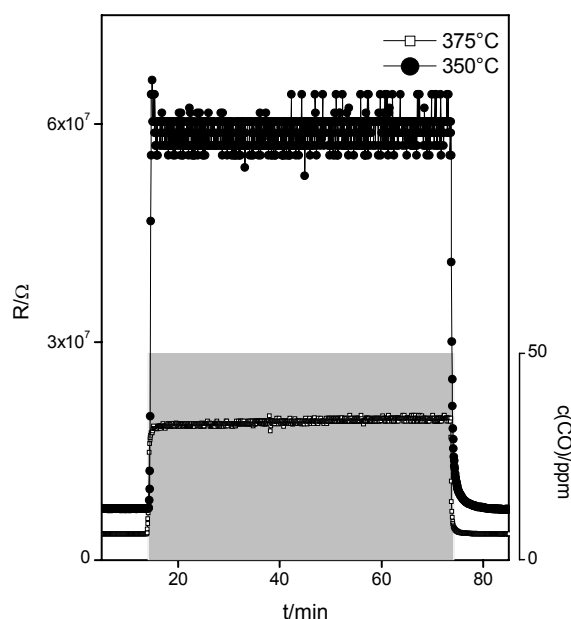


Figure 3.45: Response of Au@CoTiO₃:La to CO (T=350, 375°C).

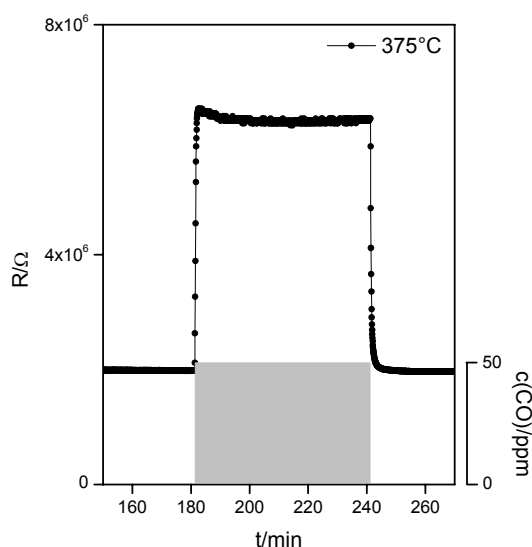


Figure 3.46: Response of Pd@CoTiO₃:La to CO (T=375°C).

3.2.5.6.2 Characterisation of Pd and Au surface dopants on CoTiO₃:La

In preparing metal surface doping one can distinguish three general stages:

- Formation of the precursor solution (aqueous solution of metal salt)
- Impregnation
- Drying and calcination including reduction

If the pores of the basic material are filled with an aqueous solution containing metal ions simply by pouring the solution, and the excess solvent is removed by evaporation, there will remain a number of micro crystals of the metal salt on the walls of the support, and after calcination/reduction will form separate metal particles. This procedure is termed impregnation. The average size of the metal particles depends on the concentration of solution and type of metal salt used, so high metal loadings tend to give larger particles than low loadings. Recent work has proven that surface morphology influences the size and distribution of clusters. For example, the presence of stepped-like surfaces in case of small nano-grains provides the conditions for good dispersion of additives [Ko05, El02]. The physical characterisation of surface dopants is a challenging problem. Transmission electron microscopy is able to image particles as small as 1 nm and below. However, the loading of the particles is still small so the location of the surface dopants remains elusive.

By use of bright and dark field high resolution transmission electron microscopy (HRTEM) and additional EDX, the surface doping on CoTiO₃:La was analysed. High-angle annular dark field (HAADF) images are formed by collection of high-angle scattered electrons with an annular dark-field detector in convenient scanning transmission electron microscopy instruments (STEM). The HAADF image contrast is approximately proportional to the square of the atomic number (termed as Z-contrast imaging), allowing heavy atoms to be detected directly from the image contrast features. Bright field (BF) and HAADF images of palladium dopant particles (concentration 1 at%) are shown in Figure 3.47. The particles were between 3 and 10 nm in diameter. Whereas under BF conditions the surface dopants were difficult to find, because of the weak phase contrast of metal oxide and dopant, under HAADF conditions the dopants were highlighted. However, the HAADF image resolution was not as high as that of BF-HRTEM images.

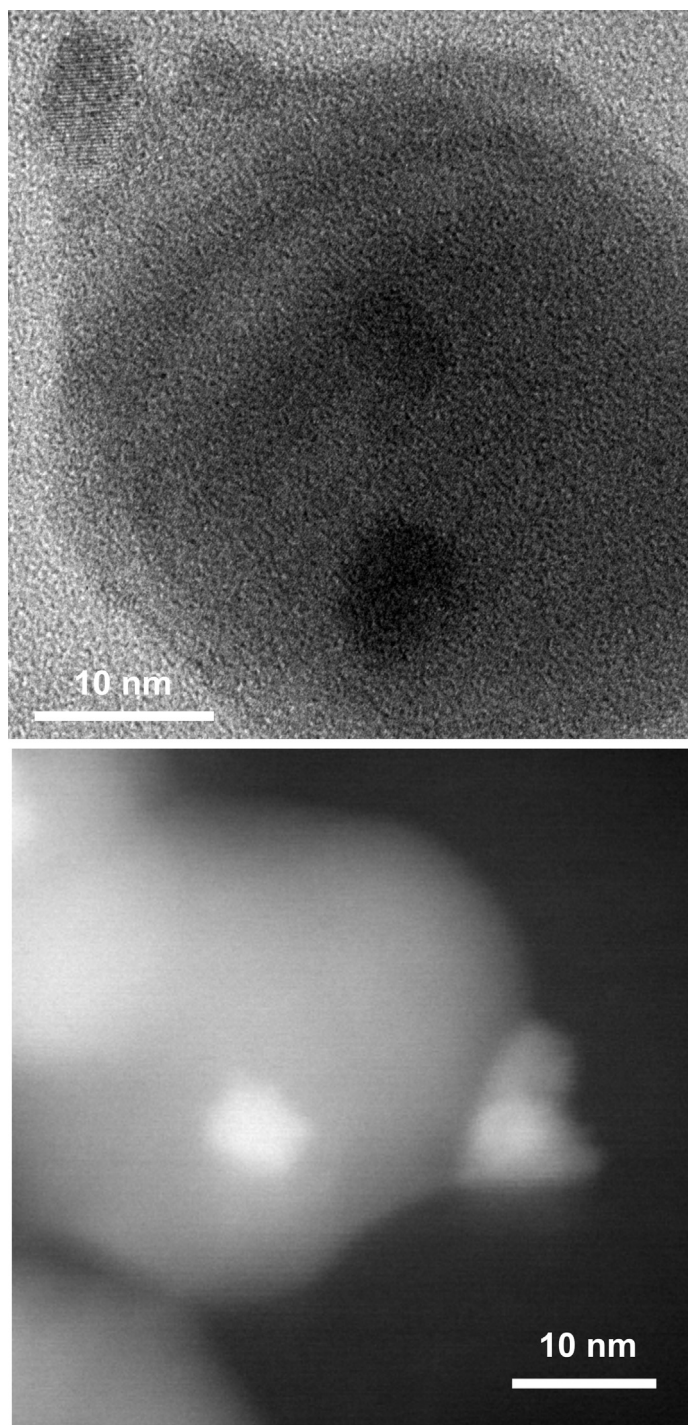


Figure 3.47: Bright and dark field HRTEM images of 1 at% Pd@CoTiO₃:La.

EDX could clearly identify the presence of the metals on the surface. The measured EDX peaks are displayed in Figure 3.48 in attendance with HRTEM images. Point 1 spotted a palladium dopant particle, while point 2 detected the base material. In case of the base material no discrete lanthanum peaks were found because they were superposed by the cobalt and titanium peaks. Copper and silicon peaks resulted from the preparation method on copper grids.

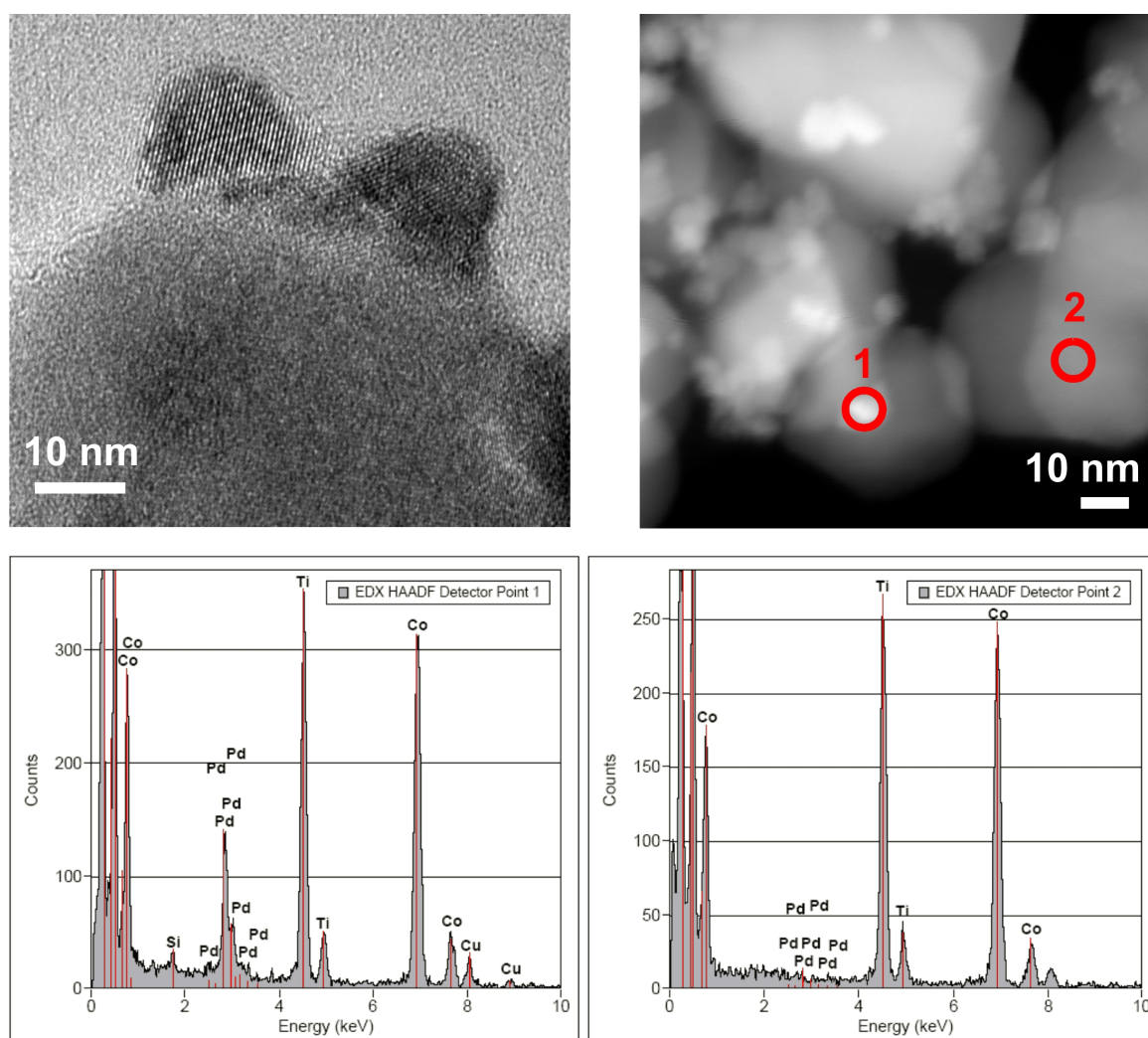


Figure 3.48: HRTEM images and EDX analysis of 1 at% Pd@CoTiO₃:La.

Figure 3.49 depicts bright and dark field HRTEM images of 0.2 at% dopant concentration, which was a realistic concentration of the here prepared sensing layers. In this 0.2 at% case, the allocation of palladium particles is much smaller than in the 1 at% case. In addition, smaller clusters were found in the BF images (around 2-4 nm) which could not be identified by HAADF analysis.

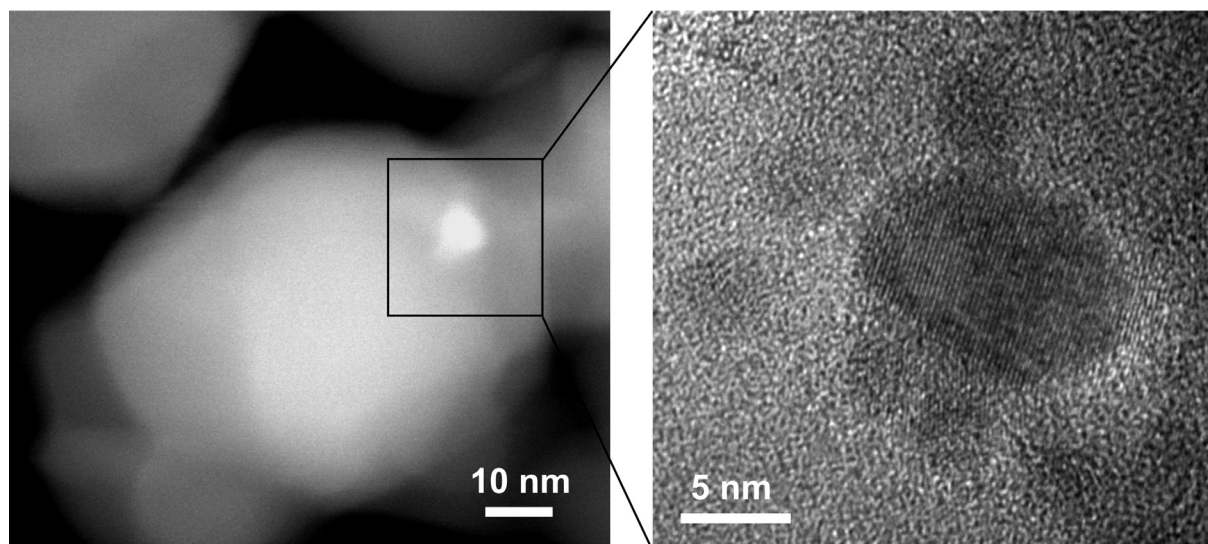


Figure 3.49: Bright and dark field HRTEM images of 0.2 at% Pd@CoTiO₃:La.

Analogue analysis was performed for gold doped samples. Figure 3.50 depicts bright and dark field HRTEM images of 1 at% Au@CoTiO₃:La. In comparison to palladium, gold clusters were rarely found; in addition, large gold islands were noticed, while palladium was deposited as homogenous clusters on the oxide. These observations were also reported by Arbiol [Ar01, Ar02] and the references therein. Arbiol and others found different types of loading depending on the nature of additives. A schematic representation of additive distribution ways on tin oxide is shown in Figure 3.51. In the case of platinum and palladium, metal clusters or nanoclusters on the semiconductor surface were seen. The typical size of these nanoclusters range from 1-8 nm; an example is shown in Figure 3.52. In very low concentrations of these metals monoatomic dispersed centres were also present. In contrast, gold not only nucleated, forming small nanoclusters, but also formed macro-agglomerated metal clusters (islands) with diameters that ranged in the size of the semiconductor grains (20-200 nm) [Ba99]. This behaviour was also observed in other systems like on Si surfaces on which Au atoms were able to diffuse to nucleated islands at temperatures above 340°C [Ro06b].

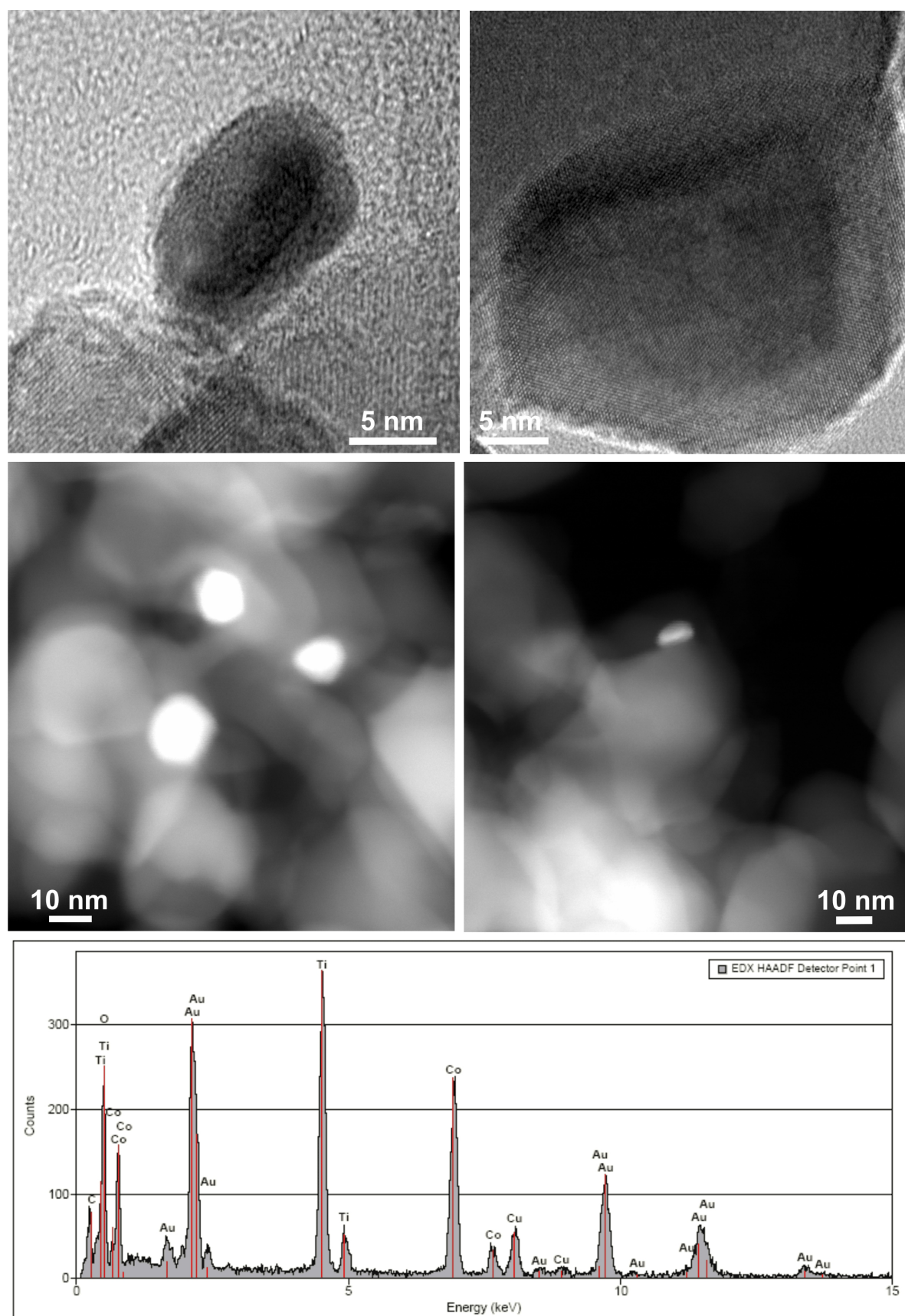


Figure 3.50: HRTEM images and EDX analysis of 1 at% Au@CoTiO₃:La.

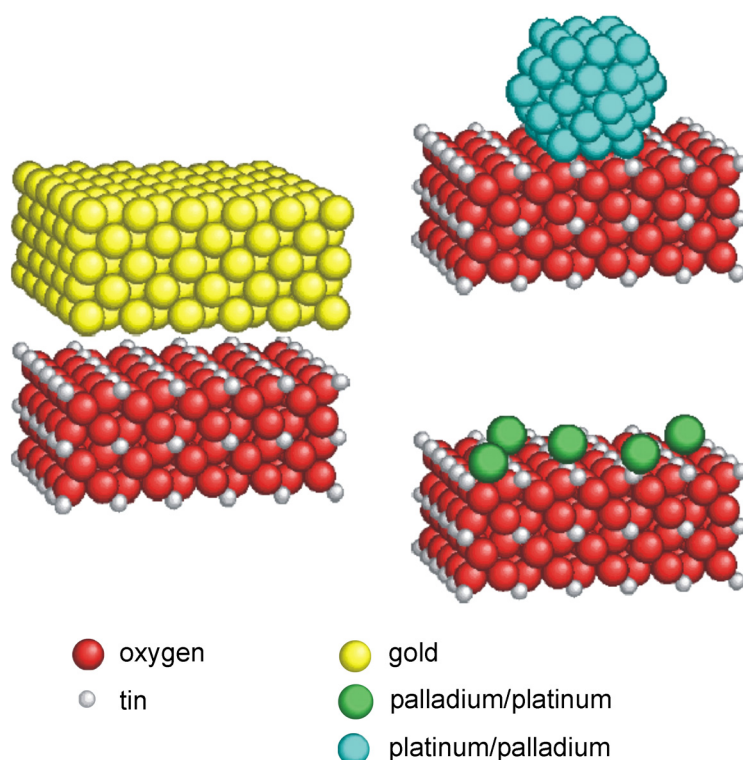


Figure 3.51: Dispersion examples of different metal additives on SnO_2 (taken from [Ar01]). Left: Macro-agglomerated metal. Right top) Superficial clustering. Right bottom) Atomically dispersed metals.

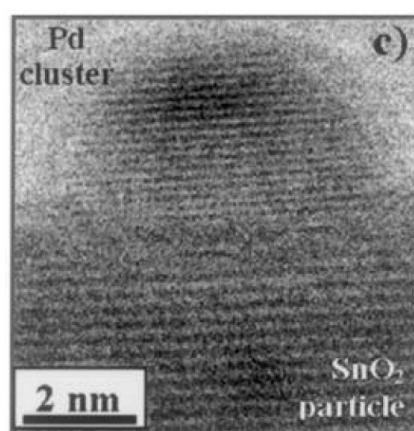


Figure 3.52: Arbiol et al. Palladium cluster on SnO_2 (taken from [Ar02]).

3.2.5.6.3 Surface doping of a Pd/Au mixture on $\text{CoTiO}_3\text{:La}$

Finally, a mixture of Pd and Au surface dopant was prepared to study the influence on the base material. 0.2 at% of each dopant was taken. Figure 3.53 shows the temperature dependence of the resistance of $\text{CoTiO}_3\text{:La}$, $\text{Au@CoTiO}_3\text{:La}$, and $\text{Pd/Au@CoTiO}_3\text{:La}$. The resistance of $\text{Pd/Au@CoTiO}_3\text{:La}$ was in the same region as was seen for the undoped and single doped material. This amount of surface dopant did not strongly affect the conductive behaviour of the base material.

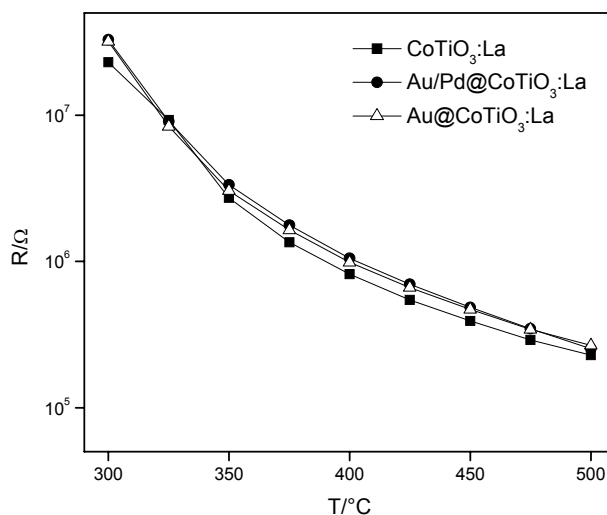


Figure 3.53: Temperature dependence of the resistance of CoTiO₃:La, Au, and Pd/Au@CoTiO₃:La.

Figure 3.54 shows the temperature dependence of the sensitivity towards the applied test gases. Doping the material with a gold-palladium mixture showed no major influence on the sensitivity in comparison to the undoped material (expected for the sensitivity towards CO). However, in comparison to the solely Au or Pd doped samples, the hydrogen sensitivity was not improved and the CO sensitivity was not larger than before. The effects of the single doping elements were not enhanced by mixing the two components.

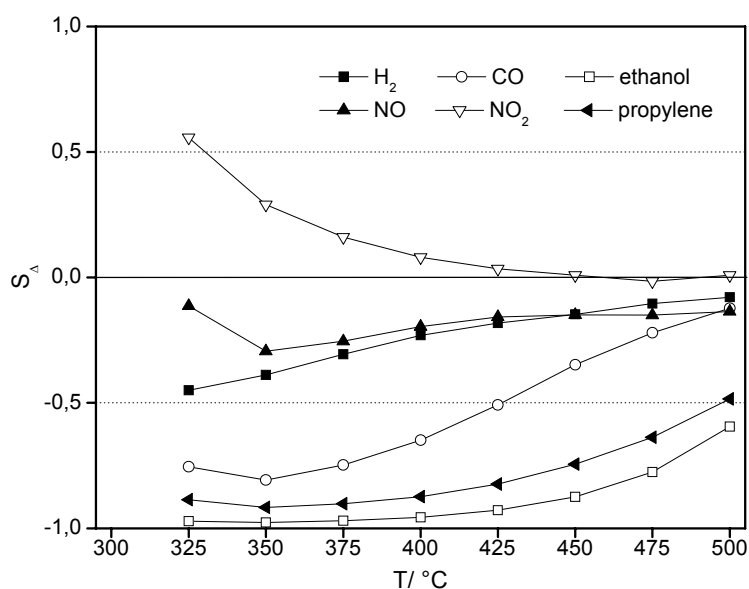


Figure 3.54: Relative sensitivity of Pd/Au@CoTiO₃ versus operating temperature (300-500°C) for various gases.

In addition, the response and recovery behaviour of the sample was tested, as shown in Figure 3.55. In contrast to the undoped material this sample showed higher sensitivity to 40 ppm of propylene than to ethanol (40 ppm). The response and recovery times were all fast. The reaction to NO was very small at this temperature.

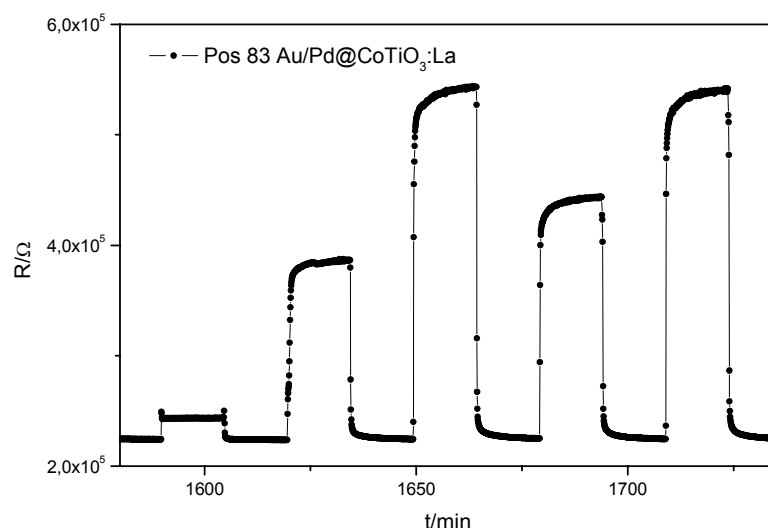


Figure 3.55: Response and recovery times at 500°C to NO (5 ppm), propylene (20, 40 ppm), and ethanol (40, 60 ppm).

3.2.5.7 Solid Surface doping of $\text{CoTiO}_3\text{:La}$

As we have seen before, surface doping with metal salts enables to change the sensing behaviour of a base material. Another interesting question is: how can the use of solid metal oxides as surface dopants influence the sensitivity in comparison to metal dopings? To investigate this, LaMnO_3 and SnO_2 were chosen as solid surface dopants. Both materials are semiconductors, whereas SnO_2 with a band gap of 3.6 eV being close to that of the base material, LaMnO_3 with a band gap of 1.1 eV shows almost metallic conductivity at elevated temperature. Both materials are known to be gas sensitive or catalytically active. Tin dioxide is, as mentioned before, the best understood and most frequently used resistive sensing material. LaMnO_3 proved to be a valuable alternative to the traditional noble metal based catalysts, e. g. for the combustion of methane [Fa06], the total oxidation of hydrocarbons and their hydrogenation [Li71]. Since LaMnO_3 showed promise in catalytic applications, this might also be valuable for surface additives in the case of sensing studies.

Both metal oxides, prepared via the polyol method [Ko06b], were ground with the base material (1at% dopant to base material), redispersed in a polyethyleneimine/water solution and deposited onto the IDC structure by the laboratory robotic system.

Figure 3.56 shows the temperature dependence of the resistance of the undoped and surface doped samples. In both cases the resistance of the base material was increased by surface doping. $\text{LaMnO}_3@\text{CoTiO}_3:\text{La}$ showed the highest resistance. Below 400°C the measurement limits were exceeded. In comparison to the metal surface dopants, the resistance of the base material was higher affected by the metal oxides. The admixing of the solid surface dopants creates new adsorption sites for the gases. The resistance is influenced by the resistance of both materials and the interfacial contacts between base material and dopant particles [Mi92]. Transition of charge carriers might be hindered because of different conduction types of the compounds. In addition, the admixed metal oxide might influence the microstructure of the sample. All these effects might cause the resistance change of the base material.

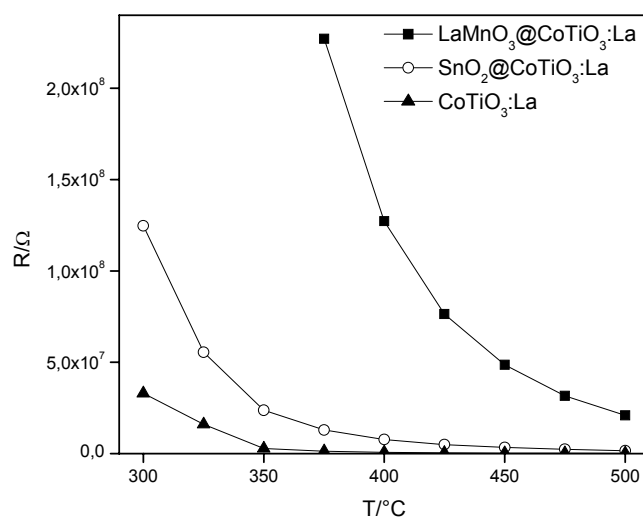


Figure 3.56: Temperature dependence of the resistance of $\text{CoTiO}_3:\text{La}$ and the surface doped samples.

Figure 3.57 depicts the sensitivity of these materials towards ethanol (40 ppm) and propylene (25 ppm). The undoped material showed highest sensitivity to ethanol over the whole temperature range. The surface doped samples showed both a high sensitivity to propylene. In addition tin dioxide showed highest sensitivity to propylene

from 475 to 375°C. With the help of these surface dopants it seemed that the chain length and double bond of propylene became more dominant for the reaction than the OH-group of ethanol. This could be caused by three reasons. On the one hand, the solid surface dopants might act catalytically on the conversion of propylene. On the other hand, the reaction of ethanol was restricted on the dopant grains and did not change the base materials' resistance i.e. no sensitivity towards ethanol was measured. Third, this might be a simple temperature effect. The maximum sensitivities of the surface doped samples might appear at temperatures below 375°C. For the tin dioxide sample a change in selectivity appeared at 375°C. Unfortunately the measurement data below 375°C exceeded the measurement limits, so no data could be analysed.

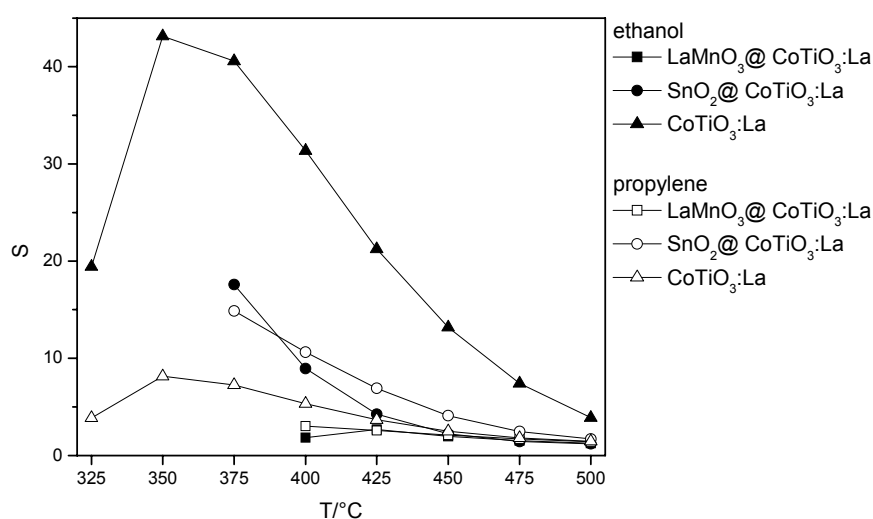


Figure 3.57: Temperature dependence of sensitivity to ethanol and propylene.

Figure 3.58 depicts the response and recovery behaviour of the tin dioxide doped sample at 475°C. A distinct sensitivity towards propylene was seen. 20 ppm of propylene showed higher sensitivity than 40 ppm of ethanol. With the help of tin dioxide as a surface dopant, selectivity to the applied hydrocarbons was changed in the temperature range between 500 and 400°C. In addition, the overall sensitivity towards propylene was the highest in this sample. Normally tin dioxide is known to show a good response towards ethanol. In combination with the p-type base material, the sensitivity to propylene is enhanced. In this case the second explanation might help to understand this behaviour. The reaction of ethanol was restricted on the tin dioxide grains and did not influence the resistance of the sensing layer.

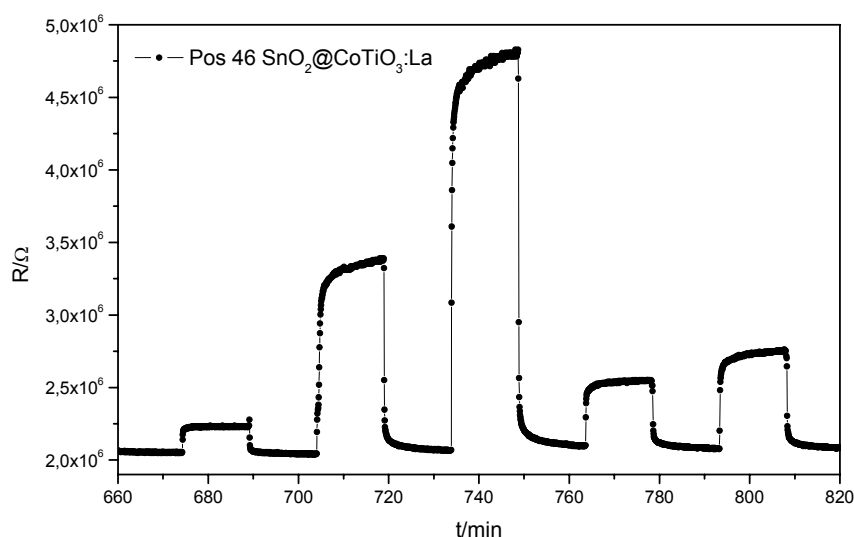


Figure 3.58: Response and recovery times at 475°C to NO (5 ppm), propylene (20, 40 ppm), and ethanol (40, 60 ppm).

Figure 3.59 shows the response and recovery behaviour of $\text{LaMnO}_3@\text{CoTiO}_3:\text{La}$ at 500°C. Because of the high resistance of the material, a smaller signal-to-noise-ratio was found even at 500°C. The material responded better to propylene than to ethanol, i.e. 20 ppm propylene showed a larger increase in resistance than 40 ppm ethanol. This selectivity might be caused by the first explanation. LaMnO_3 is reported as a catalytically active material for the combustion of methane [Fa06] and the total oxidation of hydrocarbons [Li71].

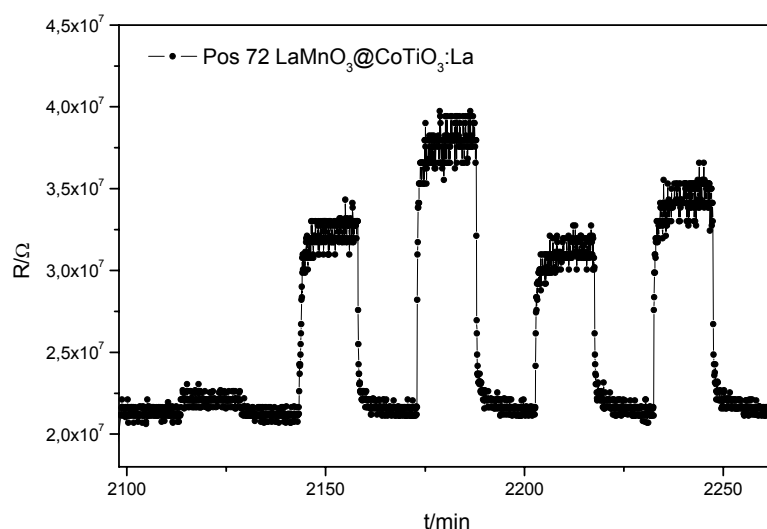


Figure 3.59: Response and recovery times at 500°C to NO (5 ppm), propylene (20, 40 ppm), and ethanol (40, 60 ppm).

The use of the chosen solid surface dopants allowed the creation of materials with higher propylene selectivity in a temperature range between 500 and 400°C. In particular, admixture of tin dioxide showed only small changes in resistance compared to the base material and excellent propylene sensitivity.

3.2.6 Summary of CoTiO₃-related investigations

CoTiO₃ turned out to be a suitable sensing material especially for hydrocarbons. Addition of volume dopants in small concentrations was able to influence the electrical and gas sensing properties of the base material. All volume dopants enhanced the conductivity of the material. The sensitivity and selectivity to ethanol and the response ability of the base material was improved. The lanthanum doped sample showed highest ethanol sensitivity and a lower resistance than the undoped material, therefore it was chosen for further investigations on the influences of surface dopants.

Addition of surface dopants in different concentrations was performed. The concentration showed no major influences on the sensitivity. Au and Pd were found to be the most effective surface dopants. They showed sensitivities towards hydrogen and carbon monoxide. In addition, the gold doped material was a suitable NO-tolerant NO₂-sensing material at around 350°C. SnO₂ doping produced only small changes in resistance compared to the base material and excellent propylene sensitivity and selectivity.

3.2.7 Capacitance analysis of doped CoTiO_3

In the literature, gas sensing materials can be found that show a change in permittivity in response to test gases or humidity. These changes in permittivity are induced by significant changes of the charge carrier density and the displacement current.

After discussion of the shown measurements, the question arises whether the capacitance that is also achieved from the measurements can be a useful tool to quantify the gas sensing properties of the materials. An advantage of using such a tool would be the possibility of measuring samples with high resistances.

The conductor pathway to each IDC differs in length and distance because of the compact array setup and the central positioning of the 64 wells on the substrate. The conductor path is parallel to the IDC, so both capacities are added. A broad distribution of capacities is found, as shown in [Si02] and [Sa04]. These parasitic effects have to be determined by a compensation measurement. For the compensation measurement, an electrode array was measured before deposition of thick films. The electrode array has some IDCs that have almost negligible parasitic pathway effects, like position 55 (see Figure 2.12) where the conductor pathways are perpendicular to each other [Si02]. These positions show the smallest capacities that result only from the IDC. These positions are taken to determine the parasitic values for the other positions [Sa04]. The achieved parasitic effects (which have to be determined every time the substrate array is changed in fabrication) are subtracted from the measured capacities. Figure 3.60 shows the comparison between measured and corrected capacities of different doped $\text{CoTiO}_3\text{:La}$ samples. After this adjustment, the homogeneity of the capacities is obvious. No influence of the surface doping was seen.

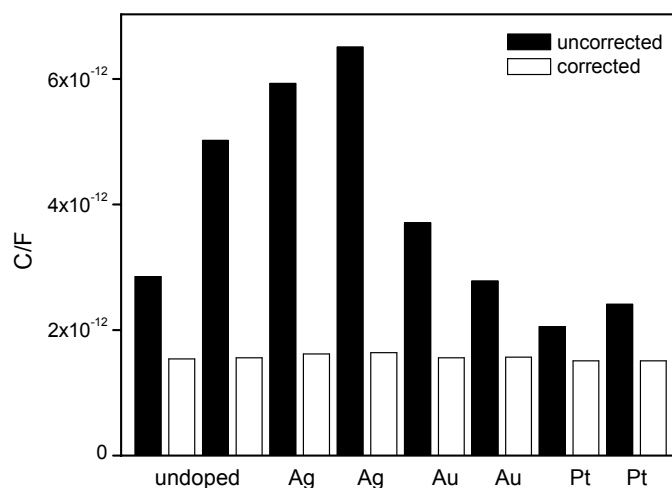


Figure 3.60: Measured and adjusted capacities (RA6351).

To compare a certain influence on the capacity, the different samples, dopants, temperatures, and test gases have to be taken into account. Figure 3.61 shows the fingerprint for $\text{CoTiO}_3\text{:Sm}$ as an example. The capacities for all test gases are depicted. No changes in capacity were observed whereby the resistance changed (as described in chapter 3.2.2).

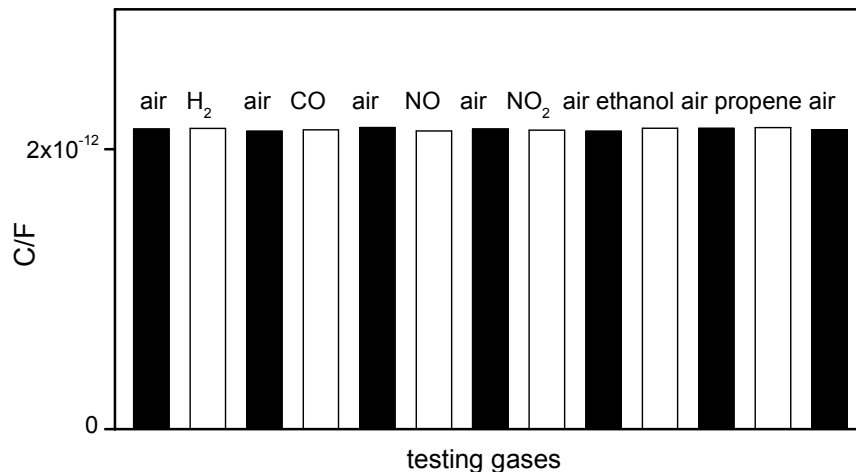


Figure 3.61: Fingerprint for $\text{CoTiO}_3\text{:Sm}$ versus all tested gases (AC1015), C from measurement.

Figure 3.62 presents the comparison between undoped and La-volume doped material. As one can see on the left hand side, the volume doping had a significant influence on the resistance of the material, while in comparison, as presented on the right hand side, the influence on the capacity under different atmospheres was negligible.

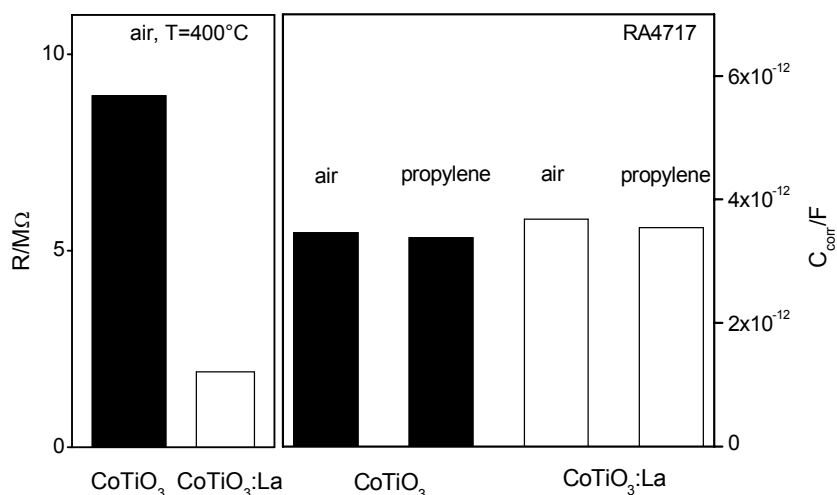


Figure 3.62: Capacities of undoped and La-volume doped $CoTiO_3$ under air and propylene (RA4717, $T=400^\circ C$).

In Figure 3.63 the presented features are combined. The corrected capacities are plotted versus the logarithm of the resistance of the materials. Capacity values from all measured temperatures, dopants, and test gases including synthetic air are shown (AC1013).

The resistance of the materials varies over more than two orders of magnitude while the capacitance remained around the same value. Capacities of zero indicated defect positions. Capacity values that are below the main value indicated partial defect electrode structures and/or mended pathways which showed a smaller capacity than the calculated ones. For refinement of these values, a compensation measurement of every blank single array would have been necessary.

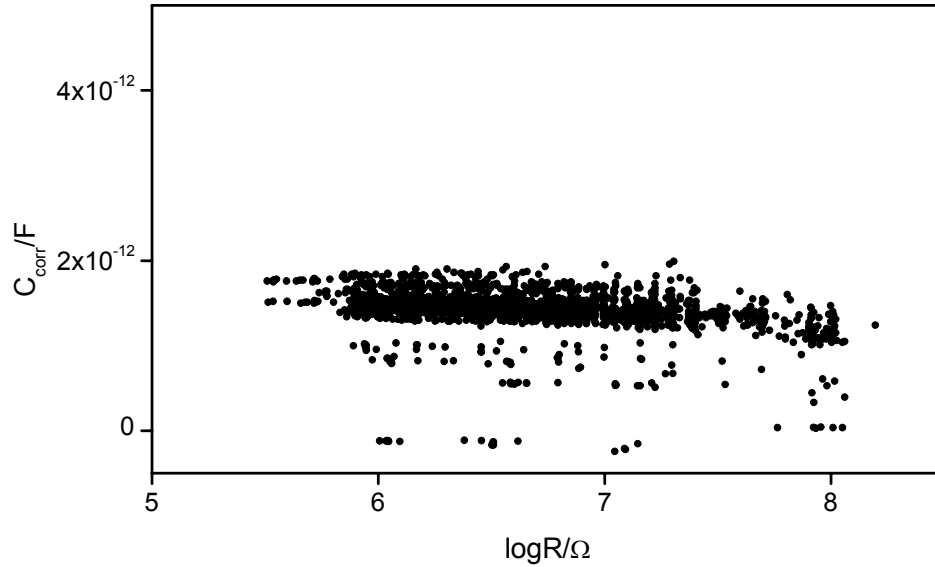


Figure 3.63: Capacity versus log resistance of all samples of substrate plate AC1013, at each temperature (25° steps) and for all test gases including synthetic air.

While the material resistance was influenced by testing gases and temperature, no marginal changes were observed in the capacitance. From these measurements, it was assumed that the testing gases showed no significant influence on the material permittivity. The capacitance, which resulted from the circuit equivalent, was given by the geometric capacitance of the array. This was also supported by the fact that different fabricated sample arrays showed different corrected capacities but no change on either temperature or test gases. In p-type materials, where the conductance is thought to be on the surface, no influences on the capacity were found. In addition, in n-type materials, where the change of the depletion zone would affect the displacement current, no influences with the same sample geometry were found [Sa04].

In summary, the data showed that capacitance cannot be used as a measuring quantity for observing the gas sensing behaviour of the samples on the here shown electrode arrays.

3.3 LnMO₃ compounds

In the following chapter the investigations on different LnMO₃ materials will be shown.

3.3.1 Preparation and characterisation of LnMO₃ compounds

The rare-earth perovskites (LnBO₃) containing transition metal ions (B) show a multitude of interesting electrical properties. They are often described as materials for catalysts [Mc90, Pe01], photocatalysts [Xi05], electrodes of fuel cells [Yo01, Mi93], magneto-optics [Ke01, Ko02] and spin valves [Sa99]. A number of perovskite oxides have been proposed as gas sensor materials previously because of their stability in thermal and chemically aggressive atmospheres. Many perovskites prepared in air show p-type semiconductive behaviour. Obayashi et al. were the first who proposed the use of (Ln, M)BO₃ (Ln=lanthanoid element, M=alkaline earth metal, and B=transition metal) perovskites as potential ethanol sensors [Ob76]. Arakawa et al. observed the rise of methanol activity for n-type LnFeO₃ (Ln=La, Pr, Nd, Sm, Eu, Gd) with decreasing ionic radius; however, that relationship was not clearly seen in LnCrO₃ (Ln=La, Nd, Sm, Eu, Gd) [Ar81]. In the group of the LnFeO₃-perovskites, LaFeO₃ and SmFeO₃ are most regarded as sensing materials for different test gases like CH₃SH, NO₂, ethanol, and CO [Ma99b]. Aono et al. tested and compared the gas sensing properties of p-type LaFeO₃, SmFeO₃, NdFeO₃, GdFeO₃ and DyFeO₃ towards NO₂ [Ao03]. Furthermore, EuFeO₃ and GdFeO₃ have been tested on gasoline and ethanol without any cross-sensitivity towards H₂ by Niu et al. [Ni04]. In the LnCrO₃ group not many investigations towards gas sensitivity have been made. LaCrO₃ is the most frequently regarded material in terms of gas sensing and catalysis e.g. towards hydrocarbons, SO₂ and NO [Fi03, Hu96]. As mentioned previously, Arakawa tested SmCrO₃, NdCrO₃, LaCrO₃, EuCrO₃ and GdCrO₃ towards their methanol activity [Ar81]. This shows that up to now, no systematic study on the effect of Ln-variation over the whole LnMO₃ group on the gas sensing properties have been made; such a study would finally allow the analysis of structure property relations and the development of design principles for highly sensitive and/or even selective gas sensors based on these materials. As far as the literature shows, the gas sensing characteristics of LnFeO₃ (Ln=Tb, Er, Tm, Yb, Lu) and LnCrO₃ (Ln=Pr, Tb, Dy, Ho, Er, Tm, Yb, Lu) are not yet published or investigated.

All materials (13 LnFeO_3 and 12 LnCrO_3 compounds) were prepared by the described polyol method. Experimental details can be found in the experimental section. The materials were found to be amorphous right after preparation. After annealing at T_3 for 2-12 h the materials turned out to be highly crystalline. The powder X-ray diffraction patterns gave evidence about the formation of single phase compounds in almost all cases as shown in Figure 3.64.

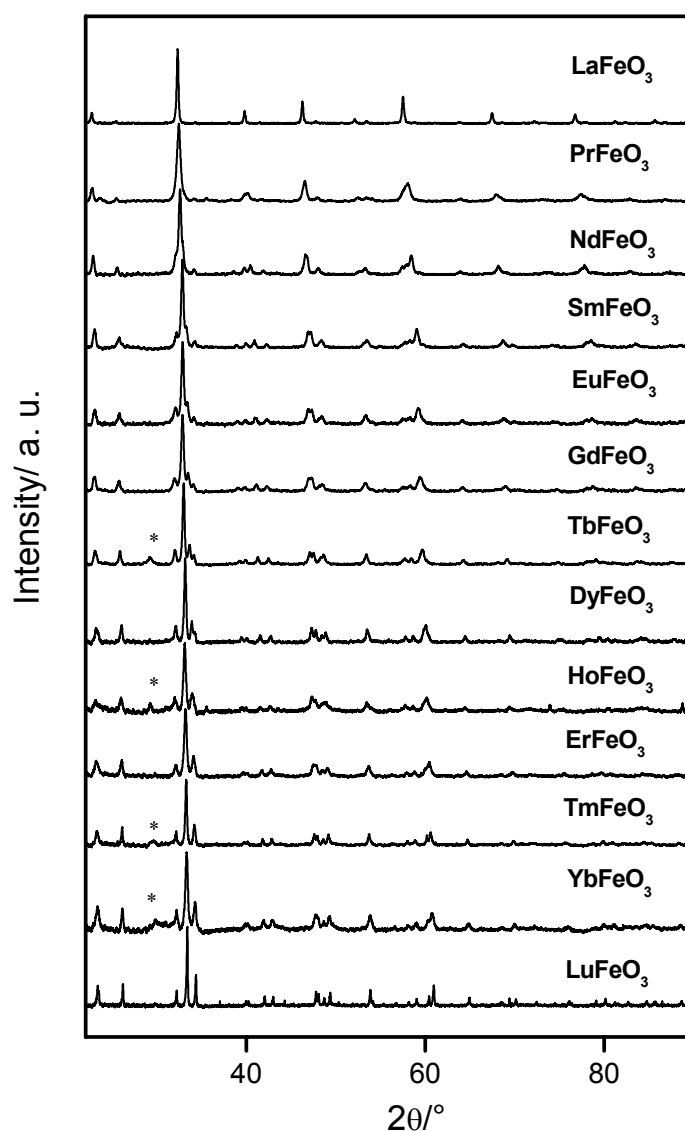


Figure 3.64a): XRD diffraction pattern of LnFeO_3 powders obtained by polyol-mediated synthesis.

Only some LnFeO_3 ($\text{Ln}=\text{Tb}, \text{Ho}, \text{Tm}, \text{Yb}$) show traces of Ln_2O_3 around $29^\circ 2\theta$ marked with an asterisk. The XRD lines of all powders were broad, indicating small particles.

All perovskites show orthorhombic phases and the refined lattice parameters are in accordance with the reference data.

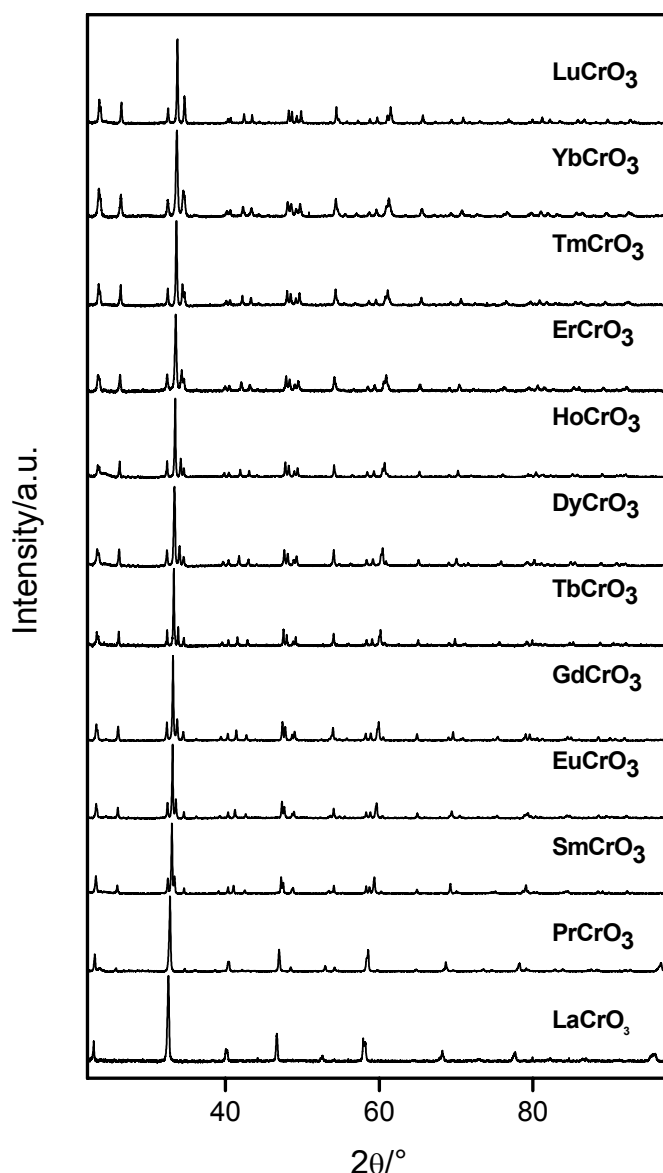


Figure 3.64b): XRD diffraction pattern of LnCrO_3 powders obtained by polyol-mediated synthesis.

As shown in the literature, the deviation from cubic symmetry (like in SrTiO_3) increased as the Ln^{3+} ionic radius decreased; it was smallest in LaMO_3 and largest in LuMO_3 [Ly99]. The average crystallite size of the samples was determined using Scherrer's equation. The particle size and morphology of the powder materials was estimated based on SEM micrographs. Thermal treatment resulted in agglomerates (secondary particles) which were irregularly packed and complicated the estimation of the primary particle size in some cases. However, the shape of the primary particles was spherical right after preparation. SEM images of all LnFeO_3 and LnCrO_3

are shown in Figure 3.65. Crystallographic data and reference numbers as well as particle and crystallite sizes of the prepared compounds are listed in Table 3.2.

Table 3.2: Prepared LnFeO_3 and LnCrO_3 oxides via polyol mediated synthesis. Literature data have been taken from: [Qu63].

compound	space group	a(Å)	b (Å)	c (Å)	ICSD/Ref.	DS(nm)	SEM(nm)*
LaFeO_3	<i>Pbnm</i>	5,555(2)	5,563(0)	7,863(4)	28255	74	30-80
PrFeO_3	<i>Pbnm</i>	5,484(3)	5,572(4)	7,790(7)	27274	42	40-100
NdFeO_3	<i>Pbnm</i>	5,449(9)	5,585(4)	7,763(8)	27275	55	50-70
SmFeO_3	<i>Pbnm</i>	5,387(6)	5,568(4)	7,703(3)	27276	55	30-60
EuFeO_3	<i>Pbnm</i>	5,369(1)	5,590(0)	7,680(3)	27277	62	50-80
GdFeO_3	<i>Pbnm</i>	5,346(5)	5,605(3)	7,663(3)	16644	55	50-80
TbFeO_3	<i>Pbnm</i>	5,317(3)	5,597(1)	7,645(3)	27279	70	40-80
DyFeO_3	<i>Pbnm</i>	5,295(3)	5,589(3)	7,615(3)	27280	71	30-70
HoFeO_3	<i>Pbnm</i>	5,274(4)	5,580(8)	7,627(9)	27281	56	highly agglomerate
ErFeO_3	<i>Pbnm</i>	5,260(5)	5,575(4)	7,602(5)	27282	57	highly agglomerate
TmFeO_3	<i>Pbnm</i>	5,249(3)	5,573(2)	7,585(6)	25658	91	40-100
YbFeO_3	<i>Pbnm</i>	5,230(7)	5,558(3)	7,575(3)	27284	56	30-60
LuFeO_3	<i>Pbnm</i>	5,213(6)	5,556(8)	7,566(2)	27285	120	highly agglomerate
LaCrO_3	<i>Pbnm</i>	5,514(8)	5,487(5)	7,751(5)	[Qu63]	84	70-90
PrCrO_3	<i>Pbnm</i>	5,448(7)	5,479(9)	7,719(3)	[Qu63]	87	80-100
SmCrO_3	<i>Pbnm</i>	5,367(9)	5,506(6)	7,645(4)	[Qu63]	131	highly agglomerate
EuCrO_3	<i>Pbnm</i>	5,345(3)	5,513(7)	7,624(0)	[Qu63]	108	60-100
GdCrO_3	<i>Pbnm</i>	5,313(8)	5,528(7)	7,608(4)	[Qu63]	101	60-80
TbCrO_3	<i>Pbnm</i>	5,293(3)	5,522(3)	7,578(4)	[Qu63]	148	80-100
DyCrO_3	<i>Pbnm</i>	5,268(9)	5,524(6)	7,559(3)	[Qu63]	94	50-100
HoCrO_3	<i>Pbnm</i>	5,244(2)	5,522(6)	7,539(5)	[Qu63]	132	60-100
ErCrO_3	<i>Pbnm</i>	5,225(1)	5,520(9)	7,523(5)	[Qu63]	82	70-90
TmCrO_3	<i>Pbnm</i>	5,209(3)	5,508(6)	7,502(9)	[Qu63]	109	50-70
YbCrO_3	<i>Pbnm</i>	5,193(7)	5,507(2)	7,493(2)	[Qu63]	77	60-80
LuCrO_3	<i>Pbnm</i>	5,177(6)	5,501(8)	7,483(0)	[Qu63]	114	highly agglomerate

*size of visible spherical primary particles

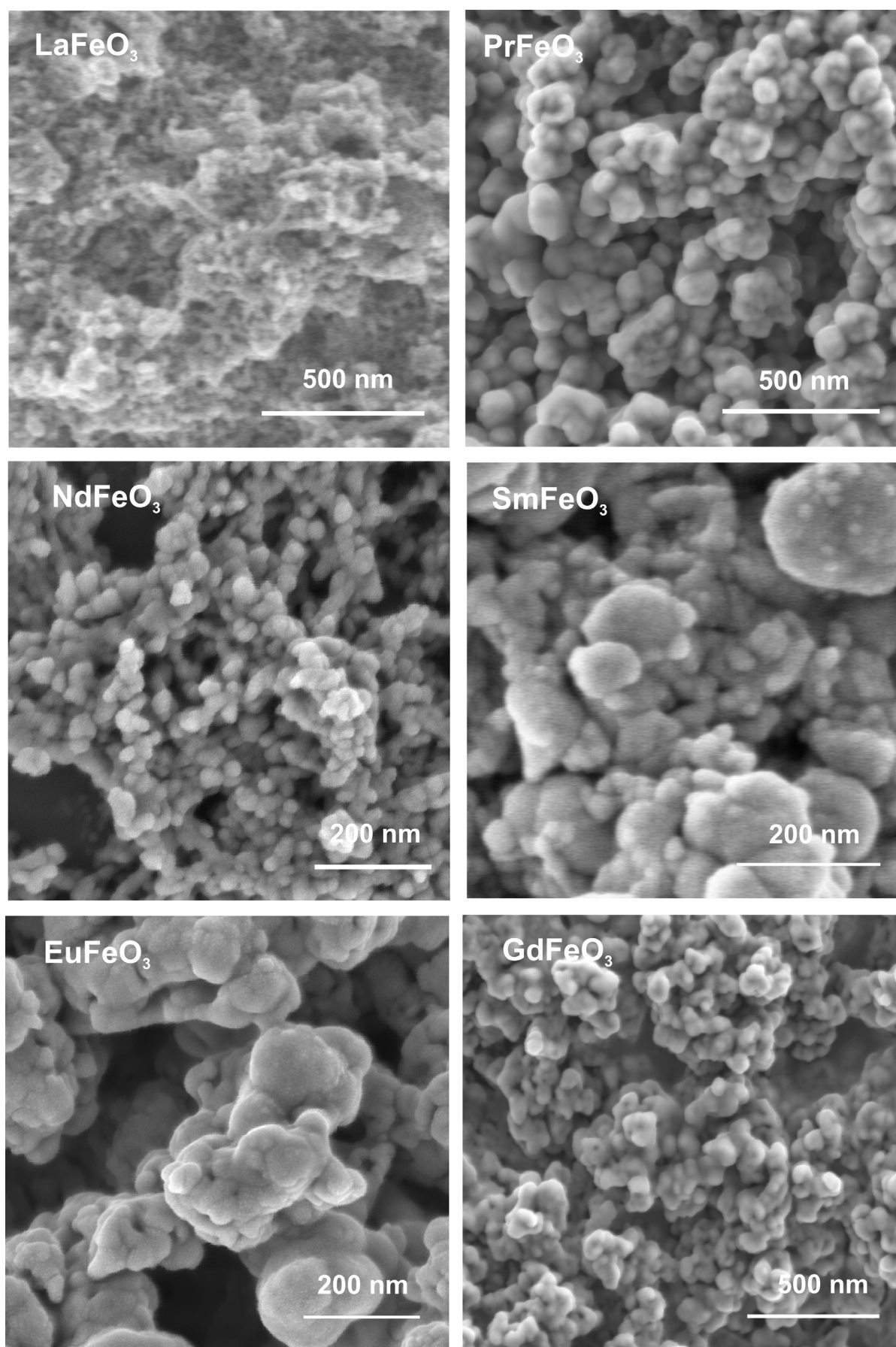


Figure 3.65a). SEM images of LnFeO_3 compounds. Particles are agglomerated due to the thermal treatment. The primary particle size differs with the reaction conditions and the starting compounds.

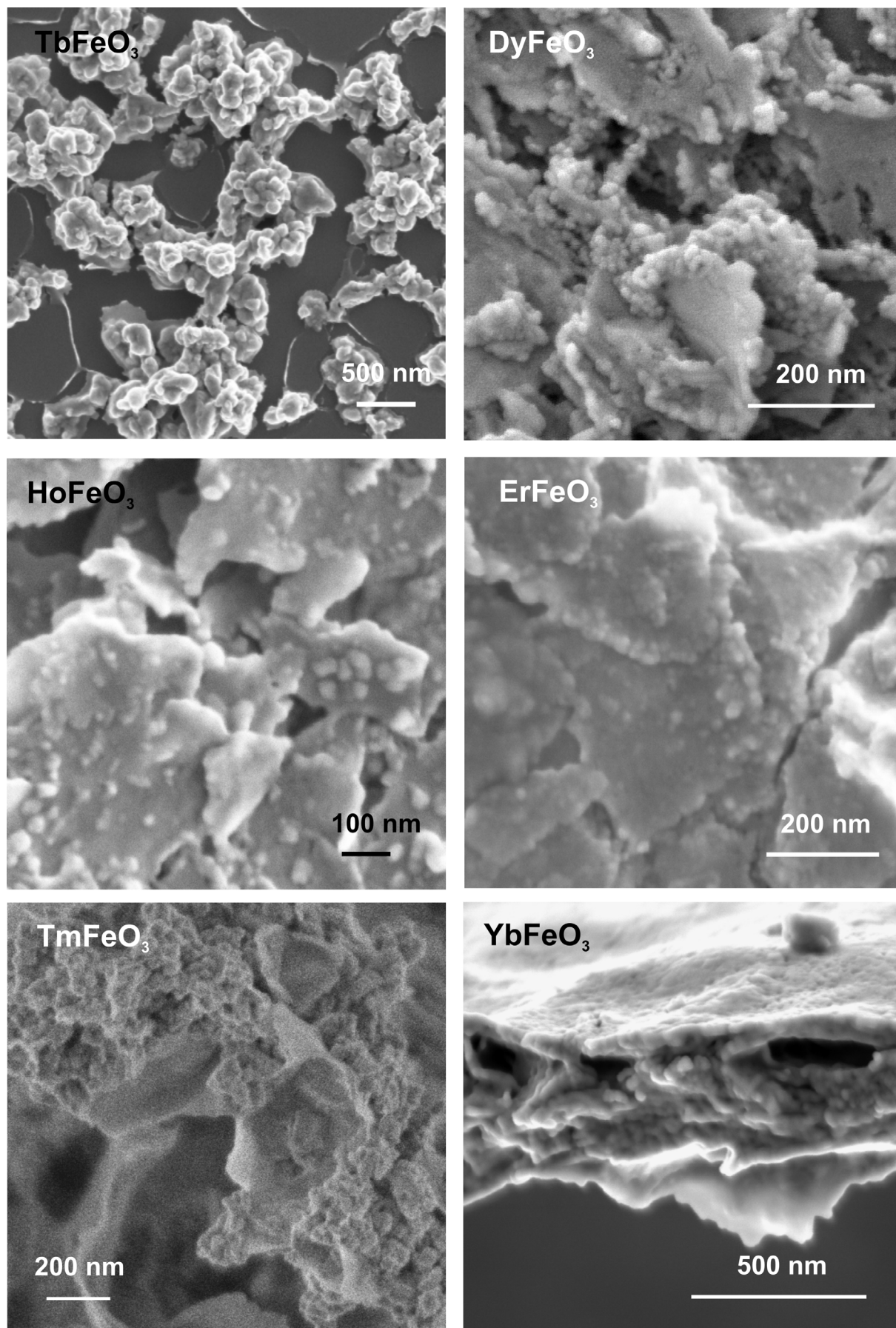


Figure 3.65a). SEM images of LnFeO_3 compounds. Particles are agglomerated due to the thermal treatment. The primary particle size differs with the reaction conditions and the starting compounds.

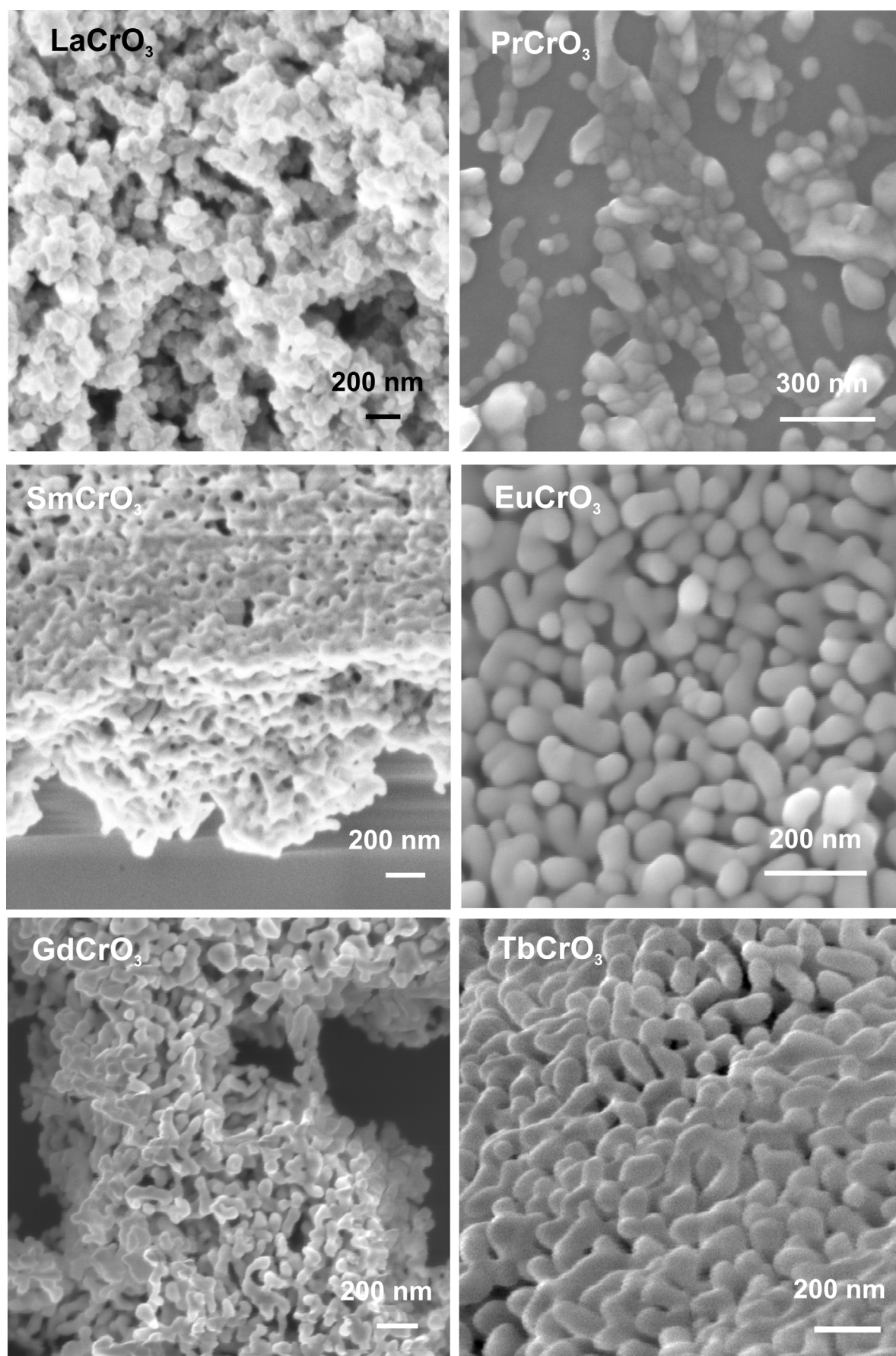


Figure 3.65b). SEM images of LnCrO_3 compounds. Particles are agglomerated due to the thermal treatment. The primary particle size differs with the reaction conditions and the starting compounds.

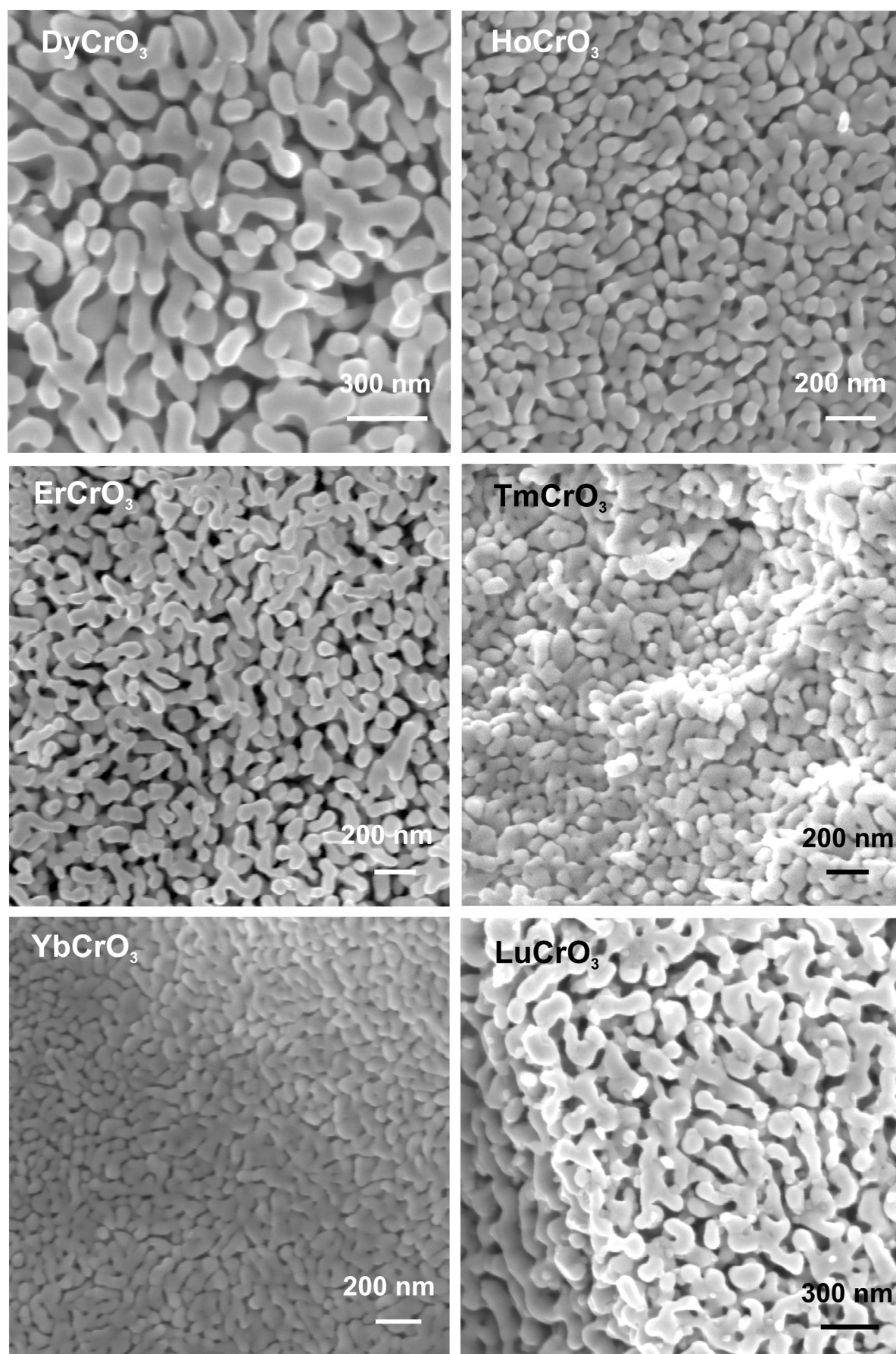


Figure 3.65b). SEM images of LnCrO_3 compounds. Particles are agglomerated due to the thermal treatment. The primary particle size differs with the reaction conditions and the starting compounds.

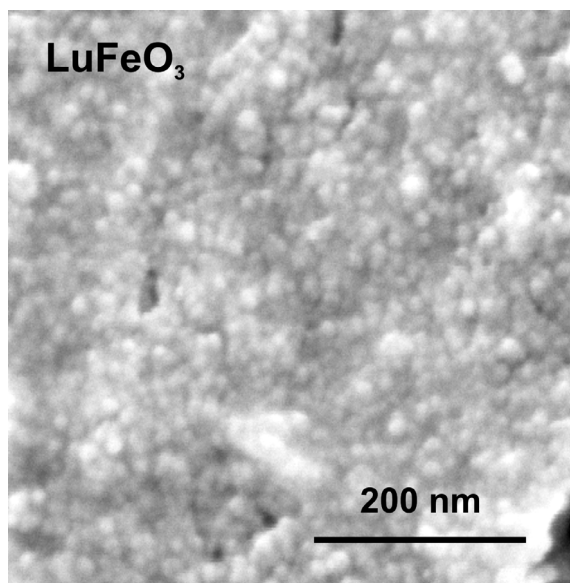


Figure 3.65c). SEM image of LuFeO₃.

The prepared materials were well suited for thick layer preparation on inter-digital electrode structures. The preparation and deposition of the suspensions was performed as described in chapter 3.2, p. 42. The electrical measurements and test gas sequence remained the same.

3.3.2 Electrical and gas sensing characterisation of LnFeO₃

Figure 3.67 shows the plot of the real part of the complex impedance versus the imaginary part (Argand plot) representative for TbFeO₃ in synthetic air, propylene, and ethanol at 300 °C. Automated data fitting allows to describe the impedance spectra as an impedance function of a circuit equivalent, consisting of a resistor and a capacitor in parallel, as described previously.

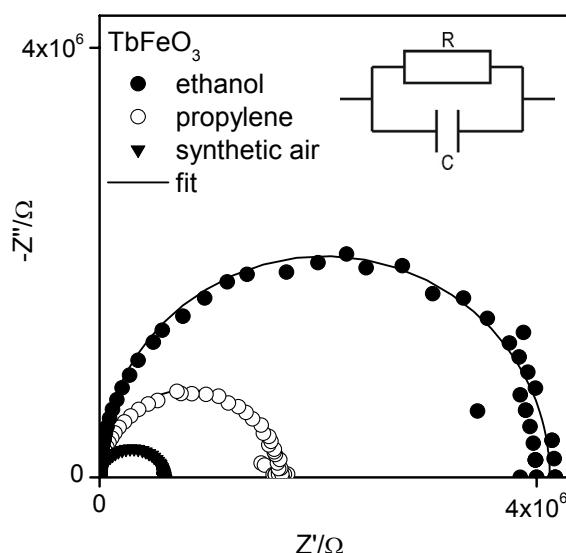


Figure 3.67: Example of an Argand plot and circuit equivalent for TbFeO_3 ($T=300^\circ\text{C}$). p-type semiconductors show an increase of resistance compared to synthetic air when reducing gases are applied.

A plot of resistivity versus temperature for the prepared compounds is shown in Figure 3.68, which indicates that the conductivity was thermally activated, as one would expect. However, the conductivity was not simply thermally activated according to the Arrhenius-relation, as the thermal activation was superposed by the temperature dependent adsorption/desorption equilibrium of oxygen on the metal oxide surface. The highest resistance was found for YbFeO_3 , the smallest for LaFeO_3 . Differences in resistance occurred not only from the difference of the Ln-cation but also from the variation of the microstructure in the prepared films.

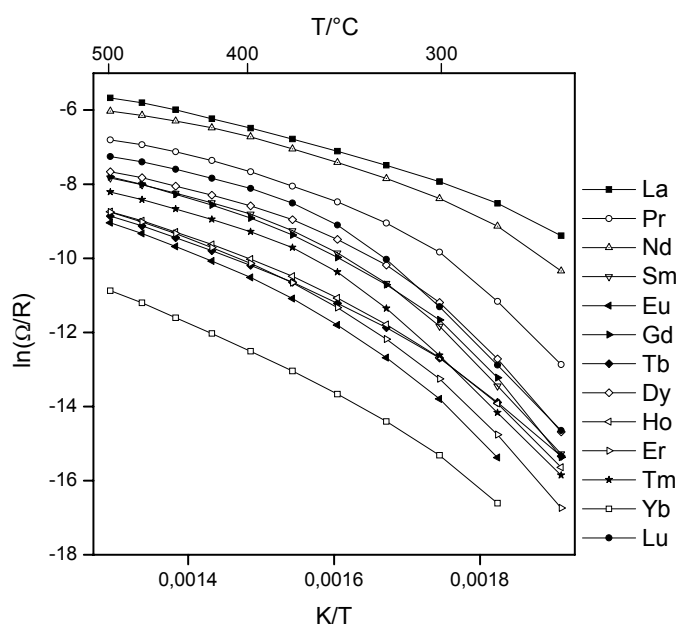


Figure 3.68: Arrhenius plot of the prepared LnFeO_3 materials under synthetic air.

Figure 3.69 shows the temperature dependence of the sensitivity of different LnFeO_3 materials, indicating that the operating temperature affected the properties of all materials. As one can see, all materials showed almost no cross-sensitivity to H_2 over the whole temperature range and only a weak sensitivity to CO below 400°C . The sensitivity to NO and NO_2 was only pronounced at lower temperatures; it was noticeable that for NO, a characteristic change was observed from oxidising ($S_\Delta > 0$) to reducing behaviour ($S_\Delta < 0$) depending on the respective materials. At temperatures above 400°C all materials showed solely sensitivity towards hydrocarbons. LaFeO_3 , the material with the biggest lanthanide radius, presented the smallest sensitivity towards all gases. It showed almost no sensitivity towards NO_x and was only a poor hydrocarbon sensing material. Measurements for YbFeO_3 could only be evaluated above 300°C . At lower temperatures the resistance of the material exceeded the measurement limits ($R > 20 \text{ M}\Omega$). This material showed high NO-sensitivity with only a weak cross-sensitivity towards NO_2 , which makes it a suitable material for a NO_2 -tolerant NO-sensor at a working temperature of around 300°C . In general, the highest sensitivities were seen with SmFeO_3 , TmFeO_3 and LuFeO_3 . They showed highest NO_2 sensitivities in the lower temperature range and highest hydrocarbon sensitivities for all temperatures below 450°C . All three showed almost no cross-sensitivities to NO at 300°C , which makes these materials suitable for NO-tolerant NO_2 -sensing materials at this working temperature.

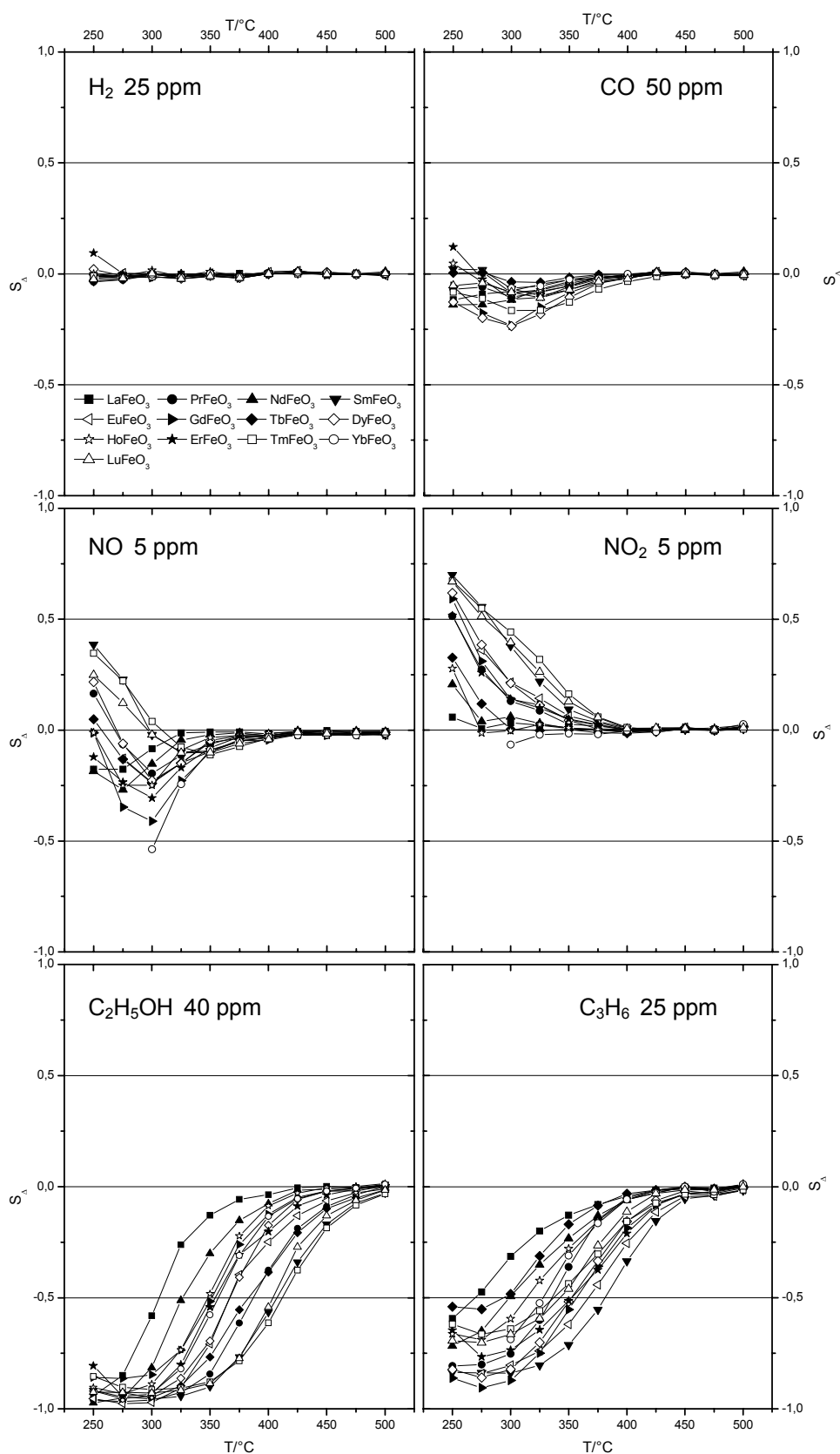


Figure 3.69. Sensitivity-temperature behaviour of the prepared LnFeO_3 materials.

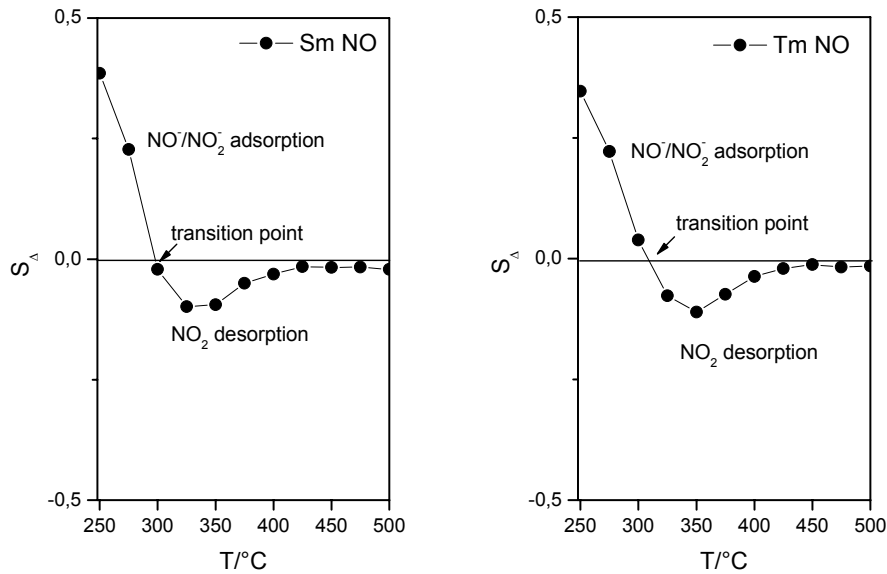
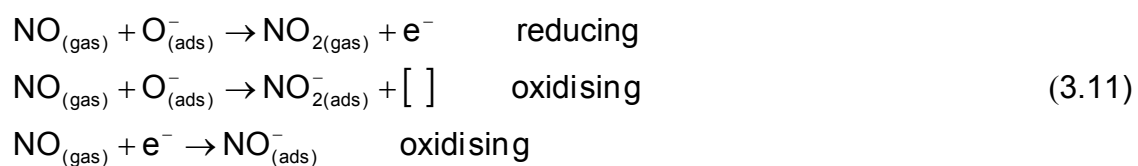


Figure 3.70: Change of the interaction of NO with the semiconducting surface.

As mentioned before, the temperature behaviour of the sensitivity of NO changed from oxidising to reducing with increasing temperature. This is shown again in Figure 3.70 exemplary for TmFeO₃ and SmFeO₃. A corresponding behaviour is reported from Sanders and Koplin for surface doped In₂O₃ and SnO₂ [Sa04, Ko06] and can be understood as follows.

At temperatures between 300 and 425°C the oxidation reaction and desorption of NO₂ actually responsible for the change in resistance were adequately activated. Above a temperature of 425°C the sensitivity vanished. According to Lampe et al. it is assumed that at temperatures below 300°C the desorption and oxidation reaction was not yet activated. The NO molecules were adsorbed on the surface and remained there. The important reactions here were the formation of NO₂⁻ or NO⁻. In the first case, a new adsorption site for oxygen was achieved. In the second case, an electron was abstracted from the semiconductor. In both cases, an increase of conductivity was observed. At around 300°C a transition point emerged. At this point the reactions competed resulting in a negligible sensitivity [La95b].



Focussing on overall sensitivity, the sequence of the best sensitivities to different test gases over the whole temperature range are listed in Table 3.3. Arakawa et al. found that the methanol sensing activity increased as the radius of the rare earth ion decreased for n-type LnFeO_3 oxides. The sequence of materials with increasing activity was $\text{Gd} > \text{Eu} > \text{Sm} > \text{Nd} > \text{Pr} > \text{La}$ [Ar81]. Here, no correlation between the sensitivity of the 13 materials studied towards the different gases and the radius of the rare-earth ions was observed.

Table 3.3: Sequence of LnFeO_3 -sensitivities to the test gases over the whole temperature range.

<i>test gas</i>	<i>sequence of highest sensitivities</i>
propylene	$\text{Sm} > \text{Eu} > \text{Gd} > \text{Dy}$
ethanol	$\text{Tm} > \text{Sm} > \text{Lu}$
NO_2	$\text{Tm} > \text{Lu} > \text{Sm}$
NO	$\text{Tm} \approx \text{Sm} > \text{Lu}$

3.3.2.1 Response times and concentration dependence

In this section, the response and recovery ability of the LnFeO_3 compounds and concentration dependence of TmFeO_3 , one of the 13 new gas sensing materials reported here for the first time, are shown. The response and recovery times are important parameters for tailoring sensors for desired applications. Different propylene concentrations were applied to study the response and recovery behaviour as well as the concentration dependence of TmFeO_3 . Figure 3.70 shows that the resistance of the material increased in a non-linear relation to the propylene concentration with an obviously short response time. While concentrations as low as 5 ppm could be measured well, the resistance seemed to reach saturation at higher concentrations. The τ_{50} -value, i.e. the time needed to reach 50 % of the final signal, is 23 s, increased slightly at concentrations below 20 ppm. In comparison the response time to 40 ppm ethanol was located in the same timescale (see Figure 3.71). On and off cycles under propylene and ethanol were repeated several times without observing major changes in the response.

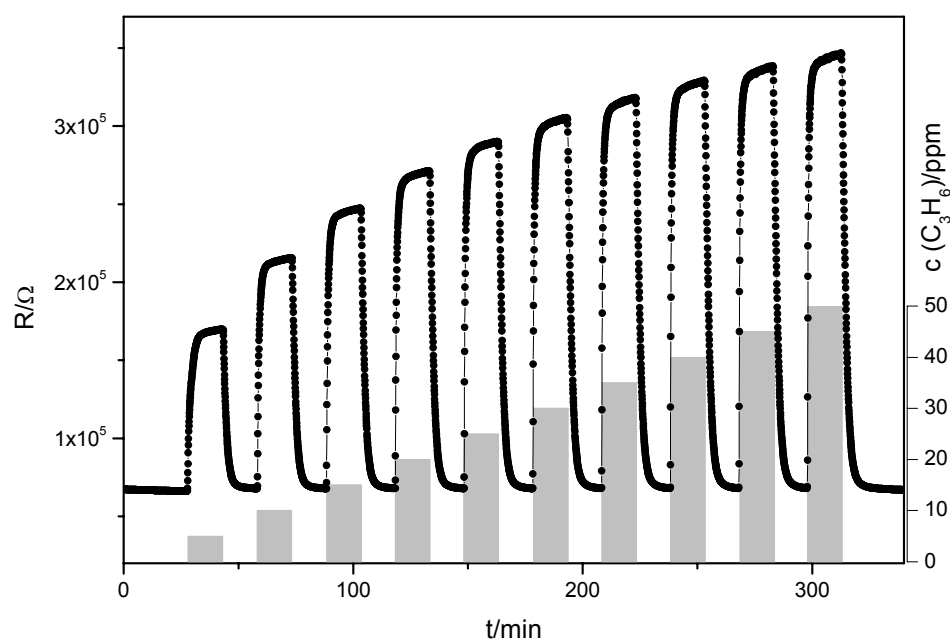


Figure 3.70: Response ability and concentration dependence (5-50 ppm) of TmFeO_3 to propylene. ($T=375^\circ\text{C}$, $f=100\text{ Hz}$, $\Delta t=15\text{ min}$)

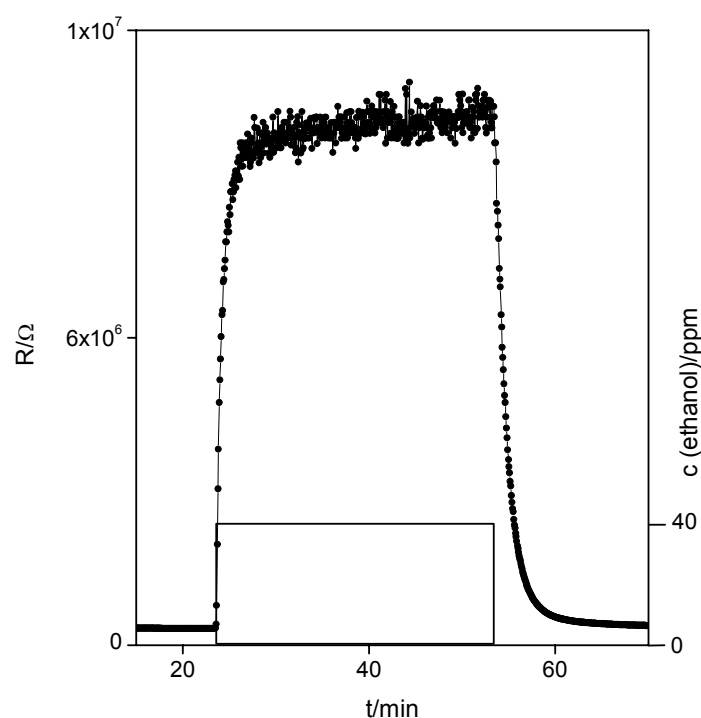


Figure 3.71: Response behaviour of TmFeO_3 to ethanol (40 ppm). ($T=325^\circ\text{C}$, $f=100\text{ Hz}$, $\Delta t=30\text{ min}$)

Response and recovery ability of all LnFeO_3 materials to 5, 10, 15 and 20 ppm of propylene and 60 ppm of ethanol are shown in Figure 3.72. The response times for 10 and 20 ppm of propylene and 60 ppm of ethanol are given in Table 3.4. Response towards ethanol was fast compared to one another, while response towards

propylene was slower. PrFeO_3 and EuFeO_3 showed the slowest response towards 10 ppm of propylene; however, equilibrium was reached during the expected time scale as seen from 3.72. LaFeO_3 as well as TbFeO_3 showed faster response than the above mentioned materials, but both recovered very slowly. ErFeO_3 showed the fastest response in all cases compared to the other materials. Obayashi et al. reported that for $\text{Ln}_{0.5}\text{Sr}_{0.5}\text{CoO}_3$ ($\text{Ln}=\text{La, Pr, Sm, Gd}$) the τ_{90} response ratio became slower as the atomic number of Ln increased, meaning as the Ln ionic radius decreased [Ob76]. In the case shown here, where all 13 materials were measured, no trends could be found. For the four elements studied by Obayashi the trend is approximately even reverse for propylene.

Table 3.4: Response times of LnFeO_3 to propylene and ethanol at 350°C.

<i>compound</i>	$\tau_{50}(10 \text{ ppm propylene})/\text{s}$	$\tau_{50}(20 \text{ ppm propylene})/\text{s}$	$\tau_{50}(60 \text{ ppm ethanol})/\text{s}$
LaFeO_3	40	24	17
PrFeO_3	67	29	<15
NdFeO_3	47	23	<15
SmFeO_3	30	19	24
EuFeO_3	61	26	26
GdFeO_3	30	16	20
TbFeO_3	47	27	25
DyFeO_3	29	23	19
HoFeO_3	20	19	<15
ErFeO_3	<15	<15	<15
TmFeO_3	26	23	<15
YbFeO_3	26	<15	<15
LuFeO_3	26	<15	<15

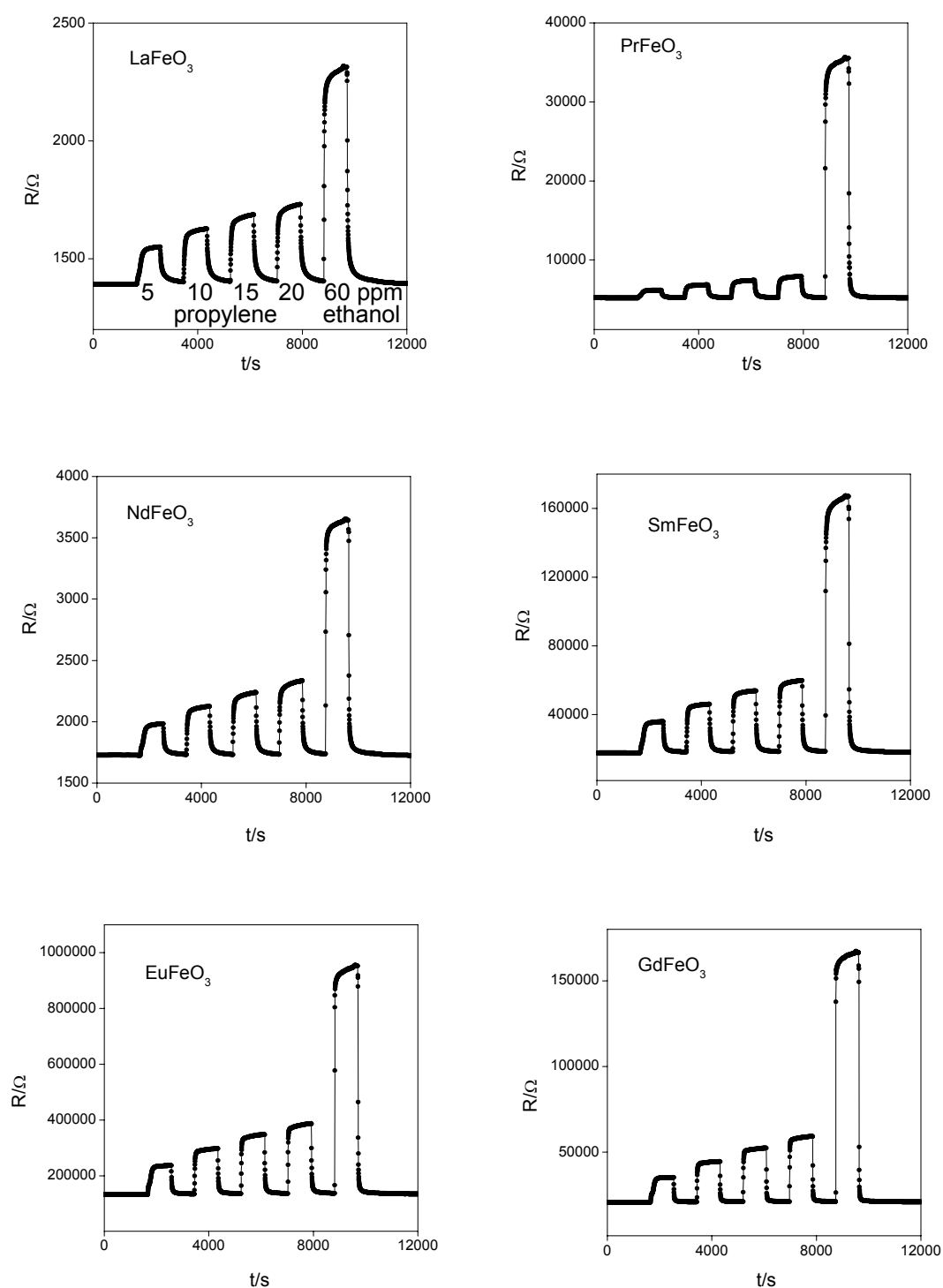


Figure 3.72a): Response and recovery ability of the prepared LnFeO_3 ($\text{Ln}=\text{La}$, Pr , Nd , Sm , Eu , and Gd) compounds. (5, 10, 15 and 20 ppm of propylene, 60 ppm of ethanol)

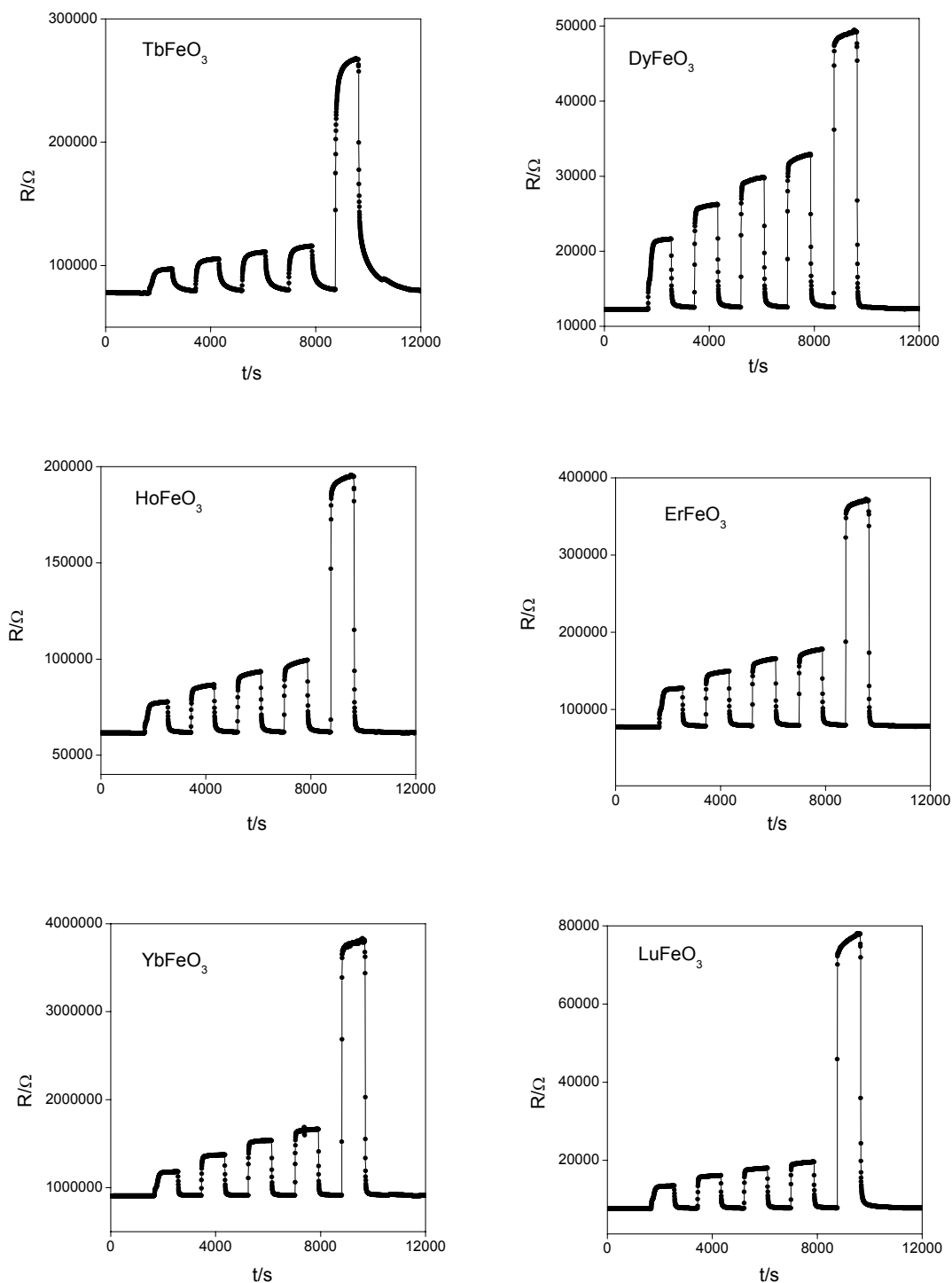
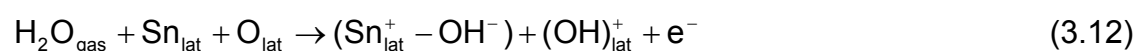


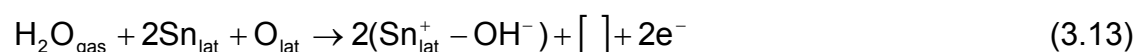
Figure 3.72b): Response and recovery ability of the prepared LnFeO₃ (Ln=Tb, Dy, Ho, Er, Yb, and Lu) compounds. (5, 10, 15 and 20 ppm of propylene, 60 ppm of ethanol)

3.3.2.2 Influence of humidity on the sensitivity of TmFeO₃

The influence of humidity on the LnFeO₃ materials was tested exemplary on TmFeO₃. In many applications, water is present as an interfering gas. The interaction of water with the semiconductor surface is of high interest. Temperature programmed desorption (TPD) and infrared (IR) studies of tin dioxide sensing layers showed that the adsorption of water vapour resulted in physisorption of hydrogen bonding of molecular water and dissociation into hydroxyl groups. Above 200°C no molecular water was present. Bârsan and Weimar reported that Heiland and Kohl assumed a homolytic dissociation of water resulting in two hydroxyl groups [Ba03]. The two mechanisms proposed are shown below.



In this step, at least two different species are formed: a hydroxylated tin ion and a protonated oxygen species. There may be an additional mechanism consuming a lattice oxygen and creating an oxygen vacancy ([]), two hydroxylated tin species and two electrons instead.



Other suggestions on the mechanisms have been made by Göpel, Henrich and Cox [He94]. However, they all observed the same macroscopic effect. In the case of the n-semiconducting SnO₂, a rise in conductivity was observed when humid air is admixed.

In the case of the p-type semiconducting TmFeO₃, an increase in resistance is observed when humid air is admixed, as shown in Figure 3.73. The sensor temperature characteristics of Figure 3.73 showed a pronounced decrease in sensor conductance from dry air to humid air (45% rh).

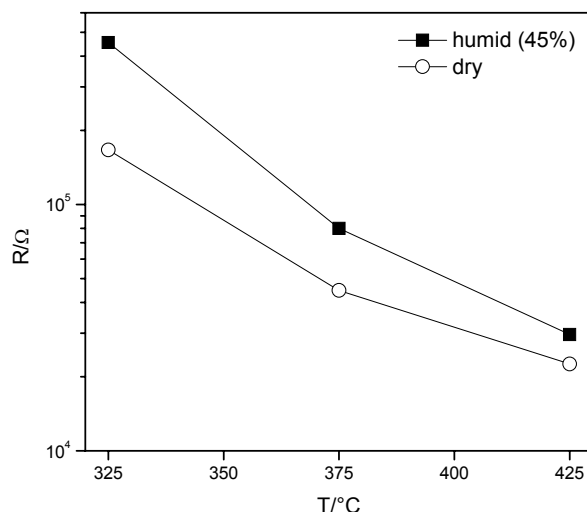


Figure 3.73: Response of TmFeO_3 to dry and humid air and 25 ppm propylene in air.

This shows that the reaction of water with the surface could be similar to the shown effect for tin dioxide. The resulting electrons from water adsorption show the opposite effect as in the case of the n-type semiconductor. Less charge carriers are present after adsorption of water.

The sensor has to work in atmospheres where both combustible gases and water vapour is present. Hence, it is desirable to know the effect of water vapour on the admixing of test gases. Figure 3.74 shows that humidity can have a remarkable effect on the response. In the case of propylene, the resistance increased in humidified air and the sensitivity was higher than in dry air. A possible explanation for this may be that the hydroxyl groups on the surface act like a reducing gas, and the reducing character of the hydrocarbons are cumulative, which results in a remarkable humidity dependence. An assumption for this is that the water molecules and the test gas molecules operate at different sites; otherwise the effect would be relatively small [Ih94]. Similar observations and explanations have been reported by Seiyama et al. for $\text{Sr}_{0.9}\text{La}_{0.1}\text{SnO}_3$ [Se83].

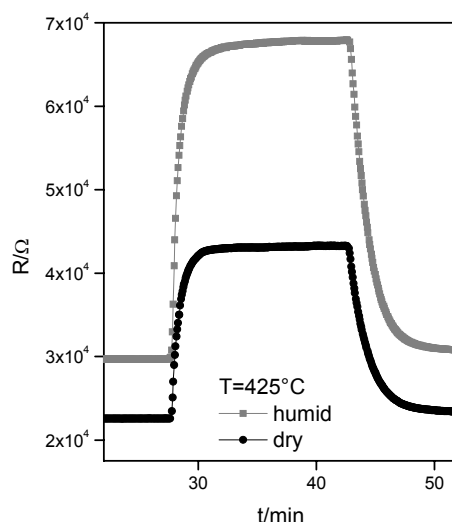


Figure 3.74: Response behaviour of TmFeO_3 to 25ppm of propylene in dry and humid air.

The opposite behaviour was found for nitrogen dioxide in humid and dry air. In this case, the sensitivity was smaller in humid air than in dry air. This effect can also be understood by adopting the assumption described above. The oxidising effect of NO_2 adsorbed on the surface competes with the reaction of water molecules. In addition, more active sites for nitrogen dioxide adsorption are present in dry air; hence the sensitivity in dry air is pronounced. Table 3.5 shows the sensitivities in dry and humid air for NO_2 and propylene at different temperatures.

Table 3.5: Sensitivites in dry and humid air.

$T/^\circ\text{C}$	test gas	concentration/ppm	S_{dry}	S_{humid}
425	C_3H_6	25	1.9	2.3
375	C_3H_6	25	3.5	4.8
325	C_3H_6	25	7.8	8.4
300	NO_2	5	6.9	2.6
300	NO_2	6	7.4	2.9

However, one has to take into account that under real sensing conditions, there is a complex mixture of air, humidity and the analyte gas. Therefore, the mechanistic picture is still incomplete and lacks applicability to real world gas sensors. Additional effects from water can also be involved in aging and unwanted signal drift effects over longer time [lh94].

3.3.3 Electrical and gas sensing properties of LnCrO_3

A plot of the logarithm of the reciprocal resistance versus the temperature (Arrhenius plot) for the LnCrO_3 compounds is shown in Figure 3.75, which indicates that the conductivity was thermally activated as was already mentioned for the previously shown materials. However, the conductivity was not simply thermally activated according to the Arrhenius-relation, as shown for LnFeO_3 . The temperature dependence of the orthochromites' resistances was lower compared to the orthoferrites. Additionally, the resistances were in the lower range of the orthoferrite resistances. The highest resistance was found for YbCrO_3 , the smallest for LaCrO_3 and PrCrO_3 . Differences in resistance occurred not only due to the difference of the lanthanide ion but also because of the variation of the microstructure in the prepared films.

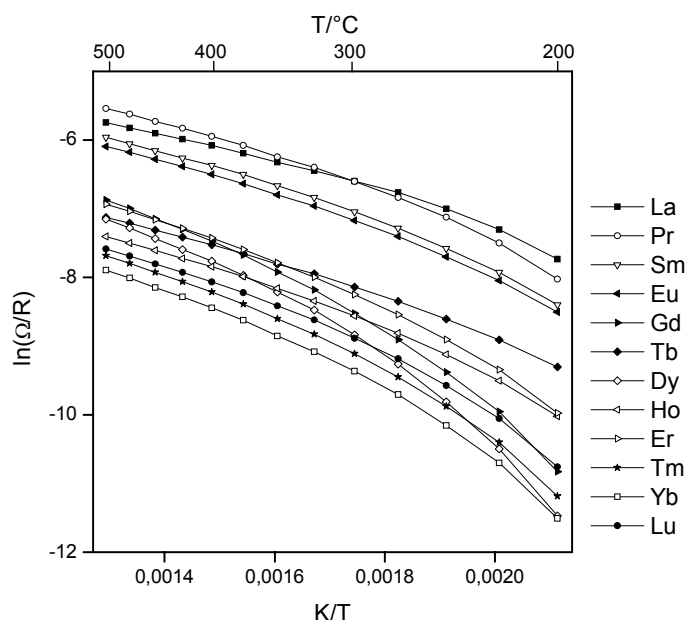


Figure 3.75: Arrhenius plot of the prepared LnCrO_3 materials under synthetic air.

Figure 3.76 shows the temperature behaviour of the sensitivity of the LnCrO_3 materials. In comparison to the LnFeO_3 materials, LnCrO_3 in general showed smaller sensitivities towards hydrocarbons and nitrogen oxides. In both material groups the sensitivity towards ethanol was much more pronounced than towards propylene. This was presumably caused by the functional OH-group of ethanol, as expected from [He00]. The temperature of maximum sensitivity was shifted to lower values. None of the materials showed cross-sensitivities towards H_2 and CO over the whole temperature range. LaCrO_3 showed the smallest sensitivity towards all gases,

whereas DyCrO_3 appeared to be the material with the highest sensitivities towards the test gases. However, the sensitivity of the LnFeO_3 materials was in all cases higher than that of the LnCrO_3 oxides.

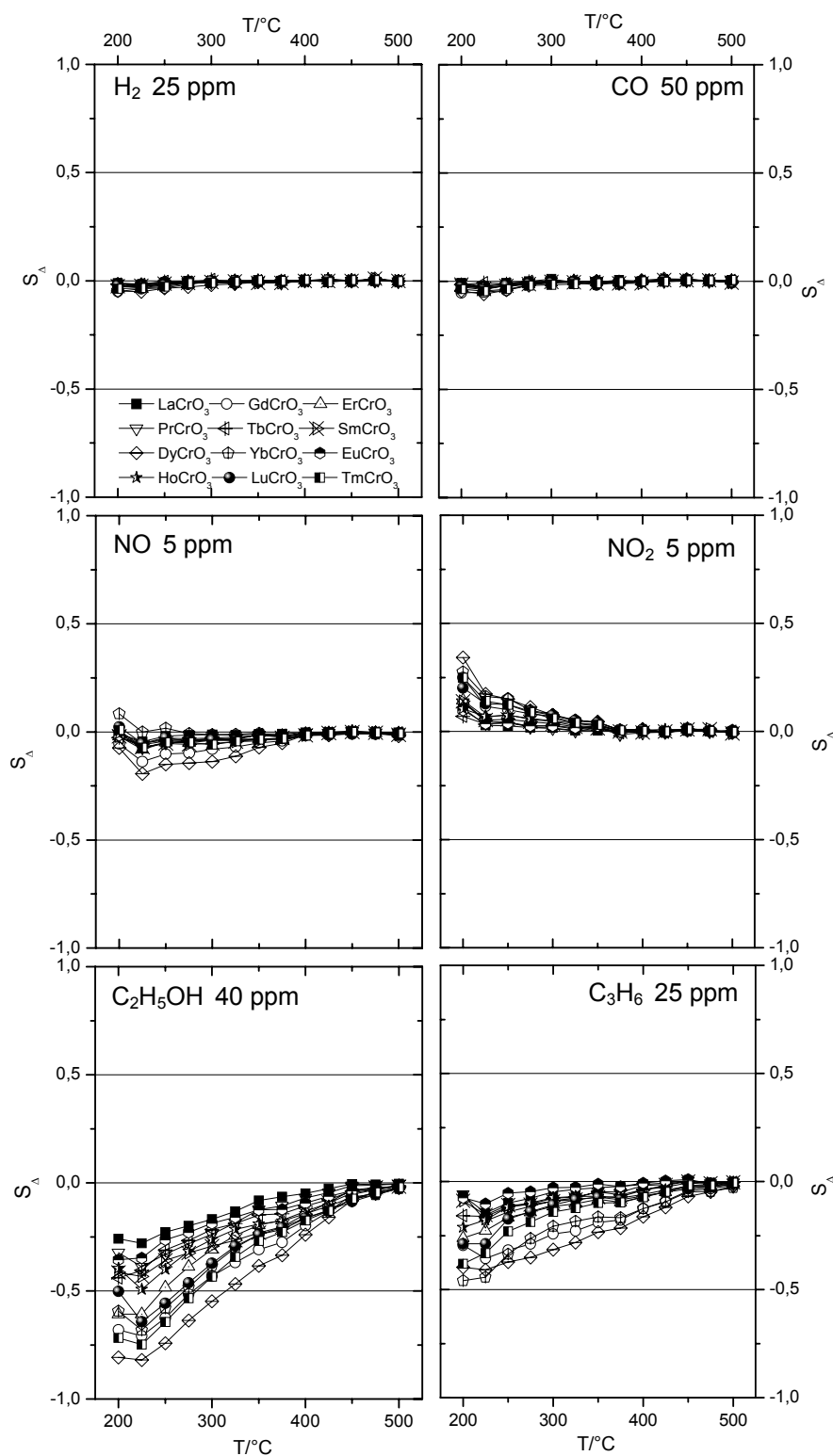


Figure 3.76. Sensitivity-temperature behaviour of the prepared LnCrO_3 materials.

3.3.4 Summary of LnMO₃-related investigations

Nanoparticles of LnMO₃ (Ln=La, Pr, Nd, Sm, Eu, Gd, Tb, Dy, Ho, Er, Tm, Yb, Lu, M=Fe, Cr) have been prepared via polyol-mediated synthesis. Single phases of perovskite-type oxides were obtained by thermal treatment. SEM revealed that after the thermal treatment materials appeared as sponge-like nanocrystalline networks. All LnFeO₃ materials showed sensitivity towards hydrocarbons and towards NO_x at lower temperatures. LaFeO₃ showed the smallest sensitivity towards all gases. SmFeO₃, TmFeO₃ and LuFeO₃ showed highest NO₂ sensitivities in the lower temperature range and highest hydrocarbon sensitivities below 450°C with almost no cross-sensitivities towards NO at 300°C. This makes these materials suitable for NO-tolerant NO₂-sensing materials. All materials showed good response and recovery properties. The LnCrO₃ oxides showed less sensitivity than the LnFeO₃ materials. DyCrO₃ was the best sensing material in this group. Its sensitivity towards ethanol was highest.

For future applications it would be possible to combine two of these shown sensors to detect NO₂ and hydrocarbons without cross-sensitivities. Combining LaFeO₃ and LuFeO₃ at a working temperature of 300°C gives a pure hydrocarbon- and NO₂/hydrocarbon-sensing material which allows differentiation between the two gases.

3.3.5 Further investigations on SmFeO_3

As mentioned before, SmFeO_3 is one of the most described materials of the lanthanide orthoferrites. It is known as sensing material for ozone [Ho05], NO_2 [To04, Tr95], CO [Ca98], volatile organic compounds, and air quality monitoring [Tr02]. However, only sparse publications on volume and surface doping of this compound can be found. Pd doping was reported by Matsushima et al. to improve the sensitivity of SmFeO_3 towards C_3H_6 [Ma00]. Volume doped $\text{Sm}_{1-x}\text{A}_x\text{Fe}_{1-y}\text{B}_y\text{O}_3$ has been prepared and published with exchange at the A-site with Sr, Bi, Ca, Y and Tb or at the B-site with Mn, Al, Cr, Co and Al. However, only $\text{SmFe}_{1-y}\text{Co}_y\text{O}_3$ ($x=0-1.0$) were shown to have ability to detect ozone and NO_2 [Ho05b], and $\text{SmFe}_{1-y}\text{Al}_y\text{O}_3$ ($x=0.00, 0.50, 0.95$) to have catalytic abilities for the combustion of CH_4 [St01]. Therefore different additives for SmFeO_3 were tested and analysed with regard to their influence on the sensing properties of the material.

3.3.5.1 Preparation of volume doped SmFeO_3

The resistance and the sensing behaviour of SmFeO_3 may be modified when a percentage of the samarium ions at the A-site or the iron ions at the B-site of SmFeO_3 are replaced by other cations, such as La, Sr, Co, Cr and Mn. In this work, different $\text{Sm}_{1-x}\text{A}_x\text{Fe}_{1-y}\text{B}_y\text{O}_3$ metal oxides were prepared by partially substituting Sm^{3+} or Fe^{3+} ions as shown schematically in Figure 3.77.

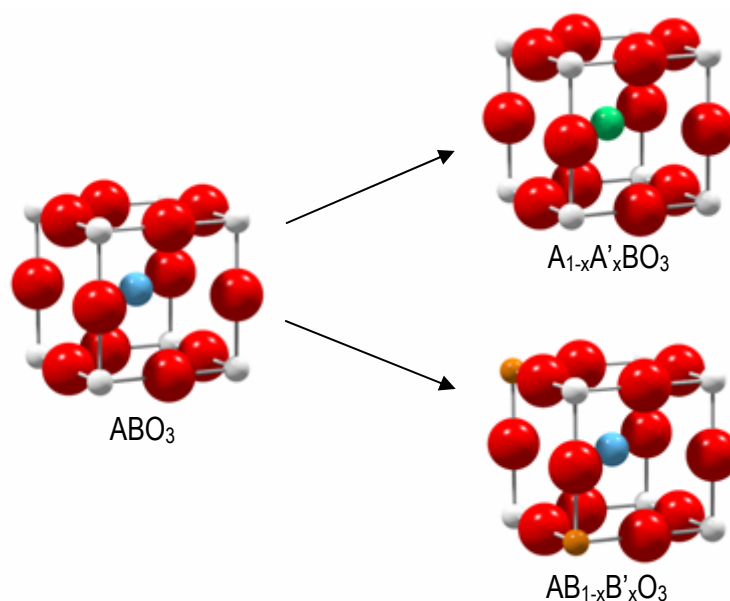


Figure 3.77: Scheme of volume doping in ABO_3 systems due to size corresponding cations.

In the case of SmFeO_3 , higher concentrations of volume dopants (10 and 20 at%) have been introduced to allow an easier characterisation of the prepared materials. This amount of material should give evidence of any by-products or changes in the lattice constants of SmFeO_3 . Different metal salts ($\text{La}(\text{NO}_3)_3 \cdot 6\text{H}_2\text{O}$, $\text{Sr}(\text{CH}_3\text{COO})_2$, $\text{Cr}(\text{NO}_3)_3 \cdot 9\text{H}_2\text{O}$, $\text{Mn}(\text{CH}_3\text{COO})_3 \cdot 2\text{H}_2\text{O}$, $\text{Co}(\text{CH}_3\text{COO})_2 \cdot 4\text{H}_2\text{O}$) have been used as volume dopants. The salts were inserted in the polyol method, described earlier. A detailed description of the synthesis can be found in the experimental data (chapter 6.1.4).

Phase identification based on X-ray diffraction results are shown in Figure 3.78 for the lanthanum and cobalt doped samples.

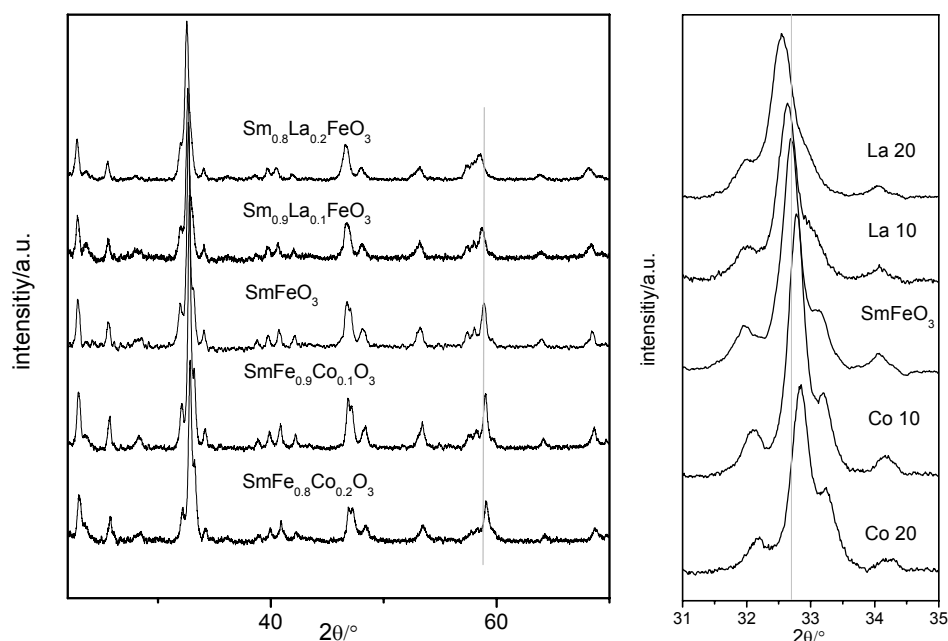


Figure 3.78: XRD pattern for undoped, lanthanum, and cobalt doped SmFeO_3 .

It was found that all doped SmFeO_3 compounds showed perovskite phase with orthorhombic structure. Because the La^{3+} ion (114 pm) is larger than the Sm^{3+} ion (100 pm), when samarium was replaced by lanthanum at the A-site, the unit cell volume became larger with increasing dopant value. The addition of Sr^{2+} (112 pm) yielded the same result. In addition, the replacement of Fe^{3+} ions (64 pm) by Cr^{3+} (63 pm) ions at the B-site influenced the lattice parameters and reduced the size of the unit cell. Also the incorporation of Co resulted in a reduced size of the unit cell, as

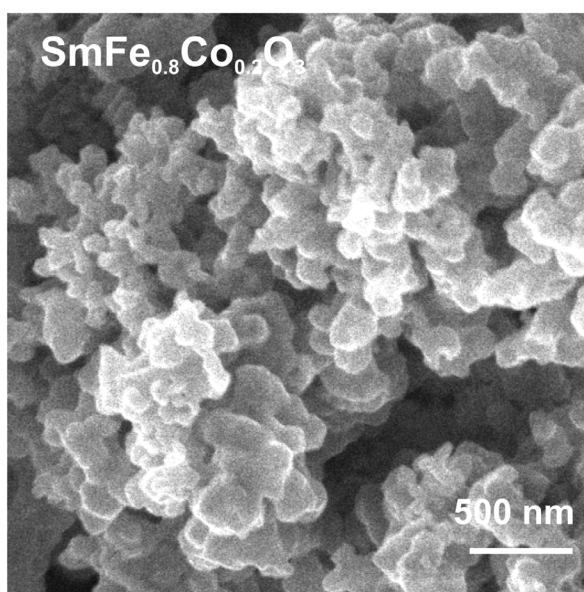
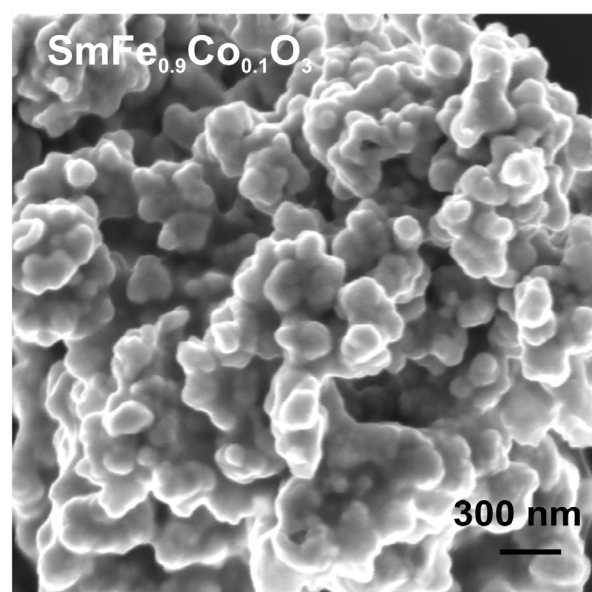
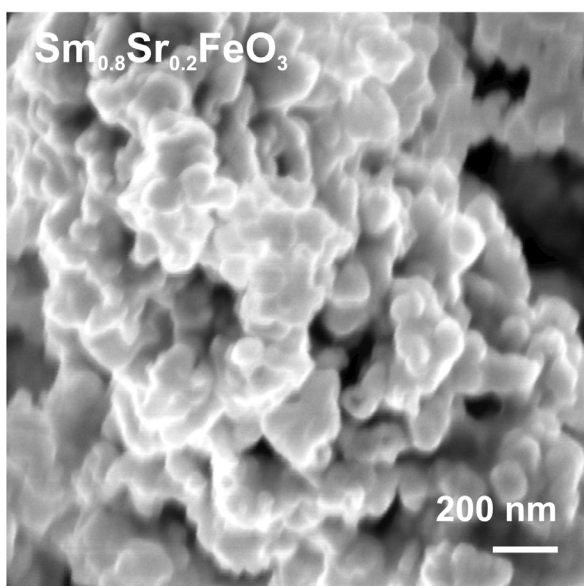
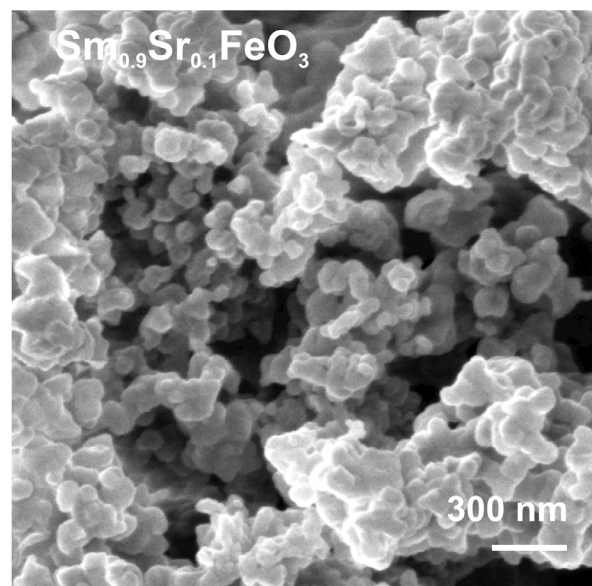
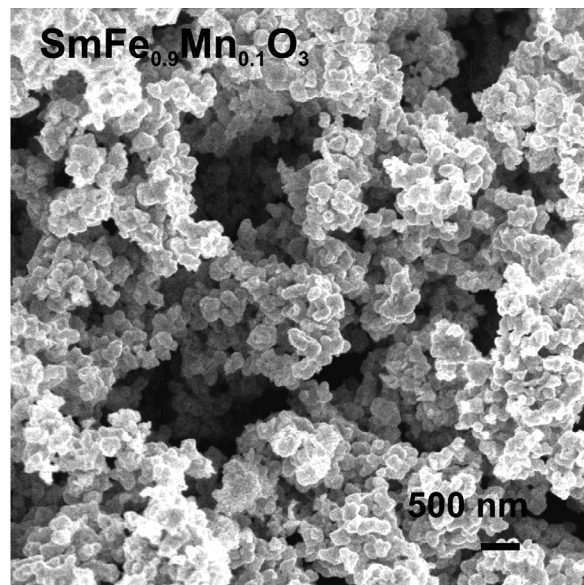
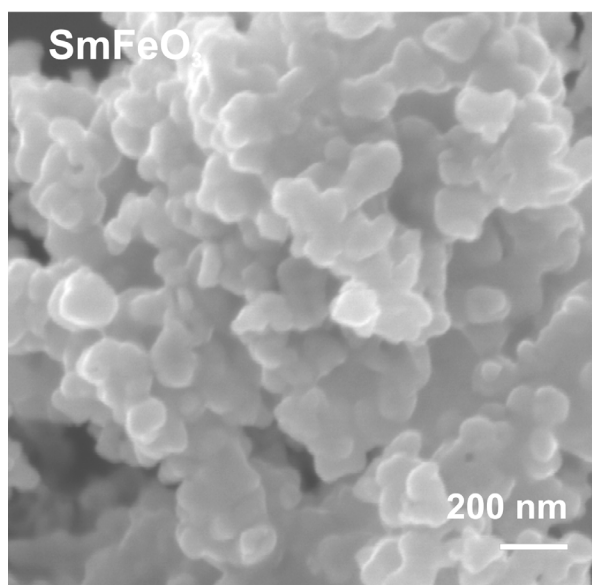
shown in Figure 3.78. While the Co^{2+} cation was inserted into the reaction, in DEG a colour change from pink to blue occurred. This may be explained by the redox potential, according to which the formation of Co^{3+} is preferred. The replacement of Fe^{3+} ions (64 pm) by Co^{3+} (63 pm) reduced the size of the unit cell, whereas an incorporation of Co^{2+} (72 pm) would have shown an increase of the unit cell volume. Negligible changes of the lattice parameters were found when Fe ions were exchanged to Mn ions. None of the prepared materials showed formation of by-products like oxides. The mean crystallite sizes (DS) were calculated from XRD peaks based on the Scherrer's equation. As shown in Table 3.6, the mean crystallite size was influenced by the replacement of samarium and iron ions.

Table 3.6: Crystallite sizes of the prepared SmFeO_3 materials

<i>dopant</i>	—	<i>La</i>	<i>La</i>	<i>Sr</i>	<i>Sr</i>	<i>Cr</i>	<i>Cr</i>	<i>Co</i>	<i>Co</i>	<i>Mn</i>
amount/at%	—	10	20	10	20	10	20	10	20	10
DS/nm	55	55	47	49	41	72	67	63	54	62

However, the SEM images gave no evidence that the volume doping restrained the growth of the particle size (see Figure 3.79). The SEM data show particles in the same size range for all undoped and doped samples. It is obvious that thermal treatment promoted aggregation of the particles. Only a few examples of non aggregated particles could be found.

The qualitative presence and homogeneous dispersion of the volume dopants was revealed by energy dispersive analysis measurements.



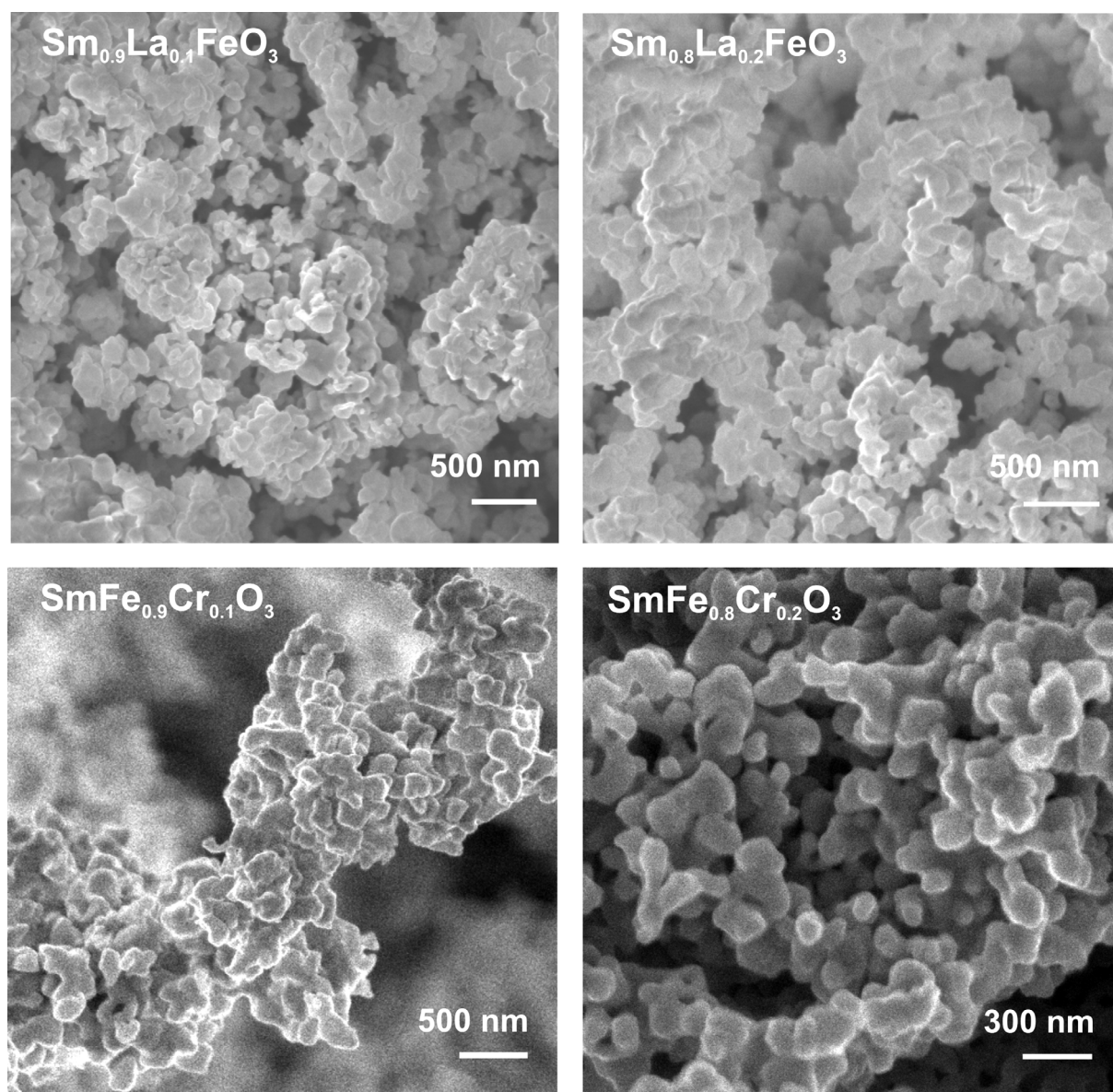


Figure 3.79: SEM images of the volume doped samples in comparison to SmFeO_3 .

The prepared materials were suitable for thick film preparation on IDC structures. A sample plate consisting of all volume doped materials and surface doped materials was prepared as described for $\text{CoTiO}_3\text{:La}$ (see p.42). Figure 3.80a) shows the allocation of the different materials on the sample plate AC2006. The prepared sample plate is shown on the photograph (see Figure 3.80b)). The applied surface doping elements were Ag (as $\text{Ag}(\text{NO}_3)$), Au (as $\text{HAuCl}_4 \cdot 3\text{H}_2\text{O}$), Ce (as $(\text{NH}_4)_2\text{Ce}(\text{NO}_3)_6$), Ir (as $\text{Ir}(\text{C}_5\text{H}_7\text{O}_2)_3$), Pd (as $\text{Pd}(\text{NO}_3)_2 \cdot 2\text{H}_2\text{O}$), Pt (as $\text{Pt}(\text{NH}_3)_4(\text{NO}_3)_2$), Rh (as $\text{Rh}(\text{NO}_3)_3 \cdot 2\text{H}_2\text{O}$), and Ru (as $\text{Ru}(\text{NO})(\text{O}_2\text{C}_2\text{H}_3)_3$), and Sb_2O_3 , WO_3 , and La_2O_3 powders. The doping elements are known to increase the sensitivity and/or selectivity of different semiconductor gas sensing material [EI04, Sh99].

The measuring procedure and test gas sequence remained as described before. Figure 3.81 shows the fingerprints for the measurements at 300°C of the SmFeO_3 sample plate (AC2006). There were two defect positions which are marked with cross-lines. The labelling in the first position shows, whether the materials are volume doped or not. The second position indicates the possible surface dopant. “ud” stands for undoped samples. Position 62, 26 and 57 which are marked with “udud” show the base material without any dopants. In the following section the three different kinds of doping (volume, surface and solid surface) are treated separately in terms of electrical and sensing properties.

	1	2	3	4	5	6	7	8
1	$\text{Sm}_{0.8}\text{Sr}_{0.2}\text{FeO}_3$	$\text{SmFe}_{0.9}\text{Mn}_{0.1}\text{O}_3$	Au@SmFeO_3	$\text{Sm}_{0.8}\text{La}_{0.2}\text{FeO}_3$	Rh@SmFeO_3	$\text{La}_2\text{O}_3@\text{SmFeO}_3$	$\text{SmFe}_{0.8}\text{Cr}_{0.2}\text{O}_3$	$\text{Sm}_{0.9}\text{Sr}_{0.1}\text{FeO}_3$
2	$\text{SmFe}_{0.9}\text{Co}_{0.1}\text{O}_3$	$\text{La}_2\text{O}_3@\text{SmFeO}_3$	$\text{SmFe}_{0.8}\text{Co}_{0.2}\text{O}_3$	$\text{Sb}_2\text{O}_3@\text{SmFeO}_3$	SmFeO_3	$\text{WO}_3@\text{SmFeO}_3$	$\text{SmFe}_{0.9}\text{Cr}_{0.1}\text{O}_3$	$\text{Sm}_{0.8}\text{La}_{0.2}\text{FeO}_3$
3	$\text{SmFe}_{0.9}\text{Cr}_{0.1}\text{O}_3$	$\text{WO}_3@\text{SmFeO}_3$	Ir@SmFeO_3	Ag@SmFeO_3	Ce@SmFeO_3	Au@SmFeO_3	$\text{Sb}_2\text{O}_3@\text{SmFeO}_3$	Ir@SmFeO_3
4	$\text{SmFe}_{0.8}\text{Cr}_{0.2}\text{O}_3$	Ru@SmFeO_3	Rh@SmFeO_3	Pd@SmFeO_3	Pt@SmFeO_3	$\text{Sm}_{0.9}\text{La}_{0.1}\text{FeO}_3$	Ru@SmFeO_3	Ag@SmFeO_3
5	$\text{SmFe}_{0.9}\text{Mn}_{0.1}\text{O}_3$	$\text{SmFe}_{0.8}\text{Co}_{0.2}\text{O}_3$	$\text{Sm}_{0.8}\text{La}_{0.2}\text{FeO}_3$	$\text{Sm}_{0.9}\text{Sr}_{0.1}\text{FeO}_3$	$\text{Sm}_{0.8}\text{Sr}_{0.2}\text{FeO}_3$	$\text{SmFe}_{0.9}\text{Co}_{0.1}\text{O}_3$	$\text{SmFe}_{0.8}\text{Co}_{0.2}\text{O}_3$	Ce@SmFeO_3
6	Pd@SmFeO_3	SmFeO_3	$\text{SmFe}_{0.9}\text{Cr}_{0.1}\text{O}_3$	$\text{SmFe}_{0.8}\text{Cr}_{0.2}\text{O}_3$	$\text{SmFe}_{0.9}\text{Mn}_{0.1}\text{O}_3$	$\text{La}_2\text{O}_3@\text{SmFeO}_3$	$\text{WO}_3@\text{SmFeO}_3$	Pt@SmFeO_3
7	$\text{Sm}_{0.9}\text{La}_{0.1}\text{FeO}_3$	Au@SmFeO_3	$\text{WO}_3@\text{SmFeO}_3$	$\text{Sb}_2\text{O}_3@\text{SmFeO}_3$	SmFeO_3	Ru@SmFeO_3	Ir@SmFeO_3	Rh@SmFeO_3
8	Pt@SmFeO_3	Ce@SmFeO_3	$\text{Sm}_{0.8}\text{Sr}_{0.2}\text{FeO}_3$	$\text{SmFe}_{0.9}\text{Co}_{0.1}\text{O}_3$	$\text{Sm}_{0.9}\text{La}_{0.1}\text{FeO}_3$	$\text{Sm}_{0.9}\text{Sr}_{0.1}\text{FeO}_3$	Ag@SmFeO_3	Pd@SmFeO_3

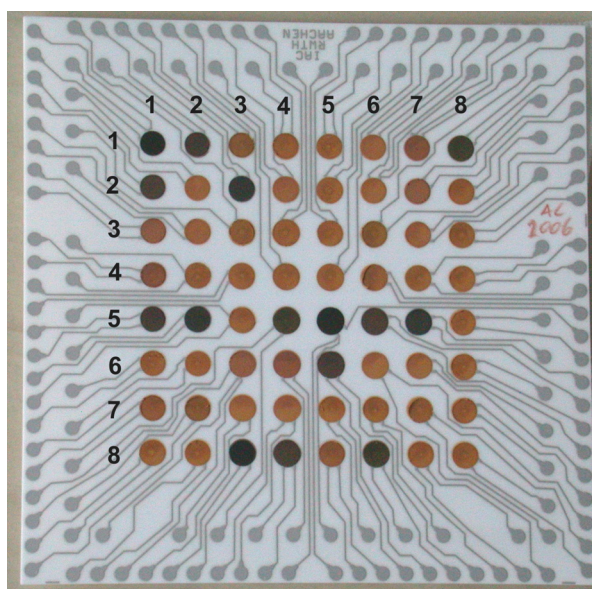


Figure 3.80: Sample plate with different doped SmFeO_3 compounds (AC2006).

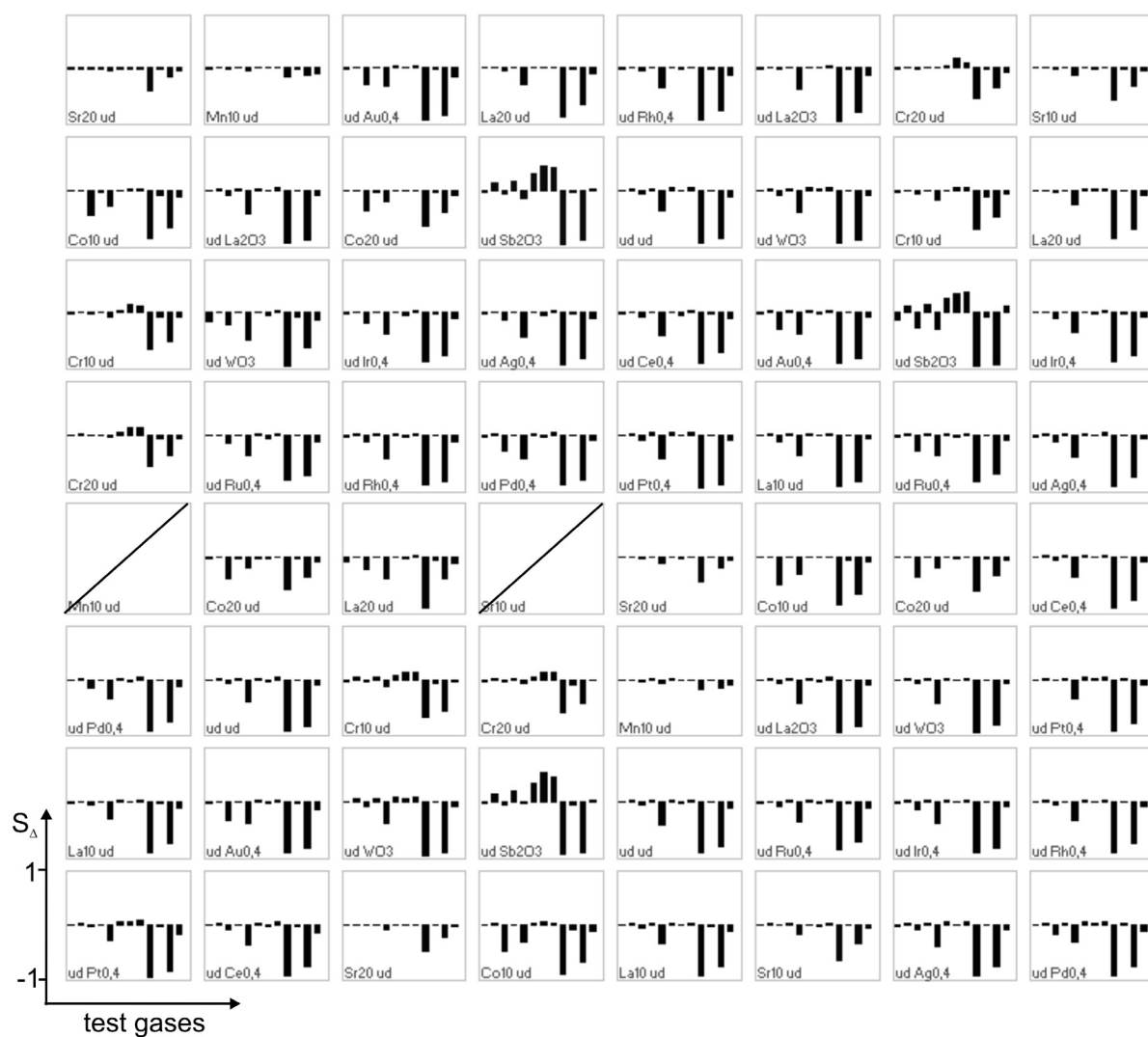


Figure 3.81: Fingerprint of the sample plate (AC2006) at $T=300^{\circ}\text{C}$. ud=undoped, first index indicates volume dopant (at%), second index indicates the surface dopant (at%). Sb_2O_3 , WO_3 , and La_2O_3 were added with 1at%.

3.3.5.2 Electrical and sensing properties of volume doped SmFeO_3

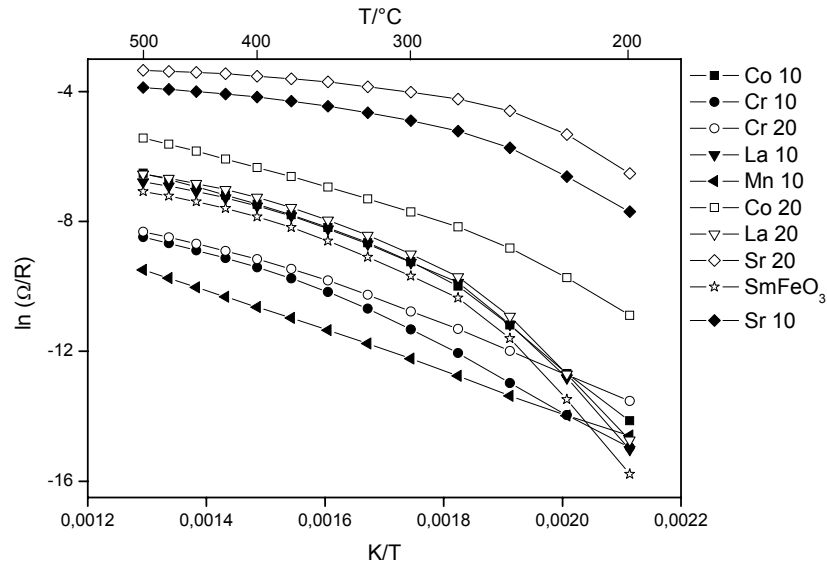


Figure 3.82: Temperature dependence of the resistance of volume doped materials.

The conductance of all volume doped sensors samples increased with increasing temperature in the whole temperature range, which is an intrinsic characteristic of semiconductors. It is obvious from Figure 3.82 that the volume doping enormously influenced the conductivity of the samples. Sr^{2+} doping enhanced the conductivity of the base material most. For SmFeO_3 , its charge carriers are holes, which are produced by the ionisation of the Sm^{3+} cation vacancy defect. When Sm^{3+} is replaced by Sr^{2+} , the carrier concentration will depend on the holes produced by the ionisation of Sr-point defects, which emerge when Sr^{2+} occupies the sites of Sm^{3+} in the crystal. As a result, the hole concentration increased which resulted in a considerably higher conductivity of Sr-doped SmFeO_3 than that of SmFeO_3 . In addition, an influence on the amount of volume dopant could be observed. In the case of lanthanum and chromium, two cations have been replaced that had the same oxidation state. In this case the change in resistance could be understood by taking the ion's radius and formation of new defects into account. However, it remains unclear why the material with the lower content of chromium showed a higher resistance. This may be explained by a change in microstructure and film formation. The highest resistance was found for the manganese doped sample in the temperature range between 500 and 225°C. However, the temperature dependence was not as strong for Mn as for the other samples. The activation energies for these samples were difficult to

calculate from the Arrhenius plot of the resistance because the samples, with the exception of $\text{SmFe}_{0.9}\text{Mn}_{0.1}\text{O}_3$, showed no simply thermally activated conductivity. For the manganese doped sample, the activation energy was calculated as 0.54 eV (see Figure 3.83). The figure also shows good reproducibility across different sample positions.

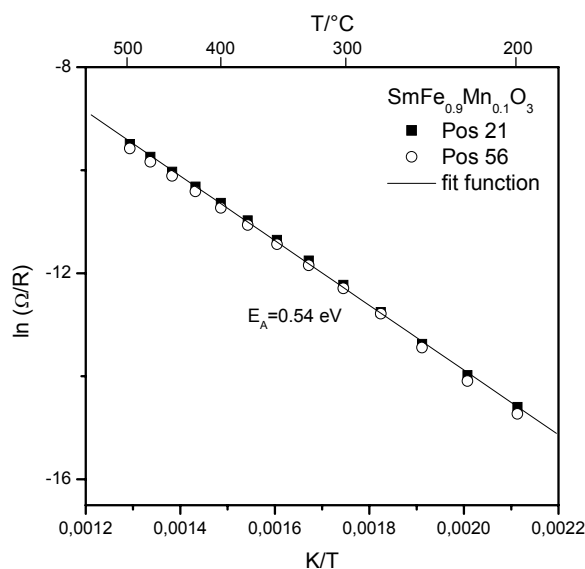


Figure 3.83: Arrhenius plot of $\text{SmFe}_{0.9}\text{Mn}_{0.1}\text{O}_3$ at two different sample plate positions.

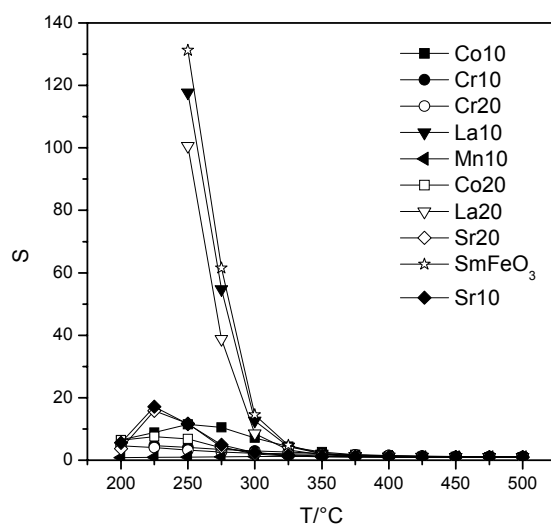


Figure 3.84: Sensitivity to ethanol (40 ppm).

The resistance of the samples increased when they were exposed to a reducing gas atmosphere, indicating that the p-type characteristics remain even after doping.

The effect of the different dopants on the gas sensitivity of SmFeO_3 was studied. Figure 3.84 shows the relationship between the operating temperature and the sensitivity of the sensors with different volume dopants to 40 ppm ethanol. All samples were practically insensitive to the applied test gases at temperatures close to 400°C . Maximum sensitivity was achieved for the undoped material at an operating temperature of 250°C . In contrast to the previously shown CoTiO_3 compounds, volume doping of SmFeO_3 , did not enhance sensitivity towards ethanol. However, the Sr-doped sample showed slightly higher sensitivities at lower temperatures (225°C). The manganese doped sample showed no sensitivity at all. In addition, the sensitivity decreased with increasing amount of volume dopant, and as shown for CoTiO_3 , the volume dopants were able to shift the temperature of maximum sensitivity. The lanthanum doped sample showed the highest sensitivity of the volume doped samples.

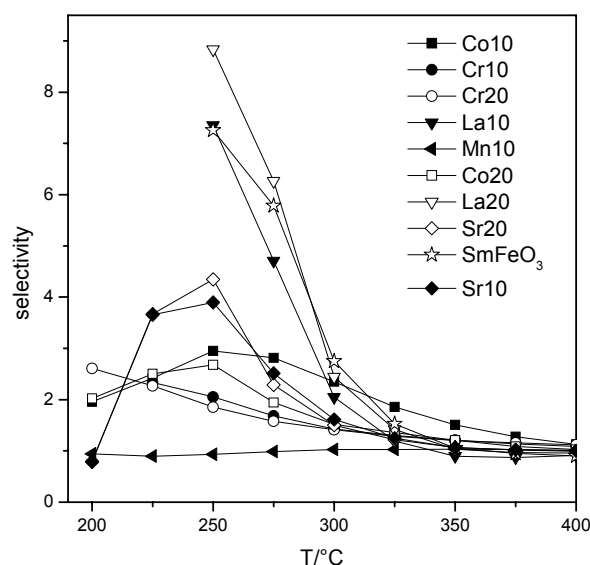


Figure 3.85: Selectivity of the volume doped materials towards ethanol.

Figure 3.85 depicts the selectivity of the volume doped materials to ethanol in comparison to propylene over the measured temperature range. The highest selectivity was seen for lanthanum doped and undoped samples in a temperature range between 300 and 250°C . Above 300°C the cobalt doped sample showed the highest selectivity, but even this was relatively low compared to the undoped material. The manganese doped sample showed no selectivity, which correlated to the negligible sensitivity of the material.

The regarded volume doped samples showed comparable sensitivities towards the other test gases as the undoped samples except for cobalt doped SmFeO_3 . This material showed high sensitivity towards carbon monoxide, as shown in Figure 3.86. In both cases of volume doping, the CO sensitivity was higher than the sensitivity towards NO_x . The sensitivity towards hydrocarbons was less pronounced than in the base material. $\text{SmFe}_{0.9}\text{Co}_{0.1}\text{O}_3$ showed good sensitivity towards NO_2 while $\text{SmFe}_{0.8}\text{Co}_{0.2}\text{O}_3$ showed almost none. In the literature, various examples can be found that describe the enhancement of CO sensitivity by doping with cobalt. Different doping methods (volume doping [So05b], impregnation, ball milling, sputtering [Le01]) are referred to, all of which enhanced the CO oxidation activity of the base material. For example, Song et al. showed that volume doping of $\text{La}_{0.8}\text{Pb}_{0.2}\text{FeO}_3$, which is a comparable system to the here used base material, with 20 at% Co on the B-site, increased the CO gas-sensing properties of the material [So05b]. Malavasi et al. proposed a model for the sensing mechanism of Co-containing perovskites with CO which included adsorbed oxygen on the surface. Malvasi suggested that some of the oxygen involved in the gas-solid equilibria are adsorbed as O^- species. The charge balance requires the oxidation of cobalt ions to shift from Co^{2+} to Co^{3+} . When CO is adsorbed on O^- and is oxidised to CO_2 , one electron is released back to the solid and the electrical conductivity is reduced [Ma04].



In addition, regarding different SmMO_3 ($\text{M}=\text{Co}, \text{Mn}, \text{Fe}, \text{Cr}$) compounds, SmCoO_3 was found to have the highest catalytic activity for CO oxidation [Zh91].

Sensing carbon monoxide is critically important for safety control in gas appliances because incomplete combustion of gases can cause serious CO poisoning. The material presented here could be used as a CO sensing material without the use of noble metal additives.

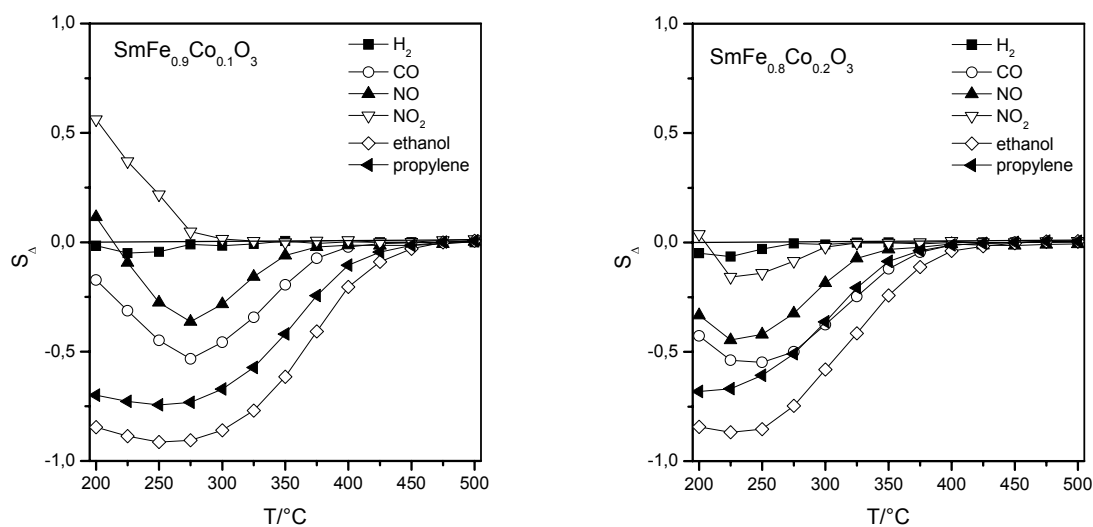


Figure 3.86: Relative sensitivity of the cobalt doped SmFeO_3 -samples.

Furthermore, response and recovery times were measured at 325°C for SmFeO_3 -based sensing layers to different gases as shown in Figure 3.87-3.91. Figure 3.87 shows the response and recovery behaviour of $\text{SmFe}_{0.9}\text{Co}_{0.1}\text{O}_3$. In this case, 15 to 50 ppm of carbon monoxide has been admixed. The material showed a fast response towards CO, and saturation was achieved in the regarded timescale. In addition step-wise concentration increases and decreases towards CO were measured at 325°C (Figure 3.88). The concentration was changed from 5 to 50 ppm CO. $\text{SmFe}_{0.8}\text{Co}_{0.2}\text{O}_3$ showed good response times even with small concentrations of CO. The stepwise concentration changes showed that the response values were reproducible.

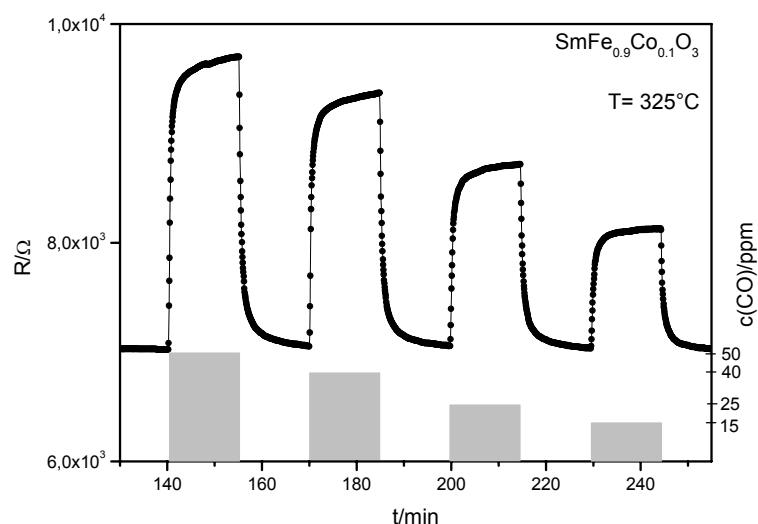


Figure 3.87: Response and recovery times for $\text{SmFe}_{0.9}\text{Co}_{0.1}\text{O}_3$ to CO (15, 25, 40 and 50 ppm).

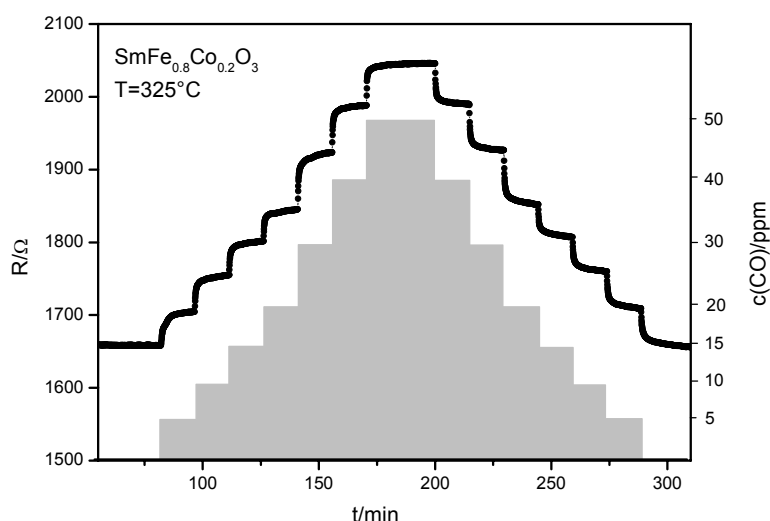


Figure 3.88: Response and recovery times for $\text{SmFe}_{0.8}\text{Co}_{0.2}\text{O}_3$ to different CO concentrations.

Figure 3.89 shows response and recovery times for SmFeO_3 to NO (5ppm), propylene (20, 40 ppm), and ethanol (40, 60 ppm). The undoped sample showed a faster response towards ethanol than towards propylene. Only a small response was observed to NO at this temperature. La-doped SmFeO_3 exhibited slightly slower response and recovery times than SmFeO_3 . However, the material fully recovered in the regarded time scale (see Figure 3.90). In addition, its selectivity towards ethanol was enhanced.

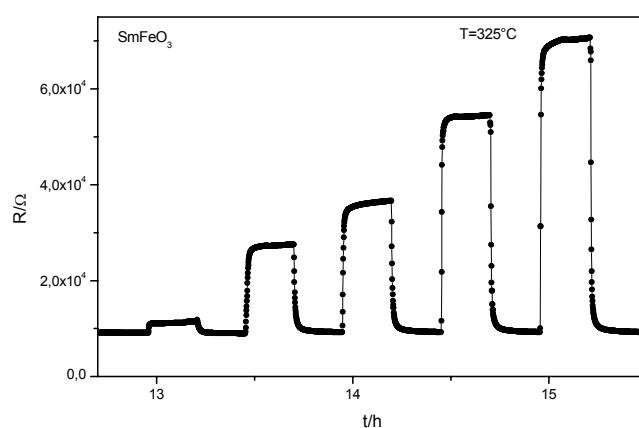


Figure 3.89: Response and recovery times for SmFeO_3 to NO (5ppm), propylene (20, 40 ppm), and ethanol (40, 60 ppm).

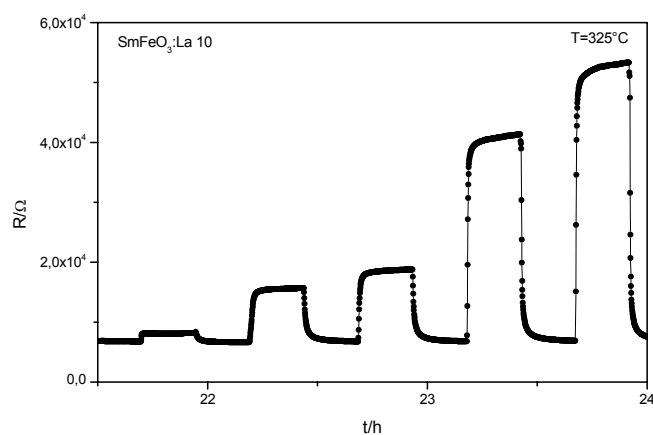


Figure 3.90: Response and recovery times for $\text{Sm}_{0.9}\text{La}_{0.1}\text{FeO}_3$ to NO (5ppm), propylene (20, 40 ppm), and ethanol (40, 60 ppm).

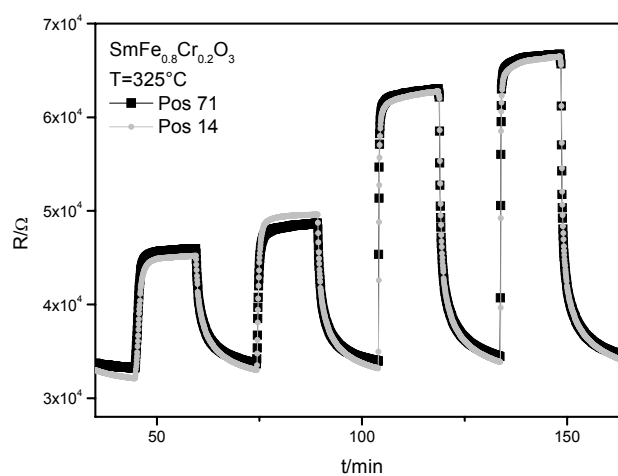


Figure 3.91: Response and recovery times for $\text{SmFe}_{0.9}\text{Cr}_{0.1}\text{O}_3$ to propylene (20, 40 ppm), and ethanol (40, 60 ppm).

In contrast, the chromium doped sample showed poor recovery behaviour towards the admixed gases and its response time to propylene was much slower (see Figure 3.91). Measurements at different positions deposited with the same material verified the effect.

The effect of the volume dopant on the response and recovery ability was also reported in other systems [So05, Ch99b]; however, its origin remains unclear at the moment. It was observed that materials with high sensitivity also showed fast response ability.

3.3.5.3 Electrical and sensing properties of surface doped SmFeO_3

Figure 3.92 shows the Arrhenius plot of SmFeO_3 and surface doped SmFeO_3 materials. The resistance of the surface doped materials did not change much in comparison to the undoped materials. As known from the literature, the amount of dopant must be high enough and the doping clusters must be a few nanometers in size to affect the resistance [Ar01]. A remarkable increase in resistance and stronger temperature dependence was found for Pt@SmFeO_3 . This could be a result of several factors. On the one hand, the Pt-particles could be placed into defect positions, which heals the surface and decreases the number of free charge carriers. On the other hand, the Pt-particles on the metal oxide surface could release electrons into the material lowering the conductance of the doped material. Sanders observed a lowering of the oxygen surface coverage by doping with Rh resulting in a decreased conductivity of the base material [Sa04]. However, this case is non-applicable here since publications report on higher oxygen surface coverage due to Pt addition [Sa85].

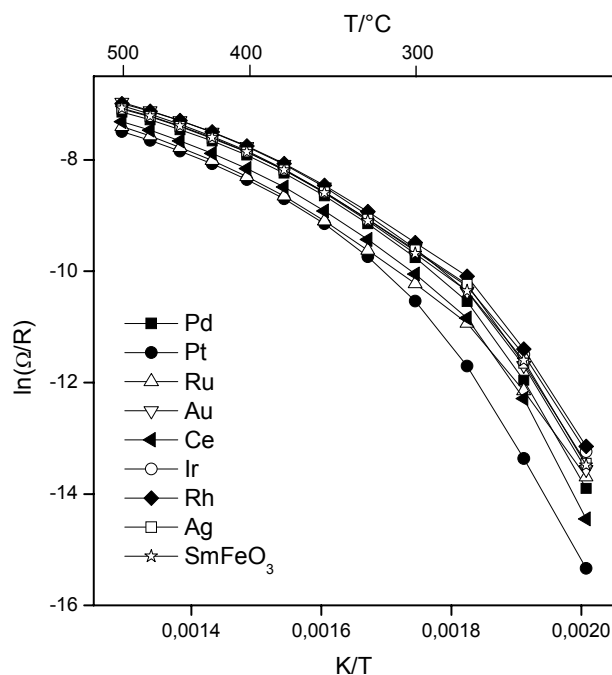


Figure 3.92: Arrhenius plot of the surface doped materials.

The effect of different dopants on the gas sensitivity of SmFeO_3 was studied. Figure 3.93 depicts the relative sensitivity of the different surface doped materials towards the test gases over the temperature range. In most of the cases no major changes in the sensitivity were observed. All materials responded to hydrocarbons and NO_x . The response towards CO was influenced by the surface dopants. The gold doped sample showed a pronounced sensitivity towards carbon monoxide. Comparable to the case of $\text{CoTiO}_3\text{:La}$, the Au-doped materials were suitable CO sensing materials. Another interesting material was the Pt-doped sample. In this case, the material was highly sensitive towards hydrocarbons even at higher temperatures, and cross-sensitivity to other test gases was reduced compared to the undoped material.

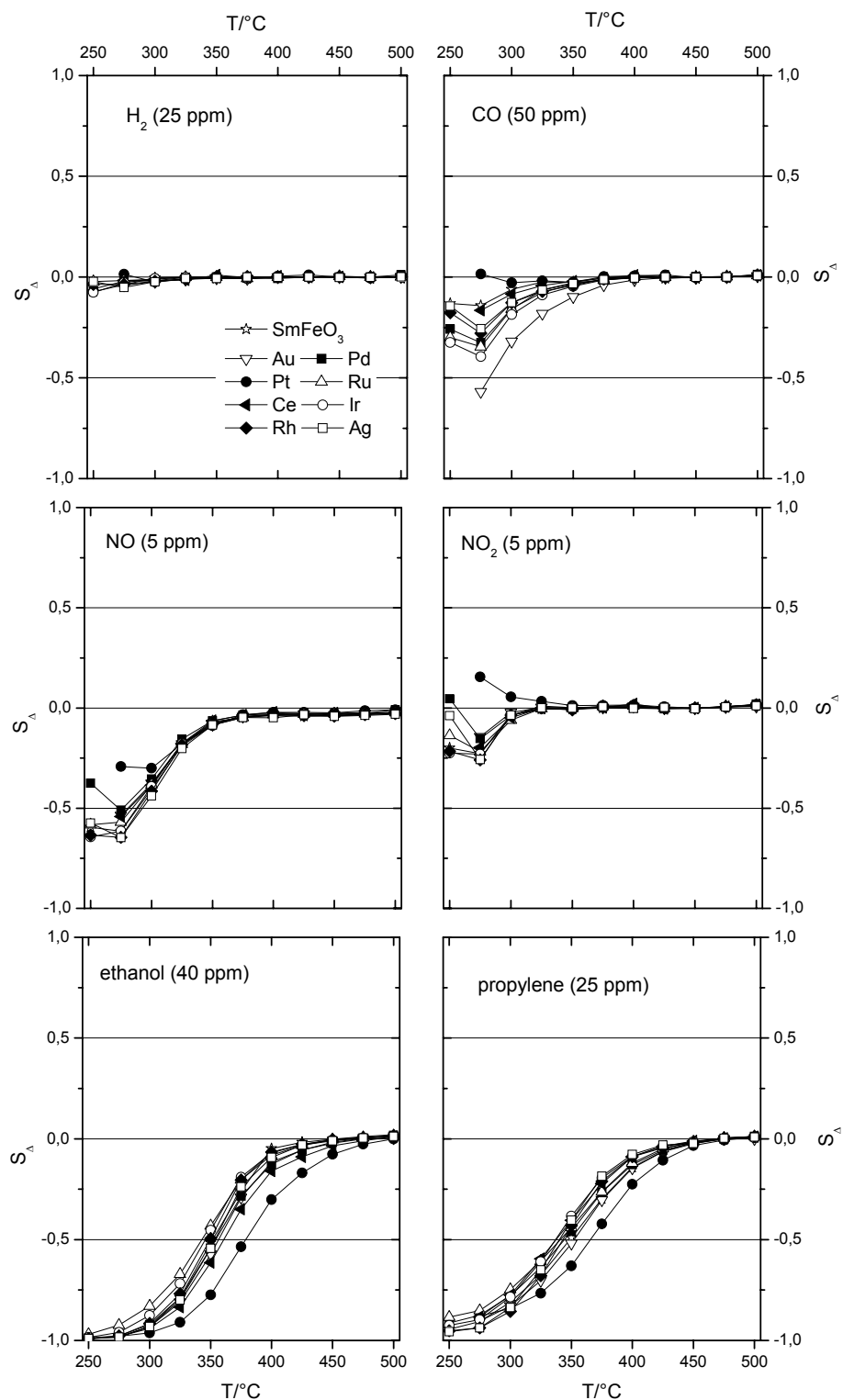


Figure 3.93 Relative sensitivity of the surface doped samples towards the test gases.

Figure 3.94 shows the relationship between the operating temperature and the absolute sensitivity of the sensors towards 40 ppm ethanol. Below 400°C no remarkable sensitivity could be observed. Between 350°C and 300°C the platinum

doped sample showed the highest sensitivity. However, below that temperature the undoped material and the gold doped sample showed highest response to ethanol. For platinum, the value at 250°C reached the measurement limits, so no sensitivity data could be obtained. The ethanol measurements showed that surface dopants were able to enhance the sensitivity of the regarded base material. However, there were also dopants like ruthenium which depressed the sensitivity the same way the volume dopants did.

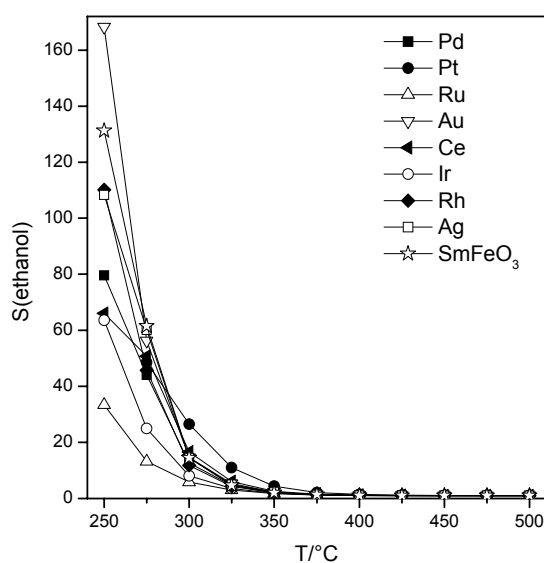


Figure 3.94: Sensitivity to ethanol (40 ppm).

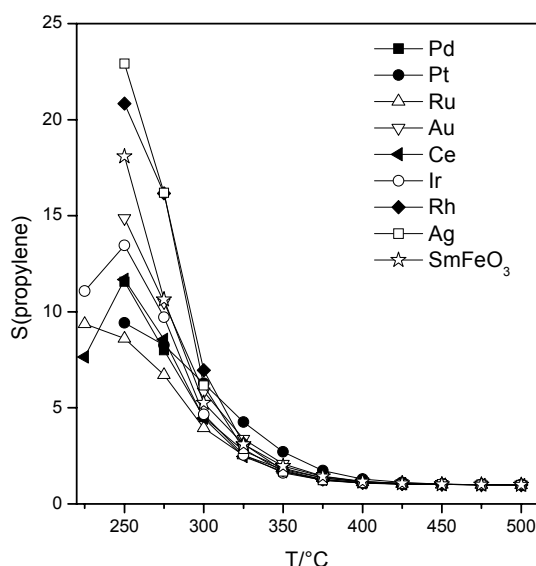


Figure 3.95: Sensitivity to propylene (25 ppm).

The sensitivity to propylene is shown in Figure 3.95. The overall sensitivity was much lower than that to ethanol. As seen before, no sensitivity below 400°C occurred. Between 350°C and 300°C, the platinum doped material again showed the highest sensitivity. Below 300°C, silver and rhodium doped SmFeO_3 showed the highest sensitivity in contrast to their low sensitivity to ethanol. This resulted in a change of selectivity towards ethanol due to surface doping. The selectivity to ethanol in comparison to propylene of the surface doped samples is shown in Figure 3.96. Between 300 and 350°C, Pt@SmFeO_3 showed the highest selectivity. Below 275°C, the gold doped sample reached the highest selectivity. The undoped material was located in the mid values. Ruthenium and iridium doped samples exhibited the lowest selectivity over the shown temperature range. Considering gold doped SmFeO_3 as the most selective and sensitive material towards ethanol one has to take into account that its cross-sensitivity towards CO and NO_2 was increased.

Addition of doping elements to the surface modifies the equilibrium state and/or velocity of the surface reactions. Au and Pt are known as catalytically active materials and have been confirmed to possess promoting effects on many semiconductor gas sensors. The doping element supports the catalytic conversion of the reducing gas into its oxidation products. As mentioned for Au and Pd, this may be caused by spill-over of activated fragments to the semiconductor surface to react with the adsorbed oxygen. This model describes the increased sensitivity of the Au-doped materials towards CO. The reaction towards hydrocarbons originated from the metal oxide in addition to the reaction on the supporting dopant. Depending on the temperature, the doped materials showed higher sensitivities towards hydrocarbons. The Pt-dopant seemed to suppress the sensitivity to other reducing test gases. This may be caused by a fast oxidation of these gases on the Pt surface without a change in resistivity of the base material. This was also proposed for CO on Pt@ZnO by Saito [Sa85].

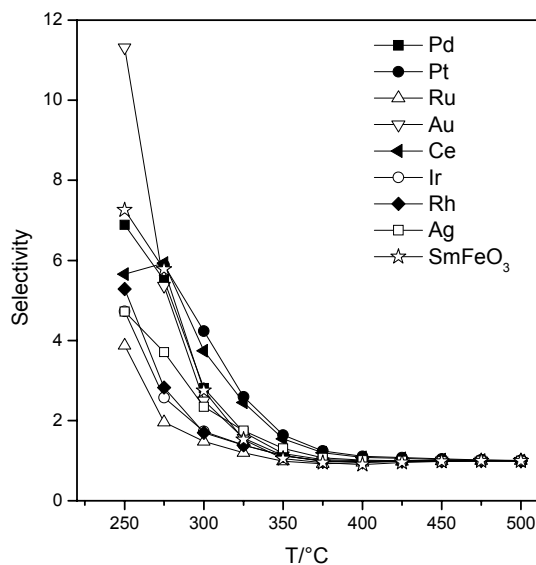


Figure 3.96: Selectivity to ethanol in comparison to propylene.

Furthermore, response and recovery times were measured at 325°C and 250°C for surface doped SmFeO₃-sensing layers to different gases as shown in Figure 3.97. In contrast to the changes observed due to volume doping and as reported in literature for Pt-doped BaSnO₃ [Re99], no changes in the response and recovery behaviour of the doped SmFeO₃ were observed in the here considered time scale. As expected, at 325°C, the platinum doped sample showed highest response to ethanol, while at 250°C, the gold doped sample showed improved sensitivity compared to the undoped SmFeO₃. However, at 250°C, the response and recovery ability was much slower than at higher temperatures. Because of the slower processes equilibrium states were not reached in the considered time-scale, as shown in Figure 3.98.

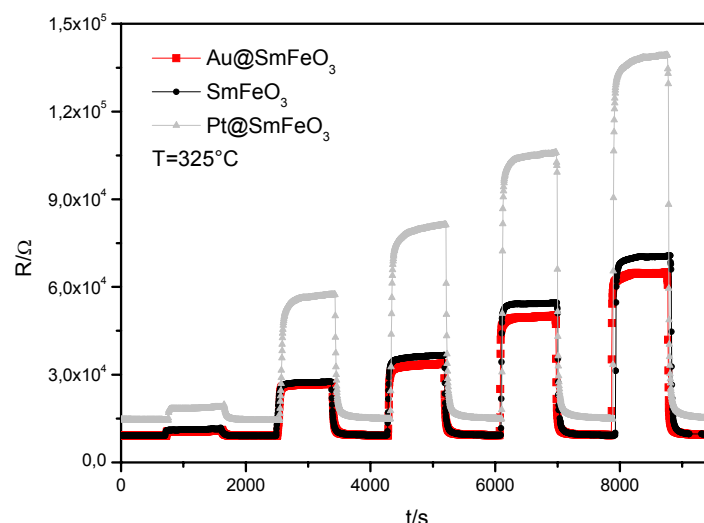


Figure 3.97: Response and recovery behaviour of Au@SmFeO₃, Pt@SmFeO₃ and SmFeO₃ to NO (5ppm), propylene (20, 40 ppm), and ethanol (40, 60 ppm).

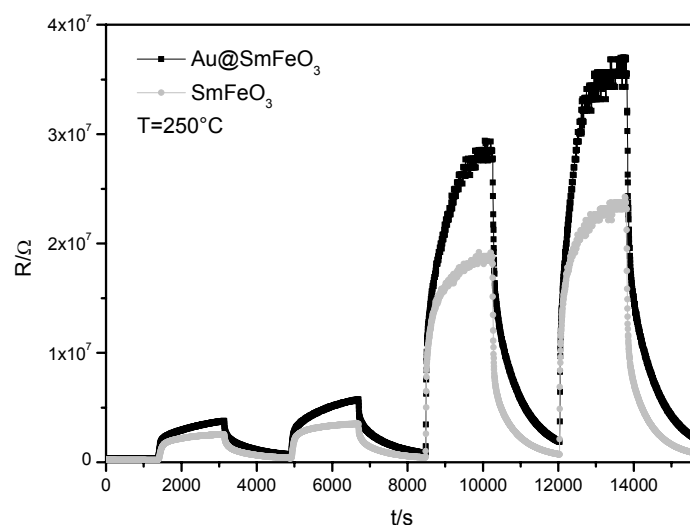


Figure 3.98: Response and recovery behaviour of Au@SmFeO₃ and SmFeO₃ to propylene (20, 40 ppm), and ethanol (40, 60 ppm).

3.3.5.4 Electrical and sensing properties of solid surface doped SmFeO₃

Also in the case of SmFeO₃ the question occurs, whether solid surface dopants influence the base material in comparison to metal surface dopants. In contrast to CoTiO₃:La tungsten oxide, antimony oxide, and lanthanum oxide were used as promising surface dopants. All three materials are known to be gas sensing materials or additives for sensing layers. Lanthanum oxide is an insulator with a band gap of 5.5 eV in a stable oxidation state. La₂O₃ was reported to enhance the sensitivity of

SnO_2 and In_2O_3 thick films towards e.g. ethanol, and CO_2 [Ya91, Pa93]. Sb_2O_3 , a semiconductor with a band gap of 3.3 eV and a variable oxidation state, was used as additive on different sensing layers like Fe_2O_3 , ZnO , TiO_2 and SnO_2 to improve the sensitivity to reducing gases [Zh04, Ti00]. WO_3 , with a band gap of 2.6 eV, is the best (almost metallic) conductor of the three and owns variable oxidation states. It is an interesting material in the field of resistive gas sensors for the detection of e.g. NO_2 , ozone or ammonia [La05, Li02]. The solid powders of dopant and base material (1 at% doping concentration) were ground in a mortar and redispersed in a polyethylene imine/water solution. Thick films were prepared as described previously.

Figure 3.99 shows the temperature dependence of the resistance of the solid surface doped materials. All dopants increased the resistance of the base material. Also as in the case of $\text{CoTiO}_3\text{:La}$, the influence of the solid surface dopants was more pronounced than for the metal dopants. The highest resistance was seen for antimony oxide. Lanthanum oxide gave only a small change to the resistance; however, it was higher than for the volume doped lanthanum samples (see Figure 3.82). This indicated that the surface dopant did not act in the same way as the volume dopant. As already seen in many other cases, no linear Arrhenius-like behaviour was found in this temperature range. The conductivity was not simply thermally activated as was also seen for the other SmFeO_3 samples.

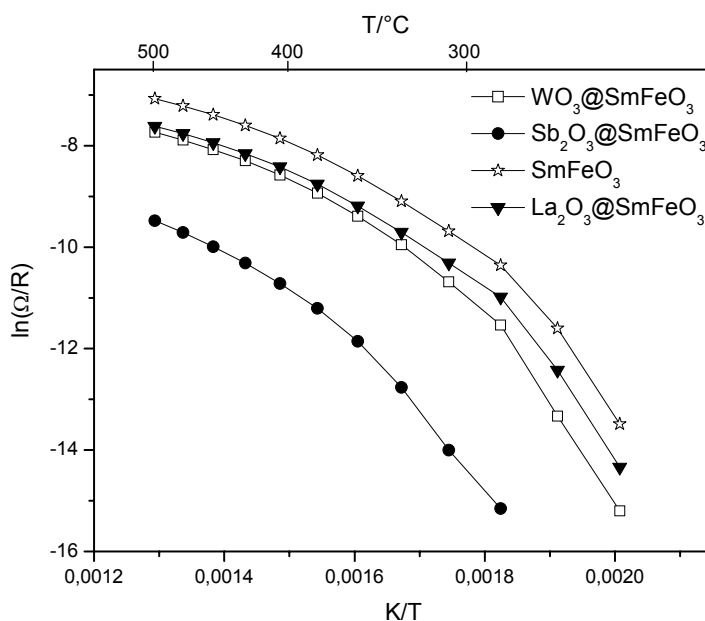


Figure 3.99: Arrhenius plot of the solid surface doped samples.

The increase of the resistance might be caused by different effects. On the one hand a partial substitution of Sm^{3+} ions with W^{6+} , Sb^{5+} and La^{3+} ions may have occurred, which changed the number of free charge carriers and the defects of the material. On the other hand, the resistance is influenced by the interfacial contacts between the dopant and base material and the microstructure of the sensing layer. Finally, the intergrain contact of the dopant metal oxide (n-conductor) and the base material (p-conductor) might affect the overall conductance of the composite material.

The sensitivity of the materials was measured and is shown in Figure 3.100-3.102. Due to the lower conductivity of the solid surface doped materials, the measurement limits were reached at higher temperatures compared to the undoped material. Tungsten oxide and lanthanum oxide doped samples showed no major changes in sensitivity compared to the undoped sample. However, antimony oxide doping shifted the sensitivity of the material towards higher temperatures. In this case, the material was already sensitive towards ethanol and propylene at 475°C . The sensitivity of $\text{Sb}_2\text{O}_3@\text{SmFeO}_3$ to nitrogen oxide was depressed. This material seemed to be suitable for high temperature application in regions where the undoped material showed no sensitivity at all. In addition, no cross sensitivities were detected down to 375°C .

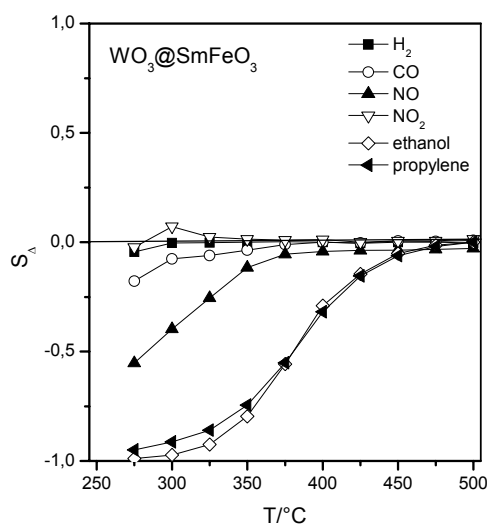


Figure 3.100: Relative sensitivity of $\text{WO}_3@\text{SmFeO}_3$.

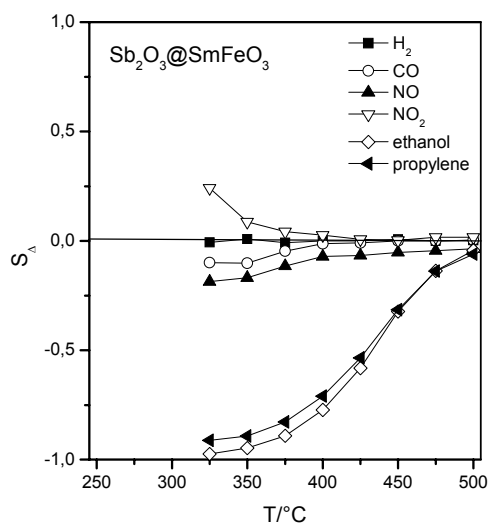


Figure 3.101: Relative sensitivity of $\text{Sb}_2\text{O}_3@\text{SmFeO}_3$.

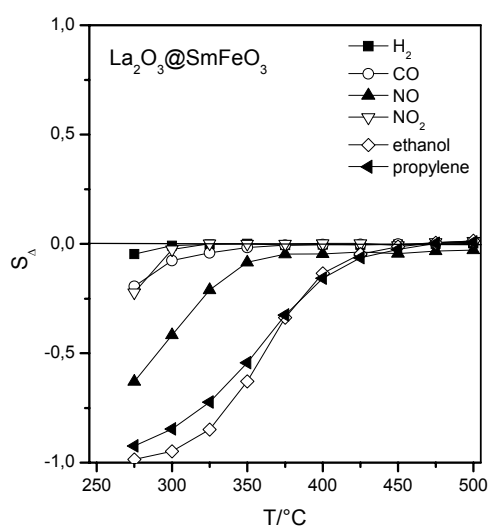


Figure 3.102: Relative sensitivity of $\text{La}_2\text{O}_3@\text{SmFeO}_3$.

Figure 3.103 depicts the selectivity of the surface doped materials to ethanol in comparison to propylene.

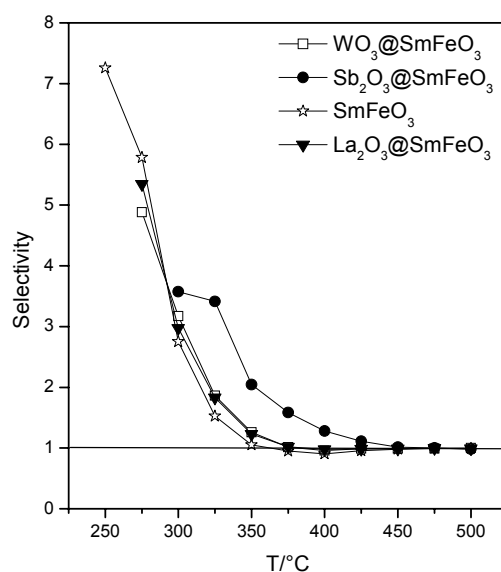


Figure 3.103: Selectivity to ethanol in comparison to propylene.

The antimony oxide doped sample was selective towards ethanol at higher temperatures. At lower temperatures, the undoped material showed the highest selectivity. The selectivity of 1at% of La₂O₃ on the surface was located in between the values achieved for 10 and 20 at% volume doping.

Furthermore, response and recovery times were measured at 325°C for SmFeO₃-based sensing layers to different gases, as shown in Figure 3.104. No changes in the response and recovery behaviour of the surface doped and undoped samples were observed in the considered time scale.

In contrast to the results achieved for SnO₂ and LaMnO₃ on CoTiO₃:La no selectivity changes from ethanol to propylene were observed. The solid surface doping increased the resistance to higher values, and except for Sb₂O₃, no advantages or new properties of the materials were found.

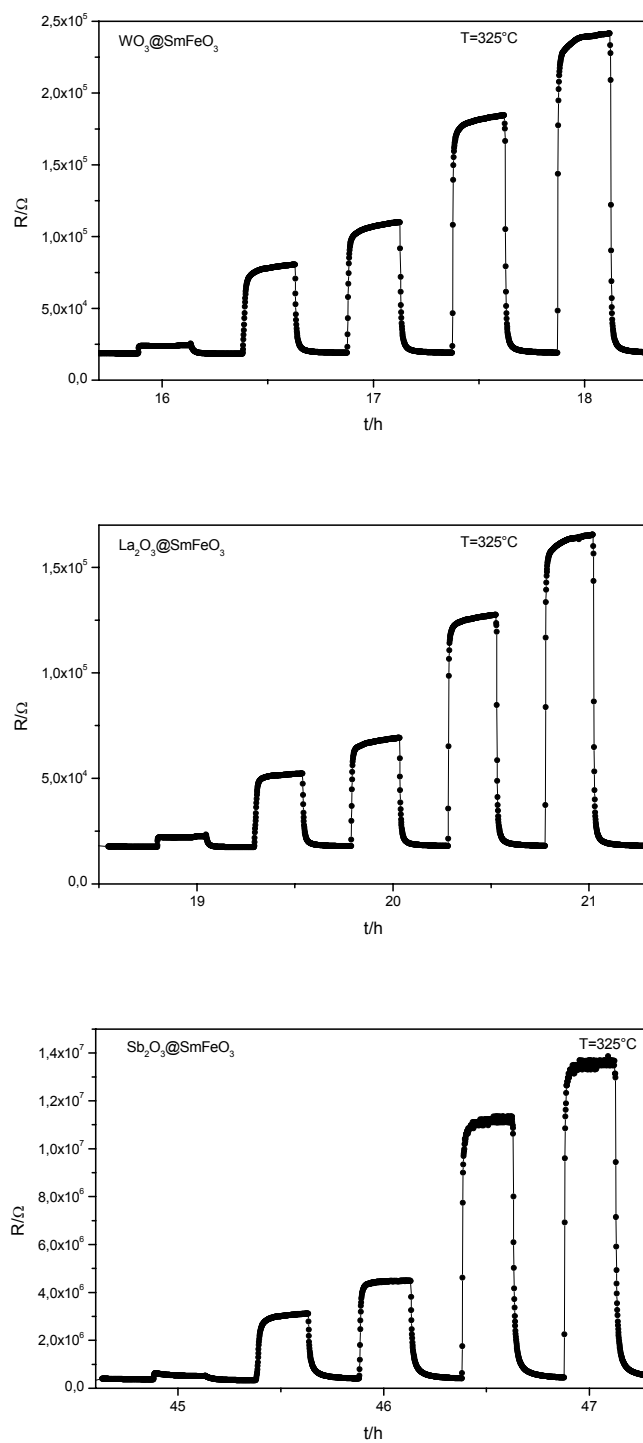


Figure 3.104: Response and recovery behaviour of the solid surface doped samples to NO (5ppm), propylene (20, 40 ppm), and ethanol (40, 60 ppm).

3.3.5.5 Summary of investigations on doped SmFeO₃

The volume doped SmFeO₃ materials were prepared by the polyol mediated synthesis. XRD patterns showed that all compounds were perovskite phase with orthorhombic structure. Incorporation of volume dopants to SmFeO₃ showed a change of the conductivity of the base material, while no improvement of sensing properties could be observed. Doping with Co resulted in a CO sensitivity improvement of the base material, which makes this material a suitable carbon monoxide sensing material.

In many cases, addition of surface dopants showed no changes of the undoped materials; however, adding gold and platinum improved the sensing properties. Gold was able to enhance the sensitivity towards CO. In addition, the Au-doped samples showed the highest sensitivity to ethanol at lower temperatures. Platinum showed good hydrocarbon sensing at higher temperatures and was able to depress cross-sensitivities towards the other test gases. In the case of solid surface dopants, antimony oxide was a promising candidate to shift the sensing properties of the base material to higher temperatures.

3.3.6 Binding energy model

After presenting and discussing the measurements the question remains whether there are trends in gas sensing performance that might improve the understanding of structure-property relationships.

The use of sensing materials with a simple perovskite basic structure that can be modified in their electronic properties without major changes to geometry may elucidate the interaction between surface chemistry and solid state chemistry of the sensing material.

Arakawa et al. found that for n-type LnFeO_3 oxides, the methanol sensing activity increased as the radius of the rare-earth ion decreased. The sequence of the activity for LnFeO_3 was $\text{Gd} > \text{Eu} > \text{Sm} > \text{Nd} > \text{Pr} > \text{La}$ [Ar81]. However, this correlation between the sensitivity of the LnFeO_3 materials studied towards the different gases studied here could not be verified, when the whole set of compounds was taken into account. Aono et al. studied the NO_2 -sensing behaviour of p-type LnFeO_3 ($\text{Ln} = \text{La, Nd, Sm, Gd, Dy}$) [Ao03]. The sensing was influenced by the Ln species and the surface coverage of Ln species. The sequence of NO_2 -activity was $\text{Sm} > \text{Dy} > \text{Gd} \approx \text{Nd} > \text{La}$. The high sensitivity of SmFeO_3 was caused by a higher surface coverage of Sm and lower dissociation energy of the Sm-O bond.

Vorhoeve et al. presented the importance of the oxygen binding energy in the lattice for the NO catalytic chemistry of perovskites [Vo75]. This has also been proposed by Arakawa et al. for methanol sensing activity of rare-earth perovskites [Ar85]. According to the different studies in catalysis [Mo66, Mo67], the changes in sensitivity of LnMO_3 might be explained in terms of changes in the strength of the metal-oxygen bond in the oxides.

The binding energy is estimated from [Ar85] with the following equation:

$$\Delta H(\text{M}-\text{O}) = \frac{1}{\text{CN} \cdot m} \left(H_f - H_s \cdot m - \frac{n}{2} D_o \right), \quad (3.15)$$

with H_f the molar formation enthalpy of M_mO_n , H_s the sublimation energy of the respective metal, D_o the dissociation energy of O_2 , and CN the coordination number of metal ions.

This equation expresses the reaction enthalpy for the formation of lattice oxygen on an oxygen vacancy [Vo75]:



The equation includes a division by the number of oxygen atoms in the molecule (given by the coordination number CN). This gives an average value over all metal-oxygen bonds for one M-O bond. This reaction enthalpy is closely related to the ability of a metal cation to ionosorb oxygen on the sensor surface. This means that the strength of oxygen binding affects the ability of the oxygen to react with an admixed test gas.

Figure 3.105 shows the correlation between the binding energy of Ln-O in LnFeO₃ compounds towards the sensitivity to ethanol, propylene, and NO₂.

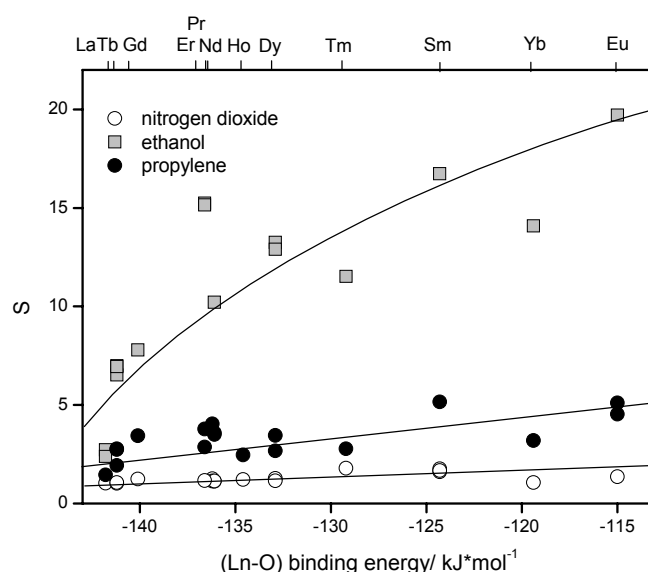


Figure 3.105: Sensitivity versus (Ln-O) binding energy according to [Ar85] at 300°C (without LuFeO₃).

In the LnFeO₃ series increasing sensitivity coincided with rank order of decreasing binding strength of oxygen. Only LuFeO₃ showed higher sensitivities as expected from this model. Considering that $\Delta H(\text{M-O})$ signifies the bond strength between metal cation on the surface and adsorbed oxygen, a weak metal-to-oxygen bond supports a reaction of the adsorbed oxygen upon attack of the testing gas species. For

stronger metal-oxygen bonds, the surface reaction would be more difficult accompanied by a lower sensitivity.

For surface oxygen with neighbours A and B, the total contribution of bonds to the reaction enthalpy is the sum of both, $\Delta H(A-O) + \Delta H(B-O)$. In accordance to the previously proposed model, Figure 3.106 shows the absolute values of ethanol sensitivities of LnFeO_3 and LnCrO_3 oxides versus the (Ln-O) binding energy. In this case ethanol was chosen because LnCrO_3 showed highest sensitivity to this test gas. In addition, the temperatures of maximum sensitivity has been chosen to compare the two material classes.

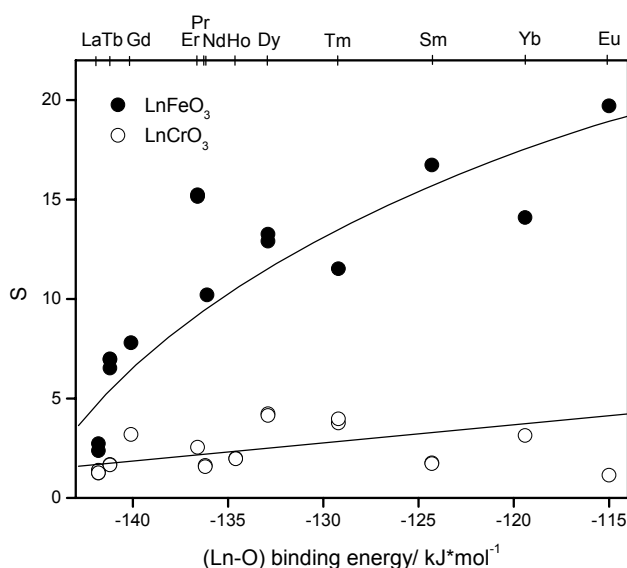


Figure 3.106: Ethanol sensitivity of LnFeO_3 ($300^\circ\text{C} = T_{S_{\text{Max}}}$) and LnCrO_3 ($225^\circ\text{C} = T_{S_{\text{Max}}}$) versus the binding energy.

First, Figure 3.106 depicts that in the case of LnCrO_3 the (Ln-O) binding energy also had an influence on the sensitivity of the material. However, the sensitivity of the LnFeO_3 was in all cases higher than of the LnCrO_3 oxides. This result can also be ascribed to the binding energy, which was higher for Cr-O than for Fe-O, leading to lower sensitivity of the orthochromite series. The change of the ion M from Fe to Cr depressed the sensitivity of the LnMO_3 in accordance to the results reported for methanol sensitivity [Ar85]. The pronounced influence of the ion exchange on the B position was also observed for the catalytic oxidation of propane and methanol by Nitadori et al. [Ni88].

Finally, systematic substitution of La^{3+} and Cr^{3+} cations in the dodecahedral and octahedral positions of SmFeO_3 was used to demonstrate the consistency of the model proposed.

SmFeO_3 showed lower binding energy than LaFeO_3 and thus higher sensitivity. Doping SmFeO_3 with 10 and 20 at% lanthanum showed a decrease in sensitivity due to enhancement of M-O binding energy. Analogous influences could be observed at the B-site. SmCrO_3 showed higher binding energy and lower sensitivity than SmFeO_3 . Inserting 10 and 20 at% of chromium into SmFeO_3 at the B-site resulted in a considerable decrease in sensitivity compared to the undoped SmFeO_3 . The experiments showed that in the case of volume doping, exchange at the B-site also had a pronounced influence. Figure 3.107 plots the volume dopant concentration (at%) versus the relative sensitivity towards ethanol.

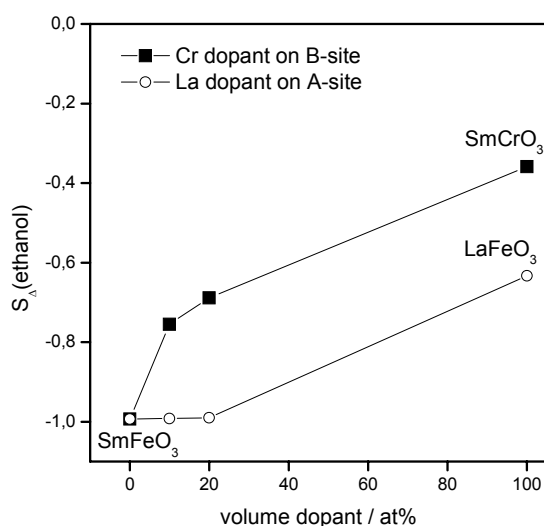


Figure 3.107: Sensitivity of the trivalent volume doped materials towards ethanol.

Finally, it has to be stressed that the model up to now cannot be transferred to other systems of the presented work. Limits of comparison are affected for example by different crystallite structures that hold different active sites or valences of the participating ions. Nevertheless, the binding energy of a compound seems to be a promising parameter for predicting sensing properties.

In conclusion and outstanding for this work, it was found that the strength of the metal-oxygen bond in the LnMO_3 perovskites was important for understanding the

sensitivity of the material. Sensitivity was inversely correlated to binding energy. Changes on the B-site had a stronger influence on the sensitivity than changes in the A-site. Finally, dopants that increased the strength of the binding energy decreased the sensitivity of the base compound.

4. Conclusion

This work describes the preparation and characterisation of thick-film gas sensors. The presented results allow to show that the polyol mediated synthesis in combination with high throughput impedance spectroscopy is an indispensable tool for gas sensor research.

The polyol method enabled the preparation of a wide range of different ABO_3 compounds. The fast and simple reaction method allowed mixing on the molecular level and bulk doping of the materials during the preparation. Nanoscaled compounds that crystallised after temperature treatment were achieved. The prepared ABO_3 materials offered various properties and possibilities for gas sensing materials, especially for high temperature use.

The prepared materials were used to fabricate active layers on electrode structures to form gas sensors. Substrate plates of diverse metal-doped oxides were rapidly synthesised and screened with the high throughput impedance spectroscopy setup. The measurements were performed between 200 and 500°C and the test gases were hydrogen, carbon monoxide, nitrogen oxides, ethanol, and propylene in synthetic air. Two different materials systems, CoTiO_3 and LnMO_3 , were presented. All prepared materials showed typical p-type semiconducting behaviour.

Some of the most interesting conclusions drawn from the experiments are summarised below. Detailed information can be found in chapter 3, and in the listed publications.

Incorporation of various volume dopants into CoTiO_3 changed the resistance and improved the sensing properties of the base material. Lanthanum doping was found to be most effective; it increased the sensitivity towards hydrocarbons and improved the response time of the base material. By introducing to CoTiO_3 :La a number of surface and solid surface dopants in different concentrations, the sensitivity was influenced. Pd and Au were found to be the most effective dopants. They both showed pronounced sensitivity towards carbon monoxide and hydrogen. In addition, the gold doped material seemed to be a suitable NO-tolerant NO_2 -sensing material at

around 350°C. SnO_2 used as a solid surface dopant showed excellent propylene sensitivity and selectivity.

Secondly, the preparation and characterisation of 25 lanthanide orthochromites and orthoferrites was described. They all showed hydrocarbon and NO_2 sensitivity. One of the outstanding materials, SmFeO_3 , was investigated further towards doping influences. By introducing different volume dopants, the resistance and sensitivity of SmFeO_3 could be influenced. Co-doping produced a remarkable sensitivity towards carbon monoxide. In experiments with the addition of surface dopants onto SmFeO_3 , Au and Pt were found to be the most effective dopants. Gold enhanced the sensitivity towards carbon monoxide and showed high sensitivity and selectivity towards ethanol at lower temperatures, while platinum showed good ethanol sensitivity and selectivity at higher temperature and depressed cross-sensitivities towards other test gases.

From the measurements on LnMO_3 materials, a trend in sensing performance as a function of composition was found. The sensitivity of these materials was inversely connected to the binding energy of the compounds. Changes of the B-site cation had more influence on the sensitivity than changes in the A-site. This was the first extensively investigated system that could be described entirely.

The materials shown here have high potential for gas sensing applications. However the investigations on these materials is not complete. With the use of high throughput impedance spectroscopy, a great number of different compounds were screened in a short amount of time. A high throughput approach is crucial for gas sensor research in order to answer new problems in this sector on a shorter time span. The most important conclusion driven from this thesis is that the strength of the metal-to-oxygen bond of a compound is a promising parameter for predicting sensing possibility.

In the future, the binding energy model could be generalised and transferred to other material systems. The characterisation of the surface oxygen binding should be expanded on XPS examinations as performed by Aono et al. [Ao03]. Theoretical calculations could also help to understand and compare the measured values.

5. References

A

[Ag91] Agilent 4192A, user manual, Agilent Technologies, (1991)

[Am02] E. J. Amis, X.-D. Xiang, J.-C. Zhao, Combinatorial Materials Science: What's New Since Edison?, MRS Bull. 4 (2002) 295-297.

[Am04] E. J. Amis, Combinatorial Materials Science: Reaching beyond discovery, Nature Materials 3 (2004) 83-84.

[Ao03] H. Aono, E. Traversa, M. Sakamoto, Y. Sadaoka, Crystallographic characterization and NO₂ gas sensing property of LnFeO₃ prepared by thermal decomposition of Ln-Fe hexacyanocomplexes, Ln[Fe(CN)₆] \cdot nH₂O, Ln=La, Nd, Sm, Gd, and Dy, Sens. Actuators B 94 (2003) 132-139.

[Ar01] J. Arbiol, Metall Additive Distribution in TiO₂ and SnO₂ Semiconductor Gas Sensor Nanostructured Materials, PhD thesis, University of Barcelona, ISBN: 84-475-2636-4 (2001).

[Ar02] J. Arbiol, F. Peiró, A. Cornet, J. R. Morante, J. A. Pérez-Ome, J. J. Calvino, Computer image HRTEM simulation of catalytic nanoclusters on semiconductor gas sensor materials supports, Mater. Sci. Engineering B 91-92 (2002) 534-536.

[Ar03] M. A. Aronova, K. S. Chang, I. Takeuchi, H. Jabs, D. Westerheim, A. Gonzalez-Martin, J. Kim, B. Lewis, Combinatorial libraries of semiconductor gas sensors as inorganic electronic noses, Appl. Phys. Lett. 83(6) (2003) 1255-1257.

[Ar81] T. Arakawa, S. Tsuchi-ya, J. Shiokawa, Catalytic activity of rare-earth orthoferrites and orthochromites, Mat. Res. Bull. 16 (1981) 97-103.

[Ar85] T. Arakawa, H. Kurachi, J. Shiokawa, Physicochemical properties of rare earth perovskite oxides used as gas sensor material, J. Mater. Sci. 20 (1985) 1207-1210.

[Ar88] T. Arakawa, K. Takada, Y. Tsunemine, J. Shiokawa, Carbon monoxide gas sensitivities of reduced perovskite oxide lanthanum cobalt oxide (LaCoO_{3-x}), Sens. Actuators 14 (1988) 215-221.

B

[Ba96] H. Baltes, W. Göpel, J. Hesse, Sensors Update Vol. 2, VCH Weinheim (1996) 2.

[Ba99] N. Bârsan, M. Schweizer-Berberich, W. Göpel, Fundamental and practical aspects in the design of nanoscaled SnO₂ gas sensors: a status report, Fresenius J. Anal. Chem. 365 (1999) 287-304.

[Ba01] N. Bârsan, U. Weimar, Conduction Model of Metal Oxide Gas Sensor, J. Electroceram. 7 (2001) 143-167.

[Ba02] S. H. Baeck, T. F. Jaramillo, C. Brändli, E. W. McFarland, Combinatorial Electrochemical Synthesis and Characterization of Tungsten-Based Mixed-Metal Oxides, *J. Comb. Chem.* 4 (2002) 563-568.

[Ba03] N. Bârsan, U. Weimar, Understanding the fundamental principles of metal oxide based gas sensors, the example of CO sensing with SnO₂ sensors in the presence of humidity, *J. Phys.: Condens. Matter* 15 (2003) R813-R839.

[Be06] K.D.Benkstein, S. Semancik, Mesoporous nanoparticles TiO₂ thin films for conductometric gas sensing on microhotplate platforms, *Sens. Actuators B: Chem.* 113 (2006) 445-453.

[Bi46] L. S. Birks and H. Friedman, Particle size determination from X-ray line broadening, *J. Appl. Phys.* 17(8) (1946) 687-692.

[Br01] Y. Brik, M. Kacimi, M. Ziyad, F. Bozon-Verduraz, Titania-Supportet Cobalt and Cobalt Catalysts: Characterization and Performances in Ethane Oxidative Dehydrogenation, *J. Catal.* 202(1)(2001) 118-128.

[Br04] T. Brinz, W. F. Maier, O. Wolfbeis, U. Simon, Gassensoren durch High-Throughput-Methoden, *Nachrichten aus der Chemie*, 52(2004) 247-251.

[Br05] T. Brinz, U. Simon, J. Jockel, D. Sanders, Device and procedure for high throughput analysis by measuring the impedance, (2005) DE 10361099 B3 20050525.

[Br53] W. H. Brattain, J. Bardeen, Surface Properties of Germanium, *Bell. Syst. Technol. J.* 32 (1953) 1-41.

[Br95] G. Briceño, H. Chang, X. Sun, P. G. Schultz, X.-D. Xiang, A class of cobalt oxide magnetoresistance materials discovered with combinatorial synthesis, *Science* 270 (1995) 273-275.

C

[Ca02] A. Cabot, A. Vila, J. R. Morante, Analysis of the catalytic activity and electrical characteristics of different modified SnO₂ layers for gas sensors, *Sens. Actuators B: Chem.* 84(1) (2002) 12-20.

[Ca98] M. C. Carotta, G. Martinelli, Y. Sadaoka, P. Nunziante, E. Traversa, Gas-sensitive electrical properties of perovskite-type SmFeO₃ thick films, *Sens. Actuators B: Chem.* 48(1-3) (1998) 270-276.

[Ch98] H. Chang, C. Gao, I. Takeuchi, Y. Yoo, J. Wang, P. G. Schultz, D. Xiang, P. R. Sharma, M. Downes, T. Venkatesan, Combinatorial synthesis and high throughput evaluation of ferroelectric/dielectric thin-film libraries for microwave applications, *Appl. Phys. Lett.* 72 (1998) 2185-2187.

[Ch99] X. Chu; X. Liu, G. Wang, G. Meng, Preparation and gas sensing properties of nano-CoTiO₃, *Mat. Res. Bull.* 34(10/11) (1999) 1789-1795.

[Ch99b] C. M. Chiu, Y. H. Chang, The structure, electrical and sensing properties of CO of $\text{La}_{0.8}\text{Sr}_{0.2}\text{Co}_{1-x}\text{Ni}_x\text{O}_{3-\delta}$ system, *Materials Science and Engineering A* 266 (1999) 93-98.

[Ch04] S. Chkoundali, S. Ammar, N. Jouini, F. Fievet, P. Molinie, M. Danot, F. Villain, J.-M. Greneche, Nickel ferrite nanoparticles:elaboration in polyol medium via hydrolysis, and magnetic properties, *J. Phys.: Condens. Matter* 16 (2004) 4357-4372.

[Co00] F. Cosandey, G. Skandan, A. Singhal, Materials and Processing Issues in Nanostructured Semiconductor Gas Sensors, *JOM-e* 52(10) (2000).

[Cr02] J. Credà, J. Arbiol, G. Dezanneau, R. Díaz, J.R. Morante, Perovskite-type BaSnO_3 powders for high temperature gas sensor application, *Sens. Actuators B: Chem.* 84 (2002) 21-25.

D

[Da98] E. Danielson, M. Devenney, D. M. Giaquinta, J. H. Golden, R. C. Haushalter, E. W. McFarland, D. M. Poojary, C. M. Reaves, W. H. Weinberg, X. D. Wu, A rare-earth phosphor containing one-dimensional chains identified through combinatorial methods, *Science* 279 (1998) 837-839.

[Du99] V. Dusastre, D. E. Williams, Gas-sensitive resistor properties of the solid solution series $\text{Ti}_x(\text{Sn}_{1-y}\text{Sb}_y)_{1-x}\text{O}_2$ ($0 < x < 1$, $y = 0, 0.01, 0.05$), *J. Mater. Chem.* 9 (1999) 445-450.

E

[EI02] A. El-Azab, S. Gan, Y. Liang, Binding and diffusion of Pt nanoclusters on anatase TiO_2 (001)-(1x4) surface, *Surf. Sci.* 506 (2002) 93-104.

[EI04] D. Elbe, T. Brinz, I. Ullmann, C. Krummel, C. Schelling, C. Heppel (Robert Bosch GmbH) (2004) DE 10319193 A1 20041118.

F

[Fa06] L. Fabbrini, I. Rossetti, L. Forni, Effect of honeycomb supporting on activity of $\text{LaBO}_{3\pm\delta}$ perovskite-like catalysts for methane flameless combustion, *Appl. Catal. B* 63(1-2) (2006) 131-136.

[Fe01a] C. Feldmann, Polyol mediated synthesis of oxide particle suspensions and their application, *Scripta Materialia* 44 (2001) 2193-2196.

[Fe01b] C. Feldmann, H. Jungk, Polyol-Mediated Preparation of Nanoscale Oxide Particles, *Angew. Chem. Int. Ed.* 40(2) (2001) 359-362.

[Fe01c] C. Feldmann, C. Metzmacher, Polyol mediated synthesis of nanoscale MS particles ($M = \text{Zn}, \text{Cd}, \text{Hg}$), *J. Mater. Chem.* 11 (2001) 2603-2606.

[Fe03] C. Feldmann, Polyol-Mediated synthesis of Nanoscale Functional Materials, *Adv. Funct. Mater.* 13(2) (2003) 101-107.

[Fe04] C. Feldmann, Darstellung und Charakterisierung der nanoskaligen Vb-Metalloxide M_2O_5 ($M = \text{V}, \text{Nb}, \text{Ta}$), *Z. Anorg. Allg. Chem.* 630 (2004) 2473-2477.

[Fi00] F. Fiévet, Polyol Process, Fine particles: synthesis, characterization, and mechanisms of growth, Tatado Sugimoto, Marcel Dekker (2000) 460-496.

[Fi02] <http://www.figaro.co.jp> (2006).

[Fi02b] D. Filippini, L. Fraigi, R. Aragón and U. Weimar, Thick film Au-gate field-effect devices sensitive to NO₂, Sens. Actuators B: Chem. 81(2-3) (2002) 296-300.

[Fi03] D. Fino, N. Russo, G. Saracco, V. Specchia, The role of suprafacial oxygen in some perovskites for the catalytic combustion of soot, J. Catal. 217 (2003) 367-375.

[Fi82] M. Figlarz, F. Fievet, J. P. Lagier, Europa Nr. 0113281, USA Nr.4539041, Finnland Nr. 74416, Japan Nr. 04024402.

[Fr04] A. Franzen, D. Sanders, J. Jockel, J. Scheidtmann, G. Frenzer, W. F. Maier, Th. Brinz, U. Simon, High-Throughput Method for the Impedance Spectroscopic Characterization of Resistive Gas Sensors. Angew. Chem. 116 (2004) 770-773, Angew. Chem. Int. Ed. 43 (2004) 752-754.

[Fr05] A. Frantzen, D. Sanders, J. Scheidtmann, U. Simon, W. F. Maier, A Flexible Database for Combinatorial and High-Throughput Materials Science, QSAR Comb. Sci. 24(1) (2005) 22-28.

[Fr06] M. E. Franke, T. J. Koplin, U. Simon, Metal and Metal Oxide Nanoparticles in Chemiresistors: Does the Naoscale Matter?, Small 2(1) (2006) 36-50.

[Fu98] K. Fukui, A. Katsuki, Improvement of humidity dependence in gas sensor based on SnO₂, Chemical Sensors A 14 (1998) 29-32.

G

[Ga69] F. S. Galasso, Structure, Properties and Preparation of Perovskite-Type Compounds, Pergamon Press, London (1969).

[Ge91] J. Gerblinger, H. Meixner, Fast oxygen sensors based on sputtered strontium titanate, Sens. Actuators B: Chem. 4(1-2) (1991) 99-102.

[Ge56] S. Geller, A. E. Wood, Crystallographic studies of perovskite like compounds. I. Rare earth orthoferrites and YFeO₃, YCrO₃, YAlO₃, Acta Cryst. 9 (1956) 563-568.

[Gi94] D. M. Giaquinta, H.-C. Zur Loye, Structural Predictions in the ABO₃ Phase Diagram, Chem. Mater. 6 (1994) 365-372.

[Go26] V. M. Goldschmidt, Die Gesetze der Krystallichemie, Naturwissenschaften 14(21) (1926) 477-485.

[Gö85] W. Göpel, SnO₂ sensors: current status and future prospects, Progr. Surface Sci. 20(1) (1985) 9-103.

[Gö95] W. Göpel, K. D. Schierbaum, Chemisorption and charge transfer at ionic semiconductor surfaces: Implications in designing gas sensors, Sens. Actuators B: Chem. 26(1-3) (1995) 1-12.

[Gö96] W. Göpel, Ultimate limits in the miniaturization of chemical sensors, *Sens. Actuators A: Phys.* 56(1-2) (1996) 83-102.

[Go04] P. Gouma, G. Sberveglieri, Novel Materials and Applications of Electronic Noses and Tongues, *MRS Bulletin*, 29(19) (2004) 697-701.

H

[Ha70] J. J. Hanak, The "multiple-sample concept" in materials research: Synthesis, compositional analysis and testing of entire multicomponent systems, *J. Mater. Sci.* 5 (1970) 964-971.

[Ha97] M. Haruta, Size- and support-dependency on the catalysis of gold, *Catal. Today* 36 (1997) 153-166.

[Ha04] Hagemeyer, A.; Stasser, P.; Volpe, Jr. A. F., Ed.; *High-Throughput Screening in Chemical Catalysis*, Wiley-VCH: Weinheim (2004).

[He94] V. E. Henrich, P. A. Cox, *The Surface Science of Metal Oxides*, Cambridge University Press (1994) 312.

[He00] L. Heinert, Systematische Struktur-Wirkungs-Untersuchungen zwischen halbleitenden Metalloxidsensoren und Kohlenwasserstoffen, PhD thesis, Justus-Liebig-University Giessen (2000).

[Ho05] Y. Hosoya, Y. Itagaki, H. Aono, Y. Sadaoka, Ozone detection in air using SmFeO_3 gas sensor, *Sens. Actuators B: Chem.* 108(1-2) (2005) 198-201.

[Ho05b] Y. Hosoya, M. Mori, Y. Itagaki, H. Aono, Y. Sadaoka, Ozone and NO_2 detection using $\text{SmFe}_{1-x}\text{Co}_x\text{O}_3$ gas sensor, *Chemical Sensors* 21(A) (2005) 16-18.

[Hu96] R.-F. Huang, W.-Y. Hwang, Effect of defect structure on gas sensitivity of LaCrO_3 , *J. Mater. Res.* 11(12) (1996) 3077-3082.

I

[Ih94] K. Ihokura, J. Watson, *The Stannic Oxide Gas Sensor*, CRC Press (1994).

J

[Ja99] B. Jandeleit, D. J. Schaefer, T. S. Powers, H. W. Turner, W. H. Weinberg, Combinatorial Materials Science and Catalysis. *Angew. Chem.* 111 (1999) 2648-2689; *Angew. Chem. Int. Ed.* 38 (1999) 2494-2532.

[Ja06] T. V. Janssens, A. Carlsson, A. Puig-Molina, B. S. Clausen, Relation between nanoscale Au particle structure and activity for CO oxidation on supported gold catalysts, *J. Catal.* 240(2) (2006) 108-113.

[Ja06b] K. Jain, R. P. Pant, S. T. Lakshmikumar, Effect of Ni doping on thick film SnO_2 gas sensor, *Sens. Actuators B: Chem.* 113(2) (2006) 823-829.

K

[Ka06] N. Kassabova, D. Stoyanova, D. Vladov, D. Mehandjiev, D. Shishkov, Spent Pd-catalyst-component for oxide catalyst, designed for CO oxidation and NO reduction, Chem. Eng. J. 120 (1-2) (2006) 107-111.

[Ka84] T. Kazuyuki, U. Yasuo, T. Shuji, I. Takashi, U. Akifumi., Catalyst Preparation Procedure Probed by EXAFS Spectroscopy. 2. Cobalt on Titania, J. Am. Chem. Soc., 106 (1984) 5172-5178.

[Ke65] K. Kennedy, T. Stefansky, G. Davy, V. F. Zackay, E. R. Parker, Rapid Method for Determining Ternary-Alloy Phase Diagrams, J. Appl. Phys. 36 (1965) 3808-3810.

[Ke01] N. Keller, J. Mistrik, S. Visnovsky, D. S. Schmool, Y. Dumont, P. Renaudin, M. Guyot, R. Krishnan, Magneto-optical Faraday and Kerr effect of orthoferite thin films at high temperatures, Eur. Phys. J. B 21(1) (2001) 67-73.

[Kh01] H. R. Khan, J. Feßmann, Keramische Dickschicht-Abgassensoren mit Perowskitstruktur, www.fem-online.de (2001) 1-8.

[Ki84] K. Kidoh, K. Tanaka, F. Marumo, H. Takei, Electron Density Distribution in an Ilmenite-Type Crystal of Cobalt(II)Titanium(IV)Trioxide, Acta Crystallogr. B, 40 (1984) 92-96 [ICSD 48107].

[Ko90] D. Kohl, The Role of Noble Metals in the Chemistry of Solid-State Gas Sensors, Sens. Actuators B: Chem. 1 (1990) 158-165.

[KOMB] „KOMBISENS“ BMBF project, PID 03C0305D, FKZ0305.

[Ko01] D. Kohl, Function and applications of gas sensors J. Phys. D: Appl. Phys. 34 (2001) R125-R149.

[Ko02] N. Kojima, K. Tsushima, Recent progress in magneto-optics and research on its application, Low Temperature Physics 28(7) (2002) 480-490.

[Ko05] G. Korotcenkov, Gas response control through structural and chemical modification of metal oxide films: state of the art and approaches, Sens. Actuators B: Chem. 107(2005) 209-232.

[Ko06] T. J. Koplin, M. Siemons, C. Océn-Valéntin, D. Sanders, U. Simon, Workflow for High-Throughput Screening of Gas Sensing Materials, Sensors, 6 (2006) 298-307.

[Ko06b] T. J. Koplin, Entwicklung und Anwendung von Hochdurchsatztechniken zur Darstellung und Unterstützung neuer nanostrukturierter Sensormaterialien, PhD thesis, RWTH Aachen (2006).

[Kr94] H. Krischner, B. Kopplehuber-Bitschnau, Röntgenstrukturanalyse und Rietveldmethode, eine Einführung, Vieweg Verlag (1994).

L

[La95] U. Lampe, J. Gerblinger, H. Meixner, Carbon monoxide sensor based on thin films of BaSnO₃, Sens. Actuators B: Chem. 25(1-3) (1995) 657-660.

[La95b] U. Lampe, J. Gerblinger, H. Meixner, Nitrogen oxide sensors based on thin films of BaSnO₃, Sens. Actuators B: Chem. 26-27 (1995) 97-98.

[La05] A. Labidi, C. Jacolin, M. Bendahan, A. Abdelghani, J. Guerin, K. Aguir, M. Maaref, Impedance spectroscopy on WO₃ gas sensor, Sens. Actuators B: Chem. 106(2) (2005) 713-718.

[Le01] H.-J. Lee, J.-H. Song, Y.-S. Yoon, T.-S. Kim, K.-J. Kim, W.-K. Choi, Enhancement of CO sensitivity of indium oxide-based semiconductor gas sensor through ultra-thin cobalt adsorption, Sens. Actuators B: Chem. 79(2001) 200-205.

[Li71] W. F. Libby, Promising Catalyst for Auto Exhaust, Science 171 (1971) 499-500.

[Li99] D. R. Liu, P. G. Schultz, Das Hervorbringen neuer molekularer Funktionen: ein Lehrstück der Natur, Angew. Chem. 111 (1999) 36-56.

[Li02] Z. Ling, C. Leach, R. Freer, A time resolved study of the response of a WO₃ gas sensor to NO₂ using AC impedance spectroscopy, Sens. Actuators B: Chem. 87(2) (2002) 215-221.

[Ly99] I.S. Lyubutin, T.V. Dmitrieva, A.S. Stepin, Dependence of exchange interactions on chemical bond angle in a structural series: cubic perovskite-rhombic orthoferrite-rhombohedral hematite, J. Exp. Theor. Phys. 88(3) 1999, 590-597.

M

[Ma00] S. Matsushima, N. Sano, Y. Sadaoka, C₃H₆ sensitive SmFeO₃ prepared from thermal decomposition of heteronuclear complexes, {Ln[Fe(CN)₆]_nH₂O}_x (Ln=La, Sm, Dy), J. Ceram. Soc. Jap. 108 (2000) 681-682.

[Ma05] L. Malavasi, C. Tealdi, G. Flor, G. Chiodelli, V. Cervetto, A. Montenero, M. Borella, NdCoO₃ perovskite as possible candidate for CO-sensors: thin films, synthesis and sensing properties, Sens. Actuators B: Chem. 105 (2005) 407-411.

[Ma87] J. R. Macdonald, Impedance Spectroscopy, Wiley (1987).

[Ma99] W. F. Maier, Kombinatorische Chemie-Herausforderung und Chance für die Entwicklung neuer Katalysatoren und Materialien, Angew. Chem. 111 (9) (1999) 1295-1296.

[Ma99b] G. Martinelli, M. C. Carotta, M. Ferroni, Y. Sadaoka, E. Traversa, Screen-printed perovskite-type thick films as gas sensors for environmental monitoring, Sens. Actuators B: Chem. 55(1999) 99-110.

[Mc90] J. G. McCarty, H. Wise, Perovskite Catalysts for Methane Combustion, Catal. Today 8(2) (1990) 231-248.

[Me00] J. Merikhi, H. Jungk, C. Feldmann, Sub-micrometer CoAl_2O_4 pigment particles-synthesis and preparation of coatings, *J. Mater. Chem.* 10(6) (2000) 1311-1314.

[Me00b] R. Memming, *Semiconductor Electrochemistry*, Wiley-VCH (2000).

[Mi67] N. C. Miller, G. A. Shirn, CO-SPUTTERED Au-SiO₂ CERMET FILMS, *Appl. Phys. Lett.* 10 (1967) 86-88.

[Mi92] M. Mitsuoka, A. Otofujii, T. Arakawa, Sensing properties of $\text{LnMO}_3/\text{SnO}_2$ (Ln= rare earth, M=Cr, Co, Mn, Fe) having a heterojunction, *Sens. Actuators B: Chem.* 9 (1992) 205-207.

[Mi93] N. Q. Minh, Ceramic Fuel Cells, *J. Am. Ceram. Soc.* 76 (1993) 563-588.

[Mo82] S. R. Morrison, Semiconductor gas sensors, *Sens. Actuators* 2 (1982) 329-341.

[Mo87] S. R. Morrison, Selectivity on Semiconductor Gas Sensors, *Sens. Actuators* 12 (1987) 425-440.

[Mo96] F.C. Moates, M. Somani, J. Annamalai, J. T. Richardson, D. Luss, R. C. Wilson, Infrared Thermographic Screening of Combinatorial Libraries of Heterogenous Catalysts, *Ind. Eng. And Chem. Res.* 35 (1996) 4801-4803.

[Mo97] P. T. Moseley, Solid state gas sensors, *Meas. Sci. Technol.* 8 (1997) 223-237.

N

[Ni04] X. Niu, W. Du, W. Du, Preparation, characterization and gas-sensing properties of rare earth mixed oxides, *Sens. Actuators B* 99 (2004) 399-404.

[Ni88] T. Nitadori, T. Ichiki, M. Misono, Catalytic Properties of Perovskite-Type Mixed Oxides (ABO_3) Consisting of Rare Earth and 3d Transition Metals. The Role of the A- and B-Site Ions, *Bull. Chem. Soc. Jpn.* 61(3) (1988) 621-626.

O

[Ob76] H.Obayashi, Y. Sakurai, T. Gejo, Perovskite-Type Oxides as Ethanol Sensors, *J. Solid State Chem.* 17 (1976) 299-303.

[Oh74] H. Ohbayashi, T. Kudo, T. Gejo, Crystallographic, Electric and Thermochemical Properties of the Perovskite-Type $\text{Ln}_{1-x}\text{Sr}_x\text{CoO}_3$ (Ln:Lanthanoid Element), *Japanese J. Appl. Phys.* 13(1) (1974) 1-7.

[Or02] M. E. Orazem, P. Shukla, M. A. Membrino, Extension of the measurement model approach for deconvolution of the underlying distributions for impedance measurements, *Electrochimica Acta* 47 (2002) 2027-2034.

P

[Pa93] S. S. Park, H. Zheng, J. D. Mackenzie, Ethanol gas sensing properties of tin oxide (SnO_2)-based thin-film sensors prepared by the sol-gel process, *Mater. Lett.* 17(6) (1993) 346-352.

[Pa01] T. M. Pan, T. F. Lei, T. S. Chao, High- k cobalt-titanium oxide dielectrics formed by oxidation of sputtered Co/Ti or Ti/Co films, *Appl. Phys. Lett.* 78(10)(2001) 1439.

[Pa04] M. Pardo, G. Sberveglieri, Electronic Olfactory Systems Based on Metal Oxide Semiconductor Sensor Arrays, *MRS Bulletin*, 29(19) (2004) 703-708.

[Pa03] C. O. Park, S. A. Akabar, Ceramics for chemical sensing, *J. Mater. Sci.* 38 (2003) 4611-4637.

[Pe01] M. A. Peña, J. L. G. Fierro, Chemical Structures and Performance of Perovskite Oxides, *Chem. Rev.* 101 (2001) 1981-2017.

[Po00] L. Poul, N. Jouini, F. Fievet, Layered Hydroxide Metal Acetates (Metal= Zinc, Cobalt and Nickel): Elaboration via Hydrolysis in Polyol Medium and comparative Study, *Chem. Mater.* 12 (2000) 3123-3132.

[Po03] L. Poul, S. Ammar, N. Jouini, F. Fievet, F. Villain, Synthesis of Inorganic Compounds (Metal, Oxide and Hydroxide) in Polyol Medium: A Versatile Route Related to the Sol-Gel Process, *J. Sol-Gel. Sci. Technol.* 26 (2003) 261-265.

Q

[Qu63] S. Quézel-Ambrunaz, M. Mareschal, Paramètres cristallins des chromites de terres rares, *Bull. Soc. Franç. Minéral. Crist.* (1963), 6 (2), 204-205.

R

[Re01] H. M. Reichenbach, P. J. McGinn, Combinatorial synthesis of oxide powders, *J. Mater. Res.* 16(4) (2001) 967-974.

[Re03] F. Rettig, R. Moos, C. Plog, Sulfur adsorber for thick-film exhaust gas sensors, *Sens. Actuators, B: Chem.* 93(1-3) (2003) 36-42.

[Re99] C. V. Gopal Reddy, S. V. Manorama, V. J. Rao, A. Lobo, S. K. Kulkarni, Noble metal additive modulation of gas sensitivity of BaSnO_3 explained by a work function based model, *Thin Solid Films* 348 (1999) 261-265.

[Ri69] H. M. Rietveld, A profile refinement method for nuclear and magnetic structures, *J. Appl. Cryst.* 2 (1969) 65-71.

[Ro05] S. C. Roy, G. L. Sharma, M. C. Bhatnager, S. B. Samanta, Novel ammonia-sensing phenomena in sol-gel derived $\text{Ba}_{0.5}\text{Sr}_{0.5}\text{TiO}_3$ thin films, *Sens. Actuators B: Chem.* 110(2) (2005) 299-303.

[Ro06] S. Roggan, C. Limberg, B. Ziemer, M. Siemons, U. Simon, The reactivity and properties of $[-\text{O}-\text{Bi}^{\text{III}}\cdots\text{O}=\text{Mo}-]_n$ chains, *Inorganic Chemistry* 45(22) (2006) 9020-9031.

[Ro06b] A. Rota, A. Martinez-Gil, G. Agnus, E. Moyen, T. Maroutian, B. Bartenlian, R. Megy, M. Hanbücken, P. Beauvillain, Au island growth on Si(111) vicinal surface, *Surf. Sci.* 600 (2006) 1207-1212.

[Ro07] S. Roggan, PhD thesis, HU Berlin (2007) in preparation.

S

[Sa04] D. Sanders, Entwicklung von Gassensoren auf Indiumoxid-Basis mittels Hochdurchsatz-Impedanzspektroskopie, PhD thesis, RWTH Aachen (2004).

[Sa05] K. Sahner, R. Moos, M. Matam, J. J. Tunney, M. Post, Hydrocarbon sensing with thick and thin film p-type conducting perovskite materials, *Sens. Actuators B: Chem.* 108(1-2) (2005) 102-112.

[Sa85] S. Saito, M. Miyayama, K. Koumoto, H. Yanagida, Gas sensing Characteristics of Porous ZnO and Pt/ZnO Ceramics, *J. Am. Ceram. Soc.* 68 (1) (1985) 40-43.

[Sa99] H. Sakakima, M. Satomi, E. Hirota, H. Adachi, Spin-valves using perovskite antiferromagnets as the pinning layers, *IEEE Transactions on Magnetism* 35 (5) (1999) 2958-2960.

[Sc04] F. Schüth, Hochdurchsatzuntersuchungen in Chemische Technik: Prozesse und Produkte, Winnacker/Küchler, Band 2: Neue Technologien, Wiley-VCH, Weinheim (2004).

[Sc18] P. Scherrer, Bestimmung der Größe und der inneren Struktur von Kolloidteilchen mittels Röntgenstrahlen, *Nachrichten von der Gesellschaft der Wissenschaften zu Göttingen, Mathematisch-Physikalische Klasse* (1918) 98-100.

[Se01] S. Sekan, Combinatorial Heterogeneous Catalysis - A New Path in an Old Field, *Angew. Chem. Int. Ed.* 40(2) (2001) 312-329.

[Se62] T. Seiyama, A. Kato, K. Fujiishi, M. Nagatami, New detector for gaseous components using semiconductive thin films, *Anal. Chem.* 34 (1962) 1502-1503

[Se66] T. Seiyama, S. Kagawa, Detector for gaseous components with semiconductive thin films, *Anal. Chem.* 38 (1966) 1069-1073.

[Se83] T. Seiyama, N. Yamazoe, H. Arai, Ceramic Humidity Sensors, *Sens. Actuators* 4 (1983) 85-96.

[Sh99] Y. Shimizu, M. Egashira, Basic Aspects and Challenges of Semiconductor Gas Sensors, *MRS Bulletin* 24(6) (1999) 18-24.

[Si02] U. Simon, D. Sanders, J. Jockel, C. Heppel, T. Brinz, Design Strategies for Multielectrode Arrays Applicable for High-Throughput Impedance Spectroscopy on Novel Gas Sensor Materials, *J. Comb. Chem.* 4(5) (2002) 511-515.

[Si04] M. Siemons, Th. Weirich, J. Mayer, U. Simon, Preparation of Nanosized Perovskite-type Oxides via Polyol Method, *Z. Anorg. Allg. Chem.* 630 (2004) 2083-2089.

[Si05] U. Simon; D. Sanders; J. Jockel, T. Brinz, Setup for High-Throughput Impedance Screening of Gas-Sensing Materials, *J. Comb. Chem.* 2005, 7(5); 682-687.

[Si06] M. Siemons, U. Simon, Preparation and gas sensing properties of nanocrystalline La-doped CoTiO_3 , *Sens. Actuators B: Chem.* 120(1) (2006) 110-118.

[SI05] A. V. Slaker, N.-J. Choi, J.-H. Kwak, B.-S. Joo, D.-D. Lee, Thick films of In, Bi and Pd metal oxides impregnated in LaCoO_3 perovskite as carbon monoxide sensor, *Sens. Actuators B: Chem.* 106 (2005) 461-467.

[So05] P. Song, H. Qin, L. Zhang, K. An, Z. Lin, J. Hu, M. Jiang, The structure, electrical and ethanol-sensing properties of $\text{La}_{1-x}\text{Pb}_x\text{FeO}_3$ perovskite ceramics with $x \leq 0.3$, *Sens. Actuators B: Chem.* 104(2) (2005) 312-316.

[So05b] P. Song, H. Qin, L. Zhang, X. Liu, S. Huang, J. Hu, M. Jiang, Electrical and CO gas-sensing properties of perovskite-type $\text{La}_{0.8}\text{Pb}_{0.2}\text{Fe}_{0.8}\text{Co}_{0.2}\text{O}_3$ semiconductive material, *Physica B* 368(2005) 204-208.

[So06] B. E. Solsona, J. K. Edwards, P. Landon, A. F. Carley, C. Herzing, Direct synthesis of hydrogen peroxide from H_2 and O_2 using Al_2O_3 supported Au-Pd catalysts, *Chem. Mater.* 18(11) (2006) 2689-2695.

[St01] V. N. Stathopoulos, V. C. Belessi, A. K. Ladavos, Samarium based high surface area perovskite type oxides $\text{SmFe}_{1-x}\text{Al}_x\text{O}_3$ ($x=0.00, 0.50, 0.95$). Part II, catalytic combustion of CH_4 , *React. Kinet. Catal. Lett.* 72(1) (2001) 49-55.

[Su95] H.-T. Sun, C. Cantalini, M. Faccio, M. Pelino, NO_2 gas sensitivity of sol-gel-derived $\alpha\text{-Fe}_2\text{O}_3$ thin films, *Thin Solid Films* 269 (1995) 97-101.

T

[Ta62] N. Taguchi, Patent 45-38200, 1962.

[Te05] Technical information of the Sierra Monitor Corporation, Interscan Corporation, and Figaro Company (2005).

[Ti00] Z. Tianshu, P. Hing, Z. Ruifang, Improvements in $\alpha\text{-Fe}_2\text{O}_3$ ceramic sensors for reducing gases by addition of Sb_2O_3 , *J. Mater. Sci.* 35(6) (2000) 1419-1425.

[To00] P. Toneguzzo, G. Viau, O. Acher, F. Guillet, E. Bruneton, F. Fievet-Vincent, F. Fievet, CoNi and FeCoNi fine particles prepared by the polyol process: physico-chemical characterization and dynamic magnetic properties, *J. Mater. Sci.* 35 (2000) 3767-3784.

[To04] M. Tomoda, S. Okano, I. Yoshiteru, H. Aono, Y. Sadaoka, Air quality prediction by using semiconducting gas sensor with newly fabricated SmFeO_3 film, *Sens. Actuators B: Chem.* 97(2-3) (2004) 190-197.

[To84] Toyama Prefecture, Jpn. Kokai Tokkyo Koho (1984) JP 59067601.

[Tr02] E. Traversa, Y. Sadaoka, M. C. Carotta, G. Martinelli, Environmental monitoring field tests using screen-printed thick-film sensors based on semiconducting oxides, *Sens. Actuators B: Chem.* 65(1-3) (2000) 181-185.

[Tr04] J. Trimboli, P. K. Dutta, Oxidation chemistry and electrical activity of Pt on titania: development of a novel zeolite-filter hydrocarbon sensor, *Sens. Actuators B: Chem.* 102(2004) 134-141.

[Tr95] E. Traversa, S. Matsushima, G. Okada, Y. Sakai, K. Watanabe, NO₂ sensitive LaFeO₃ thin films prepared by r. f. sputtering, *Sens. Actuators B: Chem.* 25 (1995) 661-664.

[Tr99] E. Traversa, S. Villanti, G. Gusmano, Design of Ceramic Materials for Chemical Sensors: SmFeO₃ Thick Film Sensitive to NO₂, *J. Am. Ceram. Soc.* 82(9) (1999) 2442-2450.

V

[va98] R. B. Van Dover, L. F. Schneemeyer, R. M. Fleming, Discovery of a useful thin-film dielectric using a composition-spread approach, *Nature* 392 (1998) 162.

[Vo75] R. J. H. Voorhoeve, J. P. Remeika, L. E. Trimble, Nitric oxide and perovskite-type catalysts: solid state and catalytic chemistry in *The Catalytic Chemistry of Nitrogen Oxides*, Plenum Press (1975).

W

[We95] U. Weimar, W. Göpel, A.C. measurements on tin oxide sensors to improve selectivities and sensitivities, *Sens. Actuators B: Chem.* 23(1-3) (1995) 13-18.

[Wi99] D. E. Williams, Semiconducting oxides as gas-sensitive resistors, *Sens. Actuators B* 57 (1999) 1-16.

X

[Xi95] X.-D. Xiang, X. Sun, G. Briceño, Y. Lou, K.-A. Wang, H. Chang, W. G. Wallace-Freedman, S.-W. Chen, P. G. Schultz, A combinatorial approach to material discovery, *Science* 268 (1995) 1738-1740.

[Xi97] X.-D. Xiang, P. G. Schultz, The Combinatorial Synthesis and Evaluation of Functional Materials, *Physica C* 282-287 (1997) 428-430.

[Xi05] N. Xinshu, L. Honghua, L. Guoguang, Preparation, characterization and photo-catalytic properties of REFeO₃ (RE=Sm, Eu, Gd), *J. Mol. Catal. A: Chem.* 232(1-2) (2005) 89-93.

Y

[Ya03] A. Yamamoto, T. Takada, T. Nakamura, A. Sato, E. Endo (Sony Corp., Japan). *Jpn. Kokai Tokkyo Koho* (2003) JP 2003200051.

[Ya03b] N. Yamazoe, G. Sakai, K. Shimanoe, Oxide Semiconductor Gas Sensors, *Catal. Surv. Asia*, 7 (2003) 63-75.

[Ya05] N. Yamazoe, Towards innovations of gas sensor technology, *Sens. Actuators B: Chem.* 108(1-2) (2005) 2-14.

[Ya91] N. Yamazoe, New approaches for improving semiconductor gas sensor, *Sens. Actuators B: Chem.* 5(1-4) (1991) 7-19.

[Yo01] H. Yokokawa, N. Sakai, T. Horita, K. Yamaji, Recent Developments in Solid Oxide Fuel Cell Materials, *Fuel Cells* 1(2) (2001) 117-131.

[Yo02] Y. K. Yoo, X.-D. Xiang, Combinatorial material preparation, *J. Phys.: Condens. Matter* 14 (2002) R49-R78.

Z

[Zh04] B. L. Zhu, C. S. Xie, A. H. Wang, D. W. Zeng, M. L. Hu, W. Y. Wang, Electrical conductivity and gas sensitivity of Zn-Sb-O thick films, *Mater. Res. Bull.* 39(3) (2004) 409-415.

[Zh04b] J. Zhao, N. L. Ross, R. J. Angel, New view of the high-pressure behaviour of GdFeO₃-type perovskites, *Acta Cryst. B* 60 (2004) 263-271.

[Zh91] H. Zheng, S. Fang, F. Ma, Infrared spectroscopic study of carbon monoxide adsorption on the perovskite-type oxides SmMeO₃, *Hangzhou Daxue Xuebao, Ziran Kexueban* 18(1) (1991) 117-118.

6. Experimental Details

Working under protective atmosphere

All reactions involving air- or moisture-sensitive compounds were performed under nitrogen or argon. For handling of dried solvents, liquids, or dissolved substances, glass and plastic injections with stainless-steel needles were used.

Chemicals

Chemicals and solvents were purchased from commercial suppliers (Acros, Aldrich, Alfa Aesar, Fluka, Merck, Riedel-de Haen and Strem Chemicals) or were available in the group. They were used as purchased without further purification.

Test gases

Table 6.1 shows the used test gases including carrier gas and purity.

Table 6.1: Test gases.

<i>analyte</i>	<i>purity</i>	<i>carrier gas</i>	<i>producer</i>	<i>concentration/ppm</i>
H ₂	3.0	synthetic air	Messer-Griesheim	104 ± 2%
CO	1.8	synthetic air	Messer-Griesheim	528 ± 2%
NO	2.5	nitrogen 5.0	Messer-Griesheim	10 ± 2%
NO ₂	1.8	synthetic air	Messer-Griesheim	10 ± 5%
ethanol	—	synthetic air	Messer-Griesheim	200 ± 1%
propylene	2.5	synthetic air	Messer-Griesheim	502 ± 2%

Characterisation of the products

All prepared materials have been characterised by powder X-ray diffraction and SEM measurements.

Powder X-ray diffraction

The characterisation of the products was carried out by powder XRD measurements (CuK α , λ = 1.54059 Å, monochromated by quartz crystal) on thin films with a Huber Image Plate (Image Foil Guinier Camera G 670) in transmission. Powder diffraction patterns were analysed using Stoe WinX^{Pow} 1.06 Software (Stoe&CIE GmbH).

Samples were measured for 120 min. In special cases, measurements overnight (900 min) have been performed.

SEM measurements

Powder morphology was examined by SEM analysis using a Zeiss DSM 982 Gemini or a LEO Supra 35VP (acceleration voltage 2 to 7 kV). All samples were sputtered with carbon. Images were partly taken at the GFE Aachen.

EDX measurements

Energy dispersive X-ray microanalysis (EDX) spectra were collected in order to check the chemical composition of the nanocrystals using a LEO Supra 35VP equipped with an EDX system (Inca Energy 200, Oxford).

TEM measurements

Specimens for TEM investigation were prepared from suspensions of each sample, pipetted onto carbon-coated copper grids. Selected area electron diffraction patterns (SADP) were obtained from the samples using an FEI Tecani F20 electron microscope operated at 200 kV. Images were taken at the GFE Aachen.

XRF measurements

X-ray fluorescence (XRF) spectra were collected in order to check the chemical composition of the nanocrystals using an Eagle μ -Probe II (Röntgenanalytik Meßtechnik GmbH).

Software

For sensor property determination, almost all used software was in-house production, further information can be found in [Sa04]. Following programmes have been used:

- Spotfire® - *Decision Site Browser*: visual Data Mining, information at www.spotfire.com
- *Trellis Plot* – in-house production: visual Data Mining
- *SQL_Miner* - in-house production: pattern recognition
- *Kombis* – in-house production: impedance analysis for multielectrode arrays
- *Quick Fit Full*- in-house production: automated data fitting

6.1 General synthesis procedure

6.1.1 Synthesis of different ABO_3

Perovskite-type particles have been synthesised according to the polyol process by precipitation from precursors dissolved in diethylene glycol (DEG). According to the guidelines given in the text (see section 3.1), the detailed experimental procedure was as follows.

Starting compounds were placed in a round-bottomed flask fitted with a reflux condenser. The presursors were dispersed in diethylene glycol (Merck, 99.99%). The solution containing the reactants was slowly heated up to T_1 under mechanical stirring at 700 RPM. Hydrolysing agent was added to the mixture after salt dissolution. Afterwards, the temperature was increased to T_2 and maintained for several hours. The solution was then cooled to room temperature. The preparation resulted in a stable suspension (1 wt% solid to DEG).

For further characterisation of the “as synthesised” material, the solid product was separated from the suspension via centrifugation in acetone and dried at 90 °C. The suspension could be transferred into the crystalline phase by temperature treatment at 400°C for one hour and after that at T_3 . Figure 1 shows two examples of used temperature ramps. Temperature treatment was performed in a Nabertherm LHT 08/17 oven (Nabertherm GmbH).

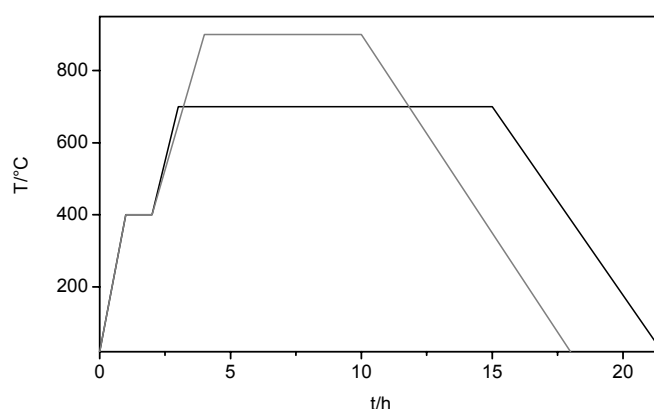


Figure 6.1: Temperature ramp for annealing at —700°C (12h) and — 900°C (6h).

Details for each compound are given in the following tables.

Table 6.2: Synthesis of various ABO_3 materials. In all cases 0.4 mL hydrolysing agent and 10 mL DEG were used, except * where 20 mL DEG were used. Bp means byproduct

<i>compound</i>	<i>precursor</i>	$T_1/^\circ\text{C}$	<i>hydrolysis agent</i>	$T_2/^\circ\text{C}$	t/h	$T_3/^\circ\text{C}$	t/h	<i>bp</i>
$\text{La}_{0.8}\text{Sr}_{0.2}\text{CoO}_3^*$	0.821 mmol $\text{La}(\text{NO}_3)_3 \cdot 6\text{H}_2\text{O}$ 99% Fluka 0.205 mmol $\text{Sr}(\text{CH}_3\text{COO})_2$ Aldrich 1.026 mmol $\text{Co}(\text{CH}_3\text{COO})_2 \cdot 4\text{H}_2\text{O}$ 99% Merck	130	HNO_3 65% p.a. Merck	180	5	700	12	—
NdCoO_3	0.450 mmol $\text{Nd}(\text{CH}_3\text{COO})_3 \cdot n\text{H}_2\text{O}$ 99% Alfa Aesar 0.450 mmol $\text{Co}(\text{CH}_3\text{COO})_2 \cdot 4\text{H}_2\text{O}$ 99% Merck	120	—	180	5	700	12	—
SmCoO_3	0.437 mmol $\text{Sm}(\text{NO}_3)_3 \cdot 6\text{H}_2\text{O}$ 99,9% Acros 0.437 mmol $\text{Co}(\text{CH}_3\text{COO})_2 \cdot 4\text{H}_2\text{O}$ 99% Merck	120	—	180	5	700	12	not identified
GdCoO_3	0.428 mmol $\text{Gd}(\text{CH}_3\text{COO})_3 \cdot n\text{H}_2\text{O}$ 99,9% Alfa Aesar 0.428 mmol $\text{Co}(\text{CH}_3\text{COO})_2 \cdot 4\text{H}_2\text{O}$ 99% Merck	120	HNO_3 65% p.a. Merck	160	5	700	12	—
HoCoO_3	0.416 mmol $\text{Ho}(\text{NO}_3)_3 \cdot 5\text{H}_2\text{O}$ 99,9% Alfa Aesar 0.416 mmol $\text{Co}(\text{CH}_3\text{COO})_2 \cdot 4\text{H}_2\text{O}$ 99% Merck	100	—	170	5	900	10	—
MnFeO_3	0.711 mmol $\text{Fe}(\text{NO}_3)_3 \cdot 9\text{H}_2\text{O}$ 98% Merck 0.711 mmol $\text{Mn}(\text{CH}_3\text{COO})_3 \cdot 2\text{H}_2\text{O}$ 97% Aldrich	130	—	180	5	700	12	—
MnFeO_3^*	2 mmol $\text{Fe}(\text{NO}_3)_3 \cdot 9\text{H}_2\text{O}$ 98% Merck 2 mmol $\text{Mn}(\text{CH}_3\text{COO})_2 \cdot 4\text{H}_2\text{O}$ 98% Merck	110	H_2O_2 30% p.a. Fluka	180	5	700	12	—

YFeO ₃	0.587 mmol Fe(NO ₃) ₃ ·9H ₂ O 98% Merck	80		180	4	900	6	—
NiMnO ₃ [*]	0.587 mmol Y(NO ₃) ₃ ·6H ₂ O 99.9% Aldrich	170	H ₂ O ₂ 30% p.a. Fluka	180	5	700	6	Ni ₆ MnO ₈ in traces
BiBaO ₃	1.4 mmol Mn(CH ₃ COO) ₂ ·4H ₂ O 98% Merck	130	NH ₃ 25% p.a. Merck	180	5	700	12	—
BiFeO ₃	1.4 mmol Ni(CH ₃ COO) ₂ ·4H ₂ O 0.286 mmol Bi(NO ₃) ₃ ·3H ₂ O 99.5% Riedel	130	—	180	5	700	12	Bi ₂ O ₃ in traces
PbTiO ₃	0.286 mmol Ba(CH ₃ COO) ₂ 99% Riedel-de Haen	130	HNO ₃ 33% p. a. Merck	180	5	700	12	TiO ₂ and PbO in traces
Ba _{0.98} La _{0.02} SnO ₃	0.362 mmol Fe(NO ₃) ₃ ·9H ₂ O 98% Merck	140	HNO ₃ 65% p. a. Merck	180	5	700	12	SnO ₂ in traces
BaSnO ₃	0.362 mmol Bi(NO ₃) ₃ ·3H ₂ O 99.5% Riedel	140	HNO ₃ 65% p. a. Merck	180	5	700	12	SnO ₂ in traces
BaTiO ₃	0.37 mmol Ti[OCH(CH ₃) ₂] ₄ 97% Aldrich	130	KOH solution (2M)	180	5	700	12	—
CdSnO ₃	0.37 mmol Pb(CH ₃ COO) ₂ ·3H ₂ O p. A. Merck	130	NH ₃ 25% p.a. Merck	180	5	750	12	SnO ₂
	0.36 mmol Ba(CH ₃ COO) ₂ 99% Riedel-de Haen							
	0.01 mmol La(NO ₃) ₃ ·6H ₂ O 99% Fluka							
	0.37 mmol Sn(CH ₃ COO) ₄ Aldrich							
	0.37 mmol Ba(CH ₃ COO) ₂ 99% Riedel-de Haen							
	0.37 mmol Sn(CH ₃ COO) ₄ Aldrich							
	0.48 mmol Ba(CH ₃ COO) ₂ 99% Riedel-de Haen							
	0.48 mmol Ti[OCH(CH ₃) ₂] ₄ 97% Aldrich							
	0.405 mmol Cd(CH ₃ COO) ₂ ·2H ₂ O 97% Fluka							
	0.405 mmol Sn(CH ₃ COO) ₄ Aldrich							

Experimental

SrFeO ₃	0.590 mmol Fe(NO ₃) ₃ ·9H ₂ O 98% Merck 0.590 mmol Sr(CH ₃ COO) ₂ Aldrich	110	HNO ₃ 65% p. a. Merck	170	5	700	12	-
--------------------	--	-----	-------------------------------------	-----	---	-----	----	---

6.1.2 Synthesis of LnCrO₃ materials

Materials were synthesised by the general preparation method described above. Cr(NO₃)₃·9H₂O (96% Alfa Aesar) was used as the chromium source. In all cases 10 mL DEG and 0.4 mL hydrolysing agent were added.

Table 6.3: Synthesis of LnCrO₃ materials.

<i>compound</i>	<i>Ln-precursor</i>	<i>T₁/°C</i>	<i>hydrolysis agent</i>	<i>T₂/°C</i>	<i>t/h</i>	<i>T₃/°C</i>	<i>t/h</i>
LaCrO ₃	0.473 mmol La(NO ₃) ₃ ·6H ₂ O 99% Fluka	110	—	175	5	700	12
PrCrO ₃	0.469 mmol Pr(NO ₃) ₃ ·6H ₂ O 99,9% Aldrich	100	—	175	5	700	12
SmCrO ₃	0.451 mmol Sm(NO ₃) ₃ ·6H ₂ O 99,9% Acros	100	—	180	5	700	12
EuCrO ₃	0.224 mmol Eu ₂ (CO ₃) ₃ ·nH ₂ O 99,9% Alfa Aesar	130	—	190	5	900	2
GdCrO ₃	0.439 mmol Gd(CH ₃ COO) ₃ ·nH ₂ O 99,9% Alfa Aesar	100	HNO ₃ 65% p.a. Merck	170	5	700	12
TbCrO ₃	0.436 mmol Tb(NO ₃) ₃ ·6H ₂ O 99,9% Acros	90	—	190	5	900	2
DyCrO ₃	0.430 mmol Dy(NO ₃) ₃ ·5H ₂ O 99,9% Alfa Aesar	90	—	170	5	700	12
HoCrO ₃	0.426 mmol Ho(NO ₃) ₃ ·5H ₂ O 99,9% Alfa Aesar	80	—	170	5	900	4
ErCrO ₃	0.211 mmol Er ₂ (CO ₃) ₃ ·nH ₂ O 99,9% Alfa Aesar	100	HNO ₃ 65% p.a. Merck	175	5	700	6
TmCrO ₃	0.420 mmol Tm(CH ₃ COO) ₃ ·nH ₂ O 99,9% Alfa Aesar	90	—	170	5	900	2
YbCrO ₃	0.414 mmol Yb(NO ₃) ₃ ·5H ₂ O 99,9% Strem	80	—	180	5	700	6
LuCrO ₃	0.411 mmol Lu(CH ₃ COO) ₃ ·nH ₂ O 99,9% Alfa Aesar	130	—	170	5	900	2

6.1.3 Synthesis of LnFeO₃ materials

Materials were synthesised by the general preparation method described above. Fe(NO₃)₃·9H₂O (98% Merck) was used as iron source. In all cases 10 mL DEG and 0.4 mL hydrolysing agent were added.

Table 6.4: Synthesis of LnFeO₃ materials.

<i>compound</i>	<i>Ln-precursor</i>	<i>T₁/°C</i>	<i>hydrolysis agent</i>	<i>T₂/°C</i>	<i>t/h</i>	<i>T₃/°C</i>	<i>t/h</i>
LaFeO ₃	0.465 mmol La(NO ₃) ₃ ·6H ₂ O 99% Fluka	120	—	160	5	700	12
PrFeO ₃	0.283 mmol Pr(NO ₃) ₃ ·6H ₂ O 99,9% Aldrich	130	—	180	5	700	12
NdFeO ₃	0.455 mmol Nd(CH ₃ COO) ₃ ·nH ₂ O 99% Alfa Aesar	120	—	160	5	700	12
SmFeO ₃	0.443 mmol Sm(NO ₃) ₃ ·6H ₂ O 99,9% Acros	120	—	160	5	700	12
EuFeO ₃	0.221 mmol Eu ₂ (CO ₃) ₃ ·nH ₂ O 99,9% Alfa Aesar	140	—	180	5	700	12
GdFeO ₃	0.433 mmol Gd(CH ₃ COO) ₃ ·nH ₂ O 99,9% Alfa Aesar	80	HNO ₃ 65% Merck	160	5	700	12
TbFeO ₃	0.430 mmol Tb(NO ₃) ₃ ·6H ₂ O 99,9% Acros	110	HNO ₃ 65% Merck	170	5	700	12
DyFeO ₃	0.424 mmol Dy(NO ₃) ₃ ·5H ₂ O 99,9% Alfa Aesar	120	—	160	5	700	12
HoFeO ₃	0.420 mmol Ho(NO ₃) ₃ ·5H ₂ O 99,9% Alfa Aesar	110	—	170	5	700	12
ErFeO ₃	0.208 mmol Er ₂ (CO ₃) ₃ ·nH ₂ O 99,9% Alfa Aesar	105	—	175	5	700	12
TmFeO ₃	0.414 mmol Tm(CH ₃ COO) ₃ ·nH ₂ O	110	HNO ₃ 65% Merck	160	5	800	12
YbFeO ₃	0.408 mmol Yb(NO ₃) ₃ ·5H ₂ O 99,9% Strem	130	NH ₃ 25% p.a. Merck	160	5	700	12
LuFeO ₃	0.414 mmol Lu(CH ₃ COO) ₃ ·nH ₂ O 99,9% Alfa Aesar	100	—	180	5	900	12

6.1.4 Synthesis of volume doped SmFeO_3

Materials were synthesised by the general preparation method described above. In all cases 10 mL DEG and 0.4 mL HNO_3 were used. All samples were annealed for 12 h at 700°C .

Table 6.5: Synthesis of volume doped SmFeO_3 materials.

<i>compound</i>	<i>precursor</i>	<i>volume dopant</i>	$T_1/^\circ\text{C}$	$T_2/^\circ\text{C}$	t/h
SmFeO_3	0.443 mmol $\text{Sm}(\text{NO}_3)_3 \cdot 6\text{H}_2\text{O}$ 99,9% Acros 0.443 mmol $\text{Fe}(\text{NO}_3)_3 \cdot 9\text{H}_2\text{O}$ 98% Merck		110	180	5
$\text{Sm}_{0.9}\text{La}_{0.1}\text{FeO}_3$	0.399 mmol $\text{Sm}(\text{NO}_3)_3 \cdot 6\text{H}_2\text{O}$ 99,9% Acros 0.443 mmol $\text{Fe}(\text{NO}_3)_3 \cdot 9\text{H}_2\text{O}$ 98% Merck	0.044 mmol $\text{La}(\text{NO}_3)_3 \cdot 6\text{H}_2\text{O}$ 99% Fluka	110	160	5
$\text{Sm}_{0.8}\text{La}_{0.2}\text{FeO}_3$	0.354 mmol $\text{Sm}(\text{NO}_3)_3 \cdot 6\text{H}_2\text{O}$ 99,9% Acros 0.443 mmol $\text{Fe}(\text{NO}_3)_3 \cdot 9\text{H}_2\text{O}$ 98% Merck	0.089 mmol $\text{La}(\text{NO}_3)_3 \cdot 6\text{H}_2\text{O}$ 99% Fluka	100	170	5
$\text{Sm}_{0.9}\text{Sr}_{0.1}\text{FeO}_3$	0.399 mmol $\text{Sm}(\text{NO}_3)_3 \cdot 6\text{H}_2\text{O}$ 99,9% Acros 0.443 mmol $\text{Fe}(\text{NO}_3)_3 \cdot 9\text{H}_2\text{O}$ 98% Merck	0.044 mmol $\text{Sr}(\text{CH}_3\text{COO})_2$ Aldrich	110	180	5
$\text{Sm}_{0.8}\text{Sr}_{0.2}\text{FeO}_3$	0.354 mmol $\text{Sm}(\text{NO}_3)_3 \cdot 6\text{H}_2\text{O}$ 99,9% Acros 0.443 mmol $\text{Fe}(\text{NO}_3)_3 \cdot 9\text{H}_2\text{O}$ 98% Merck	0.089 mmol $\text{Sr}(\text{CH}_3\text{COO})_2$ Aldrich	100	170	4
$\text{SmFe}_{0.9}\text{Co}_{0.1}\text{O}_3$	0.443 mmol $\text{Sm}(\text{NO}_3)_3 \cdot 6\text{H}_2\text{O}$ 99,9% Acros 0.399 mmol $\text{Fe}(\text{NO}_3)_3 \cdot 9\text{H}_2\text{O}$ 98% Merck	0.044 mmol $\text{Co}(\text{CH}_3\text{COO})_2 \cdot 4\text{H}_2\text{O}$ 99% Merck	100	165	4
$\text{SmFe}_{0.8}\text{Co}_{0.2}\text{O}_3$	0.443 mmol $\text{Sm}(\text{NO}_3)_3 \cdot 6\text{H}_2\text{O}$ 99,9% Acros 0.354 mmol $\text{Fe}(\text{NO}_3)_3 \cdot 9\text{H}_2\text{O}$ 98% Merck	0.089 mmol $\text{Co}(\text{CH}_3\text{COO})_2 \cdot 4\text{H}_2\text{O}$ 99% Merck	120	170	5

SmFe _{0.9} Cr _{0.1} O ₃	0.443 mmol Sm(NO ₃) ₃ ·6H ₂ O 99,9% Acros 0.399 mmol Fe(NO ₃) ₃ ·9H ₂ O 98% Merck	0.044 mmol Cr(NO ₃) ₃ ·9H ₂ O 96% Alfa Aesar	120	160	5
SmFe _{0.8} Cr _{0.2} O ₃	0.443 mmol Sm(NO ₃) ₃ ·6H ₂ O 99,9% Acros 0.354 mmol Fe(NO ₃) ₃ ·9H ₂ O 98% Merck	0.089 mmol Cr(NO ₃) ₃ ·9H ₂ O 96% Alfa Aesar	100	150	5
SmFe _{0.9} Mn _{0.1} O ₃	0.443 mmol Sm(NO ₃) ₃ ·6H ₂ O 99,9% Acros 0.399 mmol Fe(NO ₃) ₃ ·9H ₂ O 98% Merck	0.044 mmol Mn(CH ₃ COO) ₃ ·2H ₂ O 97% Aldrich	130	170	5

6.1.5 Synthesis of volume doped CoTiO₃

Materials were synthesised by the general preparation method described above. In all cases 10 mL DEG and 0.4 mL HNO₃ were used. All samples were annealed for 12 h at 700°C.

Table 6.6: Synthesis of volume doped CoTiO₃ materials.

<i>compound</i>	<i>precursor</i>	<i>volume dopant</i>	<i>T₁/°C</i>	<i>T₂/°C</i>	<i>t/h</i>
CoTiO ₃	0.730 mmol Ti[OCH(CH ₃) ₂] ₄ 97% Aldrich 0.730 mmol Co(CH ₃ COO) ₂ ·4H ₂ O 99% Merck		130	160	5
CoTiO ₃ :La _A (2 at%)	0.730 mmol Ti[OCH(CH ₃) ₂] ₄ 97% Aldrich 0.715 mmol Co(CH ₃ COO) ₂ ·4H ₂ O 99% Merck	0.015 mmol La(NO ₃) ₃ ·6H ₂ O 99% Fluka	130	180	5
CoTiO ₃ :La _B (2 at%)	0.715 mmol Ti[OCH(CH ₃) ₂] ₄ 97% Aldrich 0.730 mmol Co(CH ₃ COO) ₂ ·4H ₂ O 99% Merck	0.015 mmol La(NO ₃) ₃ ·6H ₂ O 99% Fluka	130	175	5
CoTiO ₃ :K (2 at%)	0.730 mmol Ti[OCH(CH ₃) ₂] ₄ 97% Aldrich 0.715 mmol Co(CH ₃ COO) ₂ ·4H ₂ O 99% Merck	0.015 mmol K(CH ₃ COO) 99% Merck	130	180	5
CoTiO ₃ :Sm _B (2 at%)	0.715 mmol Ti[OCH(CH ₃) ₂] ₄ 97% Aldrich 0.730 mmol Co(CH ₃ COO) ₂ ·4H ₂ O 99% Merck	0.015 mmol Sm(NO ₃) ₃ ·6H ₂ O 99.9% Acros	110	170	5
CoTiO ₃ :Sm _A (2 at%)	0.730 mmol Ti[OCH(CH ₃) ₂] ₄ 97% Aldrich 0.715 mmol Co(CH ₃ COO) ₂ ·4H ₂ O 99% Merck	0.015 mmol Sm(NO ₃) ₃ ·6H ₂ O 99.9% Acros	110	165	5
CoTiO ₃ :Li (2 at%)	0.730 mmol Ti[OCH(CH ₃) ₂] ₄ 97% Aldrich 0.715 mmol Co(CH ₃ COO) ₂ ·4H ₂ O 99% Merck	0.015 mmol LiNO ₃ 99.99% Alfa Aesar	110	160	4

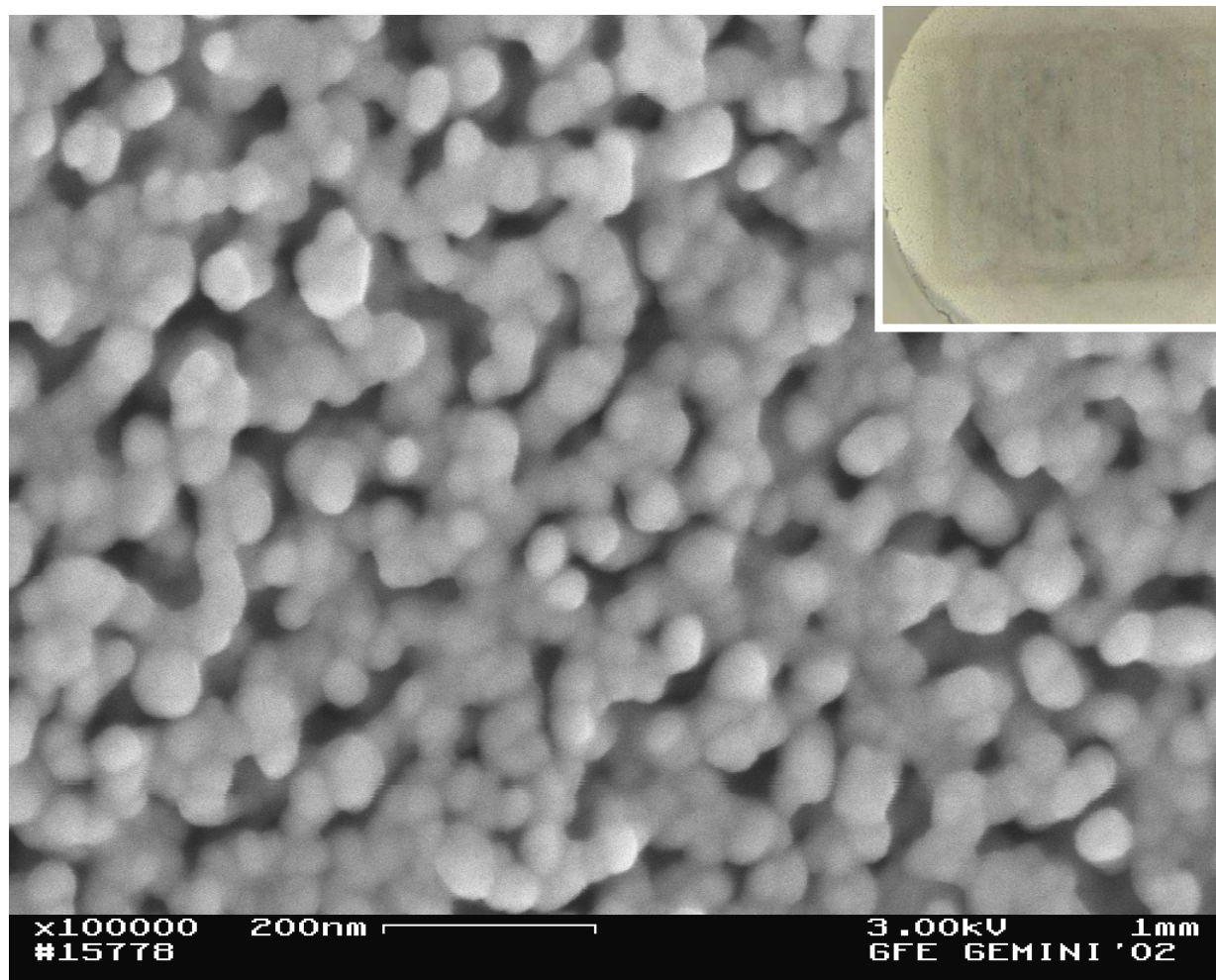
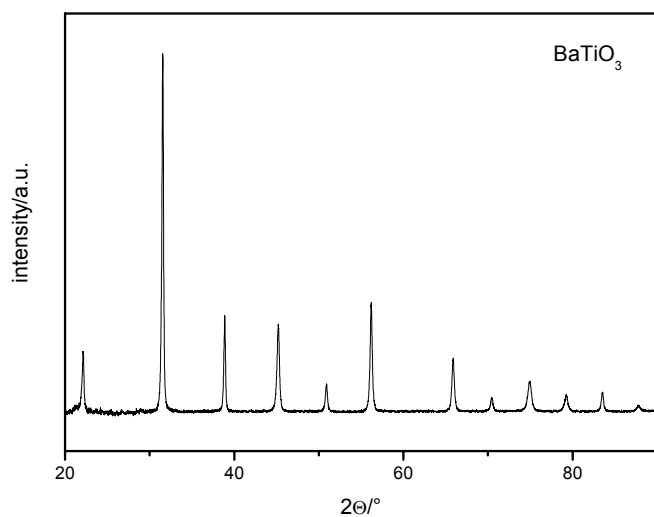
CoTiO ₃ :Gd (2 at%)	0.715 mmol Ti[OCH(CH ₃) ₂] ₄ 97% Aldrich 0.730 mmol Co(CH ₃ COO) ₂ ·4H ₂ O 99% Merck	0.015 mmol Gd(CH ₃ COO) ₃ ·nH ₂ O 99.99% Alfa Aesar	130	180	4
CoTiO ₃ :Ho _A (2 at%)	0.730 mmol Ti[OCH(CH ₃) ₂] ₄ 97% Aldrich 0.715 mmol Co(CH ₃ COO) ₂ ·4H ₂ O 99% Merck	0.015 mmol Ho(NO ₃) ₃ ·5H ₂ O 99.9% Alfa Aesar	110	180	5
CoTiO ₃ :Ho _B (2 at%)	0.715 mmol Ti[OCH(CH ₃) ₂] ₄ 97% Aldrich 0.730 mmol Co(CH ₃ COO) ₂ ·4H ₂ O 99% Merck	0.015 mmol Ho(NO ₃) ₃ ·5H ₂ O 99.9% Alfa Aesar	110	160	5
CoTiO ₃ :Sb (2 at%)	0.715 mmol Ti[OCH(CH ₃) ₂] ₄ 97% Aldrich 0.730 mmol Co(CH ₃ COO) ₂ ·4H ₂ O 99% Merck	0.015 mmol Sb(CH ₃ COO) ₃ 99.99% Aldrich	110	180	5
CoTiO ₃ :Pb (2 at%)	0.715 mmol Ti[OCH(CH ₃) ₂] ₄ 97% Aldrich 0.730 mmol Co(CH ₃ COO) ₂ ·4H ₂ O 99% Merck	0.015 mmol Pb(CH ₃ COO) ₂ ·3H ₂ O p. A. Merck	110	160	5
CoTiO ₃ :Na (2 at%)	0.730 mmol Ti[OCH(CH ₃) ₂] ₄ 97% Aldrich 0.715 mmol Co(CH ₃ COO) ₂ ·4H ₂ O 99% Merck	0.015 mmol Na(CH ₃ COO) 3H ₂ O z. A. Merck	120	180	5

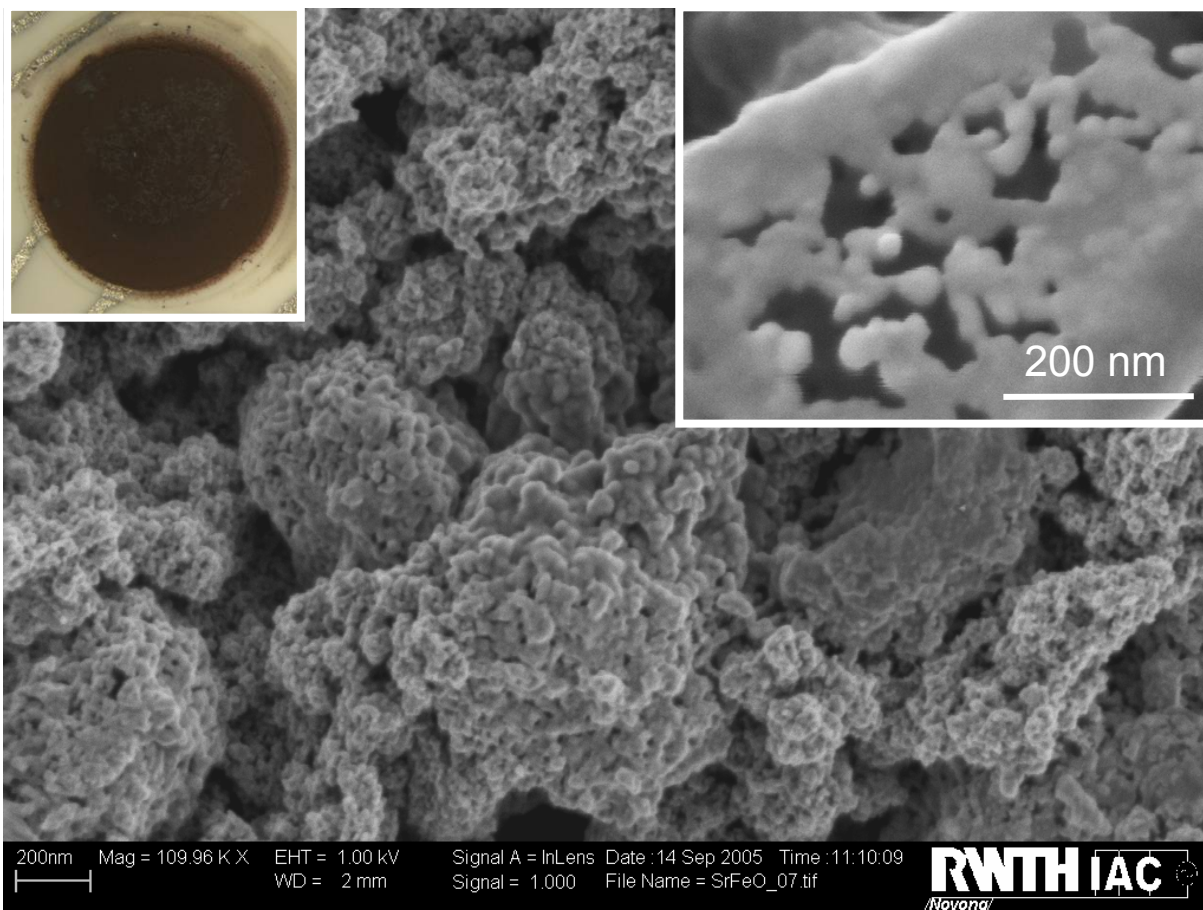
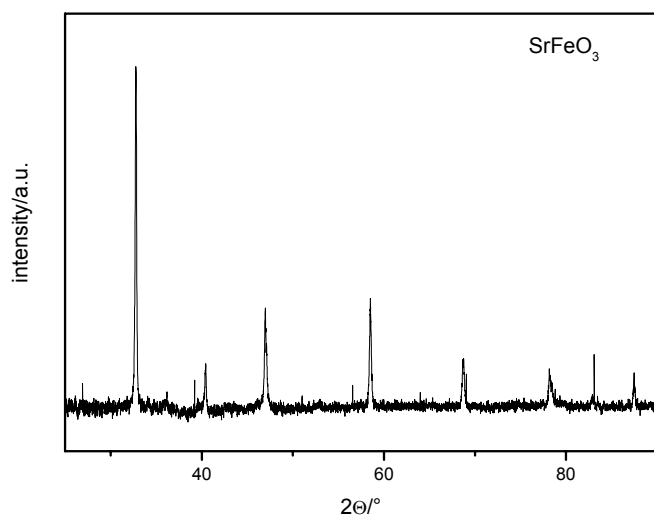
7. Appendix

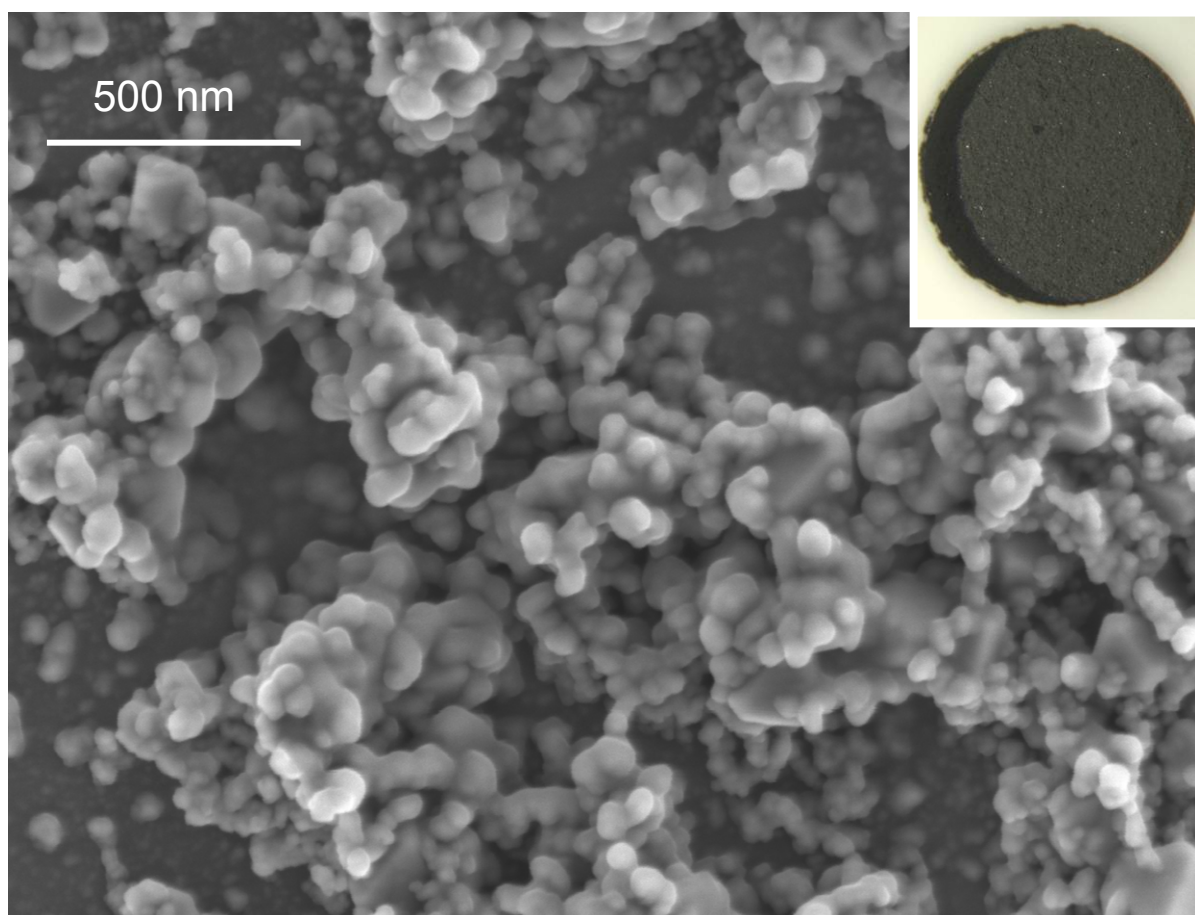
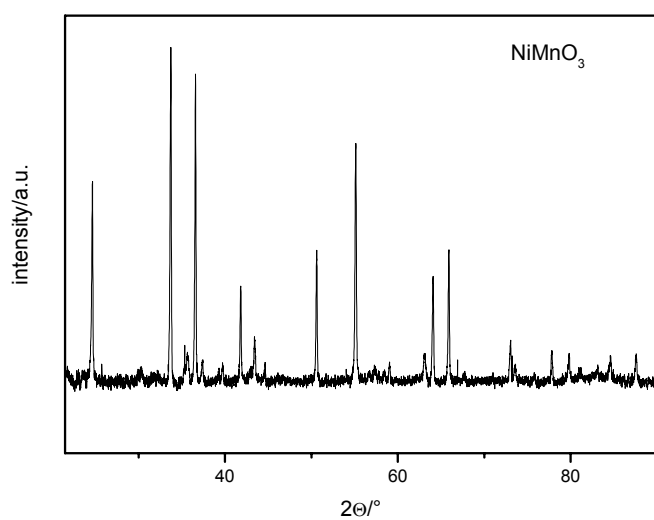
7.1 Characteristics of ABO_3 materials

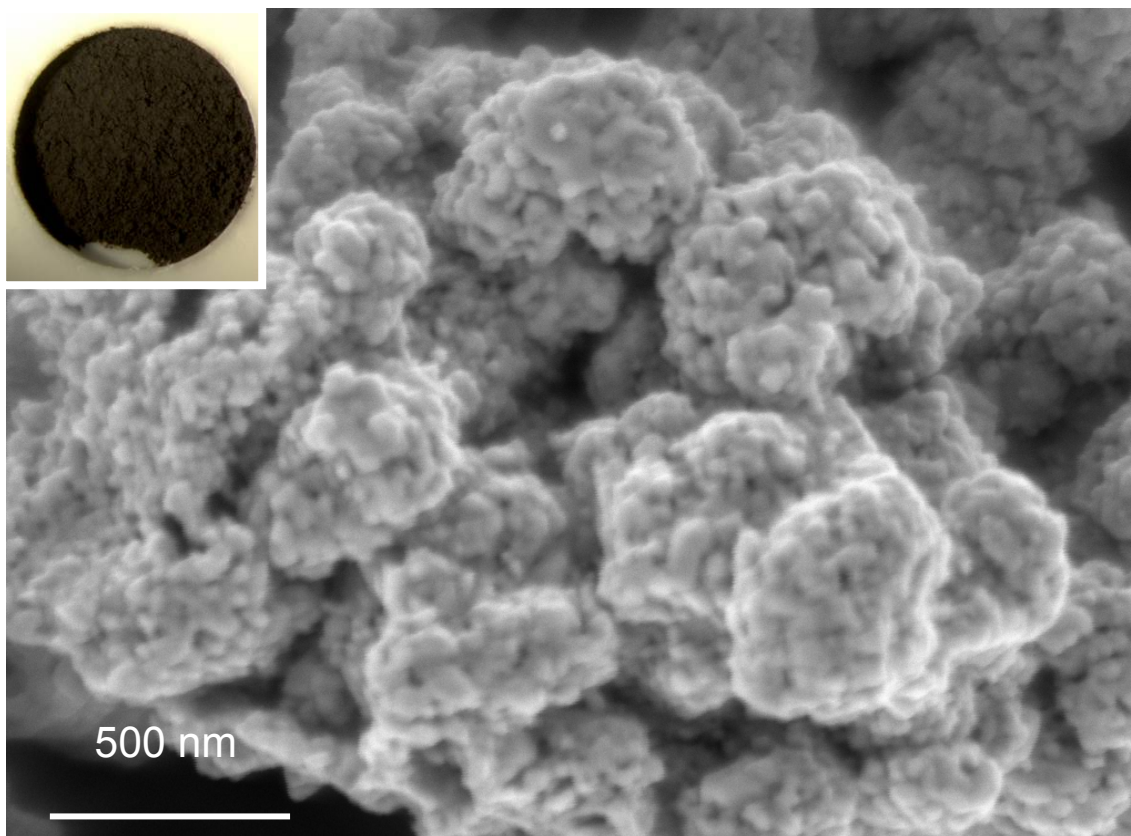
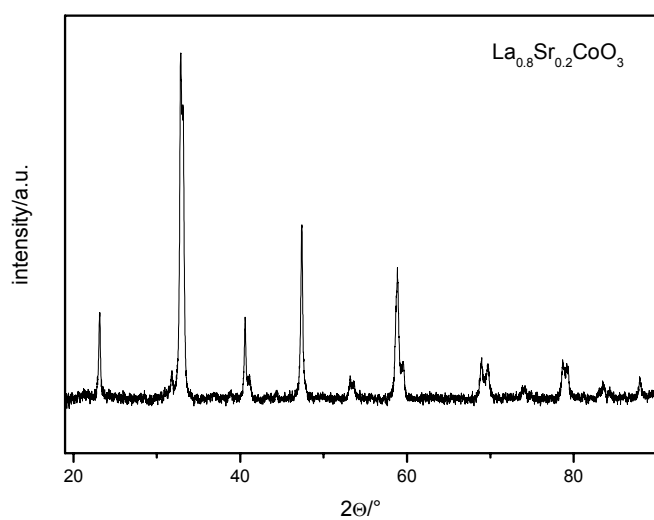
XRD, SEM and thick film pictures of materials that were mentioned in chapter 3.1

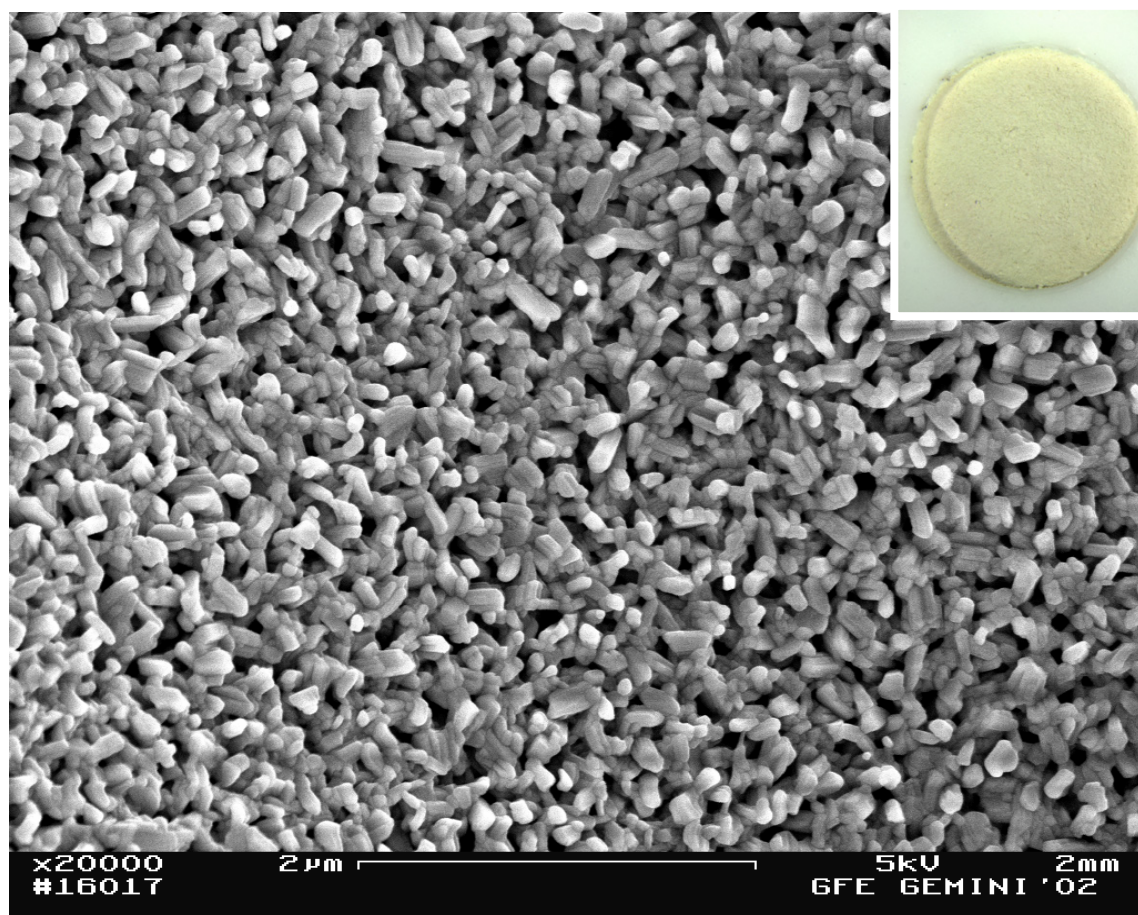
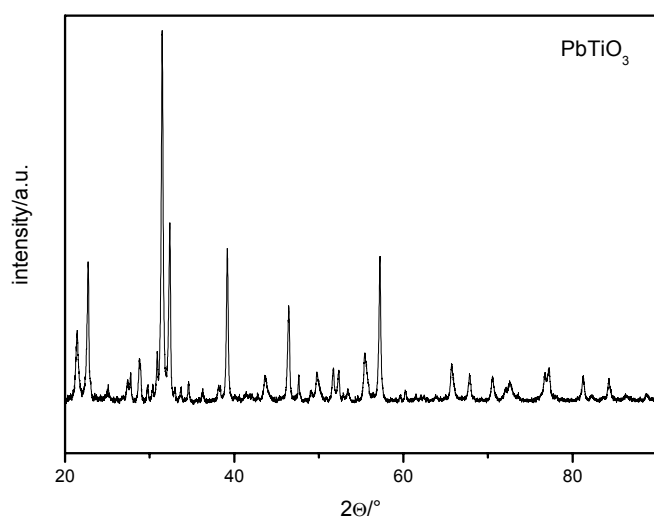
$BaTiO_3$

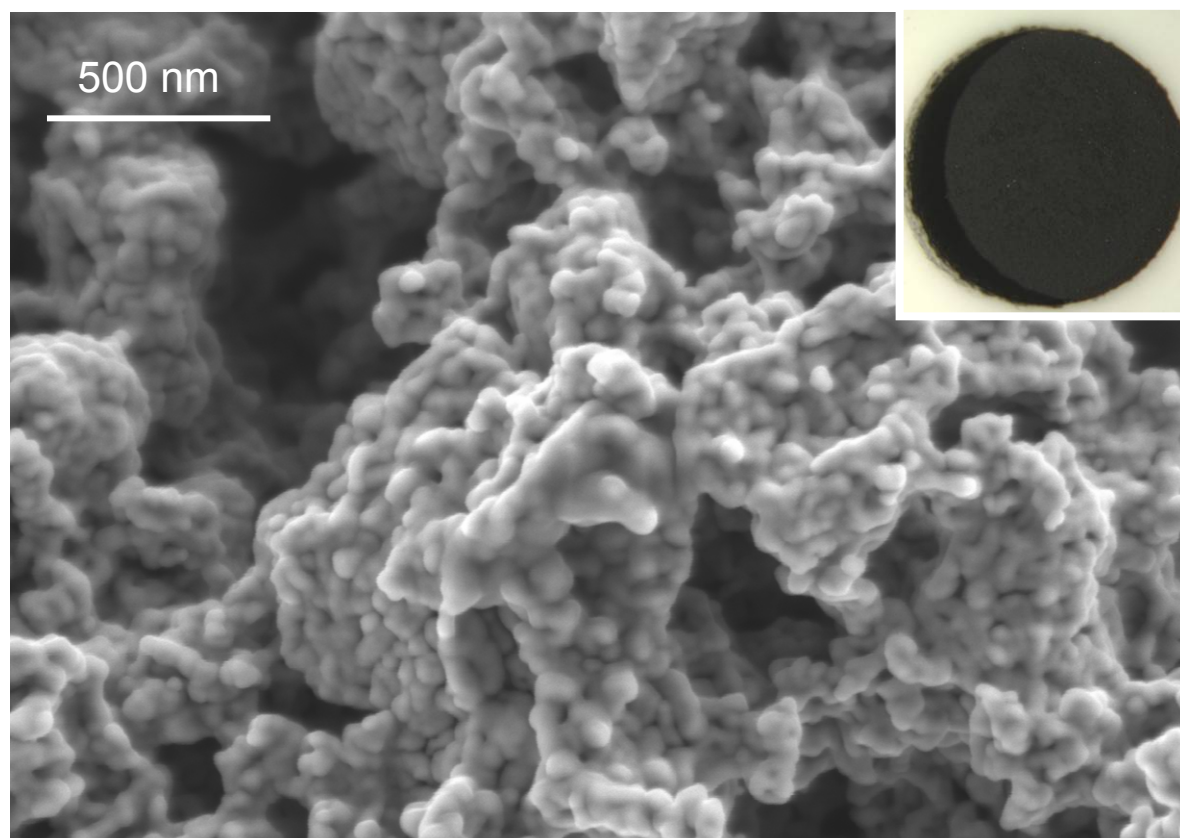
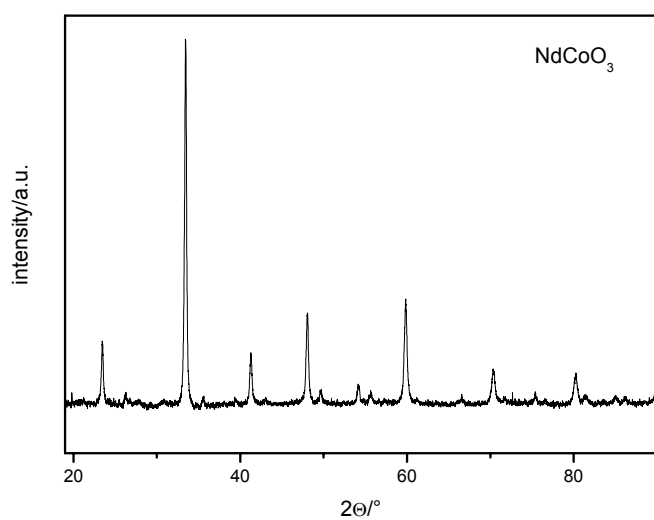


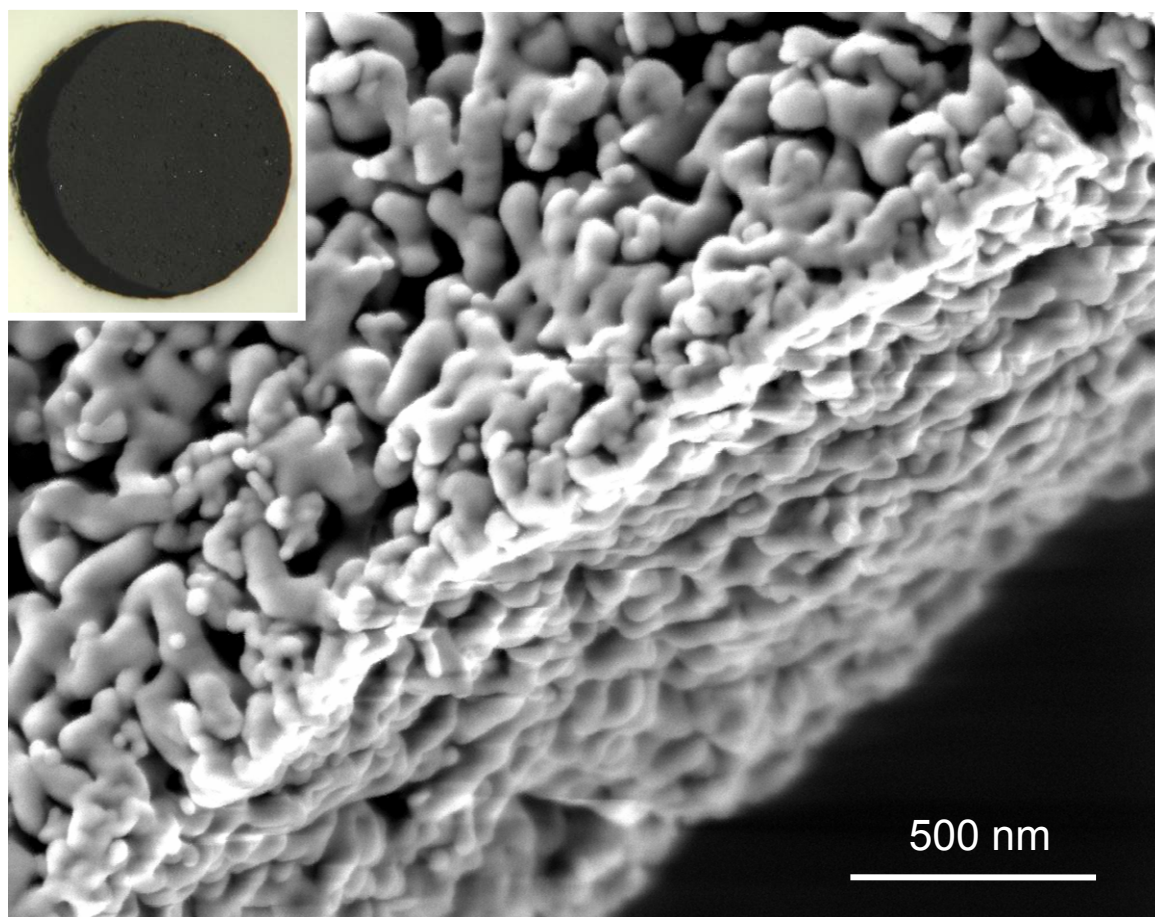
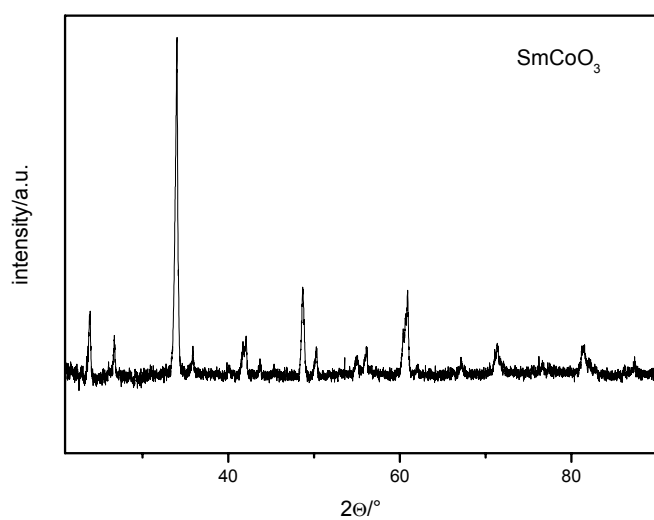
SrFeO₃

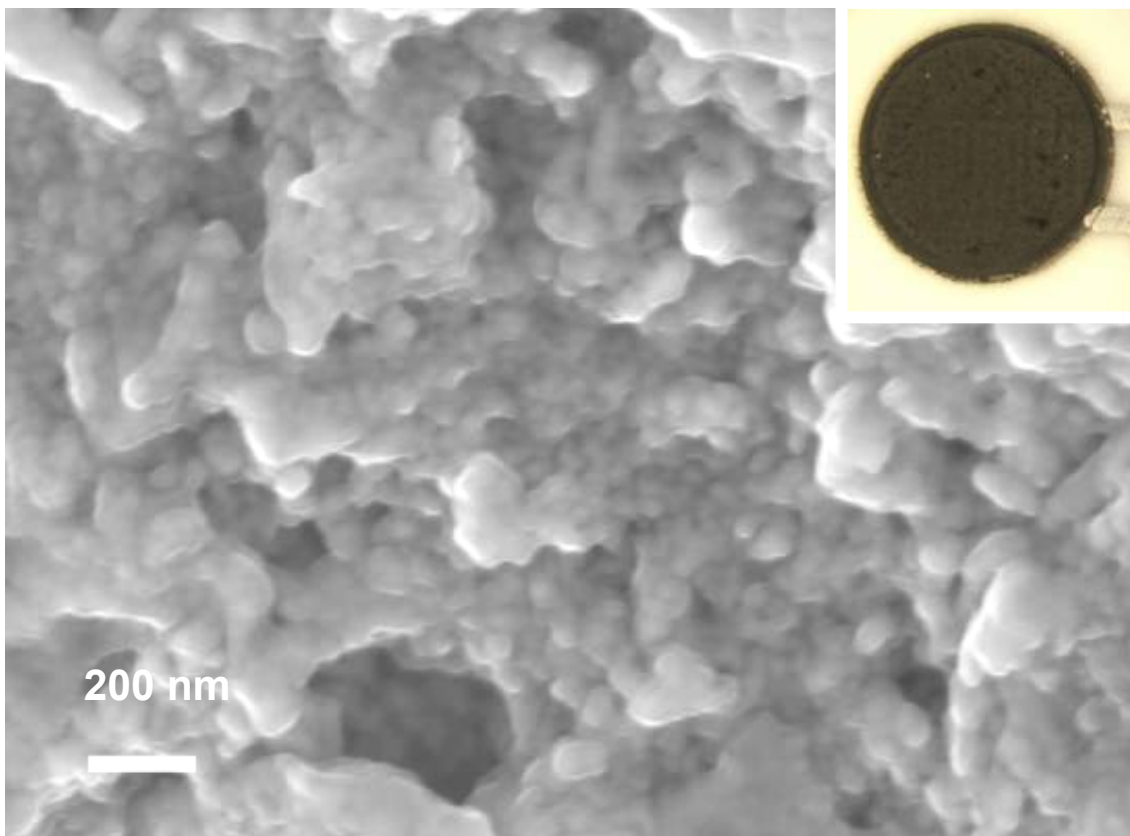
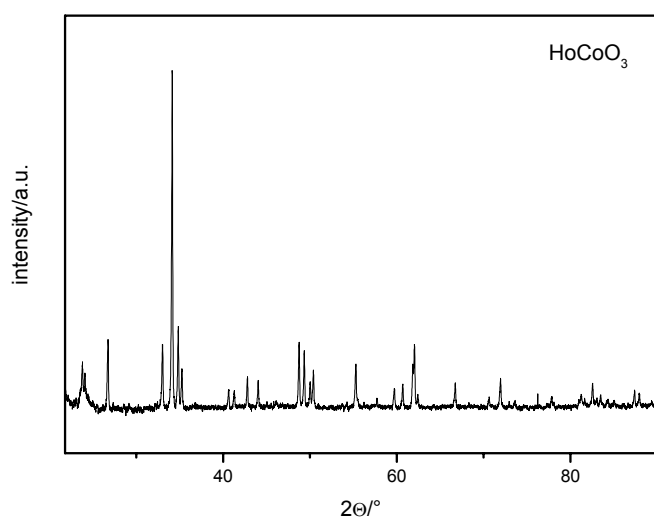
NiMnO₃

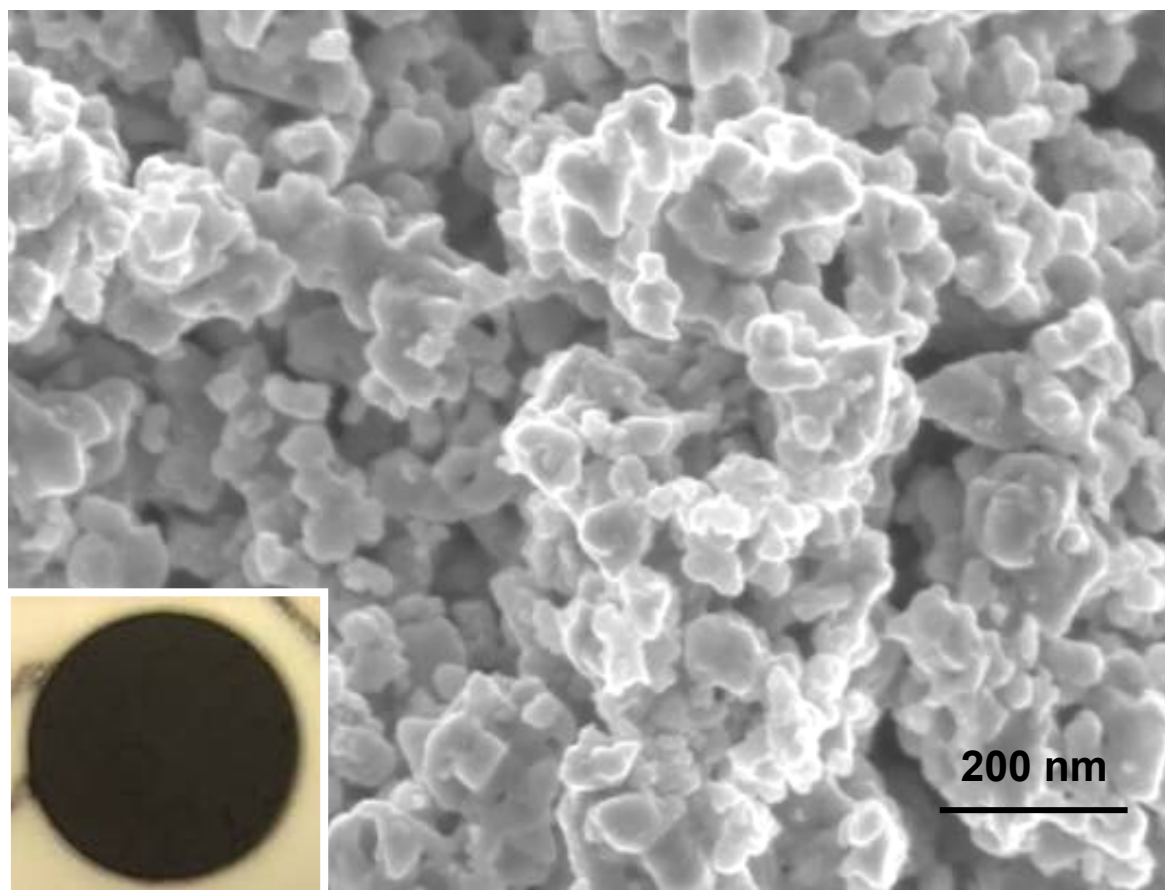
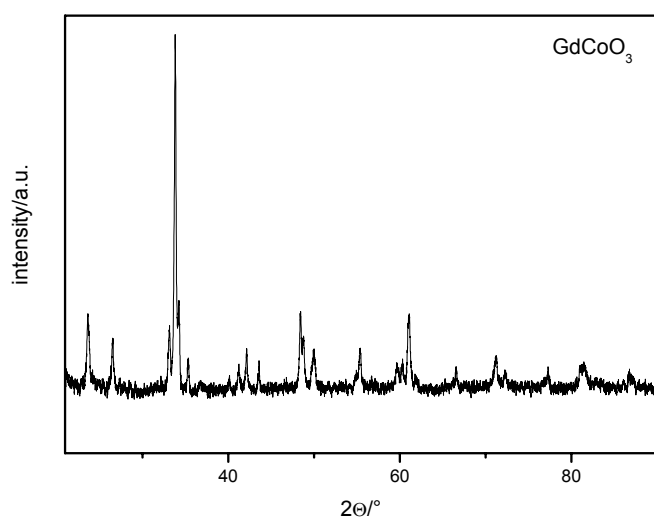
$\text{La}_{0.8}\text{Sr}_{0.2}\text{CoO}_3$ 

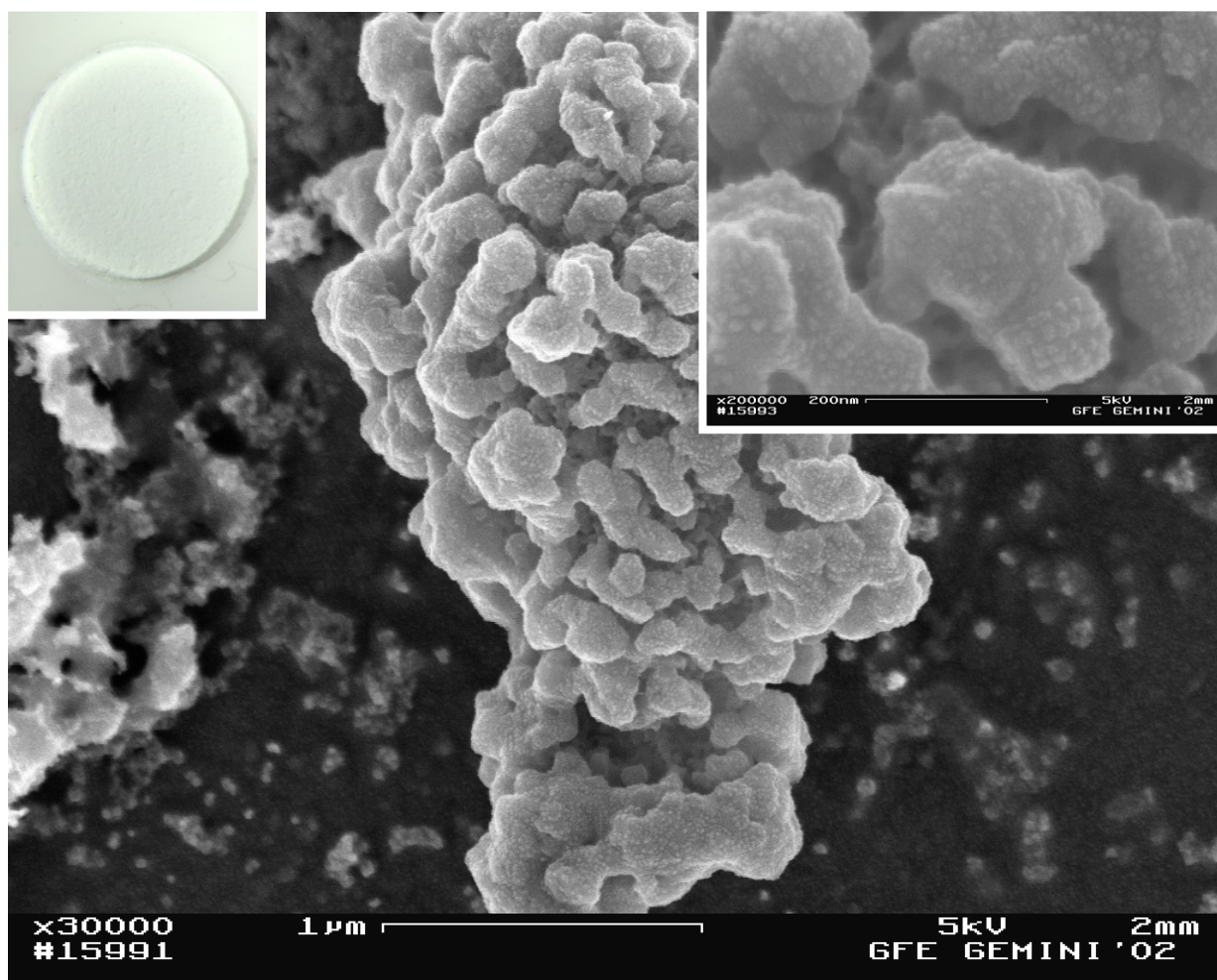
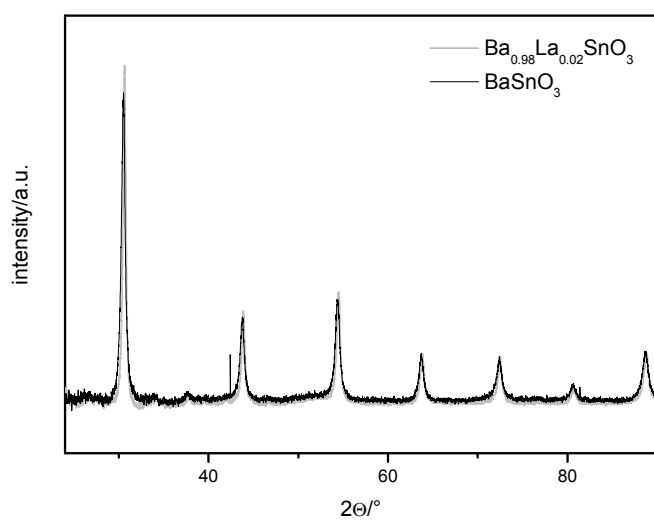
PbTiO₃

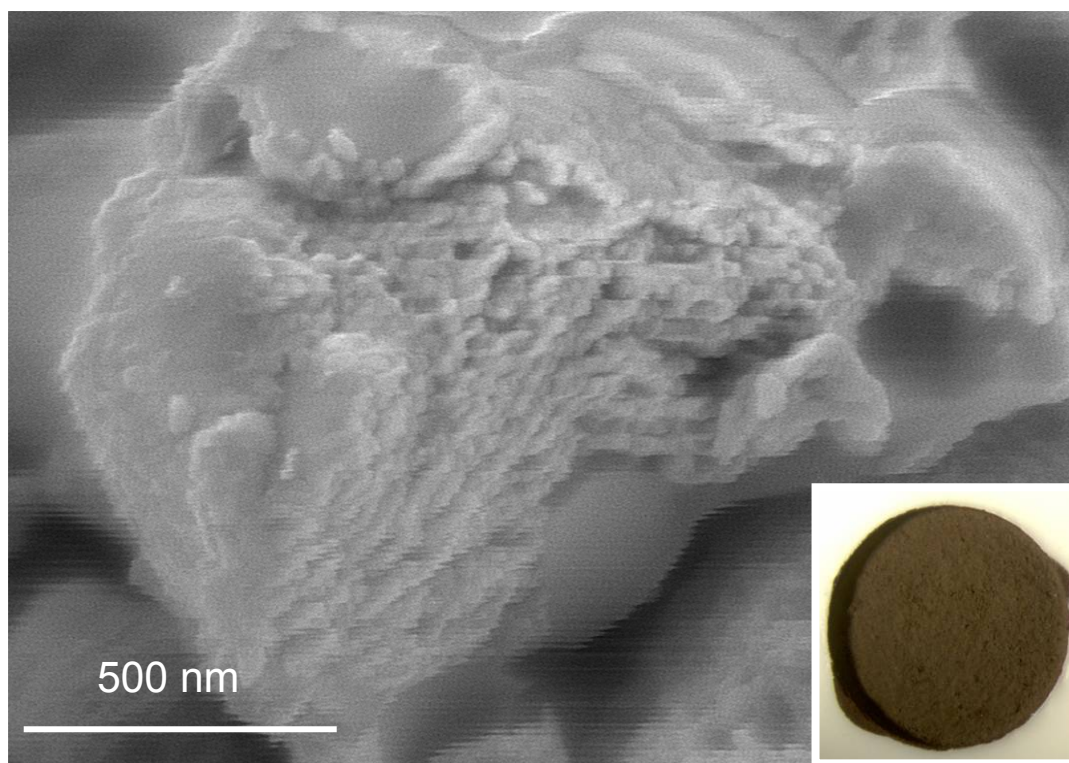
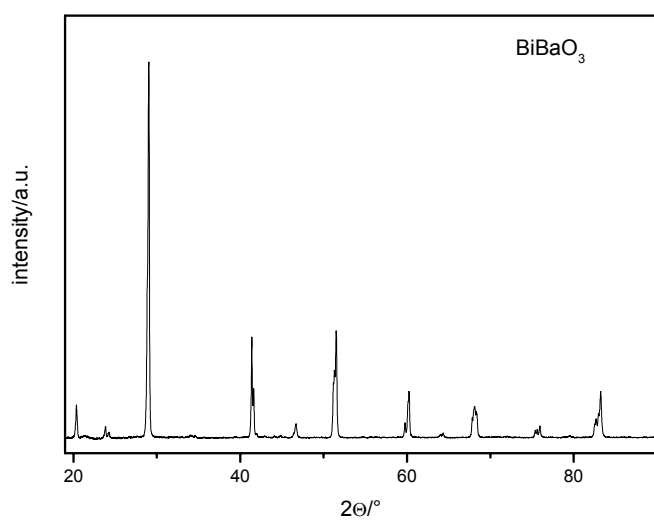
NdCoO₃

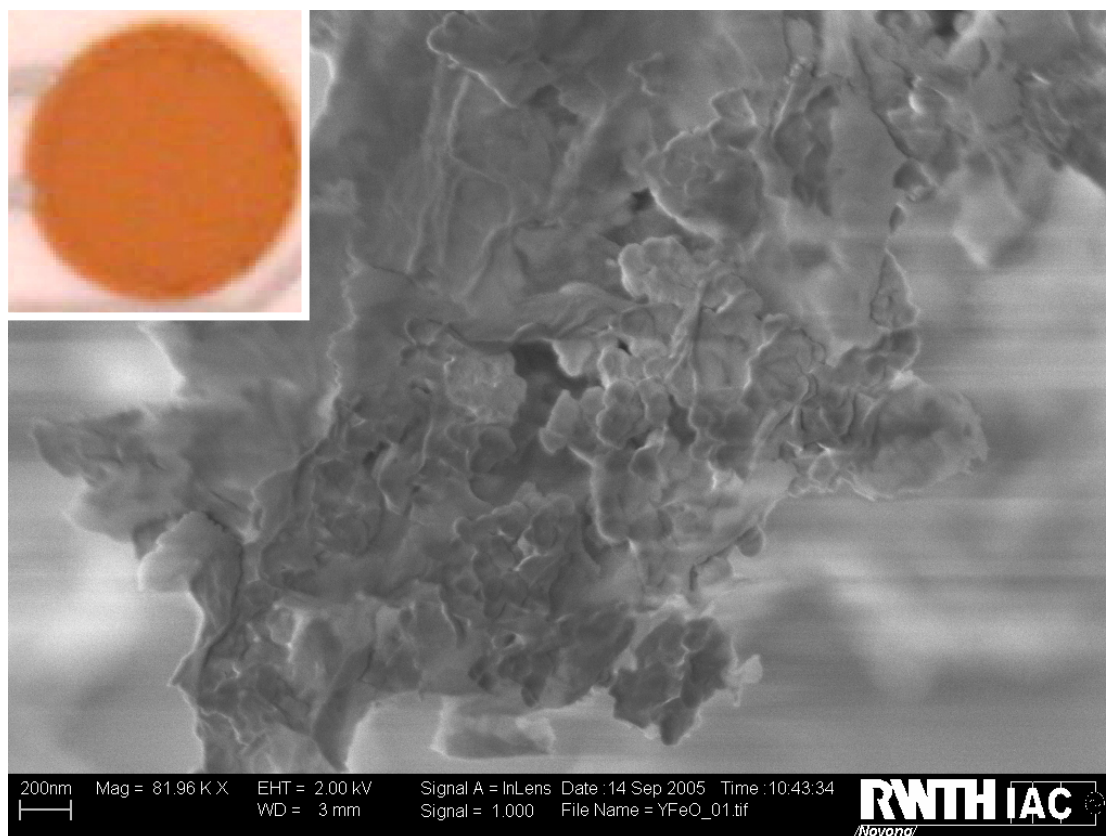
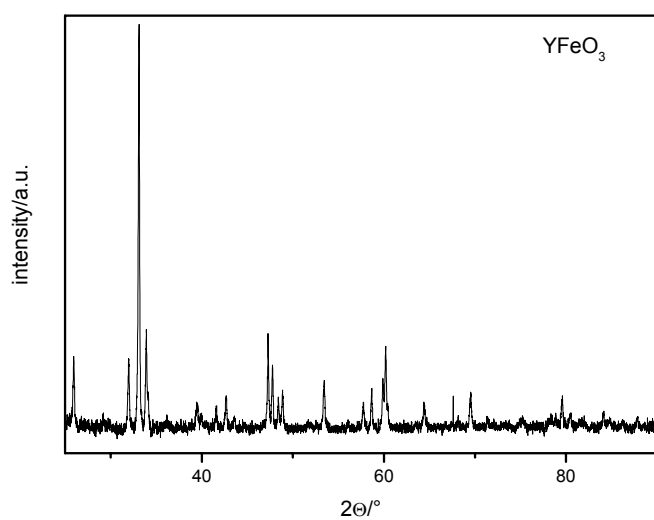
SmCoO₃

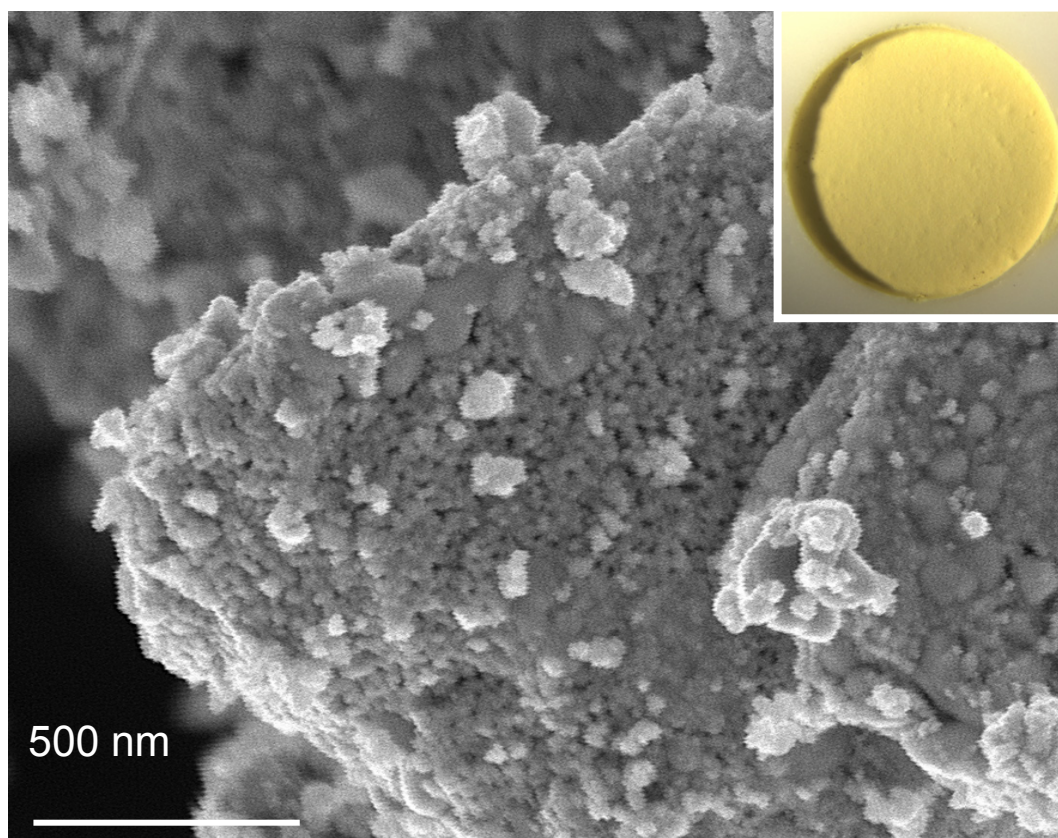
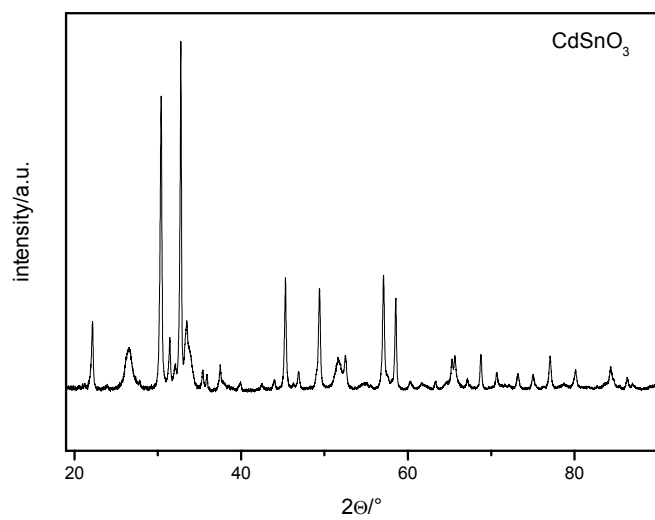
HoCoO₃

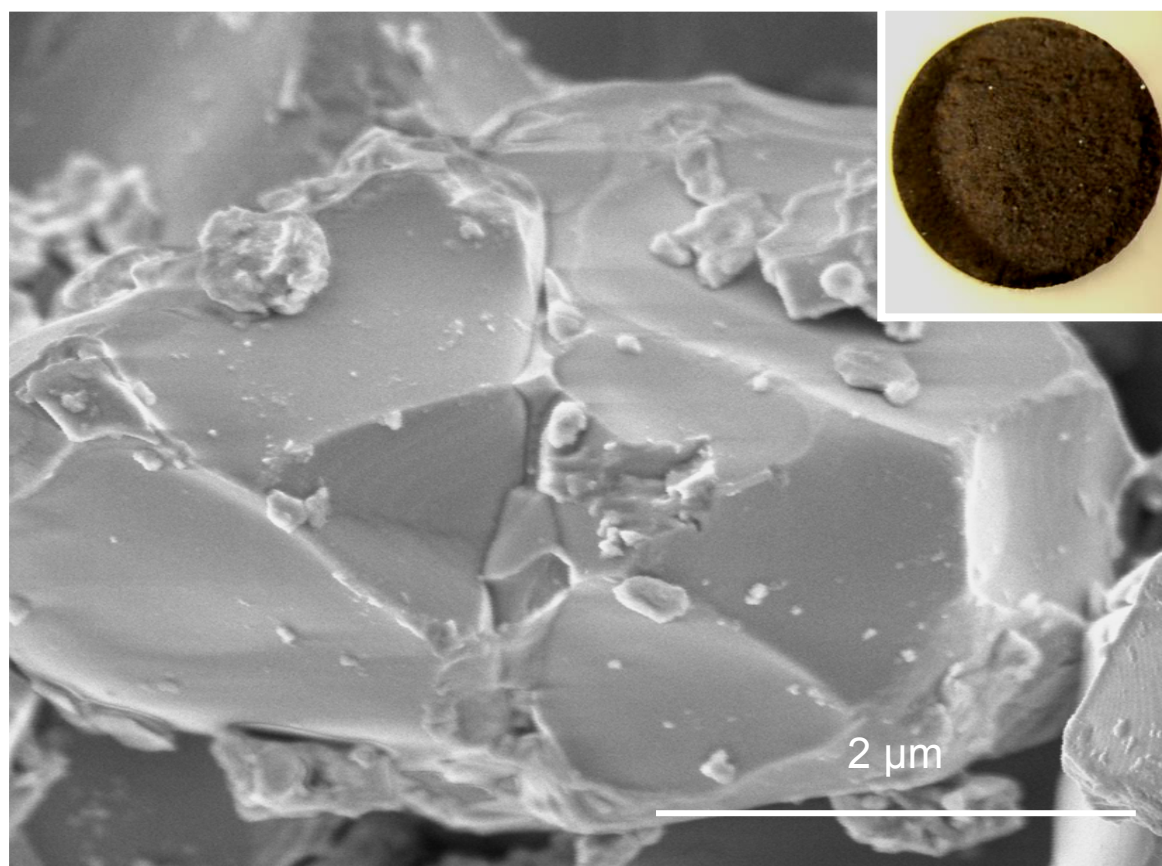
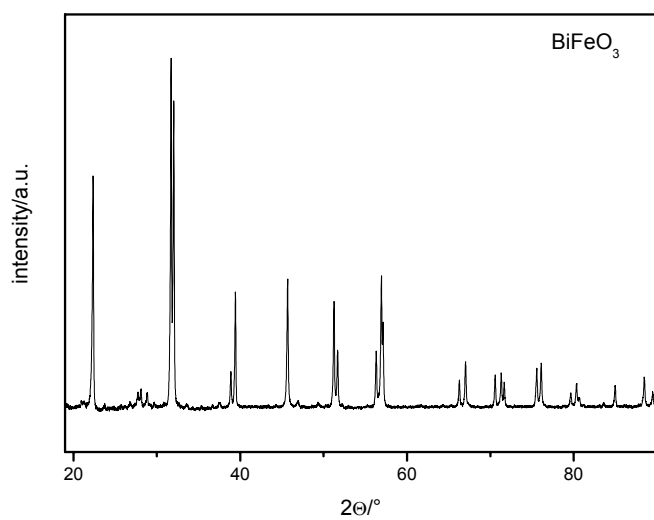
GdCoO₃

BaSnO₃ and Ba_{0.98}La_{0.02}SnO₃

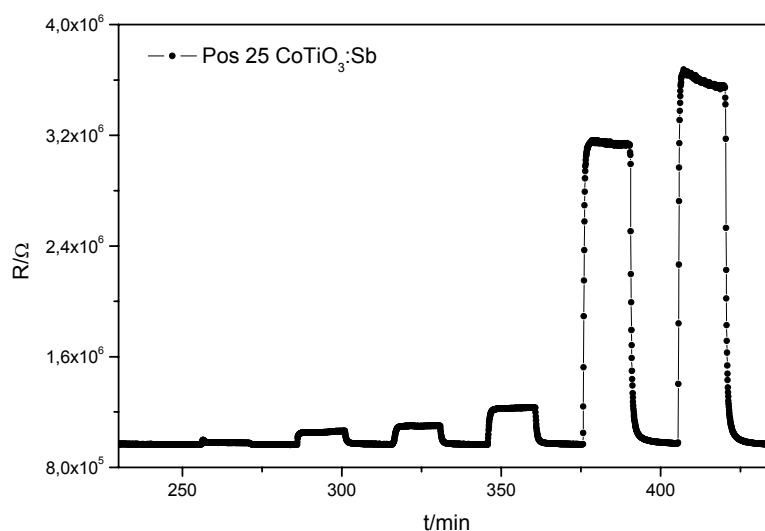
BiBaO₃

YFeO₃

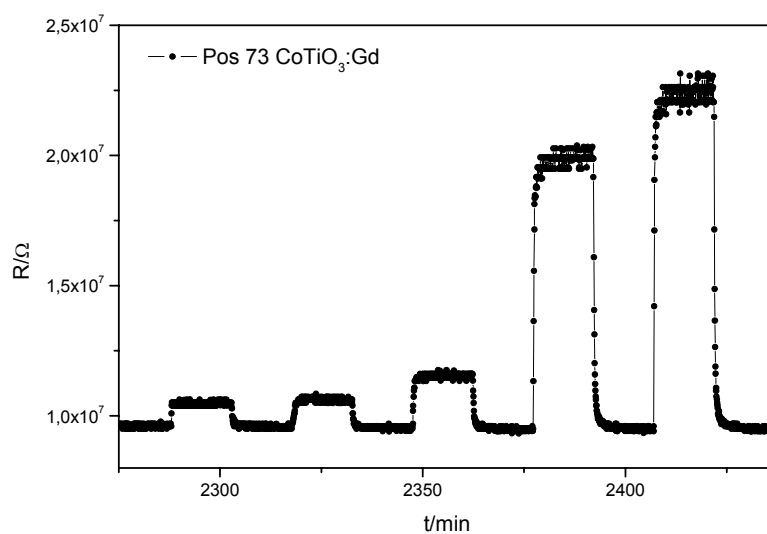
CdSnO₃

BiFeO₃

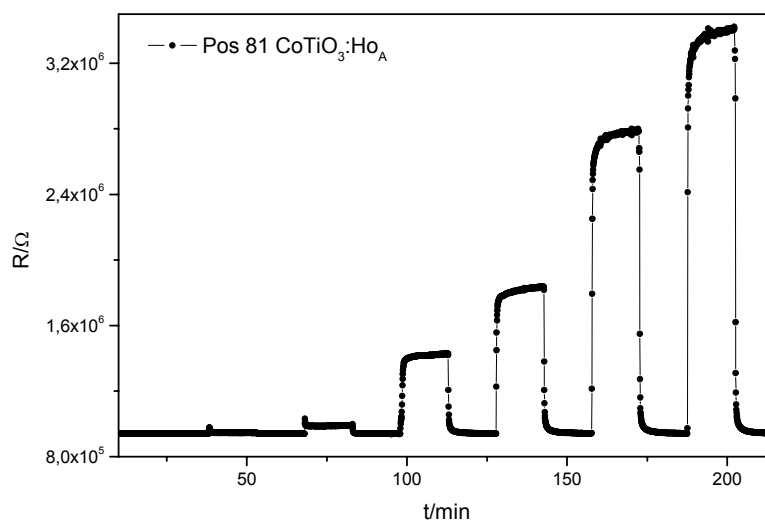
7.2 Response and recovery ability of volume doped CoTiO_3



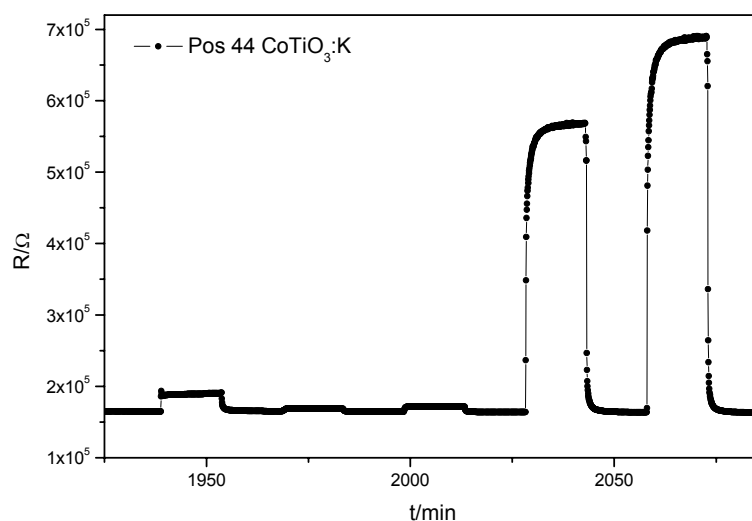
Response and recovery times of $\text{CoTiO}_3:\text{Sb}$ at 500°C to CO (25 ppm), NO (5 ppm), propylene (20, 40 ppm), and ethanol (40, 60 ppm).



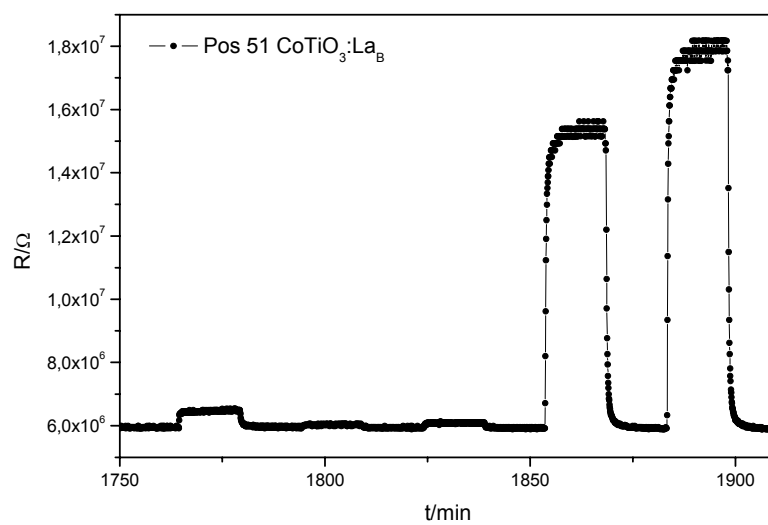
Response and recovery times of $\text{CoTiO}_3:\text{Gd}$ at 500°C to NO (5 ppm), propylene (20, 40 ppm), and ethanol (40, 60 ppm).



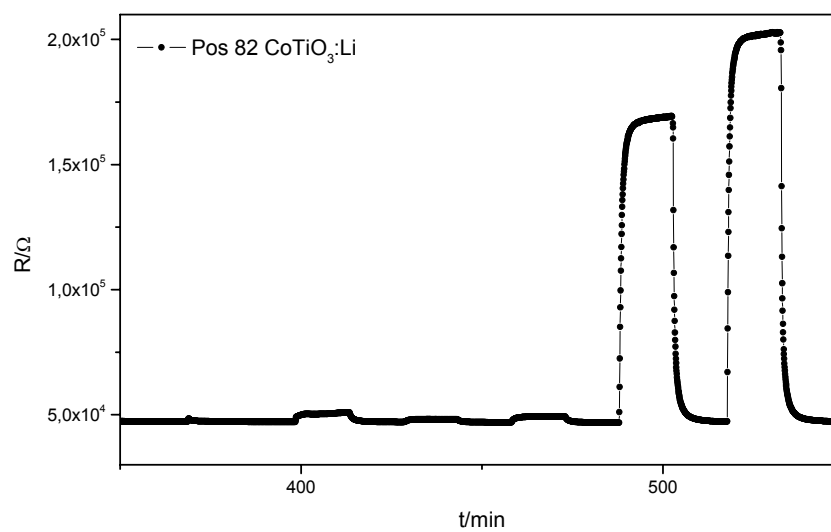
Response and recovery times of $\text{CoTiO}_3:\text{Ho}_A$ at 500°C to CO (25 ppm), NO (5 ppm), propylene (20, 40 ppm), and ethanol (40, 60 ppm).



Response and recovery times of $\text{CoTiO}_3:\text{K}$ at 500°C to NO (5 ppm), propylene (20, 40 ppm), and ethanol (40, 60 ppm).

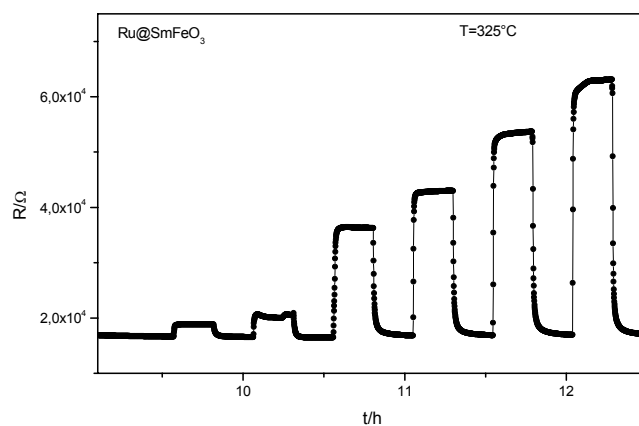


Response and recovery times of $\text{CoTiO}_3:\text{La}_B$ at 500°C to NO (5 ppm), propylene (20, 40 ppm), and ethanol (40, 60 ppm).

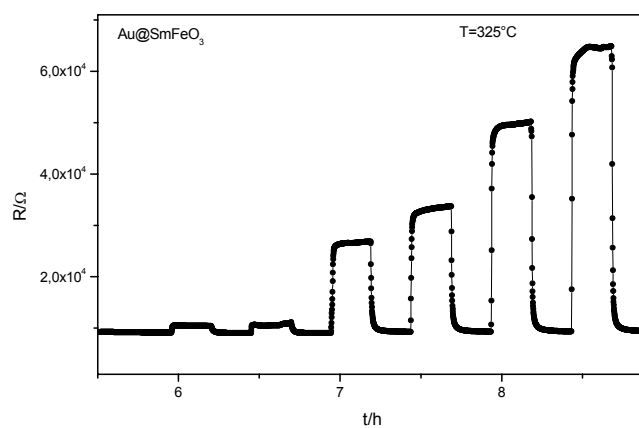


Response and recovery times of $\text{CoTiO}_3:\text{Li}$ at 500°C to CO (25 ppm), NO (5 ppm), propylene (20, 40 ppm), and ethanol (40, 60 ppm).

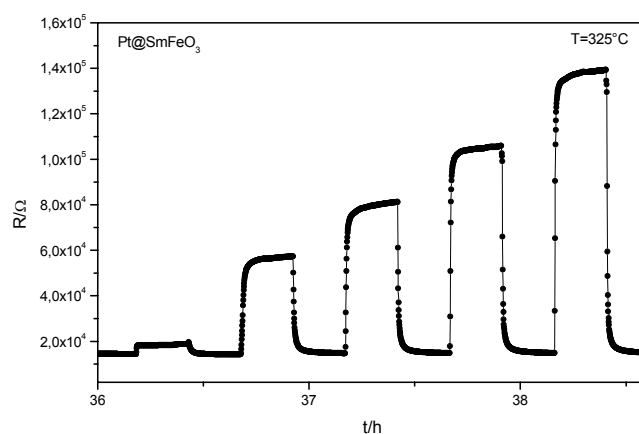
7.3 Response and recovery ability of surface doped SmFeO_3



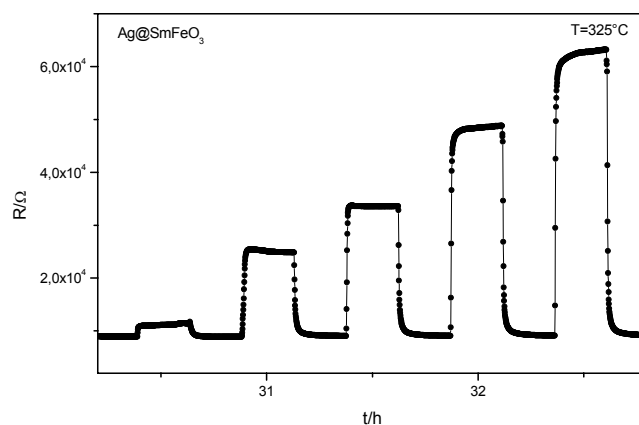
Response and recovery behaviour of Ru@SmFeO_3 to CO (25 ppm), NO (5ppm), propylene (20, 40 ppm), and ethanol (40, 60 ppm).



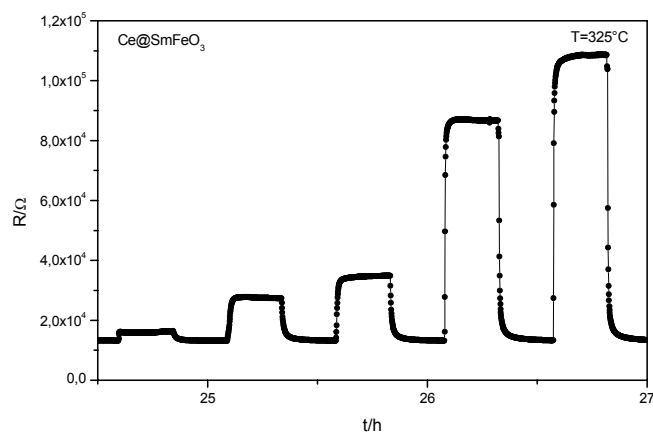
Response and recovery behaviour of Au@SmFeO_3 to CO (25 ppm), NO (5ppm), propylene (20, 40 ppm), and ethanol (40, 60 ppm).



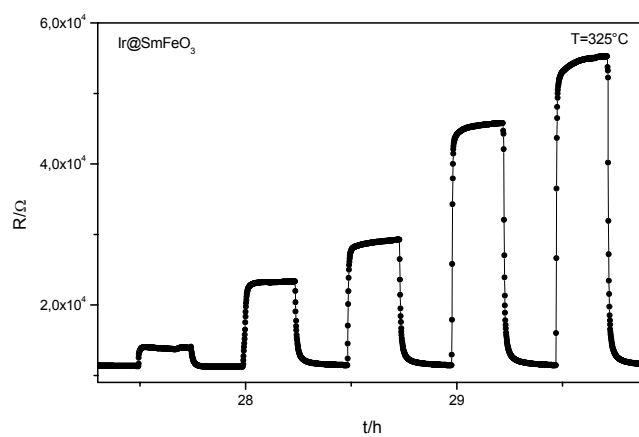
Response and recovery behaviour of Pt@SmFeO_3 to NO (5ppm), propylene (20, 40 ppm), and ethanol (40, 60 ppm).



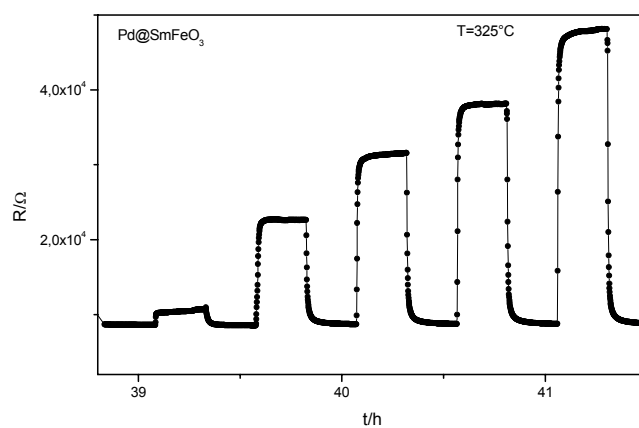
Response and recovery behaviour of Ag@SmFeO_3 to NO (5ppm), propylene (20, 40 ppm), and ethanol (40, 60 ppm).



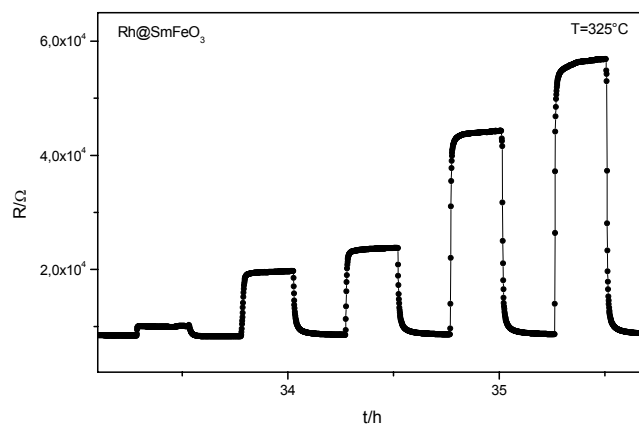
Response and recovery behaviour of Ce@SmFeO_3 to NO (5ppm), propylene (20, 40 ppm), and ethanol (40, 60 ppm).



Response and recovery behaviour of Ir@SmFeO_3 to NO (5ppm), propylene (20, 40 ppm), and ethanol (40, 60 ppm).



Response and recovery behaviour of Pd@SmFeO_3 to NO (5ppm), propylene (20, 40 ppm), and ethanol (40, 60 ppm).



Response and recovery behaviour of Rh@SmFeO_3 to NO (5ppm), propylene (20, 40 ppm), and ethanol (40, 60 ppm).

Curriculum Vitae

Personal Information:

Maike Siemons

*13.03.1978, Stolberg Rheinland

unmarried

german

Schooling:

1984-1986 elementary school Breinig, Stolberg Rheinland

1986-1988 elementary school Kornelimünster, Aachen

1988-1997 grammar school (Inda Gymnasium),
Kornelimünster, Aachen

1997 final secondary-school examinations

Academic Background:

10/1997 RWTH Aachen University

Chemistry (Diploma)

09/1999 pre-degree examination

02/2000 „Preis der Chemie“ honor

02/2001-05/2001 intership,
University of York (UK)

02/2003 diploma

diploma work title: „Nanostructured oxides as
base materials for new gas sensor systems“

06/2003 „Springorum-Gedenkmünze der RWTH Aachen“
honor

05/2003-08/2003 industrial intership BASF, Ludwigshafen

09/2003-12/2006 PhD at RWTH Aachen University
Institute for Inorganic Chemistry

Scholarship:

2001-2006 scholarship holder of Studienstiftung des
deutschen Volkes

Mein Dank gilt...

- Professor Dr. U. Simon für das interessante Doktorarbeitsthema, die Freiheit bei der Bearbeitung und die nette Betreuung.
- Professor Dr. W. F. Maier für die freundliche Übernahme des Korreferats.
- der Studienstiftung des Deutschen Volkes für finanzielle und ideelle Förderung, besonders meinem Vertrauensdozent Prof. Dr. D. Abel für die Zeit, die er mit uns verbracht hat.
- dem Bundesministerium für Bildung und Forschung (BmBF-Projekt „KOMBISENS“), sowie der Robert Bosch GmbH.
- K. Blech, M. Noyong und den Mitarbeitern des GFE unter Leitung von Prof. Dr. J. Mayer für die Anfertigung der REM- und TEM-Aufnahmen.
- der gesamten Arbeitsgruppe und den Mitarbeitern des IAC für ihre Hilfe, Diskussion und das angenehme Arbeitsklima. Besonders meinen Labormitbewohnern Dr. T. J. Koplin, Dr. D. Sanders, L. Rodriguez und K. Klöss für Diskussionsraum und alles darüber hinaus. M. Gilleßen für den kulturellen Ausgleich.
- Dr. D. Sanders für die Erleichterung meiner Arbeit durch Programmierungen für unsere Sensorwelt.
- A. Leifert für ihre engagierte Forschungsarbeit und die nette Zeit.
- V. Borisovna Zeldovich for the kindness to spend time on linguistic proof-reading.
- meinen Freunden und meiner Familie, besonders meinen Eltern und Pat, für ständigen Rückhalt, Verständnis und Geduld.
- den Leuten vom Hochschulsport für die Möglichkeit des Ausgleichs.
- all denen, die hier nicht namentlich genannt sind, aber zum Gelingen dieser Arbeit beigetragen haben.